Structure and Morphology of Sulfonated Polysulfone and Perfluorosulfonic Acid Ionomers

A Dissertation
Presented for the
Doctor of Philosophy Degree
The University of Tennessee, Knoxville

Chen Wang

August 2013

DEDICATION

This dissertation is dedicated to my wife, Chrissie, and our daughter, Ellie, who have supported and encouraged me throughout my entire academic career.

ACKNOWLEDGEMENTS

I would like to express gratitude to my principal advisor, Dr. Stephen J. Paddison, for his constant support and guidance throughout this research. I would also like to extend my thanks to my co-advisor, Dr. Gerd Duscher, for offering me a great opportunity to use the state-of-the-art experimental tools for this research. I sincerely appreciate Drs. John Dunlap, Veena Krishnan and Jihua Chen for their help in introducing me to the electron microscopy and sample preparation techniques. A special mention should be paid to Dr. Dongsheng Wu for his constant assistance in the field of computer simulations and programming. I also appreciate the help from members in our research group: Dr. Jun He, Dr. Hongjuan Zhu, Mr. Jeffrey Clark and Ms. Fatemeh Sepehr. Finally, I would like to express thanks to my parents for the support and encouragement that they have given me over the years.

This work was supported by Office of Basic Energy Sciences, U.S. Department of Energy Department of Energy, Shared Research Equipment (SHaRE) user facility at Oak Ridge National Laboratory (ORNL) and Sustainable Energy and Education Research Center (SEERC).

ABSTRACT

The limitations of conventional perfluorosulfonic acid (PFSA) based membrane materials have provoked the search for alternative materials which can function as the electrolyte in PEM fuel cells operated at higher temperatures (> 100 °C) and without humidification. A novel class of sulfonated poly(phenylene) sulfone ($sPSO_2$) ionomers have shown much higher proton conductivity than typical PFSA membranes at elevated temperatures. In this dissertation, both computational and experimental methods were used to investigate proton transfer, morphological and structural properties of $sPSO_2$ and PFSA ionomers. We have undertaken *ab initio* electronic structure calculations to understand the primary hydration and the transfer of protons in oligomeric fragments of $sPSO_2$ ionomers. Our results indicate that the interaction between neighboring sulfonic acid groups affect not only the conformation of the fragments, but also the transfer of protons in the first hydration shell. The effects of equivalent weight, molecular weight and water content on swelling properties of hydrated $sPSO_2$ ionomers were investigated by dissipative particle dynamics (DPD) simulations. The results show that the presence of continuous hydrated domains in $sPSO_2$ ionomers is nearly independent of the hydration conditions, which results in the high proton conductivity at low water content. The micro-phase separation in hydrated PFSA ionomers was studied by using BF and HAADF imaging in a TEM/STEM. The microstructural evolution as a function of water content is observed and in a good agreement with the results from previous DPD simulations. To understand local chemistry and molecular structures of ionomers, quantitative analyses were conducted based on the results from EELS in the low loss and core loss regions. Finally, the influence of phase transitions and polarization in PTFE chains was determined by comparing experimental and simulated EELS.

TABLE OF CONTENTS

Chapter 1 Introduction 1

1.1 Polymer Electrolyte Membrane Fuel Cells (PEMFC) 3
1.2 PEM Materials 6
1.3 Proton Conduction of Ionomers 10
1.4 Morphologies of PFSA Ionomers 12
1.5 Properties of Poly(phenylene sulfone) Ionomers 18
1.6 Electron Microscopy of Ionomers 21
1.7 Research Overview 25

Chapter 2 Computational Methods 26

2.1 First Principle Calculations 27
2.1.1 Schrödinger Equation 28
2.1.2 Hartree Fock Method 30
2.1.3 Density Functional Theory (DFT) 34
2.1.4 Exchange-correlation Functional 37
2.1.5 Basis Functions 40
2.2 Dissipative Particle Dynamics 43
2.2.1 Coarse-graining Theory 43
2.2.2 Dissipative Particle Dynamics Method 45
2.2.3 Flory-Huggins Theory 49
2.2.4 Scaling of Units 51

Chapter 3 Experimental Methods 53

3.1 Transmission Electron Microscopy (TEM) 53
3.1.1 Conventional Transmission Electron Microscopy (CTEM) 55
3.1.2 High Resolution TEM (HRTEM) 56
3.2 Scanning Transmission Electron Microscopy (STEM) 58
3.2.1 High Angular Annual Dark Field (HAADF) Imaging 60
3.2.2 Spectrum Imaging (SI) in STEM 62
3.3 Analytical Electron Microscopy (AEM) 65
3.3.1 Dispersive X-ray Spectroscopy (EDS) 66

3.3.2 Electron Energy Loss Spectroscopy (EELS) 67
3.3.3 Energy Filtered Transmission Electron Microscopy (EFTEM) 72
3.4 Cryo-TEM 74
3.5 Sample Preparation 75
3.6 Instrumentations 78

Chapter 4 Results and Discussion 79

4.1 Ab initio Study of Local Hydration and Proton Transfer of Polysulfone 79
4.1.1 Computational Details 79
4.1.2 Global Minimum Energy Structures 81
4.1.3 Backbone Conformation 83
4.1.4 Microsolvation 85
4.1.5 Proton Transfer 91
4.1.6 Summary 95
4.2 Modeling of Hydrated Morphologies of Polysulfone Ionomers 97
4.2.1 Modeling Details 98
4.2.2 Comparable Morphologies of Polysulfone and PFSA ionomers 101
4.2.3 Effect of Equivalent Weight 108
4.2.4 Effect of Molecular Weight 112
4.2.5 Backbone Aggregation and Flexibility 114
4.2.6 Summary 116
4.3 Electron Microscopy of PFSA Ionomers 118
4.3.1 Experimental Details 118
4.3.2 Crystallites in PFSA Membrane 121
4.3.3 Morphology of PFSA Membrane 124
4.3.4 Morphological Evolution in Hydrated Membranes 127
4.3.5 Elemental Mapping for Dry and Hydrated Membranes 129
4.3.6 Summary 130
4.4 EELS Investigations of Nafion and PTFE 131
4.4.1 Experimental Details 132
4.4.2 Simulation Details 132
4.4.3 EELS of Nafion and PTFE 136
4.4.4 Effect of Phase Transition 139

4.4.5 Polarization Dependence 143
4.4.6 Summary 146
Chapter 5 Conclusions 148
References 153
Appendices 163
Appendix A. Simulations of EELS 164
Appendix B. Selected Publications and Presentations 175
Vita 176

LIST OF TABLES

Table 4.1. Structural Data from optimized *meta-meta* and *ortho-ortho* $sPSO_2$[a] 86
Table 4.2. Binding Energies for *meta-meta*-$sPSO_2$ + *n* H_2O [a] 86
Table 4.3. Binding Energies for *ortho-ortho*-$sPSO_2$ + *n* H_2O[a] 89
Table 4.4. Macromolecule parameters for different ionomers with selected EWs and MWs 100
Table 4.5. Computed Flory-Huggins parameters χ and corresponding repulsion parameters a_{ij} describing pairwise conservative interactions of selected particles for different types of ionomers 100
Table 4.6. Morphology analysis of crystallites for dry and hydrated ionomers 123
Table 4.7. Structural parameters of temperature dependent phases of PTFE 135
Table 4.8. Peak analysis of fitted EELS spectra for PTFE 138

LIST OF FIGURES

Figure 1.1. Chemical structures of Nafion®. The equivalent weight (EW) is determined by the molecular weight (MW) of the side chain and on the choice of x, y and z..... 6

Figure 1.2. The "solvated hydronium complex" or "Eigen ion", (a) H_3O^+ $(H_2O)_3$, and the "shared proton complex" or "Zundel ion", (b) $H^+(H_2O)_2$. (see reference [67])..... 10

Figure 1.3. The mechanism of structural diffusion in water by hydrogen-bond breaking and forming processes, namely Eigen-Zundel-Eigen (EZE) mechanism. (see reference [75])..... 11

Figure 1.4. Gierke et al. established a cluster-network model for the morphology of hydrated Nafion. The side chain SO_3H groups were aggregated to form hydrated clusters embedded in the fluorocarbon phase. (see reference **[**93**]**) 14

Figure 1.5. Conceptual model for the evolution of morphological of the ionic domains in Nafion as the dry membrane is swollen with water to the state of complete dissolution.(from reference [95])..... 16

Figure 1.6. Chemical structure of sulfonated poly(phenylene sulfone) ($sPSO_2$) ionomers with EW of 360 and 220..... 18

Figure 1.7. Proton conductivity in the temperature range 110-160°C at a water pressure of $p(H_2O)$ = 1 atm for $sPSO_2$-220 and Nafion 117.(from reference [23])..... 19

Figure 1.8. SAXS profiles of sulfonated poly(p-phenylene sulfone)s and Nafion 117. (from reference [22]) 20

Figure 2.1. Different length and time scales for the simulation of soft matter. (from reference [121])..... 26

Figure 2.2. Coarse-graining of a random ethylene oxyphenyl copolymer by constructing different beads representing polymer subunits. (from help document in Materials Studio [136]) 44

Figure 3.1. Different ray diagrams representing parallel (left) and converged (right) illumination in TEM and SPOT mode (from Zeiss Libra 200MC manual)..... 54

Figure 3.2. Illustration of mass-thickness contrast showing the distribution of small gold particles and polystyrene latex spheres on a thin carbon support. (from reference [139])..... 56

Figure 3.3. (a) HRTEM image of thin film PTFE with 157 helical conformation and (b) corresponding microdiffraction pattern; (c) is a Fourier filtered image and (d) is a simulated image. (from reference [140]) 57

Figure 3.4. Ray diagram in STEM mode, where the scan and descan of beam are controlled by two pairs of deflection coils above and below the specimen. (from Zeiss Libra 200MC manual) 59

Figure 3.5. Illustration of different detectors for collecting various signals during the scan in the STEM mode (from Zeiss Libra 200MC manual) 60

Figure 3.6. Electron micrograph showing acidic clusters in a dry PSS- PMB membrane and cluster size distribution determined from the micrograph.(from reference [142]) 62

Figure 3.7. Formation of a Spectrum Image in STEM mode. (from Gatan EELS school tutorial) 63

Figure 3.8. (A) HAADF STEM image of a two-phase nanocolloid consisting of PDMS (dark contrast) and acrylate (light contrast) rich phases in amorphous ice carried by a holey-carbon support film. (B) low-loss EELS reference spectra of the PDMS (green), the acrylate copolymer (red), and amorphous ice (blue). Spectrum images derived by mapping PDMS (C), acrylate (D), and water (E).(from reference [144)..... 64

Figure 3.9. Different types of signals generated by the elastic and inelastic interactions between a high-energy beam of electrons and a thin specimen.(from reference [138])..... 65

Figure 3.10. SE and BSE micrographs of a DMFC anode catalyst layer and elemental maps for carbon (C), fluorine (F), platinum (Pt) and ruthenium (Ru) for the same region obtained by EDS mapping.(from reference [119])..... 66

Figure 3.11. An EELS of Si showing information extracted at different energy scale (Courtesy of Gerd Duscher) 68

Figure 3.12. Relationship between the unoccupied DOS and the ELNES.(from reference [138]) 69

Figure 3.13. Schematic of the transition processes in some of the spectroscopic techniques that can probe electronic structure.(from reference [146]) 71

Figure 3.14. EELS spectra of PET at the carbon K-edge with energy resolution of 0.7 eV, with the electron dose estimated to be (a) 3.2×103 C/m^2; (b) 3.2×104 C/m^2 and (c) 3.2×106 C/m^2. (from reference [147]) 71

Figure 3.15. Formation of a spectrum image in TEM mode, where parallel illumination is used to generate a series of energy filtered images (from Gatan EELS school tutorial) 72

Figure 3.16. EFTEM of a 100 nm thick 50:50 (w/w) blend of P3HT and PCBM, (a) EELS spectra from pure P3HT (red) and pure PCBM (blue), (b) Zero loss image, (c) 19 eV loss image and (d) 30 eV image.(from reference [148]) 73

Figure 4.1. Fully optimized (B3LYP/6-311G**) global minimum energy structures of $sPSO_2$ dimer distinguished by the positions of sulfonic acid groups corresponding to the central sulfone are listed in: (a) *meta-meta* $sPSO_2$ and (b) *ortho-ortho* $sPSO_2$. The corresponding trans conformation of above $sPSO_2$ dimers are displayed in (c) and (d). The total electronic energies (with ZPE corrected) of *meta-meta* structure are 2.78 kcal/mol less than those of *ortho-ortho* dimer. 82

Figure 4.2. Relative rotational energies along central C-S bonds of *meta-meta* $sPSO_2$ dimer obtained at B3LYP/6-31G**. The starting structure possesses a trans conformation where -SO_3H groups reside on opposite sides of -SO_2- group. The total electronic energies of this structure are 3.41 kcal/mol more than the corresponding global minimum structures. Two peaks of relative rotational energies are 3.29 kcal/mol and 3.43 kcal/mol respectively 84

Figure 4.3. Relative rotational energies along central C-S bonds of *ortho-ortho* $sPSO_2$ dimer obtained at B3LYP/6-31G**. The starting structure possesses a *trans* conformation where -SO_3H groups reside on opposite sides of -SO_2- group. The total electronic energies of this structure are 2.91 kcal/mol more than the corresponding global minimum structures. Two peaks of relative rotational energies are 15.54 kcal/mol and 8.17 kcal/mol. 85

Figure 4.4. Fully optimized (B3LYP/6-31G**) global minimum energy structures of *meta-meta*-$sPSO_2$ dimer with *n* water molecules: (a) *n*=0; (b) *n*=3; (c) *n*=4; (d) *n*=6. The proton dissociation occurs when three water molecules were added. 87

Figure 4.5. Fully optimized (B3LYP/6-31G**) global minimum energy structures of *ortho-ortho*-$sPSO_2$ dimer with *n* water molecules: (a) *n*=0; (b) *n*=3; (c) *n*=4; (d) *n*=6. The proton dissociation occurs when four water molecules were added 88

Figure 4.6. Relative energy profiles of proton transfer in the *meta*−*meta*-$sPSO_2$ dimer + 6H_2O at HF/6-31G** and B3LYP/6-31G** levels as a function of the asymmetric stretch coordinate. Only one −SO_3 group is involved in the transfer model. The energy barrier is 1.91 kcal/mol. 92

Figure 4.7. Relative energy profiles of proton transfer in the *ortho*−*ortho*-$sPSO_2$ dimer + 6H_2O at HF/6-31G** and B3LYP/6-31G** levels as a function of the asymmetric stretch coordinate. Only one −SO_3 group is involved in the transfer model. The energy barrier is 1.85 kcal/mol. 93

Figure 4.8. Relative energy profiles of proton transfer in the *meta*−*meta*-$sPSO_2$ dimer + 6H_2O at HF/6-31G** and B3LYP/6-31G** levels as a function of the asymmetric stretch coordinate. Two −SO_3 groups at the same side of the Zundel ion are involved in the transfer model. No apparent barrier was found. 94

Figure 4.9. Relative energy profiles of proton transfer in the *meta*−*meta*-$sPSO_2$ dimer + H_2O at HF/6-31G** and B3LYP/6-31G** levels as a function of the asymmetric stretch coordinate. Two −SO_3 groups at opposite sides of Zundel ion are involved in the transfer model. The energy barrier is 0.66 kcal/mol. . 94

Figure 4.10 Macromolecular structures of various ionomers in the simulations: (a) $sPSO_2$ ionomers with EWs of 360, 430, 781 and 1014 g/mol; (b) Highly sulfonated $sPSO_2$ ionomer with EW=220 g/mol; (c) Nafion and (d) SSC PFSA ionomers. EWs and MWs of ionomers are determined by the choice of parameters: *m, n* and *p*. 99

Figure 4.11. Comparison of equilibrium morphologies of the $sPSO_2$ (EW=1014) and Nafion (EW=1244) ionomers with water content λ=7, 11 and 15. Hydrophobic backbones of ionomers are represented by beads *A, F, O* and *O′* showing in red, while beads of sulfonated side chains and water clusters are in green and blue, respectively..... 102

Figure 4.12. Contour plots of the densities of water particles mapped on the cross sections of simulation boxes for $sPSO_2$-1014 and Nafion at water content λ=7, 11 and 15. The water-rich regions are shown in red while backbone matrix is in blue. The densities of water and backbone beads are indicated by the intensities of colors. 103

Figure 4.13. Comparison of equilibrium morphologies of the $sPSO_2$ (EW=781) and SSC (EW=828) ionomers with water content λ=7, 11 and 15. Hydrophobic backbones of ionomers are represented by beads *A, F, O* and *O′* showing in red, while beads of sulfonated side chains and water clusters are in green and blue, respectively..... 104

Figure 4.14 Contour plots of the densities of water beads mapped on the cross sections of simulation boxes for $sPSO_2$-781 and SSC-828 at water content λ=7, 11 and 15. The water-rich regions are shown in red while backbone matrix is in blue. The densities of water and backbone beads are indicated by the intensities of colors. 105

Figure 4.15. Radial distribution function of water particles for different ionomers with water content λ=7, 11 and 15: (a) $sPSO_2$-1014; (b) Nafion; (c) $sPSO_2$-781 and (d) SSC-828. 106

Figure 4.16. Comparison of radial distribution functions of water particles for different ionomers at the same water content (a) λ=7; (b) λ=11 and (c) λ=15, and (d) the average size of water clusters in these ionomers as a function of water content. 107

Figure 4.17. Equilibrium morphologies of the $sPSO_2$ with EWs of 220 and 360 g/mol at water content λ=7, 11 and 15. Hydrophobic fragment of ionomers are represented by beads *A* showing in red, while beads of sulfonated groups and water clusters are in green and blue, respectively. 109

Figure 4.18. Contour plots showing the densities of water particles mapped on the cross sections of simulation boxes for $sPSO_2$ ionomers with EWs of 220 and 360 g/mol at water content λ=7, 11 and 15. The water-rich regions are shown in red while backbone matrix is in blue. The densities of water and backbone beads are indicated by their intensities. 110

Figure 4.19. Radial distribution functions of water particles for $sPSO_2$ ionomers with different EWs at water content λ=7, 11 and 15: (a) $sPSO_2$-220 and (b) $sPSO_2$-360. 110

Figure 4.20 Average size of water clusters of different $sPSO_2$ ionomers as a function of (a) EWs and (b) water content. 111

Figure 4.21. Average size of water clusters as a function of hydration levels for various ionomers with different MWs: (a) $sPSO_2$-220; (b) $sPSO_2$-360; (c) $sPSO_2$-430; (d) $sPSO_2$-781; (e) $sPSO_2$-1014 and (d) Nafion. 113

Figure 4.22. Root mean square endpoint distances (of simulated mesomolecules as a function of water content for (a) $sPSO_2$ ionomers with 200 beads per backbone chain; (b) $sPSO_2$ ionomers with 400 beads per backbone chain; (c) PFSA ionomers with 400 beads per backbone chain. 115

Figure 4.23. Log-log plot of root mean square endpoint distances as a function of number of backbone beads per molecule for $sPSO_2$ ionomers at different water content (a) $sPSO_2$ -220 (b) $sPSO_2$-360. 116

Figure 4.24. Chemical structures of PFSA ionomers: (a) Nafion; (b) 3M ionomer and (c) Solvay Solexis Aquivion ionomer. Each of them has a single sulfonic acid ($–SO_3H$) pendant group on the side chain. The

equivalent weight (EW) is determined by the molecular weight of the side chain and on the choice of x, y and z. 119

Figure 4.25. (a) High Resolution (HR) TEM bright field image of the dry 3M-636 ionomer (non-ion exchanged) and (b) STEM Z-contrast image of the same area in dry 3M-636 ionomer. 122

Figure 4.26. Comparison of the morphology of Nafion-1100: (a) HAADF (Z-contrast) images of dry ionomer samples prepared by solution casting at room temperature; (b, c) Contour plots of water density distribution obtained from DPD simulations for Nafion with EW=1244 at water content of $\lambda = 9$, and $\lambda = 15$, respectively. Bright regions in the Z-contrast image are areas containing high density of the sulfonic acid groups. 125

Figure 4.27. Comparison of the morphology of 3M-636: (a) HAADF (Z-contrast) images of dry ionomer samples prepared by solution casting at room temperature; (b, c) Contour plots of water density distribution obtained from DPD simulations for 3M PFSA ionomer with EW=635 at water content of $\lambda = 9$, and $\lambda = 15$, respectively. 126

Figure 4.29. Comparison of the morphology of Aquivion-830: (a) HAADF (Z-contrast) images of dry ionomer samples prepared by solution casting at room temperature; (b, c) Contour plots of water density distribution obtained from DPD simulations for Aquivion with EW=849 at water content of $\lambda = 9$, and $\lambda = 15$, respectively. 126

Figure 4.30. Comparison of Z-contrast images obtained from cryo-STEM and DPD simulation results for the same system: (a) Z-contrast image of dry 3M-636 ionomer; (b-c) Z-contrast images of hydrated 3M-636 ionomer prepared by cryo-plunger; (d) water distribution representation of the same ionomer at low water content ($\lambda = 6$) from our previous work[41]; (e) 'artist' depiction of the 3D continuous network (light blue regions) of ionic clusters (black dots) in a semi-crystalline fluorocarbon matrix (dark blue 'rods')[104]; (f) water distribution representation of the same ionomer under fully hydrated condition ($\lambda = 24$) from our prior simulations. [41] 128

Figure 4.31. TEM and Z-Contrast images of cryo-plunged hydrated 3M-636 samples and corresponding EDS maps for carbon (blue), fluorine (green), oxygen (magenta) and sulfur (yellow). 129

Figure 4.32. Cryo-EFTEM Map of cryo-plunged 3M-636 samples (a) C-K map; (b) S-L map; (c) O-L map; (d) Elastic filtered image and (e) composite RGB color map (green: carbon, red: sulfur, blue: oxygen). 130

Figure 4.33. Molecular structures of PTFE chains in different polymorphic phases as temperature increases from 19 °C to 330 °C 134

Figure 4.34. Unit cell structure of PTFE H-157, where helical PTFE chains are oriented in the direction of *c* axis. 134

Figure 4.35. Comparison of EELS spectra of Nafion and PTFE acquired in the same experimental conditions: (a) low-loss (0-30eV); and (b) C-K ELNES (280-310 eV) 137

Figure 4.36. Quantitative analysis and fitting of EELS for PTFE: (a-b) Low loss; (c-d) Core loss C-K ELNES 138

Figure 4.37. Simulated low loss and carbon K-shell excitation spectra for PTFE with different conformation (planar, H136, H157 and defected) are compared with experimental results. 140

Figure 4.38. Real and imaginary part of dielectric functions ε and corresponding energy loss function for PTFE with different conformations. 141

Figure 4.39. Projected Density of States (PDOS) of carbon calculated from band structure calculations for PTFE with different conformations 142

Figure 4.40. Calculated low loss EELS as a function of the direction of momentum vector q for (a) planar PTFE and (b) helical H157 PTFE. The highlighted area shows the characteristic peak at 6 eV corresponding to the longitude component of polarization ($\mathbf{q} \parallel c$) illustrated on the right. 144

Figure 4.41. Calculated C-K ELNES as a function of the direction of momentum vector **q** for (a) planar PTFE and (b) helical H157 PTFE. The highlighted areas show the characteristic features in the range of 287-295 eV that are correlated with transverse component of polarization $\mathbf{q} \perp c$ illustrated on the right. 145

Figure A.1. Calculated low loss EELS and C-K ELNES for PTFE using TDDFT-RPA method. The highlighted areas show the features dependent upon the presence of helical conformations. 164

Figure A.2. Calculated real and imaginary parts of the dielectric function and corresponding energy loss function of planar PTFE as a function of momentum transfer **q**. 165

Figure A.3. Calculated real and imaginary parts of the dielectric function and corresponding energy loss function of helical H136 PTFE as a function of momentum transfer **q**. 166

Figure A.4. Calculated real and imaginary parts of the dielectric function and corresponding energy loss function of helical H157 PTFE as a function of momentum transfer **q**. 167

Figure A.5. Calculated real and imaginary parts of the dielectric function and corresponding energy loss function of helical defected PTFE as a function of momentum transfer **q**. 168

Figure A.6. Calculated low loss EELS and C-K ELNES for PTFE-H136 as a function of momentum transfer **q**. 169

Figure A.7. Calculated low loss EELS and C-K ELNES for defected PTFE as a function of momentum transfer **q**. 170

Figure A.8. Calculated low loss EELS and C-K ELNES for planar PTFE using TDDFT-RPA method with and without consideration of the local field effect. 171

Figure A.9. Calculated low loss EELS and C-K ELNES for PTFE H157 using TDDFT-RPA method with and without consideration of the local field effect. 172

Figure A.10. Calculated low loss EELS and C-K ELNES for planar and helical H157 PTFE using TDDFT-RPA method compared with experimental results. 173

Figure A.11. Calculated C-K ELNES for planar H157 PTFE using BSE method compared with experimental results. 174

Chapter 1 Introduction

The development of a global economy has directed the growing demand for more environmentally friendly energy sources that do not rely heavily on fossil fuels. Among many novel energy technologies, fuel cells have become a leading candidate to replace internal combustion engines due to their high efficiency and low emission of pollutants. A variety of fuel cell designs have been developed in the past two decades. Polymer electrolyte membrane fuel cells (PEMFC's) in particular have attracted considerable interest as one of the most promising energy conversion systems for automobiles and portable device applications.[1, 2]

Since operational efficiency of PEM fuel cells greatly relies on the rate of proton transport through the electrolyte, it is crucial to use membrane materials possessing high proton conductivity (≥ 0.1 S cm^{-1}) over a range of operating conditions.[3, 4] The membrane serves as an important component that impacts the efficiency of the fuel cell, and consequently, numerous studies have been undertaken to develop highly proton conductive membrane materials.[5-16] Perfluorosulfonic acid (PFSA) ionomers, such as Nafion®, are commonly used as the electrolyte material but only exhibit high proton conductivity when fully hydrated (i.e., 100% relative humidity).[17-19] The limitations associated with the use of Nafion have propelled the search for alternative materials, which can function as the electrolyte in fuel cells at higher temperatures (>100 °C) and without humidification. In the years following the introduction of Nafion, several alternative membrane materials have been developed by Dow and 3M, such as a perfluorinated polymers with short side chains[20]; however, Nafion remains the primary membrane material used in commercial fuel cells to date, and a number of new types of membranes are under continued investigation.

A novel class of sulfonated poly(phenylene) ($sPSO_2$) ionomers consisting of aromatic rings and sulfone units ($–SO_2–$) have recently been synthesized and characterized.[21-23] These ionomers show considerable thermo-oxidative and hydrolytic stability due to the highly electron-deficient phenyl rings and electron-accepting sulfone units in the backbone. At high temperatures (110-160°C) and under 100% relative humidity atmosphere ($p(H_2O)$ = 1 atm) $sPSO_2$ ionomers exhibit from 5 to 7 times higher proton conductivity than observed in Nafion. The highly sulfonated $sPSO_2$ ionomers, in contrast to the hydrophobic polytetrafluoroethylene (PTFE) backbone in Nafion, are water-soluble due to the highly sulfonated phenylene backbone. The water diffusion is greatly affected by the microstructure, where the formation of hydrophilic domains upon hydration are quite narrow among highly concentrated protogenic groups ($–SO_3H$). In addition, sulfone units ($–SO_2–$) play important roles in forming intermolecular hydrogen bonding with the $–SO_3H$ groups, which potentially influence the structural and chemical properties of the ionomer.

While various theoretical studies have elucidated the fundamental proton transfer mechanism in typical proton conducting solvents such as water or imidazole[24-27], the proton transfer property in sulfonated aromatic systems is still unclear. First-principle electronic structure calculations can offer a fundamental insight into the local hydration of polysulfone systems, and are helpful to identify the important aspects to enhance proton transfer in membranes operating at high temperatures.

It is known that the presence of water and the chemistry of the side chains affect not only the proton conductivity but also the morphological properties of the PFSA ionomers.[28] Under hydrated conditions, the aggregation of sulfonic acid groups on the side chains form hydrophilic "ionic cluster" domains where protons dissociation and transfer occurs. Meanwhile, hydrophobic regions are formed by chemically stable fluorocarbon backbones. As a result, micro-phase

separation is observed between hydrophilic and hydrophobic domains. A fundamental insight into the chemical microstructure and nanoscale morphology for PFSA ionomers is critical to: optimizing performance, enhancing durability, and designing low cost devices. A wealth of research has been undertaken to elucidate structure–morphology relationships over the past two decades through a variety of experimental[29-36] and multi-scale modeling approaches.[37-42]

This dissertation focuses on understanding microstructure and transport properties of proton exchange membranes through multiscale simulations and experimental methods. Specifically, proton conduction and binding of water in the ionomer fragments were examined with electronic structure calculations. The hydrated morphology of various membranes were simulated and compared with TEM/STEM results. Chemical structures and degradation of the ionomers were investigated by EELS experiments. The goals of this work are to correlate the chemical structure, hydrated morphology, and proton transport properties of membranes. A combination of theoretical and experimental studies can provide insightful knowledge to understand and improve membrane's performance in fuel cell applications.

1.1 Polymer Electrolyte Membrane Fuel Cells (PEMFC)

Fuel cells are energy conversion devices that convert stored chemical energy in the fuel to electrical energy through electrochemical reaction. The fuel is supplied to the anode and is oxidized by a metal catalyst. At the same time, the oxidant is fed to the cathode to produce a continuous electrical current. Therein, the reaction continues to produce electrical energy for as long as the fuel is supplied, in contrast to typical electrochemical energy storage devices like batteries. Fuel cells also have an attractive feature of being more efficient compared to other devices. Fuel cells directly convert chemical to electrical energy, while contemporary thermal engines are limited by the Carnot efficiency. A successful demonstration of a fuel-cell-powered

vehicle suggests the possibility for ubiquitous fuel cell applications in the automobile industry. As a potential replacement for fossil fuel-based power, fuel cells may become one of the most important power sources in the future.

A diverse array of fuel cell systems have been developed using different fuel sources (e.g., hydrogen and methanol), different electrode designs (e.g., the modified electrode surface), and different electrolyte materials (e.g., liquid or solid phase materials).[43] Fuel cells are typically classified by the type of electrolyte used, and hence there are polymer electrolyte membrane fuel cells (PEMFCs), alkaline fuel cells (AFCs), phosphoric acid fuel cells (PAFCs), molten carbonate fuel cells (MCFCs), and solid oxide fuel cells (SOFCs). All of these fuel cells have different operating temperature ranges. For example, the operating temperatures of MCFC's and SOFC's are in the range of 650 to 1000 °C, and are much higher than the other three classes, which range from 40 to 200 °C. Among the PEMFC, AFC, and PAFC classes being tested as vehicle power sources, PEMFCs have proven to be the winner due to their relatively high power densities at low operating temperatures.

Unlike other commonly used fuel cells, PEMFCs use a solid polymer electrolyte instead of a liquid. By avoiding the use of liquid acids, as in phosphoric acid fuel cells, or bases, as in alkaline fuel cells, they are more safely operated, sealed, handled, and assembled. Furthermore, their light-weight stack structures make them more suitable for portable power applications. Low operating temperature and superior power density are two distinctive features of PEMFCs. Specifically, the chemical properties of the polymer backbone permit operating temperatures in the range of 0 to 90 °C, and the ionic conductivity within the membranes permit a high relative power density. These two advantages satisfy the primary power generation requirements of

automobiles, which are quick-starting at ambient temperatures and a constant supply of high electrical current.

The electrochemical reactions at the anode and cathode of a PEMFC can be written as follows:

Anode: $H_2 \Rightarrow 2H^+ + 2e^-$,

Cathode: $2H^+ + \frac{1}{2}O_2 + 2e^- \Rightarrow H_2O$.

The oxidization of hydrogen gas at the anode produces protons and electrons. Along the external circuit, free electrons arrive at the cathode and form the electrical current. The protons pass through the membrane due to the potential gradient between the anode and cathode, and react with the oxygen supplied at the cathode to produce water. Due to electroosmosis, certain water molecules are dragged with the protons, i.e., electroosmotic drag, resulting in an imbalance in the distribution of the water. PEMFC performance depends on the electrolyte water content, and consequently, a sophisticated water management is crucial to ensure an optimally hydrated membrane for maximum PEMFC performance.

Other challenges associated with PEMFCs are thermal management and the use of reformed hydrocarbons. Since the operation of PEMFCs requires appropriate hydration of the membranes, over-heating, and corresponding local dehydration needs to be avoided. This requirement results in an expensive thermal management system in fuel cells. Reformed hydrocarbons are a possible pure hydrogen fuel source alternative due to the issues associated with the production, storage, and transport of pure hydrogen. Unfortunately, CO poisoning is problematic at the low temperatures if reformed hydrocarbons are used as a fuel. The platinum catalyst is highly sensitive to the presence of CO contained in the fuel. Even small amounts of CO will poison the catalyst sites and depress catalyst activity, which correspondingly reduces fuel cell performance. Two approaches that reduce this effect include the enhancement of catalyst resistance to CO by

using new alloys, and increasing the operating temperature. Reasonable temperatures that diminish CO poisoning are above 120 °C, at which the chemisorption of CO is markedly reduced.[1]

Consequently, improvements have to be made to raise the operating temperature and minimize the humidification requirements in PEMFCs. Numerous efforts have been made in designing electrodes, selecting appropriate materials for catalysts and membranes, and developing new operating devices. Of significant importance is the improvement of membrane materials, since, not only do membranes separate the anode from the cathode, but are also fundamentally relevant to fuel cell performance.

1.2 PEM Materials

When the first solid polymer fuel cells were developed for NASA's Gemini space flights in 1960, the ion-exchange membrane they used was a polymer made of cross-linked polystyrene with sulfonic acid side chains.[44] Unfortunately, this membrane material was insufficiently durable to chemical oxidation and degraded at operating temperatures. The use of Nafion®, a perfluorosulfonic acid polymer manufactured by DuPont, in the 1970s not only successfully solved this problem but also enabled PEMFC's to become a viable technology in the future.[45] The chemical structure of Nafion is shown in Figure 1.1.

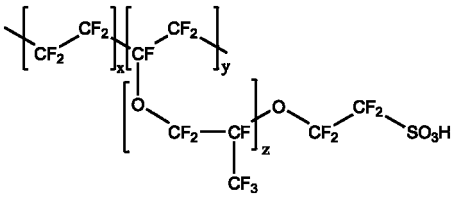

Figure 1.1. Chemical structures of Nafion®. The equivalent weight (EW) is determined by the molecular weight (MW) of the side chain and on the choice of x, y and z.

In order to attain maximum chemical stability, the polymer backbone was replaced by a carbon-fluorine structure similar to that of Teflon®. The strength of the C-F bond gives the membrane outstanding thermal and chemical stability in the presence of strong bases and acids at temperatures up to 125 °C.[43] In addition, the high electronegativity of the fluorine atoms increases the acidity of the sulfonic acid group and potentially promotes proton dissociation at low water contents. Although Nafion has been commonly used due to its prominent proton conductivity and stability, it has a limited operating temperature due to full hydration requirements. In addition, Nafion is not a suitable membrane for use in direct methanol cells due to its poor selectivity for methanol.

To overcome these drawbacks, numerous efforts have attempted to modify Nafion. Hygroscopic oxide materials, such as silica-gel and titanium dioxide[46], have been added to Nafion to enhance water retention, and nonaqueous, low volatile solvents, like phosphoric acid[47], have been incorporated into Nafion to increase the operating temperature. In addition, some solid inorganic protonic conductors, such as zirconium phosphates, heteropolyacids[18], and metal hydrogen sulfate[48], have been incorporated into Nafion to produce composite structures.

An alternative to Nafion membrane modification is to construct proton conducting membranes from non-fluorinated polymers. In order to maintain chemical and thermal stabilities comparable to fluorinated polymers, the beginning backbone polymers have typically been selected to be silicone polymers, such as polysiloxanes, and aromatic polyhydrocarbons, such as polyarylenes, polyethersulfones, polyetherketones, and polybenzimidazoles. Siloxane based polymers[49-52] are relatively stable due to the Si-O network structures, and are usually functionalized by inserting organic groups into the inorganic network to obtain improved electrolyte performance. Aromatic polyhydrocarbon polymers are also thermally stable due to the strong bonding in the benzene

rings. Unfortunately, fully aromatic structures lack flexibility, resulting in poor mechanical properties. Therefore, side groups offering an increased degree of flexibility are introduced into aromatic polyhydrocarbon structures, such as -SO_2- in polysulfone, -NHCO in polyamides, -COO- in polyesters, and -CO- in polyketones.[53]

After using the modified non-fluorinated polymer as a backbone, several methods have been employed to achieve desirable proton conductivity, such as direct sulfonation of the backbone, doping of acids into basic polymers, and the immobilization of protogenic groups on the backbones. Direct sulfonation is one of the simplest treatments that can be applied to many polyarylene polymers, such as polyphenylenesulfide (PPS) and polyaryleneethersulfone (PES), and heterocyclic polymers, such as polybenzimidazole (PBI) and polyphenylquinoxaline (PPQ).[12] Since these polymers are inherently not conductive, their performance greatly depends on the degree of sulfonation. Unfortunately, high sulfonation results in excessive polymer swelling and subsequently poor mechanical properties. Therefore, the long-term durability of sulfonated polymers remains uncertain.

Some basic polymers, such as polyethyleneoxide (PEO), polyvinylalcohol (PVA), polyacrylamide (PAAM), polyethylenimine (PEI), can be doped with amphoteric acids, such as phosphoric acid and sulfuric acid, to enhance proton conductivity.[11, 54] These acid-base complexes are promising because they are capable of maintaining high proton conductivity without humidification at relatively high temperatures. Polybenzimidazole/phosphoric acid (PBI/H_3PO_4) in particular has received significant attention due to its superior proton conductivity and excellent mechanical properties at temperatures up to 200 °C.[55] Unfortunately, phosphoric acid loss requires complicated procedures to balance the amount of acid in fuel cells, and further, the corrosive phosphoric acid quickly poisons platinum catalysts.[56] Therefore,

perfluorinated[57] and other acids including hydrochloric, perchloric, and nitric acid[58], have been used to mitigate the high over-potentials resulting from platinum poisoning of the cathode.

Another approach to enhancing proton conductivity is to immobilize amphoteric groups in the main chain and promote intrinsic proton conduction. Some nitrogen-containing aromatic heterocycles, like imidazole, pyrazole, and benzimidazole, have been proven to have the similar proton transport characteristics to those of water molecules[59]. In addition to comparable proton conductivity, these aromatic structures offer excellent thermal and chemical stabilities that permit their operation at temperatures above 100 °C. Hence, they have been employed to replace water as a proton solvent. Nafion/imidazole systems exhibit similar conductivities as hydrated systems, but only at much higher temperatures.[60] Unfortunately, their volatility becomes a critical problem, especially at high temperatures. Immobilizing these proton solvents to the polymer backbone is the central idea that addresses this issue. Instead of long-range diffusion in pure imidazole, intermolecular proton transfer determines the proton conductivity in the immobilized proton solvent. Therefore, to immobilize imidazole polymers, long flexible spacers have been inserted between the imidazole groups and the backbone chains to achieve higher proton conductivities.[60] This is consistent with the explanation by Kreuer, that flexible spacers would increase the degree of local freedom of the mobilized proton solvent while simultaneously limiting long-range diffusion.[61]

Other studies have been concentrating on the selection of backbone polymers and modification of currently used polymers. Novel polyphosphazenes were proposed as an alternative backbone polymer to be functionalized by sulfonic or phosphonic acid.[16] Functionalized polyphosphazenes were observed by Allcock et al.[62] to have proton conductivities up to 0.1 S cm^{-1}. Polymer blends of sulfonated polyetheretherketone (PEEK) and PBI[63-65] have

also exhibited improved mechanical and chemical properties over both PEEK and PBI separately due to polymer chain interactions, specifically, ionic interactions and hydrogen bonding.

1.3 Proton Conduction of Ionomers

Proton conduction is a common phenomenon observed in nature and is responsible for such processes as photosynthesis in green plants.[66] It is also considered to be a determinant factor in the efficiency of electrochemical fuel cells, electrochemical sensors, and electrochemical reactors. Therefore, discussions of proton transfer, structural reorganization, and diffusion are important to provide insight into the mechanism of proton conductivity in specific materials.[66]



(a) (b)

Figure 1.2. The "solvated hydronium complex" or "Eigen ion", (a) H_3O^+ $(H_2O)_3$, and the "shared proton complex" or "Zundel ion", (b) $H^+(H_2O)_2$. (see reference [67])

There has been extensive investigation into explaining the unusually high proton mobility in water, since water is the simplest and most important proton solvent. In 1806, Grotthuss proposed the idea of "Grotthuss water wires" to explain proton conduction in water via "structural diffusion."[68] Two major complex forms, the Eigen ion (i.e., $H_3O^+(H_2O)_3$) and the Zundel ion (i.e., $H^+(H_2O)_2$), were introduced to describe structural diffusion in water.[69-72] As depicted in Figure 1.2, the Eigen ion is a hydronium ion solvated by three water molecules, while the Zundel ion is a water dimer shared with an excess proton.[67] These two complexes are

considered mutually exclusive concepts for the explanation of structural diffusion until a more detailed interpretation of the proton conduction mechanism was obtained from Car-Parrinello molecular dynamics (CPMD) simulation and NMR data.[25, 73, 74]

These data proved that both conceptual complexes are required to appropriately describe the proton transfer mechanism[75]. As shown in Figure 1.3, the translocations of proton defects are coupled to the conversion of the two complexes: Eigen and Zundel ions. Specifically, the transformation of complexes is largely determined by the making and breaking of the hydrogen bond network surrounding the center excess proton. This phenomenon is termed "structural diffusion" because the protonic defect propagates along the hydrogen bond arrangement. Another feature of this mechanism is the contraction of the hydrogen bond in regions containing excess protonic charge. This contraction leads to barrier-less proton transfer within the complexes, and to hydrogen-bond dynamics (i.e., hydrogen-bond breaking and forming) in the outer shell of the complexes in a more thermodynamically favorable fashion. The self-diffusion of water also contributes to the total proton conductivity, which is termed "vehicular diffusion." Both computational and experimental investigations[24, 25, 76-78] have demonstrated that the formation and breakage of the hydrogen bond network (i.e., fast fluctuation in the local tetrahedral arrangement) largely accounts for the high proton diffusivity in water.

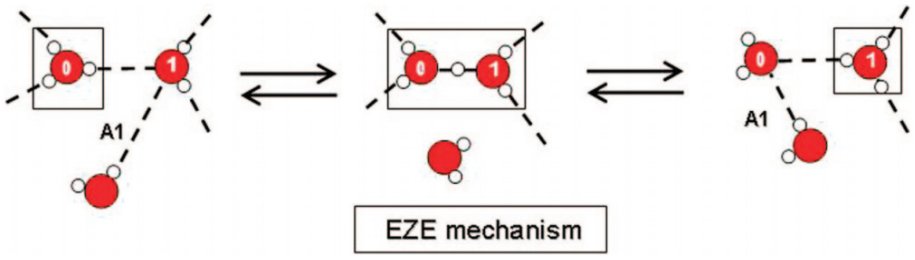

Figure 1.3. The mechanism of structural diffusion in water by hydrogen-bond breaking and forming processes, namely Eigen-Zundel-Eigen (EZE) mechanism. (see reference [75])

In the previous years, water-based proton transport mechanism has been studied for some low temperature proton-conductive PFSA polymers such as Nafion.[79-84] The dissociated protons in this ion exchange membrane material are derived from the solvation of the sulfonic acid groups in side chains. Since the presence of water is a crucial fact in either charge carrier formation or transport enabling, proton transfer mechanism in this two-phase system is always described by both the structural mechanism (i.e., proton hopping) and vehicular mechanism.

Electronic structure calculations were suggested to understand fundamental aspects in polymeric membrane materials such as structural and chemical properties of the polymeric backbone and/or side chains, and proton transfer mechanisms under minimal hydration conditions. Some of the earliest work in this area focused solely on the primary hydration in single fluorinated sulfonic acid systems.[85, 86] In addition, other single functional acid groups, including sulfonyl imides,[87] carboxylic acid,[88] imidazole,[89] phosphoric acid,[90] and phosphonic acid,[91] were studied with electronic structure calculations. Investigations were also undertaken on systems involving more than one acidic group including oligomeric fragments of the short side chain (SSC) PFSA membranes [93] These results elucidated the important correlation between conformational changes (i.e. flexibility) of side chains and the transfer and stabilization of dissociated protons as a function of the degree of hydration and separation of the protogenic groups.

1.4 Morphologies of PFSA Ionomers

There have been growing interests in both fluorinated and non-fluorinated ionomers due to their important applications as proton conducting membranes in fuel cells. The unique morphological properties of these materials are mainly due to the micro-phase separation between hydrophobic and hydrophilic segments of the macromolecules. Studies of proton

transport in various ionomers have revealed that protons conduction occurs through the hydrophilic domains formed by this micro-phase separation.[92] To understand the hydrated morphology of the ionomers, both experimental techniques (e.g., scattering, microscopy and spectroscopy methods) and multiscale modeling (e.g., atomic, molecular, mesoscale and statistical simulations) have been employed.

It is known that the presence of water greatly affects the morphological properties of PFSA ionomers.[20, 28] With sufficient number of hydrophilic side chains and in a fully hydrated condition, protons dissociate from sulfonic acid groups and transfer through water-swollen domains formed by aggregated "ionic clusters" and hydrophobic backbones. The length scales of the phase separation are typically nanometers. These morphological structures of PFSA lead to unique permeability characteristics of PFSA ionomers: good proton conductivity, good barrier properties for diffusion of hydrogen and oxygen, strong dependence of the proton conductivity on water content, etc. It should be noted that, in addition to the degree of hydration, equivalent weight (EW), and the processing history of ionomers also may have significant effect on their morphology.

Historically, the morphology of PFSA membrans has chiefly been investigated through small-angle X-ray scattering (SAXS)[29-32] and small-angle neutron scattering (SANS)[33, 34]. In scattering spectra for a PFSA ionomer, a characteristic ionomer peak is observed in the medium angular range and an upturn at low angles. It has been shown that the ionomer peaks are closely related to the appearance of ionic clusters and highly sensitive to the hydration level and EW of the ionomer. This peak tends to increase in intensity and shift to lower angles as the EW decreases, and with the increasing water content. The information generated from these scattering methods has been used to perform quantitative analysis and develop conceptual morphological models.

However, the complexities of the morphology limit the use of simple two-phase models and preclude the development of a definite model-based description.

To fit the calculated and observed scattering profiles and thus interpret microstructures and transport phenomena, a number of models have been proposed in the last thirty years. Three most prevalent models were proposed in the early years: a cluster-network model by Gierke et al.[93], a three-phase model by Yeager et al.[94] and a lamellar model by Haubold et al.[32]. Essentially, all of these models attempt to recognize the aggregated ionic clusters in the perfluorinated polymer matrix, where the cluster network forms and facilitates the water swelling and ionic transport. Although information about ionic cluster size can be extracted, the spatial distribution of ionic cluster and crystalline domains were predicted poorly by all of the models. Thus, a model inclusive of a complete description of morphology of PFSA ionomer needs a consideration of both the presence of a pervasive ionic network and the existence of crystallites.

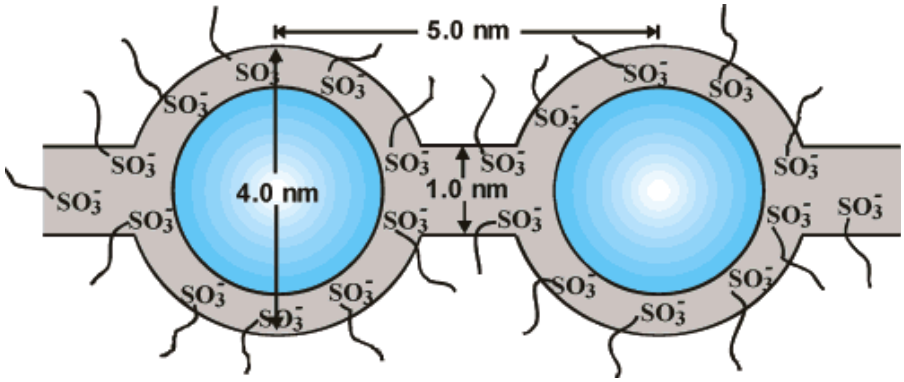

Figure 1.4. Gierke et al. established a cluster-network model for the morphology of hydrated Nafion. The side chain SO_3H groups were aggregated to form hydrated clusters embedded in the fluorocarbon phase. (see reference [93])

More recently, the evolution of microstructures in PFSA ionomers from the dry state through the water-swollen state to solution was studied by Gebel[95] using small-angle scattering methods. A conceptual model was proposed to describe the morphology changes as a function of water

content. The water swelling and dissolution process are shown in Figure 1.5. This model shows that ionic groups in a dry ionomer membrane aggregate and form spherical ionic clusters (size of ~1.5nm in diameter) separated with the center-to-center distance of ~2.7 nm. As water content is increased, swollen ionic clusters are observed with the water surrounded by ionic groups. When the water volume fraction increases to between 0.3 and 0.5, water channels are formed between spherical ionic clusters and percolation takes place. The structural reorganization continues with the addition of water. This leads to the onset of structure inversion such that the spherical clusters are reconstructed and surrounded by water. A connected network of polymer rods is formed and eventually "dissolves" into solution to yield a colloidal dispersion of the polymer. Although a complete description of the evolution in structures of membrane is given by this model, it lacks valid thermodynamic justification for the phase inversion process and is difficult to rationalize by the scattering profiles near the phase inversion point.

Different from the scattering methods, microscopy techniques (e.g., TEM, SEM, AFM and other imaging methods) are able to provide a direct visualization of morphological characteristics without the need of a particular model. The results can be employed to analyze sizes, shapes, and spatial distribution of ionic clusters, crystallites, and the backbone matrix. TEM investigation of dry Nafion membranes provide direct evidence of the existence of 3-10 nm diameter spherical ionic clusters and inter cluster spacing of 4-15 nm that was proposed by the model.[29] TEM studies of solution cast Nafion membrane (50-100nm thickness) was first performed by Xue and coworkers.[96] In this study, the staining agent RuO_2 was used to oxidize the side domain to give enhanced contrast between hydrophilic and hydrophobic regions. TEM imaging (zero-loss bright filed) of recast Nafion membranes were also studied by Porat and coworkers.[97] The results show that the backbone is more likely to maintain a planar zigzag conformation in orthorhombic

crystallites, which is the same as polyethylene, but different from helical conformation of poly(tetrafluoroethylene). They also observed that sulfonate groups are distributed in ionic clusters of about 5 nm in size.

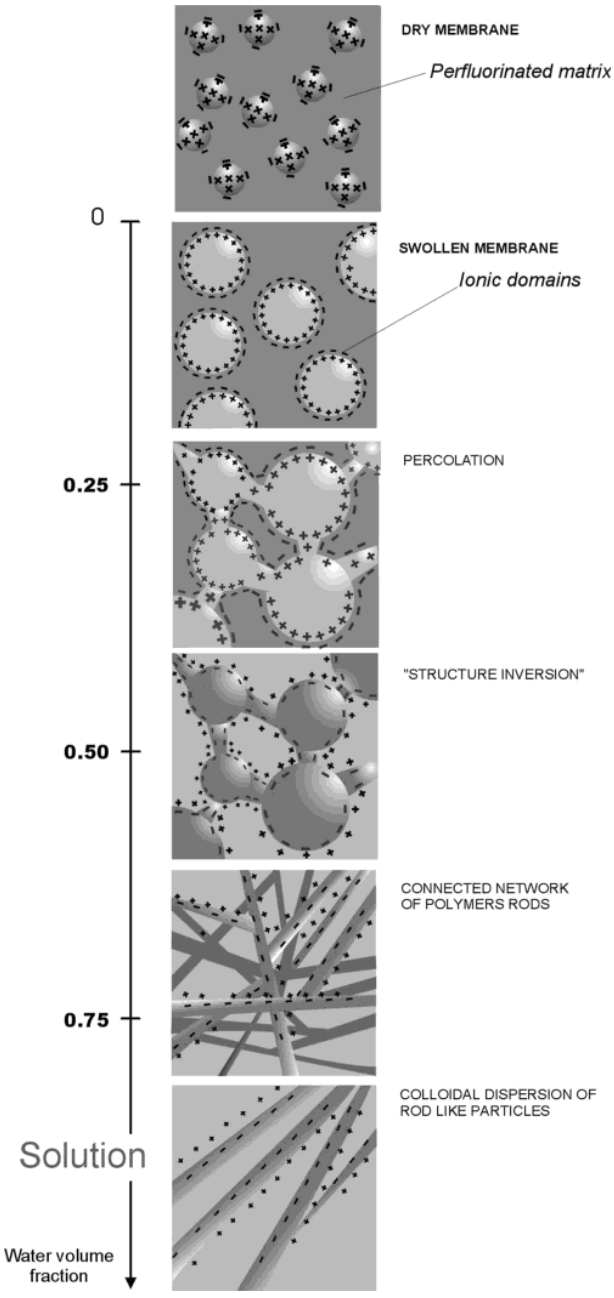

Figure 1.5. Conceptual model for the evolution of morphological of the ionic domains in Nafion as the dry membrane is swollen with water to the state of complete dissolution.(from reference [95])

In addition to experimental approaches, various modeling methods have been utilized to understand the process of micro-phase separation in PFSA membrane. The microscopic changes of morphology are considered as a result of molecular properties and processing conditions, and can be modeled at different length of scales. The atomic simulations[98-100] based on molecular dynamics (MD) and Monte Carlo (MC) methods, and quantum mechanical[101-103] methods are only capable of providing molecular descriptions of small systems, and have proven very useful to investigate the aggregation of the sulfonic acid groups and the proton transfer in PFSA membranes. However, they are less able to describe nanoscale morphology in complex inhomogeneous phases (i.e., hydrophobic, hydrophilic and water phases in PFSA ionomers) due to the lack of an adequate number of atoms and long equilibration times. To obtain information in a comparable scale with experimental SAXS data (5-200 nm), various mesoscale modeling techniques were used in these particular systems. The inter-molecular interactions in systems are usually described by two types: coarse-grained (particle-based) and continuum (field-based) methods. In particle-based models, characteristic chemical groups (or a segment) of a complex polymer can be simply replaced by individual conceptual sites with suitable non-bonded interaction parameters. For field-based methods, in contrast, local concentration fields with collective variables are used to describe self-organizing structures in systems. In mesoscale models, the typical length scales are 10–10^3 nm and typical time scales are up to milliseconds or even seconds. This allows the simulation of much larger system sizes that may provide results comparable to experimental data. The morphology evolution and eventual phase separation has been examined for a variety of ionomer systems with mesoscale modeling using dissipative particle dynamics (DPD) simulations.[39-41, 104, 105] Of additional interest, self-consistent mean-field

(SCMF) simulations[37] have also been used to investigate the effects of temperature and water content on phase separation and morphology in PFSA membranes.

1.5 Properties of Poly(phenylene sulfone) Ionomers

As the key component of PEMFC's, a desirable membrane material must have a high proton conductivity and zero electronic conductivity, sufficient mechanical strength, chemical and thermal stability in aggressive environmental conditions, low gas permeability to avoid excessive gas crossover, and low levels of swelling.[2, 7] Particularly for automobile applications, an ideal membrane material must possess proton conductivity greater than 0.1 S cm^{-1} at a temperature above 120 °C. In contrast to perfluorosulfonic acid membranes, poly(arylene) materials become more attractive due to their potentially lower water and methanol "crossover" and excellent mechanical properties.[106] However, most recently synthersized aromatic ionomer materials such as sulfonated poly(ether ketone), poly(ether sulfone), poly(imide) and poly(benzimidazole) are unable to be used as the electrolyte in PEM fuel cells due to their poor proton conductivity.

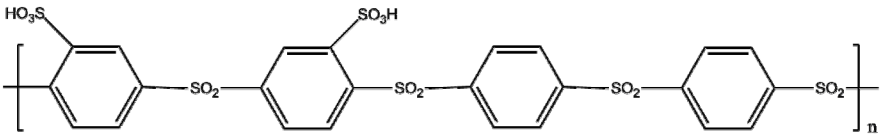

$sPSO_2$-360

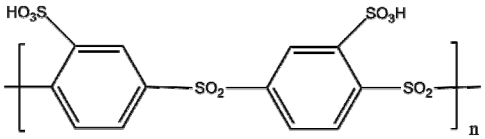

$sPSO_2$-220

Figure 1.6. Chemical structure of sulfonated poly(phenylene sulfone) ($sPSO_2$) ionomers with EW of 360 and 220.

Highly sulfonated poly(phenylene sulfone) ionomers have been synthesized recently and considered to be an alternative to commonly used PFSA ionomers such as Nafion. The chemical

structures of $sPSO_2$ ionomers are shown in Figure 1.6. This new class of sulfonated polymers contains extremely electron-poor poly(phenylene) backbones. The phenyl rings, bridged by electron-accepting sulfone units (-SO_2-), are functionalized by sulfonic acid groups. A noticeable enhancement of hydrolytic stability was achieved by direct sulfonation on phenyl rings without introducing electron-donating groups such as ether linkages. In addition, the flexible ion exchange capacity can be achieved by copolymerizing sulfonated and non-sulfonated monomers or even with other polymers to form block copolymers. The rigid aromatic backbones give rise to the exceptional stability and high proton conductivity in these materials.

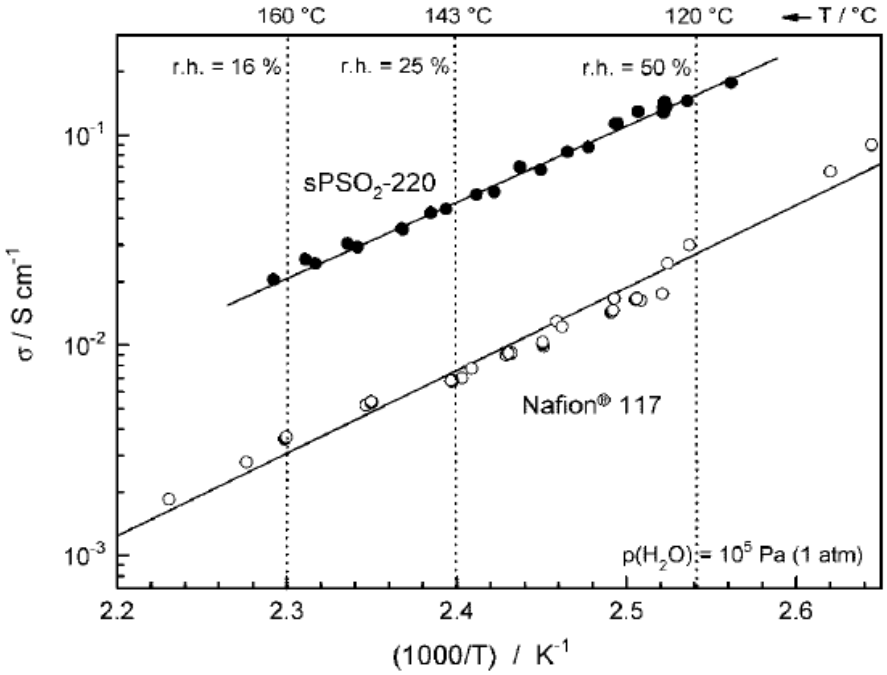

Figure 1.7. Proton conductivity in the temperature range 110-160°C at a water pressure of $p(H_2O)$ = 1 atm for $sPSO_2$-220 and Nafion 117.(from reference [23])

Recent research has shown that these membranes preserve high thermo-oxidative stability and superior proton conductivity even at high temperature and low humidity condition.[21] As shown in Figure 1.7, the conductivity of $sPSO_2$ ionomers increases more significantly with increasing

temperature. The ionomers with 100% degree of sulfonation ($sPSO_2$-220) with IEC of 4.45 meq/g show proton conductivity 5-7 times higher than observed in Nafion at high temperatures.[23] However, the presence of highly packed ionic clusters makes $sPSO_2$-220 very brittle in the dry state, water-swollen when hydrated, and soluble in water.

The unique microstructures of $sPSO_2$ polymers were also studied by SAXS methods.[22] Similar to Nafion, all $sPSO_2$ ionomers show pronounced ionomer peaks as seen in Figure 1.8. With the decrease in the EW of an ionomer, intensity of the corresponding ionomer peak increases while the location of the peak shifts to the regions of high q values. When the degree of sulfonation is greater than 50% (i.e., $sPSO_2$-360 and $sPSO_2$-220), the correlation peak tends to narrow to about half the width of typical Bragg reflections. It indicates a reduced size of hydrated hydrophilic domains (with a correlation length of 1.44 nm) and more disperse water channels among ionic clusters. Hence, $sPSO_2$ ionomers are expected to contain more water than Nafion at a given RH (because of the higher density of sulfonic acid groups).

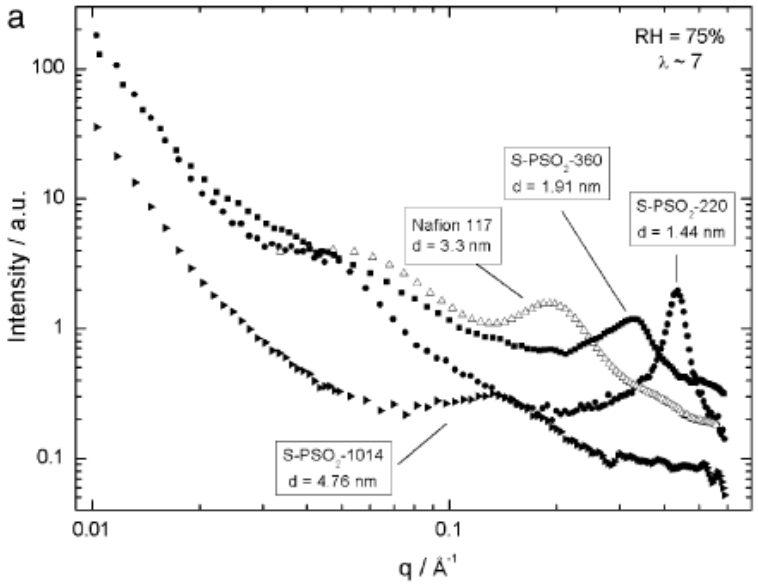

Figure 1.8. SAXS profiles of sulfonated poly(p-phenylene sulfone)s and Nafion 117. (from reference [22])

With the very high charge carrier concentration due to the high degree of sulfonation and very high water uptake at a given relative humidity, hydrated $sPSO_2$ ionomers are more likely to form a well-connected aqueous domain with narrow spacing. This leads to not only the long range transport of water but also facilitates proton transport through fine diameter channels. Much of research undertaken in this dissertation is aimed at understand the particular microstructure and unique proton transport for this type of ionomer at low water contents.

1.6 Electron Microscopy of Ionomers

Over the years, Transmission Electron Microscopy (TEM) has developed into a powerful tool capable of investigating morphological details of polymeric materials at length scales from micrometers to nanometers. Different techniques and methods in the field of electron microscopy, such as bright/dark-field imaging, electron diffraction, high-resolution imaging, and analytical microscopies have all been applied to understand structure–property correlations in polymers. Systems like ionomers, defined as polymers that have ionic groups covalently bonded to the backbone as pendant moieties, are considered to comprise nanoscale ionic aggregates due to the micro-phase separations between ionic groups and host backbones. Historically, this unique morphological property was mainly studied by scattering techniques such as SAXs and SANs. With the development of electron microscopy techniques, direct visualization and quantitative chemical analysis now can be used to better understand microstructures in these materials.

Similar to biological systems, synthetic polymers consist largely of light elements whose elastic interaction with electrons is relatively weak. Consequently, the contrast generated in bright-field (BF) images is potentially reduced. In addition, the strong inelastic interaction between polymers and electrons lead to the substantial radiation damage, which makes the achievable spatial resolution very limited. Ionomers, particularly PFSA membranes, are more

electron-sensitive than typical hydrocarbon polymers. Thus, special investigation techniques must be carried out to obtain high resolution images with minimal electron exposure.

Early investigation of ionomers only used conventional TEM and took advantage of the mass-thickness contrast in BF images that are enhanced by selectively heavy element staining of polymer samples. Typical staining treatment of polymer was usually done by using heavy metal staining agents that can preferentially react with or localize themselves in some component of a polymeric material. For instance, osmium tetraoxide, tends to permanently bond with unsaturated carbon-carbon bonds whereas ruthenium tetroxide preferentially reacts with aromatic rings. For ionomers, acidic groups can be stained by neutralizing with heavy metal cations. Ceynowa first explored the morphologies of Nafion by staining membranes with $Pb(NO_3)_2$ and identified 3-6 nm diameter ionic clusters that are homogenously distributed in the polymeric matrix.[107] In the work of Pineri et al.,[108, 109] metal oxides (Fe_2O_3 and $RuO+xH_2O$) were incorporated and precipitated in Nafion. The fairly large size of metal hydroxide precipitates (~20-100 nm) were formed inside Nafion after immersing ion-exchanged sample into hydroxide solution. In addition, RuO_4 were used by Xue et al.[96] to positively stain both ether side chains and localized water bonded to the sulfonate groups. An average size of 2-3 nm spherical ionic clusters were observed to be uniformly distributed in Nafion. However, the spatial resolution in BF images is very limited and quantitative microstructure information is difficult to obtain.

To overcome the spatial resolution limits and gain useful chemical information about microstructures in Nafion, the principles of analytical electron microscopy were used. Rieberer et al.[108] first applied spectroscopic methods, Energy Dispersive x-ray Spectrometry (EDS) and Electron Energy Loss Spectroscopy (EELS), to enhance image contrast and obtain information on cross-linked structure, composition, and ion exchange efficiency of the membrane. Artifact-

free images of the material were obtained for membranes without staining. The damage of membranes was controlled by use of low-dose and cold-stage methods. Therefore, both electron diffraction and x-ray analysis may be conducted to examine cross-linked structure and ion exchange efficiency. In addition, chemical composition of fluorocarbon chains was provided by EELS data of carbon, fluorine and oxygen. The investigation of unstained solution cast Nafion membranes was conducted by Parat et al. [97] by energy filtered imaging. The energy filter was used to remove inelastically scattered electrons and form zero-loss image of unstained samples. This technique remarkably enhanced the contrast between light elements in polymeric materials. Three window methods were used to obtain energy filtered images of sulfur distribution. By comparing the sulfur map with zero-loss bright field image of the same area, size, and distribution of sulfur rich ionic domains can be determined.

Different from image formation mechanism of BF images in TEM mode, the contrast of high-angle annular dark field (HAADF) images acquired in a STEM mode is due to the strong scattering of high atomic number (Z) elements. Thus, HAADF images provide direct information on distribution of ionic clusters in ionomers. Bright regions found in these images are usually interpreted as high concentration of high Z atoms in the ionic aggregates. One of the successful applications of this technique is the investigation of ethylene- and styrene-based ionomers neutralized with various cations, such as Zn-EMAA and Cs-SMAA.[109-111] Most recently, a spectrum-imaging approach that combines spatially-resolved EELS with cryo-STEM has been used by Libera et al. [112-114] to study the hydrated morphology of polymers. It has been shown that amorphous ice in frozen hydrated polymers exhibits substantially different low-loss spectrum features from those of the polymer matrix, which can be utilized to map water rich domains embedded in hydrophilic polymeric segments. However, beam damage to hydrated polymers has

to be minimized to obtain quantitative data at the nanometer scale. In addition to the techniques mentioned above, modified sample preparation methods[115-117] and other analytical electron microscopy approaches[118, 119] have been employed to understand PFSA ionomers and membrane electrolyte assembly (MEA) that incorporates multiple components and phases.

Various electron microscopy techniques have been used to characterize morphologies and chemistry of ionic clusters, but progress has been limited by practical problems of visualizing clusters. Two major problems are radiation damage and overlap of clusters in projection.[120] Considering beam exposure limitations in different EM modes, BF in the TEM mode seems to be the most efficient and able to provide good images without introducing severe radiation damages. However, the information in such images is often difficult to interpret even with the enhanced contrast by using analytical EM methods. In contrast, HAADF in the STEM mode is preferable if samples can withstand a bit higher electron exposure. Direct visualization of ionic clusters containing heavy elements can be accomplished since the contrast of HAADF images is strongly dependent upon the high atomic number elements in samples. Chemical composition of ionomers can also be analyzed by core loss EELS and EDS. However, they are not practical for all ionomers since a significantly longer exposure is require to record spectra with acceptable signal-to-noise ratio (SNR). Low loss EELS analysis combined with HAADF is considered the best way to obtain clear images of ionic cluster and localized chemical information. Better data obtained from all EM techniques can be achieved by using thin samples. Although cryo-sectioning is the best way to prepare samples that preserve properties of bulk materials, it is extremely difficult to produce thin enough sections. Solution casting provides an easy way to obtain thin samples with controllable thickness although the morphology may be different from

that of bulk materials. Use of thin samples in EM not only gives better data but overcome the overlap problems associated with the projection.

1.7 Research Overview

In the research undertaken in this dissertation, both computational and experimental methods were used to understand the proton transport and morphological properties of aromatic and PFSA ionomers. In the first part of the dissertation, *ab initio* electronic structures calculations were undertaken on oligomeric fragments of $sPSO_2$ ionomers each with a few added water molecules to ascertain differences in the hydration and energetics associated with proton transfer. In the following part, mesoscale simulations employing DPD methods were performed to investigate $sPSO_2$ ionomers morphologies as function of hydration levels, EW and MW. To obtain a direct visualization of ionomer morphologies and understand local chemical bondings in ionic domains, different electron microscopy methods are also adopted. TEM and STEM were used to obtain both BF and HAADF images and compared with simulated images from the DPD calculations. To understand local chemistry and molecular structures of ionomers, quantitative analyses were conducted based on the results from EELS in the low loss and core loss regions. These results were compared with simulated EELS spectra using DFT methods to investigate the phase transitions and polarization effects in PTFE chains.

Chapter 2 Computational Methods

Although the implementation of computational methods is still not sufficient to exactly describe every aspect of chemistry and physics, they have provided an accessible approach to solve a number of problems in a qualitative or approximately quantitative way. A number of computational methods have been devised to solve problems in chemistry and material science at multiple spatial and temporal scales. They are typically distinguished by four characteristic length levels as shown in Figure 2.1: quantum mechanics (QM) scale (~10^{-10} m), atomistic (~10^{-8} m), mesoscopic (~10^{-6} m) and macroscopic scale (~10^{-4} m) simulations.

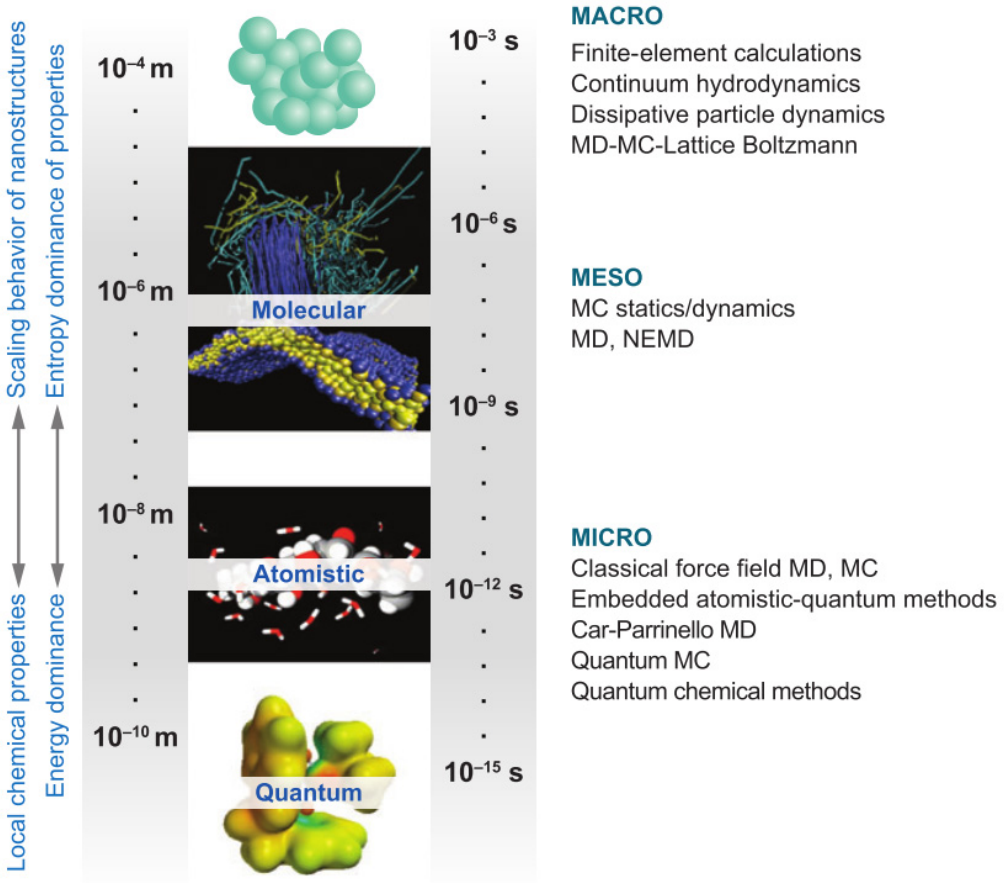

Figure 2.1. Different length and time scales for the simulation of soft matter. (from reference [121])

At the finest scale, quantum mechanics principles are applied to determine electronic structure of materials. It is the most accurate but also computational expensive way to obtain information about chemical bonding, interactions and corresponding energies for atoms and molecules. At the second level where atoms are the players, interatomic potentials are used while details of interaction between electrons are omitted. In mesoscale simulations, the larger molecules such as polymers are usually treated as a collection of groups with similar chemical composition or properties. Therefore, microstructural change such as phase separation can be examined by these simulations. Finally, macroscale properties of materials are studied by applying a constitutive law governs the behavior of a continuous medium. Effects such as density, velocity, temperature, displacement, and stress field are involved in such simulations. In this dissertation, the first and third levels of simulation, namely electronic structure calculations and mesoscale simulation, are performed to study chemistry and microstructures of ionomers.

In the first section of this chapter, a brief description of quantum mechanics and applicable methods are provided. Different approximation techniques are also covered in this section. Theoretical and practical aspects of Dissipative Particle Dynamics (DPD) simulations are then presented in the following section.

2.1 First Principle Calculations

Among the various ways computational chemistry is used, one of the important applications is to explicitly understand the properties of molecules. It is widely accepted that the behavior of electrons can be properly described in a QM manner. However, exact solutions are limited to one-electron systems (e.g., H atom and He^{+}). For the many electron systems, therefore, the appropriate approximations have to be made to obtain satisfactory computational results. Accordingly, the selection of approximations is an essential task for computational researchers.

Whether the approximation is valid for a given system and how accurate the results are expected to be two central problems. The particular approximations may satisfy only certain systems, and hence the misapplication of them accounts for inevitable inaccuracy. Moreover, the highest level calculations (which may give the best results) are extremely computationally expensive.

2.1.1 Schrödinger Equation

In quantum mechanics, the properties of the system are described by the wave function of the particles' positions.[122, 123] The energy of the system can be obtained by solving the time-independent Schrödinger equation:

$$\hat{H}\Psi = E\Psi \,, \tag{2.1}$$

where $\hat{H}$ is the Hamiltonian operator, E is the electronic energy, and Ψ represents the wave function of the system. The form of Equation (2.1) is referred to an eigenfunction/eigenvalue equation where E is the eigenvalue of the eigenfunction Ψ. The probabilistic descriptions of physical properties (e.g., the probabilities of finding electrons at certain positions) can be interpreted as the square of the wave function $|\Psi|^2$, where it is equal to the product of Ψ with its complex conjugate Ψ^*, which is $|\Psi|^2 = |\Psi^*\Psi|$. The probability of determining the particle over all space leads to a normalization requirement of the wave function:

$$\int_{-\infty}^{\infty} \Psi(x)^* \Psi(x) dx = 1 \,. \tag{2.2}$$

There is also an orthogonal requirement for the wave functions Ψ_m and Ψ_n ($m \neq n$) due to the particle only occupying one state at a given moment in time:

$$\int_{-\infty}^{\infty} \Psi_m(x)^* \Psi_n(x) dx = 0 \,. \tag{2.3}$$

The Hamiltonian operator generally can be defined as the combination of kinetic and potential energies of electrons and nuclei. Specifically, the total Hamiltonian operator H_{tot} is comprised of five terms, which are kinetic energies of the electrons and nuclei (T_e and T_n), the attraction of the electrons to the nuclei V_{ne}, and the repulsion within electrons and nuclei (V_{ee} and V_{nn}). This may be expressed as

$$H_{tot} = T_e + T_n + V_{ne} + V_{ee} + V_{nn}. \tag{2.4}$$

For the system containing i electrons and k nuclei, the Hamiltonian can be expanded into

$$H_{tot} = -\sum_i \frac{\nabla_i^2}{2} - \sum_k \frac{\nabla_k^2}{2} - \sum_i \sum_k \frac{Z_k}{r_{ik}} + \sum_i \sum_{j>i} \frac{1}{r_{ij}} + \sum_k \sum_{l>k} \frac{Z_k Z_l}{r_{kl}}, \tag{2.5}$$

where ∇^2 is the Laplacian operator, Z is the atomic number, and r_{ab} is the distance between particles a and b.

The Hamiltonian in Equation (2.5) implies that the particles do not move independently due to correlation effects (i.e., the attraction and repulsion of particles). Hence, the solving of the Schrödinger equation becomes complex and approximation is necessary. From the physical point of view, the nuclei are moving much more slowly than the electrons due to their heavier mass. As a result, the electrons respond instantaneously to the change in the positions of the nuclei. This suggests that it is possible to decouple the motion of electrons from the motion of nuclei. This is the Born-Oppenheimer (B-O) approximation which when applied to compute the electronic energy, E_{elec}, results in the electronic Schrödinger equation:

$$H_{elec}\Psi_{elec}(\mathrm{r_i};\mathrm{r_k}) = E_{elec}\Psi_{elec}(\mathrm{r_i};\mathrm{r_k}). \tag{2.6}$$

For the fixed position of nuclei, the kinetic energy component of the nuclei is ignored and the nuclear-nuclear repulsion becomes a constant which is solely dependent on the nuclear positions

r_k. The electronic wave function, Ψ_{elec}, is a function of electronic positions r_i only, while the nuclear positions are parameters. Thus, the second term in Equation (2.5) is eliminated, and the fifth term is isolated as a constant, the electronic Hamiltonian , H_{elec}, is therefore

$$H_{elec} = -\sum_i \frac{\nabla_i^2}{2} - \sum_i \sum_k \frac{Z_k}{r_{ik}} + \sum_i \sum_{j>i} \frac{1}{r_{ij}}. \tag{2.7}$$

In order to simplify the Hamiltonian, we introduce a compact set of notation: $h_i = -\frac{1}{2}\nabla_i^2 - \sum_k \frac{Z_k}{r_{ik}}$ and $g_{ij} = \frac{1}{r_{ij}}$, where h_i is the one-electron operator describing the motion of electron i in the field of all of the nuclei, and g_{ij} is the two-electron operator corresponding to electron-electron repulsion. The electronic Hamiltonian H_{elec} can then be simplified to

$$H_{elec} = \sum_i h_i + \sum_i \sum_{j>i} g_{ij}. \tag{2.8}$$

2.1.2 Hartree Fock Method

Having invoked the B-O approximation, the main challenge turns out to be the solving of the electronic Schrödinger equation, Equation (2.6). However, the Coulombic electron-electron repulsion terms in Equation (2.7) make it difficult to separate the electronic Schrödinger equation independently and solve it analytically. It is fairly natural to come up with an approximation that every electron moves in an orbital within the average field generated by all other electrons.[124, 125] This leads to a Hartree product where the *N*-electron wave function may be expressed as the product of *N* independent spin orbitals, according to

$$\Psi = \chi_1(\mathrm{x}_1)\chi_2(\mathrm{x}_2)\ldots\chi_{N-1}(\mathrm{x}_{N\text{-}1})\chi_N(\mathrm{x}_N). \tag{2.9}$$

The $\chi_i(\mathrm{x}_i)$ term represents a spin orbital that contains both spatial coordinates $\psi_i(\mathrm{r}_i)$ and spin coordinates α or β. Arising from this assumption, the many-electron problem is simplified to a number of single-electron equations that can be solved in a convenient manner. However, this approximation does not obey the antisymmetric requirement (i.e., Pauli principle), which says that the interchange of the coordinates of any two electrons should change the sign of the electronic wave function.

To achieve the antisymmetry of the wave function, the Slater Determinants (SDs) are employed. The wave function Ψ having N electrons and N spin orbitals then can be rewritten in the form of a SD:

$$\Psi = \frac{1}{\sqrt{N!}} \begin{vmatrix} \chi_1(\mathrm{x}_1) & \chi_2(\mathrm{x}_1) & \cdots & \chi_N(\mathrm{x}_1) \\ \chi_2(\mathrm{x}_2) & \chi_2(\mathrm{x}_2) & \cdots & \chi_N(\mathrm{x}_2) \\ \vdots & \vdots & & \vdots \\ \chi_1(\mathrm{x}_N) & \chi_2(\mathrm{x}_N) & \cdots & \chi_N(\mathrm{x}_N) \end{vmatrix}, \tag{2.10}$$

where the spin orbitals must be orthonormal: $\langle \chi_i | \chi_j \rangle = \delta_{ij}$. The factor $1/\sqrt{N!}$ before the determinant ensures the normalization of the wave function Ψ. Additionally, the SD becomes zero when two electrons are put into the same orbital due to the Pauli Exclusion Principle.

The SDs can be further simplified by use of permutations operator P and antisymmetrizing operator A. If the diagonal product of the determinant is denoted as Π, then it becomes

$$\Psi = A\left[\chi_1(\mathrm{x}_1)\chi_2(\mathrm{x}_2)\ldots\chi_N(\mathrm{x}_N)\right] = A\Pi, \tag{2.11}$$

where

$$A = \frac{1}{\sqrt{N!}} \sum_{p=0}^{N-1} (-1)^p P^p. \tag{2.12}$$

The antisymmetrizing operator A makes the wave function Ψ antisymmetric to satisfy the Pauli principle. It is also worth noticing that operator A commutes with H, (i.e., $AH = HA$), and the dual A operator obeys $AA = \sqrt{N!}A$. On the other hand, the permutations operator P^p interchanges orbitals between two electrons, where p is the number of interchanges.

By making use of the simplied form of the Hamiltonian from Equation (2.8) and the wave function of Equation (2.11), the electronic energy E_{elec} can be calculated from

$$E_{elec} = \langle \Psi | H_{elec} | \Psi \rangle = \langle A\Pi | H_{elec} | A\Pi \rangle = \sum_{p=0} (-1)^p \langle \Pi | H_{elec} | P^p \Pi \rangle . \tag{2.13}$$

The energy of one-electron operator acting on coordinate 1 (i.e., h_1) then can be writen as:

$$\begin{aligned} E_{h_1} &= \sum_{p=0} (-1)^p \langle \Pi | h_1 | P^p \Pi \rangle \\ &= \langle \Pi | h_1 | \Pi \rangle - \langle \Pi | h_1 | P\Pi \rangle + \langle \Pi | h_1 | P^2 \Pi \rangle ... + (-1)^p \langle \Pi | h_1 | P^p \Pi \rangle . \\ &= \langle \chi_1(\mathrm{x}_1) | h_1 | \chi_1(\mathrm{x}_1) \rangle = h_1 \end{aligned} \tag{2.14}$$

Then its generalized form becomes:

$$E_{h_i} = \langle \Pi | h_i | \Pi \rangle = h_i . \tag{2.15}$$

For the two-electron operator corresponding to coordinate 1 and 2 (i.e., g_{12}), the energy is

$$\begin{aligned} E_{g_{12}} &= \langle \Pi | g_{12} | \Pi \rangle - \langle \Pi | g_{12} | P\Pi \rangle + \langle \Pi | g_{12} | P^2 \Pi \rangle ... + (-1)^p \langle \Pi | h_1 | P^p \Pi \rangle \\ &= \langle \Pi | g_{12} | \Pi \rangle - \langle \Pi | g_{12} | P\Pi \rangle \\ &= J_{12} - K_{12} \end{aligned} . \tag{2.16}$$

The term J_{12} is called the Coulomb integral which stands for the energy of Coulombic interaction between two electrons in different orbitals. The term denoted as K_{12} is the exchange

integral describing the antisymmetrization effect that results from interchanging electron pairs. Therefore, the energy of electron-electron interaction can be defined as

$$E_{g_{ij}} = \langle \Pi | g_{ij} | \Pi \rangle - \langle \Pi | g_{ij} | P\Pi \rangle = J_{ij} - K_{ij} . \tag{2.17}$$

Combining Equations (2.15) and (2.17), we have the electronic Hartree-Fock energy E_{HF}:

$$E_{\mathrm{HF}} = \sum_i h_i + \sum_i \sum_{j>i} \left(J_{ij} - K_{ij} \right) . \tag{2.18}$$

Through some mathematical transformations, the resulting Hartree-Fock equation can be expressed as follows:

$$F(\mathrm{x}_1)\chi_i(\mathrm{x}_1) = \varepsilon_i \chi_i(\mathrm{x}_1), \tag{2.19}$$

where the Fock operator F is defined in terms of Coulomb and exchange operators $J_j(\mathrm{x}_1)$ and $K_j(\mathrm{x}_1)$:

$$F(\mathrm{x}_1) = h(\mathrm{x}_1) + \sum_j \left[J_j(\mathrm{x}_1) - K_j(\mathrm{x}_1) \right]. \tag{2.20}$$

The Fock operator provides a description of the energy of an electron involved in the interaction with all other electrons and nuclei. More explicitly, the first term of the Fock operator is associated with the kinetic energy of a single electron and the attraction from all the nuclei; whereas the sum of $J_j(\mathrm{x}_1)$ and $K_j(\mathrm{x}_1)$ accounts for the electron-electron repulsion due to all other electrons. The HF treatment, however, employs a single Slater determinant as the trial function only to calculate the variational energy where the electron correlation is ignored.

Unlike the Schrödinger equation, the Hartree-Fock equation is a way of describing the wave function of a particular molecular orbital. Thus, it is plausible to interpret the multiplier ε_i as representing the energy of the ith molecular orbital $\chi_i(\mathrm{x}_1)$. The molecular orbitals are typically

expanded as a Linear Combination of Atomic Orbitals (LCAO). Hence, we expand the molecular orbital χ_i in terms of a set of basis functions φ_a as

$$\chi_i = \sum_a c_{ai}\varphi_a \,. \tag{2.21}$$

The coefficients c_{ai} are solved by substituting Equation (2.21) into the Hartree-Fock equation, Equation (2.19). The resulting equations can be further simplified by introducing the Fock and overlap matrices, which gives:

$$Fc = Sc\varepsilon \,, \tag{2.22}$$

where F and c are the Fock and coefficient matrices, S stands for the overlap matrix of the basis functions, and ε represents the diagonal matrix of orbital energies. Since the Fock matrix is unknown unless we obtain the matrix of coefficients c, an initial guess of c for a set of MOs must be made first. With the coefficients, we could construct a new Fock matrix and obtain a new set of coefficients from $Fc = Sc\varepsilon$. This circular computation will continue until there is no change in the energy of the molecular orbitals. Such an iterative process is also called the self-consistent field (SCF) method.

2.1.3 Density Functional Theory (DFT)

Unlike one-electron systems, accurately solving many electron wave functions suffers from tremendous difficulties because of the presence of electron-electron correlation. However, the finding of a one-to-one correspondence between ground state electron density and ground state wave functions makes it possible to address this problem.[126] This prescription is called Density Functional Theory (DFT)[127, 128], by which the energy and other observable properties is directly derived from the electron density rather than the wave function.

In contrast to the wave function where one deals with 3*N* variables and the complex Schrödinger equation, the electron density is only dependent on three spatial variables and is directly mapped to the ground state energy. It is this one-one correspondence that makes it possible to attain the exact energy directly. Moreover, some electron correlation is included in the calculation based on the electron density. These two features ensure that DFT methods are as fast as the HF methods and more accurate even than some electron correlation corrected method such as MP2.[127]

As a useful physical quantity, the electron density is essentially associated with the ground state of the system. This relationship was first realized by Hohenberg and Kohn in 1964.[129] They first proved that the non-degenerate ground-state density, $\rho(\vec{r})$, not only determines the external potential, $V_{ext}(\vec{r})$, uniquely, but is also conjunct to the Hamiltonian and wave function. In addition to the first theorem that confirms the existence of such a one to one connection, the second theorem shows that the density also obeys the variational principle. Hence it is possible to calculate the ground-state energy from the Hamiltonian and wave function determined by the density. However, the calculation that follows this direction still relies on the solution of the Schrödinger equation which in turn leads to considerable complexity. This problem was solved by Kohn and Sham[130] who suggested a method that expands the Hamiltonian into a set of one-electron operators. In particular, this methodology assumes a non-interacting electronic system that possesses the same density as the fully interacted one. This can be done by rewriting each energy component as a functional of the density:

$$E[\rho] = T_e[\rho] + U_{ne}[\rho] + U_{ee}[\rho] + \Delta T_e[\rho] + \Delta U_{ee}[\rho], \tag{2.23}$$

where $T_e[\rho]$ is the kinetic energy of the electrons without interaction, $U_{ne}[\rho]$ and $U_{ee}[\rho]$, are the nuclear-electron attraction and electron-electron repulsion, respectively. Two terms ($\Delta T_e[\rho]$ and

$\Delta U_{ee}[\rho]$) are added to correct the $T_e[\rho]$ and $U_{ee}[\rho]$. We can take a sum over individual electronic energies and rewrite the above equation as

$$E[\rho] = \sum_i \langle \chi_i | -\frac{1}{2}\nabla_i^2 | \chi_i \rangle - \sum_i \langle \chi_i | \sum_k \frac{Z_k}{|r_i - r_k|} | \chi_i \rangle + \sum_i \langle \chi_i | \frac{1}{2}\int \frac{\rho(r')}{|r_i - r'|} dr' | \chi_i \rangle + E_{XC}[\rho], \tag{2.24}$$

where the correction terms $T_e[\rho]$ and $U_{ee}[\rho]$ are added together to the exchange-correlation energy term denoted by $E_{\mathrm{XC}}[\rho]$. This term includes the energetic corrections from quantum mechanical effects, classical interactions and modification in comparison with the electron-interacting system. The energy is minimized with the Lagrange method, and gives pseudo-eigenvalue equations:

$$h_i^{\mathrm{KS}} \chi_i = \varepsilon_i \chi_i, \tag{2.25}$$

where the Kohn-Sham (KS) one-electron operator h_i^{KS} is defined as:

$$h_i^{\mathrm{KS}} = -\frac{1}{2}\nabla_i^2 - \sum_k \frac{Z_k}{|r_i - r_k|} + \int \frac{\rho(r')}{|r_i - r'|} dr' + V_{\mathrm{XC}}, \tag{2.26}$$

and the functional derivative (i.e., exchange-correlation potential) is given by:

$$V_{XC} = \frac{\delta E_{\mathrm{XC}}}{\delta \rho}. \tag{2.27}$$

The sum of one-electron operator, h_i^{KS}, in Equation (2.25) over N orbitals gives an explicit expression for the Hamiltonian in a non-interacting system of electrons, which is

$$\sum_i h_i^{\mathrm{KS}} | \chi_1 \chi_{2\ldots} \chi_N \rangle = \sum_i \varepsilon_i | \chi_1 \chi_{2\ldots} \chi_N \rangle. \tag{2.28}$$

This indicates that the Kohn-Sham method performed in a fictitious system could attain the same density as in a real system.

A number of similarities can be found in the form of a Kohn-Sham operator in Equation (2.26) and that of Fock operator in Equation (2.20). Except for the exchange-correlation term, both of the two operators contain the same components inclusive of kinetic energy, attractive, and repulsive interactions. Moreover, the solutions to the Kohn-Sham equation could be achieved by similar iterative procedures as the SCF method used in HF theory. On the other hand, the DFT seems to provide much more ease for the calculation, because it includes solely 3 variables while the Fock operator is a function of $3N$ coordinates. It is also worth noticing the fundamental difference between DFT and HF. DFT is an exact method of solving the KS equations described by electron density, but suffers from difficulties in seeking the proper approximate E_{XC}. In contrast, the HF method is derived from several deliberate approximations and aims to solve the equations exactly.

2.1.4 Exchange-correlation Functional

Although DFT has been proven to be an exact theory giving considerable accuracy, the exact exchange-correlation functional E_{XC} is unknown and thus no systematic approximation can be made for solving relevant equations. In practice, there have been numerous attempts to develop reasonable functionals.[128] Normally, the functionals are reconstructed by eliminating some terms or incorporated with several empirical parameters from experiments. One of the simplest approximations is the Local Density Approximation (LDA). It samples the local points in a uniform electron density or tied with a slowly varying electron density. This assumption can be differentiated from a non-local method in which the density applies on the gradient of each point and the area around this point. For an electron gas having a uniform density, the exchange energy is given by the Dirac formula:

$$E_{\mathrm{x}}^{\mathrm{LDA}}[\rho] = -C_x \int \rho^{4/3}(\mathrm{r}) d\mathrm{r}\,, \tag{2.29}$$

where C_x is an empirical parameter for a given atom. For a more general result, the LDA can be replaced by the Local Spin Density Approximation (LSDA) where the electrons of different spin (α and β) are taken into consideration in a homogeneous electron gas. This leads to an approximation that the sum of α and β densities raised to the 4/3 power (i.e., $\rho^{4/3}$) is substituted by the sum of individual electron densities raised to the 4/3 power (i.e., $\rho_\alpha^{4/3}(\mathrm{r}) + \rho_\beta^{4/3}(\mathrm{r})$), which yields

$$E_{\mathrm{x}}^{\mathrm{LSDA}}[\rho] = -2^{1/3} C_x \int \left(\rho_\alpha^{4/3}(\mathrm{r}) + \rho_\beta^{4/3}(\mathrm{r})\right) d\mathrm{r}\,. \tag{2.30}$$

Since the electron spins have been included, LSDA is mostly appropriate for the system with unpaired electrons (e.g., radicals) or the system where the electrons tend to be unpaired (e.g., molecules in non-equilibrium states). For the system where electrons are fully paired (i.e., closed shell system), the LSDA is identical to the LDA. Overall, the geometries, frequencies and properties related to electron-distribution can be calculated accurately through LSDA while the dissociation energies tend to be very poor.

The approximation based on a uniform electron gas system has a serious drawback because the densities of the electrons actually vary greatly with their positions. An improved LSDA method, which is relevant to a non-uniform electron gas, is the Generalized Gradient Approximation (GGA) method. In addition to the electron density, the first derivative of the density is also taken as a variable. They are sometimes called non-local functionals to differ from the local ones like LDA and LSDA functionals. One of the simplest GGA exchange functionals is Becke's (B or B88) functional,[131] which has the form:

$$E_{\mathrm{x}}^{\mathrm{B88}}[\rho] = E_{\mathrm{x}}^{\mathrm{LDA}} - b\int \rho^{4/3} \frac{x^2}{1 + 6bx\,sinh^{-1}x}, \tag{2.31}$$

where $x = \frac{|\nabla\rho|}{\rho^{4/3}}$ is a gradient variable used to determine the parameter *b* by fitting to data from rare gas atoms. The errors coming with the LSDA functional then are greatly reduced by the implementation of Becke's functional because of the additional gradient variables. An example of the GGA based correlation energy functional is the Lee-Yang-Parr (LYP) functional, where the Gaussian-type functions are chosen in the expression of the KS orbitals. The combination of LYP correlation functional and B88 exchange functional produce a BLYP mixed functional.

To achieve a more accurate functional form, the DFT exchange-correlation energy is added to the exchange energy calculated by HF methods. A method of using HF/DFT mixed functionals was first proposed by Becke, which has the form of a half HF component and another half contribution from LSDA:

$$E_{\mathrm{xc}}^{\mathrm{HH}} = \frac{1}{2}E_{\mathrm{x}}^{\mathrm{HF}} + \frac{1}{2}\left(E_{\mathrm{x}}^{\mathrm{LSDA}} + E_{\mathrm{c}}^{\mathrm{LSDA}}\right). \tag{2.32}$$

This type of functional that combines exact exchange energy from HF theory and gradient-corrected exchange energy given by DFT is named a hybrid functional. One of the most widely used hybrid functionals is B3LYP that mixes the Becke 3-parameter functional and LYP correlation-energy functional in the form:

$$E_{\mathrm{xc}}^{\mathrm{B3LYP}} = (1-a)E_{\mathrm{x}}^{\mathrm{LDA}} + aE_{\mathrm{x}}^{\mathrm{HF}} + b\Delta E_{\mathrm{x}}^{\mathrm{B88}} + (1-c)E_{\mathrm{c}}^{\mathrm{LDA}} + cE_{\mathrm{c}}^{\mathrm{LYP}}. \tag{2.33}$$

Among the widely tested energy functionals, the B3LYP functional is the most popular one in current computations. This is due to the accuracy of the B3LYP results obtained for a large range of compounds, particularly organic molecules. Although several new density functionals significantly outperform this popular hybrid functional for predicting some properties, B3LYP

still remains a valid and particularly efficient functional for the "average" quantum chemistry problem.[132] For the most of properties we are interested in this work, such as hydrogen bonding and proton transport, B3LYP is still able to compete with the other sophisticated density functionals in accuracy, and often at a fraction of the CPU time associated.[85, 90, 91, 133] This is particularly important to perform geometric optimizations and binding energy calculations for systems containing a few of water molecules with complicated hydrogen bonding configurations. However, weak interactions among molecules (i.e., π- π interaction and nonbonded interactions) are not well represented by neither B3LYP nor the more sophisticated density functionals. Therefore, the determination of truly reliable results across a wide range of compounds is rather difficult, which is in need of most state-of-the-art density functionals.

2.1.5 Basis Functions

To compute the Kohn-Sham orbital, χ_i, one resorts to an expansion in a suitable set of basis functions and construct a secular equation to carry on the SCF process.[128, 134] Different approaches are adopted to construct basis functions for molecules and crystals.

The most widely used basis functions for molecules are those based on the LCAO approximation. They are fully mathematical functions that have some similarities to the simple wave functions. Two type of functions: Slater-type orbitals (STOs) and Gaussian Type Orbitals (GTOs), which are distinguished by their different behavior as a function of the radial coordinate. STOs more closely resemble the true behavior of atomic wave functions but are only restricted to the monoatomic and diatomic systems. In contrast, GTOs are easier to handle numerically and can be linearly recombined to construct a new basis function to obtain comparable accuracy as STOs. The accuracy of such an approximation (i.e., a contracted basis function) is dependent on the number of Gaussian type functions used in the combination. The

STO approximated by a combination of three GTOs is proven optimal because it balances both speed and accuracy of the calculation. The basis set of this type is denoted as STO-3G.

Taking into account the different chemical environment of electrons, we may separate the core electrons from the valence electrons of a single atom. This is mainly because the inner shell electrons interact less with the electrons from other atoms when compared to the outer shell electrons. Therefore another basis set is developed, and it treats the core electrons with a minimal basis set while splitting the valence electrons into larger basis sets. This type of basis set is the so-called split-valence basis set. For instance, 6-311G basis functions are made of 6 Gaussians for inner, and 3, 1 and 1 Gaussians in the valence component (triple-ζ basis sets). Moreover, the p-type GTOs are added to hydrogen atom and d-type functions are incorporated with second-row elements to polarize with their own s and *p*-type GTO. This additional polarization functions are denoted by adding a star '*' at the end of basis set such as 6-31G* or written as 6-31G(d). In the case of treating atoms with extra electrons or in excited states, the utility of polarization basis set may be diminished by the presence of diffuse effects. Consequently, an updated basis set inclusive of diffuse functions is designed to address this problem. The diffuse functions are similar to the standard *s* and *p* functions but have smaller orbital exponentials. In Pople's nomenclature, they are indicated by adding a sign of plus '+'. As an example, 6-31++G* is constructed from a 6-31G* basis set with additional *s* and *p* type diffuse functions on non-hydrogen atoms and one *s* type on hydrogen atoms.

For the periodic systems such as crystals, plane waves are often considered the most obvious basis set to solve the Kohn-Sham equations. A plane wave is defined as a wave of constant frequency (as a function of energy), with wavefronts consisting of an infinite series of parallel planes (of the same amplitude). Therefore, various waves of different frequency in a plane wave

basis set can be used to represent the system wavefunctions. To characterize the properties of valence electrons, it is common only to consider explicitly the valence electrons in the calculation and to include the core electrons into the nuclear core. However, the representation of valence electron wavefunctions with a plane-wave basis set shows rapid oscillations near to the atomic nuclei. A very large number of plane waves are required to properly model the large kinetic energy associated with these oscillations. This corresponds to taking many terms in the plane-wave expansion of the K-S orbitals. This problem becomes even worse for the heavy elements where more core electrons lead to a more pronounced oscillation behavior. To deal with this problem, a much weaker potential referred to as a pseudopotential is used to replace the 'true' potential in these core regions. A pseudopotential is a potential function that resembles the shape of the true wavefunctions outside the core region but with fewer nodes inside the core region. By using this approach, the number of terms required for the plane wave expansion of the wavefunction is greatly reduced, which thus leads to a drastically reduced computational cost.

The various pseudopotentials differ in the number of plane waves that are required for their representation and in the degree to which they can be transferred between different atomic environments. Pseudopotentials are usually derived from all-electron atomic calculations. The valence electron pseudopotential is required to produce the same behavior and properties of the valence electrons in the full calculation. If the same energies and amplitude (and thus density) outside a chosen core cutoff radius can be derived by the pseudo and all electron valence states, the pseudopotentials are called "non-local norm-conserving". So-called 'soft' pseudopotentials always use larger cutoff radius and require fewer plane waves and are therefore computationally more attractive, but less transferable. The 'ultrasoft' or 'supersoft' pseudopotentials were subsequently developed, which require even fewer plane waves. But they are also less accurate

to reproduce realistic features in different environments. The pseudopotential approach is very convenient because it reduces the number of electrons treated explicitly, making it possible to perform density-functional calculations on periodic systems with tens of thousands of electrons.

2.2 Dissipative Particle Dynamics

In contrast to QM methods, which incorporate complete descriptions of electronic structures, mesoscale simulations are often used to characterize nanoscale properties without resolving atomistic detail. These methods have bridged the gap between atomistic modeling and continuum modeling, and have been utilized to model systems that show self-organization on the nanometer scale. Mesoscale simulations can be realized with both particles and fields-based methods. The beads-based methods describe the system in terms of discrete interaction sites that consist of fictitious particles, or beads. Each coarse-grained bead is chosen to represent a group of atoms with the similar chemical properties and environment. One example of a particle-based simulation method is dissipative particle dynamics (DPD). In this section, the simulation technique is described in detail and a discussion of how it can be related to the Flory-Huggins theory of polymeric fluids is given. The description of the theory is based on a paper by Groot and Warren.[135]

2.2.1 Coarse-graining Theory

In a coarse graining approach, the atomic structure is mapped on a less detailed description than what is typically described in atomistic modeling. When compare to the starting structure, the coarse grained structure will only remain certain details of topological properties while neglect the information about position of individual atoms. To some extent analogous to atoms in atomistic modeling, beads play a central role in coarse-grained simulations. While atomic structure is replaced by different types of beads, the atomistic bonds between individual groups

of atoms are substituted by connectors joining the beads. The interaction between beads is associated to the definition of the beads type and force field.

Similar to the way that properties of atoms are defined by their chemical element type, the properties of beads are defined by their bead type. Properties of the atom group, such as mass and radius, can be used to define the bead type. In addition, different force filed types can be assigned the individual bead. Therefore, bead types can be also classed in degree of polarity, acidity, or hydrophilicity, which are determined by the force field parameters. By using many bead types associated with different force field types, coarse graining methods not only create the hierarchical mesoscale structure but also capture the essential chemical information of the system. Thus, this approach would efficiently reduce the complexity of a large system but is still able to resolve microstructure details with acceptable accuracy.

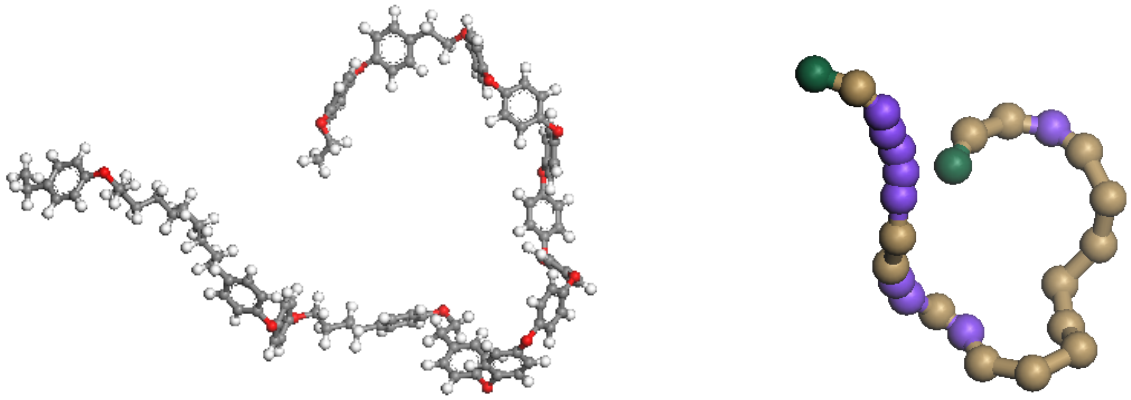

Figure 2.2. Coarse-graining of a random ethylene oxyphenyl copolymer by constructing different beads representing polymer subunits. (from help document in Materials Studio [136])

Systems suitable for mesoscale modeling are typically mixtures of several components that show morphological properties on the nanometer scale, such as polymer solutions, suspensions of colloidal particles, vesicles, and cells. For example, a random ethylene oxyphenyl copolymer

(as shown in Figure 2.2) is coarse grained to a mesomolecule constructed by different beads representing ethylene or oxyphenyl unit individually. The green beads represent the terminal ethylene units, the brown beads correspond to oxyphenyl subunits, and the purple beads represent polymeric ethylene units.

2.2.2 Dissipative Particle Dynamics Method

Although molecular dynamics (MD) simulation method has provided an accurate way to simulate the dynamics of an atomistic system, it is limited to simulating the system of a few thousand molecules over a few nanoseconds. For the system with larger spatial and time scale, coarse grained methods are required.

A new simulation technique, called Dissipative Particle Dynamics (DPD), was originally introduced by Hoogerbrugge and Koelman in 1992.[137] It is a combination of molecular dynamics, lattice-gas automata and Langevin dynamics. The starting structure is represented by a set of 'beads' that interact with other beads via soft potentials. The motion of beads is calculated by solving the equations of motion over a certain time span.

The coarse grained system consists of a set of beads with mass m. The position and velocity of bead i are denoted as $\mathbf{r}_i$ and $\mathbf{v}_i$, individually. Time evolution of this system is described by Newton's equations of motion:

$$\frac{\partial \mathbf{r}_i}{\partial t} = \mathbf{v}_i, \quad \frac{\partial \mathbf{v}_i}{\partial t} = \frac{\mathbf{f}_i}{m} \tag{2.34}$$

It is the definition of the forces that makes dissipative particle dynamics different from molecular dynamics. All forces in DPD simulations are 'soft', allowing the use of a much larger time step and correspondingly shorter simulation times.

The force $\mathbf{f}_i$ acting on bead i has the following form:

$$\mathbf{f}_i = \sum_{i \neq j} \left(\mathbf{F}_{ij}^C + \mathbf{F}_{ij}^D + \mathbf{F}_{ij}^R \right) + \mathbf{f}_i^S + \mathbf{f}_i^A . \tag{2.35}$$

The interaction between bead i with its neighbor j is described by the terms in the bracket. This term contains three types of force: a harmonic conservative force ($\mathbf{F}_{ij}^C$), a dissipative force representing the viscous drag between moving beads ($\mathbf{F}_{ij}^D$), and a random force to maintain energy in opposition to the dissipation ($\mathbf{F}_{ij}^R$).The remaining terms are forces due to bonded interactions: springs ($\mathbf{F}_{ij}^S$) and angles ($\mathbf{F}_{ij}^A$). The conservative, dissipative, and random forces are all short range with a fixed cutoff radius, r_c, which have the common form:

$$\mathbf{F}_{ij} = \begin{cases} C_{ij}\omega(r_{ij})\mathbf{e}_{ij} & r_{ij} < r_c \\ 0 & r_{ij} \geq r_c \end{cases}, \tag{2.36}$$

where $C_{ij} (= C_{ji})$ is a symmetric force amplitude, r_{ij} is the distance between beads i and j, and $\mathbf{e}_{ij}$ is the unit vector $\left(\mathbf{r}_i - \mathbf{r}_j \right) / r_{ij}$. The radial dependence of the force is determined by function $\omega(r)$. The force only acts over an interaction shell with radius r_c, thus the force becomes zero when $r \geq r_c$. The force is seen to be repulsive if $C_{ij} > 0$ and attractive if $C_{ij} < 0$.

The conservative force, $\mathbf{F}_{ij}^C$, in DPD is given by:

$$\mathbf{F}_{ij}^C = a_{ij}\omega^C(r_{ij})\mathbf{e}_{ij}, \tag{2.37}$$

where $a_{ij} = a_{ji} > 0$, indicating that this force is always repulsive. A linear weight function $\omega^C(r) = 1 - r/r_c$ is used to describe the conservative force. The dissipative force, $\mathbf{F}_{ij}^D$, is proportional to the velocity with which two beads approach each other:

$$\mathbf{F}_{ij}^D = -\gamma_{ij}\omega^D(r_{ij})\left(\mathbf{v}_{ij} \cdot \mathbf{e}_{ij} \right)\mathbf{e}_{ij}, \tag{2.38}$$

where $\gamma_{ij} = \gamma_{ji} > 0$ and $\mathbf{v}_{ij} = \mathbf{v}_i - \mathbf{v}_j$ is the velocity difference. The central component, $\mathbf{v}_{ij} \cdot \mathbf{e}_{ij}$, is positive if two beads move toward each other and is negative if they move away from each other. In either of two cases, the dissipative force is always seen to reduce the relative central velocity. DPD uses a quadratic function for the dissipative force: $\omega^D(r) = (1 - r / r_c)^2$ for $r < r_c$.

The random force $\mathbf{F}_{ij}^R$ between pairs of beads can be defined as:

$$\mathbf{F}_{ij}^R = \sigma_{ij} \omega^R(r_{ij}) \xi_{ij} \frac{1}{\sqrt{\Delta t}} \mathbf{e}_{ij}, \tag{2.39}$$

where $\sigma_{ij} = \sigma_{ji} > 0$ and Δt is the time step with which the equations of motion (Equation (2.34)) are solved. Similar to the conservative force, the random force is also weighted by: $\omega^R(r) = 1 - r / r_c$ for $r < r_c$. The noise term $\xi_{ij} = \xi_{ji}$ is a random number with zero mean and unit variance. The random number, ξ_{ij}, is drawn independently for each interacting pair at each time step. Because ξ_{ij} can have either sign, the random force can be either repulsive or attractive. In DPD, the random (and dissipative) forces obey Newton's third law: $\mathbf{F}_{ij} = -\mathbf{F}_{ji}$. This is in contrast to Brownian dynamics, in which the random (and dissipative) forces on two particles are uncorrelated.

For the mesomolecules constructed by connected beads, there are additional bonded interactions. The spring force experienced by bead i is $\mathbf{f}_i^S = -\partial U^S / \partial \mathbf{r}_i$, where U^S is the total bonded potential:

$$U^S = \sum_b \frac{1}{2} \mathrm{C}_b \left(r_c - r_c^0 \right)^2, \tag{2.40}$$

where the sum runs over all bonds. Each spring is parameterized by a modulus, C, and a length, r_0. By default, all bonds have the same modulus, which is equal to the spring constant (the

default is $4E_{ref}/r_c^2$ with $E_{ref}=k_BT$). The force experienced by bead i due to angular interactions is $\mathbf{f}^S=-\partial U^A/\partial\mathbf{r}_i$, where U^A is the total angular potential.

$$U^A=\sum_a k_a\left(1-cos\left(\theta_a-\theta_a^0\right)\right) \tag{2.41}$$

where the sum runs over all angles. The angle potential is parameterized by the modulus, k, and the equilibrium angle, θ_0. The modulus sets the stiffness of the chain.

Because the dissipative force, and therefore the total force, is dependent on velocity, the velocity-Verlet algorithm must be modified to be an iterative predictor-corrector scheme. The initial positions and velocities of beads are assigned as $\mathbf{r}(0)$ and $\mathbf{v}(0)$. The forces in this state are calculated from Equation (2.35) and then integrated to obtain $\mathbf{r}(\Delta t)$ and $\mathbf{v}(\Delta t)$ using the following algorithm:

$$\begin{aligned}
\mathbf{r}_i(t+\Delta t)&=\mathbf{r}_i(t)+\mathbf{v}_i(t)\Delta t+\mathbf{f}_i(t)\frac{1}{2}(\Delta t)^2/m\\
\mathbf{w}_i(t)&=\mathbf{v}_i(t)+\lambda\mathbf{f}_i(t)\Delta t/m\\
\mathbf{f}_i(t+\Delta t)&=\mathbf{f}_i\left(\mathbf{r}_i(t+\Delta t),\mathbf{w}_i(t)\right)\\
\mathbf{v}_i(t+\Delta t)&=\mathbf{v}_i(t)+\frac{1}{2}\left[\mathbf{f}_i(t)+\mathbf{f}_i(t+\Delta t)\right]\Delta t/m
\end{aligned} \tag{2.42}$$

First, new positions $\mathbf{r}(t+\Delta t)$ can be calculated from $\mathbf{r}(t)$, $\mathbf{v}(t)$, and $\mathbf{f}(t)$ that are given in the initial condition. The auxiliary velocities $\mathbf{w}_i(t)$ are calculated by introducing a tunable parameter λ to obtain a self-consistent solution. To achieve a stable integration of the equations of motion with a large timestep, this parameter is often chosen to be 0.65 as proposed by Groot and Warren.[135] Then, the new force is calculated from Equation (2.35) using the new positions and the auxiliary velocities. Finally, from the new forces and the new positions, the new velocities, $\mathbf{v}_i(t+\Delta t)$, are calculated.

2.2.3 Flory-Huggins Theory

In practice, interactions between DPD particles are usually described by a set of interaction parameters generated from different level of theory. Among several of available microscopic theories, Flory and Huggins theory is seen to be the simplest but most reliable to describe phase behavior of binary polymer mixture. It is possible to link the DPD parameters to the Flory Huggins χ parameter by comparing DPD with this theory. The DPD parameters calculated from χ can then be used to study more complex phase behavior in the system with many components.

According to Flory-Huggins theory, the change in free energy ΔF on mixing two components A and B at constant temperature T is written as:

$$\frac{\Delta F}{k_B T} = \frac{\varphi_A}{N_A} ln\,\varphi_A + \frac{\varphi_B}{N_B} ln\,\varphi_B + \chi \varphi_A \varphi_B \tag{2.43}$$

where k_B is Boltzmann's constant, N_A and N_B are number of lattice sites occupied by component A and B, φ_A and φ_B are volume fraction of units of type A and B. The degree of phase separation in this binary system is associated with the value of χ parameter. When χ is negative the components interact favorably and they will mix; if χ is a positive value, it indicates that the optimal interaction is achieved in the pure state. With large positive values of χ, phase separation occurs. To determine the minimal value of χ at which phase separation occurs, set the derivative of free energy with respect to the component A to be zero, then we have:

$$\chi = \frac{1}{\varphi_B - \varphi_A}\left(\frac{1}{N_A} ln\,\varphi_A - \frac{1}{N_B} ln\,\varphi_B + N_A - N_B \right) \tag{2.44}$$

To establish the connection between DPD and Flory-Huggins theory, the equation-of-state that describes the free energy density in a binary system is derived:

$$\frac{f_V / \rho}{k_B T} = \frac{\varphi_A}{N_A} ln\,\varphi_A + \frac{\varphi_B}{N_B} ln\,\varphi_B + \frac{\alpha}{k_B T} \rho \left(2a_{AB} - a_{BB} - a_{AA}\right) \varphi_A \varphi_B \tag{2.45}$$

where ρ is the density, α is a constant, a_{AB} , a_{AA} and a_{BB} are interaction parameters between the same and different components. By comparing this expression with the Flory-Huggins free energy-of-mixing in Equation (2.43), χ parameter can be expressed as:

$$\chi = \frac{\alpha}{k_B T} \rho \left(2a_{AB} - a_{BB} - a_{AA}\right) \tag{2.46}$$

Thus, we have made a linear relation between χ parameter and interaction parameters ($\Delta a = a_{AB} - \left(a_{AA} + a_{BB}\right) / 2$) in DPD simulations.

To obtain the coefficient of this linear relation, several DPD simulations were performed by Groot and Warren.[135] They confirmed a linear relation as shown in Equation (2.46) and found $\chi / \Delta a$ = 0.286 at a density of 3 particles per unit volume. At a higher density of 5, this coefficient was found to be 0.689. When compare to experimental values for simple component such as water, an expression of interaction parameter between component A and B is given as (in reduced units):

$$a_{AB} = \begin{cases} 25 + 3.50\chi & \rho = 3 \\ 15 + 1.45\chi & \rho = 5 \end{cases} \tag{2.47}$$

Given the χ parameter, now we can use this linear relationship to calculate the interaction parameters used in DPD simulations. In addition to the experimental results that are available for many of polymer blends, Flory-Huggins parameters can be also calculated from atomistic and statistic modeling. If the excess entropy terms in Equation (2.44) are neglected, we have

$$\chi = \frac{1}{\varphi_A \varphi_B}\left(\frac{\Delta E}{k_B T}\right) \tag{2.48}$$

where ΔE is the energy of mixing which can be calculated from molecular dynamics simulations. However, it requires additional calculations based on both pure and mixed systems and either of them are considerable expensive. A simple alternative way is to us "mixing rule" that assumes the interaction between different component is related the interaction between like components. Therefore, no separate simulations are needed as in MD simulations. It gives:

$$\chi = \frac{V}{k_B T}\left(\delta_A - \delta_B\right)^2 \tag{2.49}$$

where δ_A and δ_B are solubility parameters for component A and B, and V is the volume associated with a bead. The solubility parameter is related to the cohesive energy E_c by $\delta = \sqrt{E_c / V}$. The cohesive energy can be calculated from MD simulation as the average intermolecular energy or simply calculated from statistical method.

2.2.4 Scaling of Units

In molecular dynamics simulations, the forces are placed on atoms with known sizes determined by experimental measurement. In DPD calculations, however, the size of particle is no longer represented by the real size of atom or molecule. It is manually set to be the size of a small region of material interacting via phenomenological forces. Regions are chosen such that they possess the same mass, m , and interaction radius, r_c .

Since all beads are defined by the same mass and interaction radius, a reduced system of units is introduced in DPD simulations. In this system, the unit of mass and length are defined as the bead mass and interaction radius. An additional unit, the reference energy, is set to be the thermal energy $E_{ref} = k_B T$ at a fixed temperature. Consequently, the rest of units can be derived.

The forces are scaled in units of E_{ref} / r_c, time is measured in units of $r_c\sqrt{m / E_{ref}}$ and pressure or stress are in units of E_{ref} / r_c^3. Thus, all properties can be reported in the reduced units m, r_c, and E_{ref}. All these properties can also be converted to real units by simply substitution of the value of reduced units. For example, typical values of reduced units are m = 0.1 kg mol-1, E_{ref} = 2478 J mol-1, r_c = 0.8 nm, with a time unit of $r_c\sqrt{m / E_{ref}}$ = 0.005 ns.

Chapter 3 Experimental Methods

Since the first transmission electron microscope (TEM) was built by Ernst Ruska at the University of Berlin in 1931, tremendous improvements have been made in the past few decades.[138] Nowadays, TEM has become an instrument that offers a broad range of characterization techniques with both high spatial and analytical resolution to understand nanascale properties. A TEM can appear in several different forms based on different operation mode (e.g., CTEM, HRTEM, STEM) or type of information collected (e.g., AEM). Modern TEM often combines many of these techniques into a single instrument, which makes TEM a versatile tool to do both qualitative and quantitative research for almost any kind of materials.

In this chapter, we briefly review different TEM techniques used in this dissertation. Basic theory and applications to polymeric materials are also covered in each section. A description of sample preparation techniques and instrument settings are presented at the end of the chapter.

3.1 Transmission Electron Microscopy (TEM)

In a light microscope, light generated from a light source is used to illuminate an object (sample) forming an enlarged image and projected into human eyes. In a TEM, however, a beam of electrons emitted from the electron gun is transmitted through an ultrathin specimen. An image is formed by the interaction between electrons and specimen and focused onto an imaging device such as a fluorescent screen, or detected by a CCD camera.

The TEM main unit consists of three primary systems: microscope column, vacuum system, and high voltage transformer and power supply systems. The microscope column section is the most important part of a TEM. This system consists of the following: the illumination system, the objective lens and stage, and the imaging system (as viewed from the top in Figure 3.1).

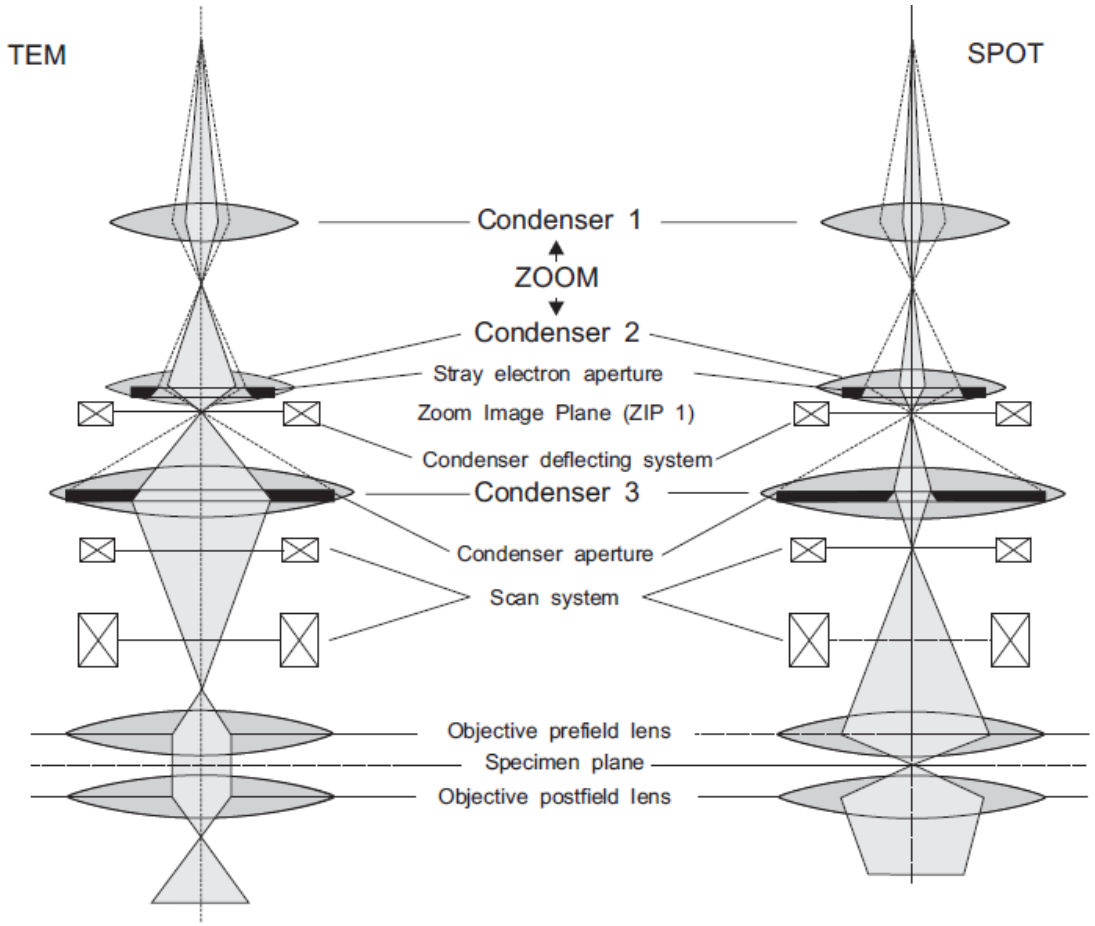

Figure 3.1. Different ray diagrams representing parallel (left) and converged (right) illumination in TEM and SPOT mode (from Zeiss Libra 200MC manual)

Electrons emitted from electron gun with high energy (typically 20~300 keV) first pass through a series of condenser lens to form an electron beam with desirable brightness and size. The illumination system in the Zeiss Libra 200MC TEM consists of three condenser lenses. The first and second condensers together form a zoom system which images the crossover of the gun into the constant Zoom Image Plane (ZIP). In TEM mode, the third condenser lens transmits the crossover image to the front focal point of the objective prefield lens forming parallel illumination on a specimen. The condenser aperture is placed in the main plane of the third condenser lens to limit the illuminated area. By controlling the excitation of the third condenser, a converged beam can be formed when the third condenser images the crossover into the

entrance image plane of the objective prefield lens. In this illumination mode (SPOT mode), a very fine illumination can be used for scanning (STEM) imaging, X-ray microanalysis (EDS), electron spectrometry (EELS) and convergent beam electron diffraction (CBED).

The central part of a TEM is the objective lens and the specimen holder system where all of the beam-specimen interactions take place. The images and diffraction patterns (DP) are created by objective lens and subsequently magnified in the imaging system for viewing and recording. The magnified images or the DP are then observed on a fluorescent viewing screen or recorded by a CCD or TV camera.

3.1.1 Conventional Transmission Electron Microscopy (CTEM)

In a TEM image, contrast variation is governed by a different contrast forming mechanism during an electrons scattering event. For instance, the contrast of images formed in a conventional TEM is primarily due to the thickness and composition of the specimen.

The mass-thickness contrast arises from incoherent elastic scattering of electrons. Thicker regions of the sample scatter a higher fraction of the incident electrons due to multiple scattering effects. Many of the scattered electrons are absorbed by the objective diaphragm, so that the corresponding regions in the image appear dark. Since the cross section for elastic scattering is a function of the atomic number (Z), regions containing higher atomic number elements scatter more electrons than those with lighter elements. Thus, the heavy element stained regions always appear dark relative to their surroundings.

Figure 3.2 shows the distribution of small gold particles and larger polystyrene (PS) spheres on a thin carbon coated film. The gold particles appear darker than other components due to the high density of heavier gold elements in these small regions. The influence of a locally increased specimen thickness on contrast formation is shown by the PS particle in the center of the image.

The carbon support film is much thinner than the large PS particle, which causes the bright background in the image.

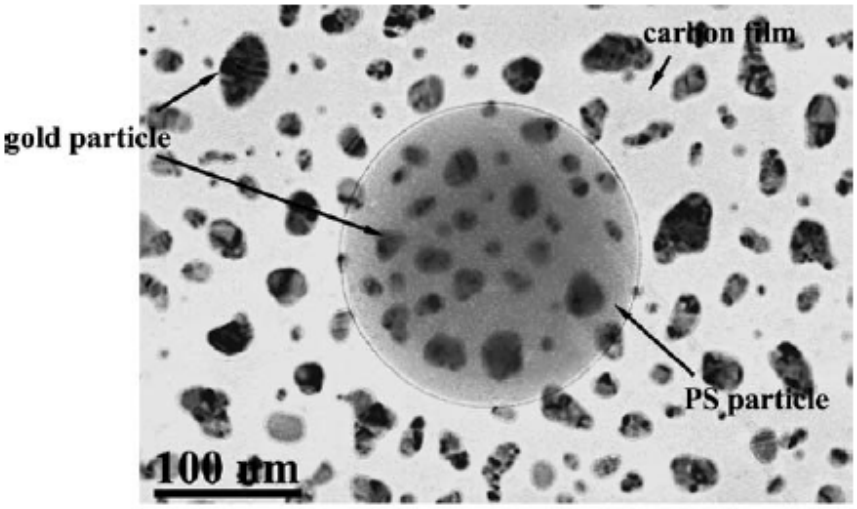

Figure 3.2. Illustration of mass-thickness contrast showing the distribution of small gold particles and polystyrene latex spheres on a thin carbon support. (from reference [139])

The mass-thickness contrast is also affected by the size of the objective aperture and the accelerating voltage. Smaller apertures will increase the difference in the ratio of scattered and transmitted electrons and thus leads to an enhanced mass-thickness contrast. A similar effect is found when lower accelerating voltages are used. The relative contrast between higher mass and lower mass regions is increased as the scattering angle and cross section are increased.

3.1.2 High Resolution TEM (HRTEM)

High-resolution transmission electron microscopy (HRTEM) corresponds to an imaging mode in TEM that provides sufficient resolution to resolve atomic details in a crystal structure. In addition to the conventional TEM investigations of polymers, this technique allows one to image the local packing of molecules into a crystalline lattice found in crystalized polymeric materials. However, this technique not only requires a TEM with a high resolution module and perfect

beam alignment, but also a properly prepared specimen that is thin enough to be treated as a weak phase object. Additionally, optimum defocus conditions (Scherzer focus) must be applied. Although application of HRTEM to various inorganic materials has become very common, the use of this technique for most polymeric materials has been limited due to the rapid degradation of the material in the electron beam.

The contrast formation in an HRTEM is determined by the phase difference of the electron waves scattered through a thin specimen. Dissimilar to the conventional bright and dark field imaging in TEM mode where only the central electron beam or a single diffracted beam is used, two beams and commonly many beams condition is utilized to form the phase contrast. To convert the small phase differences of these beams into intensity differences in the final image, additional phase shifts need to be introduced using spherical aberration and defocusing effects.

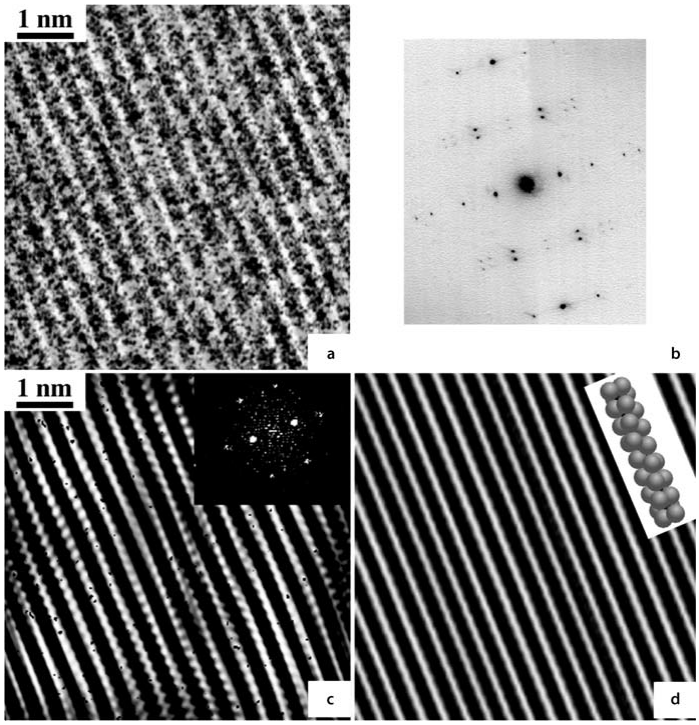

Figure 3.3. (a) HRTEM image of thin film PTFE with 157 helical conformation and (b) corresponding microdiffraction pattern; (c) is a Fourier filtered image and (d) is a simulated image. (from reference [140])

One example of applying this technique for polymers is illustrated in Figure. 3.3, where the lattice images of highly oriented PTFE thin film are shown. The HRTEM image (a) shows high degrees of ordering, which is consistent with an extended chain single crystal structure. With Fourier filtering, the resulting image (c) shows sub-molecular structure reflecting the helical chain conformations that were reported by X-ray diffraction measurement.[140] To obtain the information that is buried in the HRTEM image due to a poor signal-to-noise ratio, a computer simulated image (d) was generated and compared with the experimental images.

3.2 Scanning Transmission Electron Microscopy (STEM)

To obtain localized signal in a small region of interest, TEM is combined with an SEM technique creating scanning TEM (or STEM). In STEM, a very fine electron probe is focused down to a small spot and scanned through a thin sample. The ray diagram in STEM mode is illustrated in Figure 3.4. As explained in the previous section, a focused beam (in SPOT mode) is created by changing the excitation of the third condenser. Once STEM mode is activated, the static deflecting systems above and below the sample become dynamic deflecting systems. The move of the beam on the sample is controlled by the scan system above the sample. The deflected beam is then compensated by a synchronized descan system below the sample. Signals from scattered electrons and ionized atoms are both recorded. The image is formed simply by detecting the electron flux scattered in some direction as a function of the probe position. At the same time, chemical and bonding information along each projected atomic column may be obtained. The point analysis is realized by collecting signals either from the characteristic X-ray (EDS) or a certain amount of energy lost by the transmitted electrons due to the core and valence excitation (EELS). The performance of a STEM is largely determined by how small a spot the

electron beam can be focused to, and how much current can be maintained in that beam, which needs both devices to correct lens aberrations and careful alignment.[141]

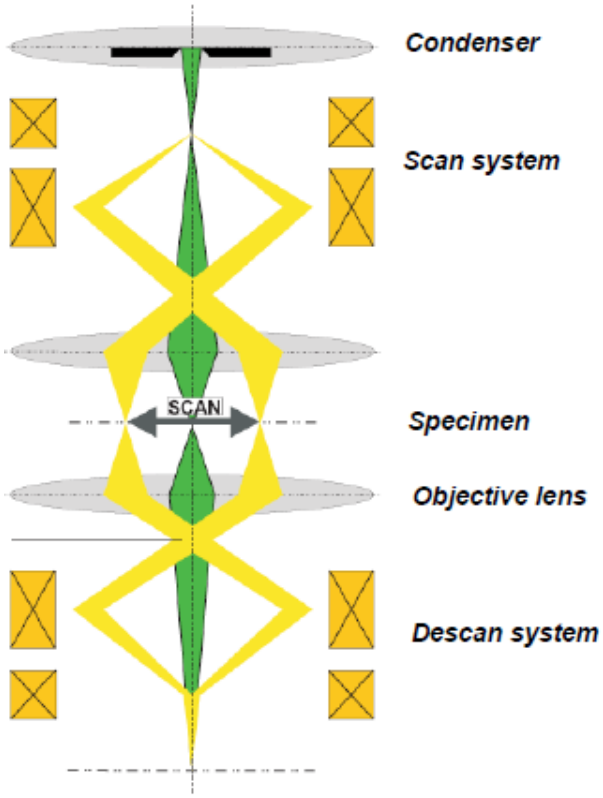

Figure 3.4. Ray diagram in STEM mode, where the scan and descan of beam are controlled by two pairs of deflection coils above and below the specimen. (from Zeiss Libra 200MC manual)

Different detectors placed above and below the specimen are responsible for processing different signals generated when a focused electron beam interacts with a sample. Figure 3.5 shows different detectors and their position relative to the sample. Above the sample, an SE detector is used to collect low energy secondary electron signals due to the inelastic scattering on specimen surface and form SEM like images. Characteristic X-ray signals are obtained by an EDX detector above the specimen to acquire EDS spectra. The transmitted electrons scattered

under high angles are detected by an annual detector (HAADF detector) below the sample. The contrast in corresponding HAADF images is mainly due to the local composition of the specimen. Therefore, the image in this form is also called a Z-contrast image. Below the center hole of the HAADF detector, a detector with a Faraday cage is used to collect unscattered transmitted electrons and forms a coherent/incoherent bright field image.

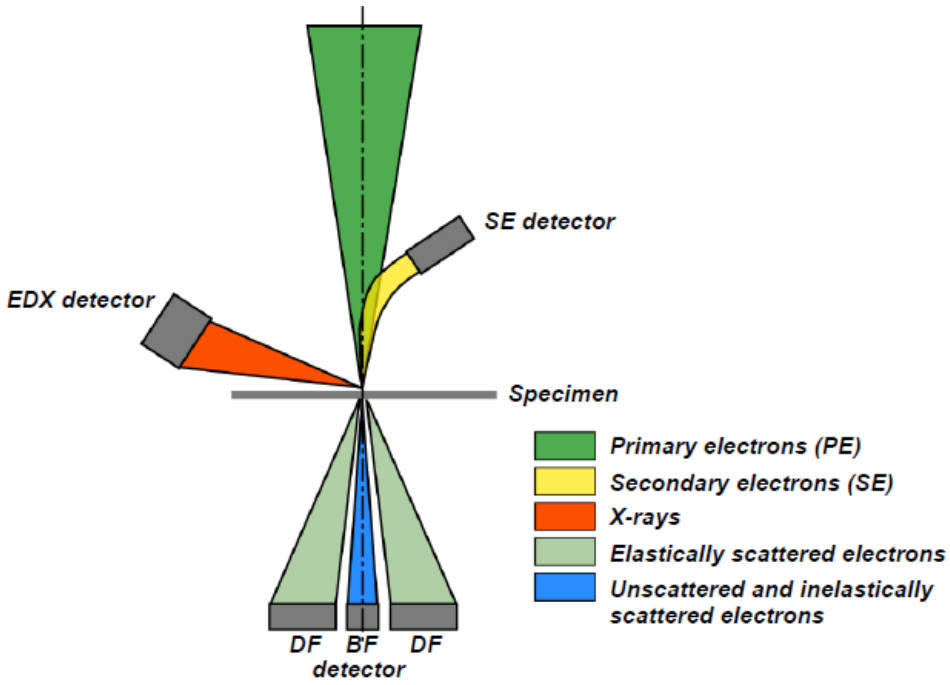

Figure 3.5. Illustration of different detectors for collecting various signals during the scan in the STEM mode (from Zeiss Libra 200MC manual)

3.1.1 High Angular Annual Dark Field (HAADF) Imaging

The Image formation in the scanning mode is fundamentally different from static-beam TEM image formation. In a dedicated STEM, no post lenses are required for forming or projecting final images. Bright field and dark field images are derived from signals of transmitted electrons with different scattering angles at the same time. The signal from high-angle scattering mainly results from electrons that have experienced nuclear interactions. Therefore, the signal is

incoherent and the contrast of the resulting HAADF image is highly sensitive to the atomic number (Z-number). Spatial resolution is largely dependent upon the size of the probe. Correctly adjusted spherical aberration on a fine probe leads to an atomic resolution with enhanced contrast. Providing the high spatial resolution and simultaneous point-to-point analysis, HAADF imaging has emerged as the primary imaging technique for AEM applications.

Dark field (DF) images in TEM and STEM are formed by different mechanism. In conventional TEM imaging, DF images are usually formed by permitting only a fraction of the scattered electrons to enter the objective aperture. HAADF imaging in STEM however collects most of the scattered electrons hitting the ADF detector. In addition, HAADF image contrast is greater than TEM DF image and related to the atomic number of specimen, which allows the direct interpretation of results with fewer ambiguities. The contrast in a HAADF image is dependent on the ratio of the number of electrons hitting the detector to the number of electrons going through the hole, and can be easily optimized with different camera length.

HAADF imaging has been successfully applied for investigations of some polymeric materials that show nanoscale morphology. Typical ionomers are random copolymers with a portion of ionic monomeric units (typically acids) and nonionic monomeric units. The microphase separation between ionizing and nonionizing groups in an ionomer can be visualized by partially or fully neutralization with ions, leading to the formation of nanoscale ionic aggregates. In a conventional TEM, nanoscale crystalline particles can typically be imaged by use of diffraction contrast when particles are positioned in a Bragg condition. However, the nanoscale aggregates in ionomers are largely amorphous and their detection by mass-thickness contrast is often diminished by the phase contrast contributions of the surroundings, which results in a similar

appearance. Thus, the highly sensitivity of Z-number contrast in HAADF mode provide a clearer and easier to interpret image.

HAADF and BF imaging in STEM have been used to study different shapes, sizes, and aspect ratios of the aggregates in various ionomers. For example, spherical and vesicular shape of ionic aggregates were found in poly(ethylene-co-methacrylic acid) neutralized with zinc (Zn-EMMA) and poly(styrene-co-methacrylic acid) neutralized with cesium (Cs-SMMA).[110, 111] Most recently, the morphology of poly(styrene sulfonate)-b-poly(methylbutylene) (PSS−PMB) copolymer without ion exchange was studied with HAADF imaging. As shown in Figure 3.6, honeycomb morphology and nonoscale ionic clusters (bright spots) were observed. The ionic clusters (~1.5 nm) are found to be uniformly distributed near the top and bottom surfaces and are concentrated in the honeycomb wall structure.

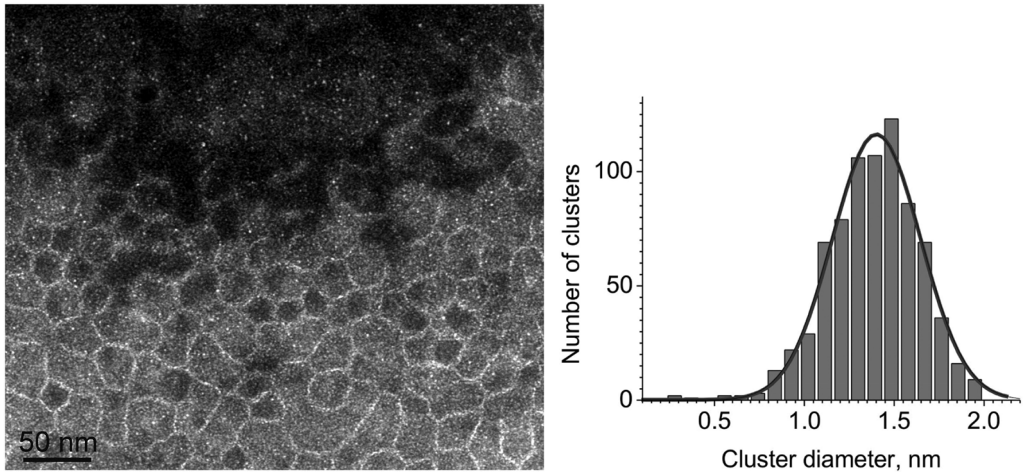

Figure 3.6. Electron micrograph showing acidic clusters in a dry PSS- PMB membrane and cluster size distribution determined from the micrograph.(from reference [142])

3.1.2 Spectrum Imaging (SI) in STEM

The inelastic interactions between energetic electrons and materials can be characterized with electron energy-loss spectroscopy (EELS). This technique provides a variety of information

about chemical, physical and even optical properties of materials. There exists two different ways of combining EELS with high spatial resolution imaging in a TEM/STEM. In the configuration for energy filtered TEM (EFTEM), the fixed parallel beam is used and filtered images are acquired with a certain range of energy loss. In another configuration, a focused beam scans a sample and an EELS spectrum is taken at each pixel of the scan. The latter technique, called spectrum imaging (SI), is commonly used in a STEM with EELS installed.

The formation of a SI data cube in the STEM mode is shown in Figure 3.7. One of the key advantages of this technique is the EELS signal can be obtained simultaneously with an atomic-resolution HAADF image. The data cube of the spectrum image thus contains both 2-D spatial information represented by the Z-contrast (x and y direction) and energy loss information at each pixel (ΔE direction). With the very fine probe and advanced techniques in aberration corrector, STEM is now able to provide atomic scale spatial resolution.[143] By allowing the acquisition of the spectrum signals with a resolution down to the single atomic column level, invaluable information about the chemical and physical properties of materials can be obtained.

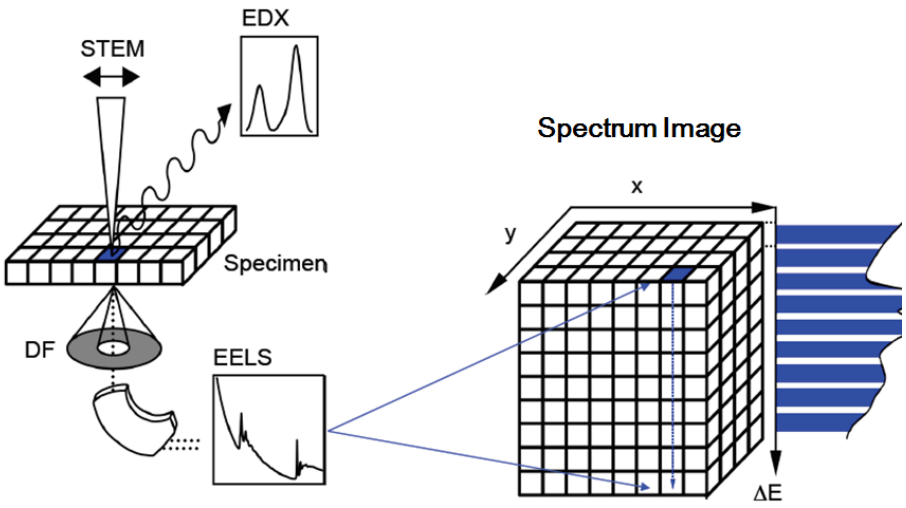

Figure 3.7. Formation of a Spectrum Image in STEM mode. (from Gatan EELS school tutorial)

Spectrum imaging both in core-loss and low-loss modes has been employed to study several aspects of multiphase polymer morphology in various types of blends, composites and block copolymers. For example, morphology of a biphasic poly(dimethyl siloxane) [PDMS]-acrylate copolymer nanoparticles were studied with low loss spectrum imaging showing in Figure 3.8. Different phases (water, PDMS, and acrylate) can be distinguished based on their characteristic features of low-loss spectra showing in Figure 3.8. (B). The corresponding component maps presented in Figure 3.8 (C-E) confirms the formation of the biphasic nanoparticle with PDMS-rich and polyacrylate-rich lobes showing in the HAADF image Figure 3.8 (A).

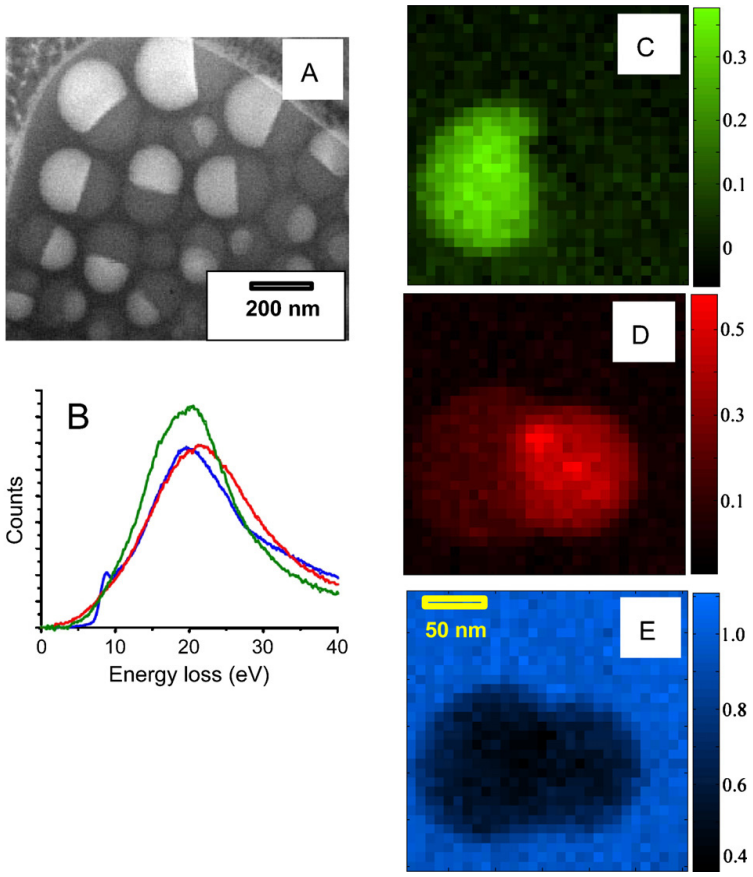

Figure 3.8. (A) HAADF STEM image of a two-phase nanocolloid consisting of PDMS (dark contrast) and acrylate (light contrast) rich phases in amorphous ice carried by a holey-carbon support film. (B) low-loss EELS reference spectra of the PDMS (green), the acrylate copolymer (red), and amorphous ice (blue). Spectrum images derived by mapping PDMS (C), acrylate (D), and water (E).(from reference [144)

3.3 Analytical Electron Microscopy (AEM)

When an accelerated beam of electrons hits on a sample, both elastic (without energy loss) and inelastic (with some energy transferred to individual atoms) interactions take place. A wide range of signals are produced by these two kinds of interactions and can be collected and analyzed in different forms of electron microscope, some of which are summarized in Figure 3.9. In principle, all these products of primary beam interaction can be used to derive information on the nature of the specimen. Most of elastically scattered electrons are used in forming images in conventional TEM and scanning TEM. More quantitative analysis can be accomplished in analytical electron microscopy (AEM) given the information produced during various inelastic interactions. The spectra extracted from the signals generated from characteristic x-rays and inelastically scattered electrons are especially useful to identify different elements and chemical bonding in a small area of interest. They correspond to two techniques in AEM: X-ray energy-dispersive spectrometry (EDS) and electron energy-loss spectrometry (EELS).

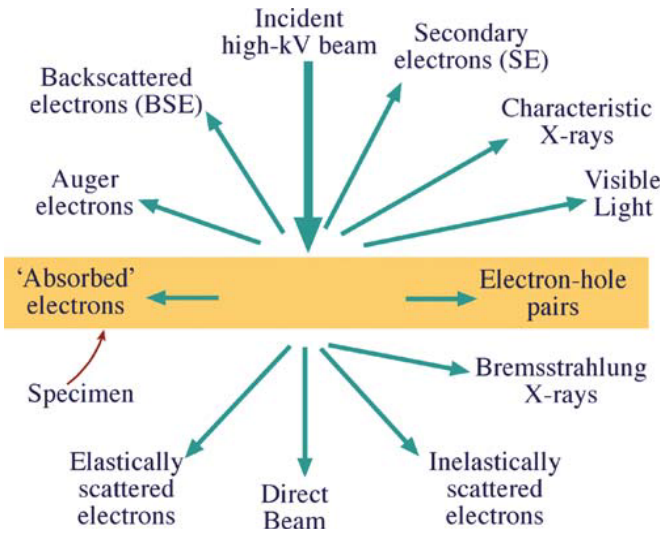

Figure 3.9. Different types of signals generated by the elastic and inelastic interactions between a high-energy beam of electrons and a thin specimen.(from reference [138])

3.3.1 Dispersive X-ray Spectroscopy (EDS)

One of signal that is generated due to the inelastic interaction between incident electron beam and specimen is the characteristic X-ray. The corresponding X-ray spectrum consists of element-specific characteristic peaks superimposed on a non-characteristic background. When an atom is ionized by high energy electrons and returns to ground state, it emits unique X-ray with well-defined energies. When electrons are slowed by electrostatic interaction with the nucleus they produce a continuum of bremsstrahlung X-rays and together the characteristic peaks and the bremsstrahlung background comprise the X-ray spectra that can be detected by EDS. In TEM, a converged beam in spot mode is usually used to gather X-ray information due to the low number of counts in the parallel beam condition. Combined with point-by-point scanning in STEM, EDS enables elemental mapping and quantitative analysis of materials composition.

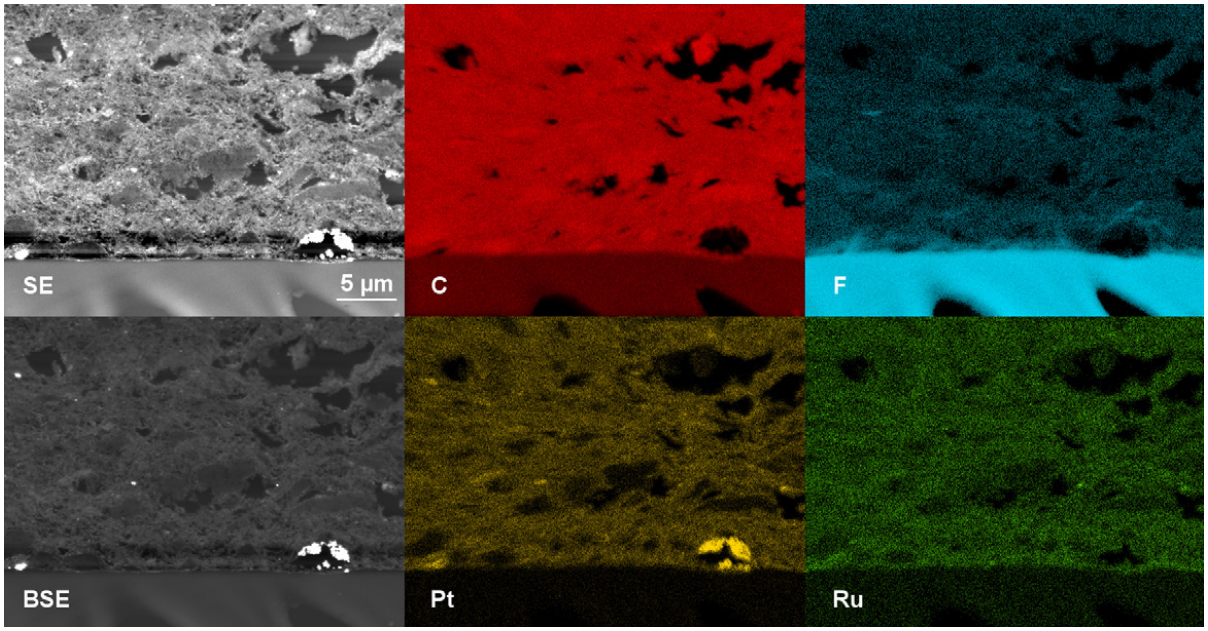

Figure 3.10. SE and BSE micrographs of a DMFC anode catalyst layer and elemental maps for carbon (C), fluorine (F), platinum (Pt) and ruthenium (Ru) for the same region obtained by EDS mapping.(from reference [119])

Although EDS is a powerful tool to conduct chemical analysis, it suffers several limitations when it applies to polymer materials. First, the presence of scattered electrons and X-rays tend to degrade the quality of the generated EDS spectrum and may lead to false peaks in the resulting spectrum. Thus, precautions have to be taken to ensure the collected X-ray signal is only from the area of your interest and without false signals from sample holder or grid. Additionally, microanalysis based on EDS relies on the sufficient number of counts generated during the electron interaction and thus is primarily conducted for mapping heavy element. Most of polymer consists of light elements and very sensitive to the electron beam, which makes mapping X-ray signals on HAADF images is quite challenging. However, when this technique is associated with SEM imaging, it generally yields better signal-to-noise ratios. For instance in Figure 3.10, elemental distribution in the DMFC catalyst layer is investigated by using EDS in a SEM, where the signals from carbon and fluorine are used to generate mapping of the carbon black and PFSA polymers.

3.3.2 Electron Energy Loss Spectroscopy (EELS)

Electron energy loss spectroscopy (EELS) in the TEM is a technique that measures the energy distribution of electrons after they interact with a specimen. The energy loss during the inelastic interaction can be ascribed to the excitation of conduction or valence electrons (low-loss) and atomic ionization (core-loss). The features of these spectra are used to probe optical, chemical and structural properties of solid. The spatially resolved EELS that combines with STEM/TEM imaging has become a powerful tool to investigate local chemical and physical properties of various nano-structured materials.

As shown in Figure 3.11, three principle regions of energy loss are often used to characterize a spectrum: zero-loss, low-loss and core-loss region. The most intense and narrow peak at 0 eV is

called the zero-loss peak (ZLP), which consists primarily of elastically scattered electrons. The full width at half maximum (FWHM) of the ZLP defines energy resolution of the electron source and is important in calibration of the spectrum and calculation of relative thickness of samples. The low-loss (or valence loss) region contains electron with energy loss up to ~70 eV. The features in low-loss region primarily arise from collective resonance response of free electrons (i.e, plasmon peak) and transitions of electrons in valence and conduction states (i.e., interband transition and excitons). Plasmons are longitudinal wave-like oscillations of weakly bound electrons. The intensity and width of plasmon peaks is related the local charge density which can be utilized to characterize different phases. The weakly bound outer-shell electrons, involved in the inter- or intra-band transitions, are responsible for the response to an external field. Therefore, the features in low-loss region can also be used to characterize the dielectric and optical properties of material.

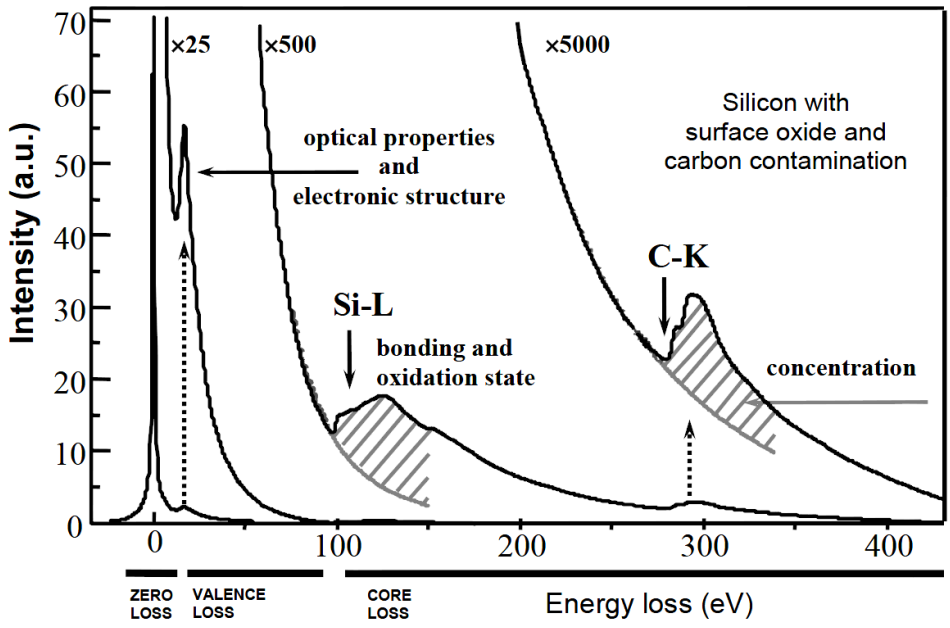

Figure 3.11. An EELS of Si showing information extracted at different energy scale (Courtesy of Gerd Duscher)

The tightly bound inner-shell or core electrons can be excited to conduction band when they are interacted with high-energy incident electron. The energy loss associated with this ionization process is called ionization edge in the high-loss region of an EELS spectrum. A certain level of intensity variations of EELS are also observed above this onset energy. The stronger oscillations often occur within about 30–50 eV of the onset of the edge (ELNES) and the weaker ones extend out for several hundred eV as the edge intensity diminishes (EXELFS). The onset energy (ΔE) and fine structures near the ionization edge (ELNES) provide details about how the ionized atom is bonded, the coordination of that specific atom, and its local density of states. Furthermore, distribution of other atoms around the ionized atom can be determined by the radial-distribution function (RDF) which is derived from the extended energy-loss fine structure (EXELFS). ELNES effectively mirrors the unoccupied density of states (DOS) as illustrated in Figure 3.12. Fermi energy (E_F) is equivalent to the ionization edge onset (ΔE). The peaks appear in ELNES correspond to electrons with the greatest density of unfilled states. Thus, ELNES can be calculated through methods based multiple scattering theory or density functional theory.[145, 146]

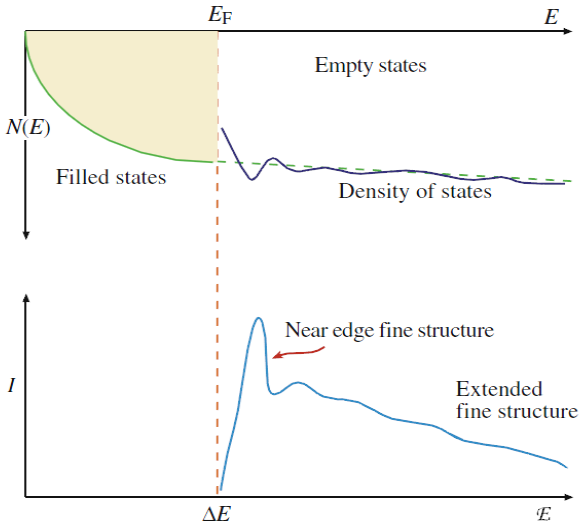

Figure 3.12. Relationship between the unoccupied DOS and the ELNES.(from reference [138])

There exist many experimental techniques that probe the transition of electrons between electronic states. In principle, they all are capable of providing details of electronic structure of materials. They are different from EELS by the source of radiation, depth of interaction and type of electronic transitions. A schematic of the transitions in some of the available techniques is shown in Figure 3.13. Similar to ELNES, X-ray absorption spectroscopy (XAS) excites an electron from a core state into unoccupied states, but uses photos instead of electron as radiation source. Thus, X-ray Absorption Near Edge Structure (XANES), also known as Near edge X-ray absorption fine structure (NEXAFS) provides nearly identical information about electronic excitation as ELNES but with limited spatial resolution due to the smaller cross section of X-ray interaction. Another technique that uses X-ray to detect the electronic excitation is so called X-ray photoelectron spectroscopy (XPS) or ESCA (electron spectroscopy for chemical analysis). It measures the binding energy of the core state, which is correlated to the transition of core electrons to vacuum. When photons in the ultraviolet range are used as incident radiation (UPS), the valence band states can be probed. However, both of them are surface-sensitive techniques which only probe the properties of sample surface with several atomic layers and lack of sufficient spatial resolution. When electron is ejected from a core level, the atom can decay by emission of an X-ray or Auger electron. These two different processes correspond to X-ray emission spectroscopy (XES) and Auger emission spectroscopy (AES).

Energy loss techniques have become powerful tools to investigate polymeric material composition and local bonding states. In the high energy loss region, the K-edges of light elements in the polymers (such as C, N, and O) can be well defined and analyzed since they lie in the sub-1000 eV range that is especially well suited for using spectrometers commercially available for modern TEMs/STEMs. In addition, features in low-loss regions due to the variety

of both sigma and pi bonding states of carbon can be utilized to distinguish spatial variations in local compositions involving mixtures of two or more of similar polymers.

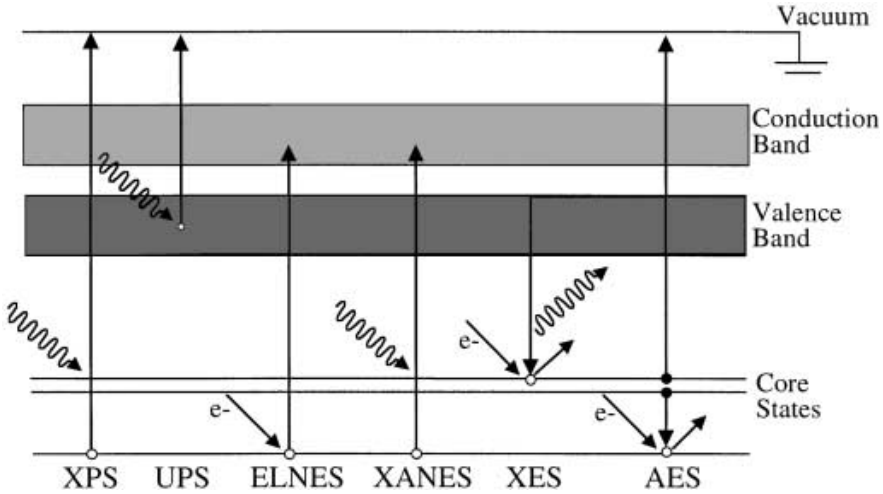

Figure 3.13. Schematic of the transition processes in some of the spectroscopic techniques that can probe electronic structure.(from reference [146])

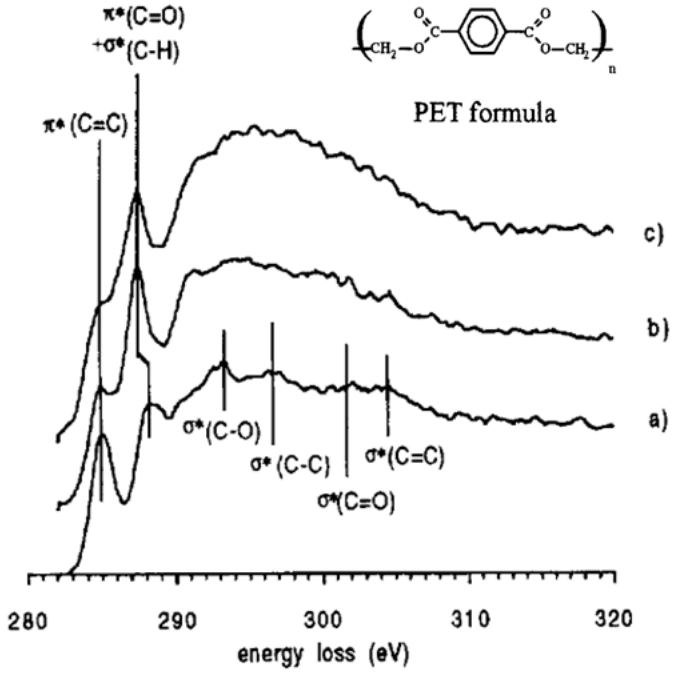

Figure 3.14. EELS spectra of PET at the carbon K-edge with energy resolution of 0.7 eV, with the electron dose estimated to be (a) 3.2×103 C/m^2; (b) 3.2×104 C/m^2 and (c) 3.2×106 C/m^2. (from reference [147])

In core-loss analysis, compositional information is given by the position and net integrated intensity of an edge, and chemical information is given by the fine structure within an edge. An example of using carbon K-edge to study irrational damage of poly(ethylene terephthalate) (PET) is shown in Figure 3.14. The detailed chemical bonding in PET is reflected by the peaks in ELNES. These peaks can be attributed to different chemical functionalities, such as C=C π^* (285 eV); C=O π^* (287.9 eV); C–O σ^* (293.3 eV), and C–C σ^* (296.7 eV). The shift of C=O π^* in spectra with the increasing electron dose indicates the possible crosslinking between carbonyl group and ethylenic groups that is induced by the high-energy electrons.

3.3.3 Energy Filtered Transmission Electron Microscopy (EFTEM)

Spectroscopic imaging can also be achieved in the TEM through use of an energy filter. This technique provides an alternative source of contrast for the efficient mapping of composition, chemistry, and the distribution of phases in materials without the need for heavy-element stains.

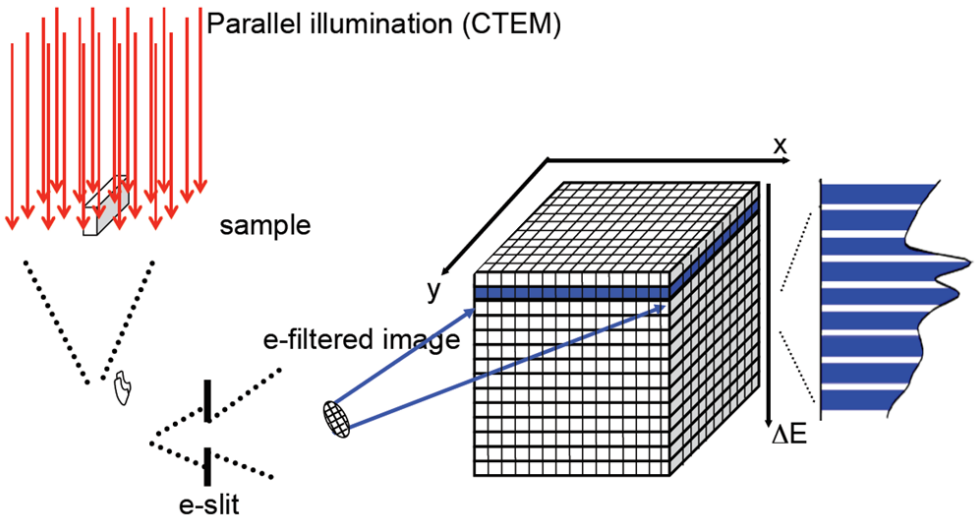

Figure 3.15. Formation of a spectrum image in TEM mode, where parallel illumination is used to generate a series of energy filtered images (from Gatan EELS school tutorial)

In contrast to SI in STEM, EFTEM images are generated with the parallel illumination in a conventional TEM. As illustrated in Figure 3.15, energy selected images are recorded with spectral information integrated over a particular energy-loss range defined by the width of an energy-selecting slit. Thus, the data cube of a SI in TEM mode is composed of a stack of energy-filtered images acquired within a certain range of energy-loss. Unlike SI in STEM where full spectral information is obtained at each point of scan, EFTEM mode only records a portion of energy-loss information defined by the energy-selecting slit at each acquisition of an energy-filtered image. Although detailed spectral information can be obtained at a small region with atomic resolution in STEM, it suffers spatial drift and poor signal-to-noise ratio which require specially designed sample stage and aberration corrector. In EFTEM, however, these two problems can be resolved thanks to the parallel acquisition. Thus, EFTEM is especially suited for the applications that require fast acquisition of chemical distributions with adequate accuracy.

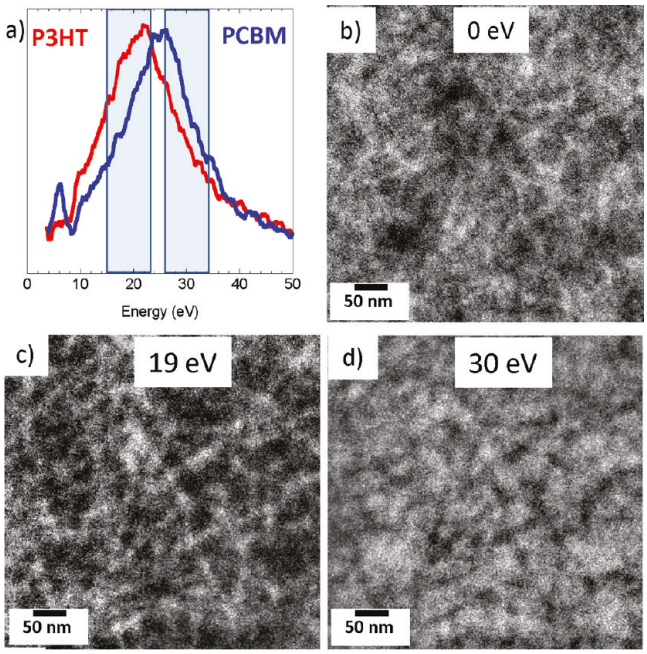

Figure 3.16. EFTEM of a 100 nm thick 50:50 (w/w) blend of P3HT and PCBM, (a) EELS spectra from pure P3HT (red) and pure PCBM (blue), (b) Zero loss image, (c) 19 eV loss image and (d) 30 eV image.(from reference [148])

Different selection of energy windows are correlated with different EFTEM mode, such as zero-loss, thickness mapping and elemental mapping. Zero-loss imaging does not yield element-specific information, but it is often applied to improve the image quality of bright-field images. All inelastically scattered electrons that cause chromatic aberration are removed in this mode, thus contrast and resolution can be improved in resulting zero-loss filtering images. Elemental information and chemical distribution can be obtained from core-loss imaging of different elements. Since the elemental signal is superimposed on a background in the spectrum, a three window method (i.e., acquisition of two pre-edge and one post-edge energy filtered images) is often used to subtract the background contribution and form a net elemental mapping. Although many of individual phases in heterogeneous polymers can be identified thought elemental mapping, the irradiation damage due to the high intensity of the incident electron beam in this mode has limited the application of this technique in polymeric materials. For systems consist of polymers with similar structures, low-loss spectrum imaging is useful to distinguish phase separation by selecting different features due to interband transition or plasmon resonation. For instance, Figure 3.16 shows the study of phase separation in a mixture of P3HT and PCBM polymers by use of low-loss features (different plasmon peaks in pure polymers) in EELS. Energy filtered images obtained at two plasmon peaks (19eV for P3HT and 30eV for PCBM) corresponding to pure polymers are used to map and analyze how these component are distributed in the polymer blend.

3.4 Cryo-TEM

Cryo-electron microscopy (cryo-EM) was initially developed to examine biological samples in its native environment by preparing and observing them at low temperature. Recently, the

application of this technique has been extended into the research of hydrated morphology in several polymeric materials.[112, 114, 149]

Before cryo-TEM becomes commercially available, hydrated samples had to be fully dehydrated before they were examined on a conventional TEM. This process typically leads to a number of artifacts associated with the removal of water, such as distortions, flattening, disruption of structural integrity and mass loss. To preserve its native hydrated state, the sample is typically frozen very fast below the "vitrification temperature" of water. By using this method, the frozen water would not form ice crystal but remain in disordered, glass-like "vitreous" state similar to liquid water. When the frozen sample is transferred into a cryo-TEM, the vitreous water in the sample would remain stable under vacuum for prolonged periods of time at low temperature.[150] In combination with analytical methods such as EELS, the detailed structure and chemical information can be obtained for samples in hydrated states.

Many polymers can be spectroscopically differentiated from each other and from many solvents based on their characteristic fingerprints in the low-loss regime. Provided the unique low-loss spectrum features that are substantially different from those of most hydrocarbon polymers, mapping of the spatial distribution of water has been recently achieved with a spatial resolution of 10 nm.[114] However, this level of resolution is limited by the radiation sensitivity of the specimen, leading to the reduction of incident probe size and poor signal to noise ratio in the resulting energy-loss spectra.

3.5 Sample Preparation

Sample preparation is a critical step in the TEM analysis of materials. The polymeric materials in various shapes, forms and sizes can be studied by electron microscopy with appropriate sample preparation method. There are several problems associated with the direct investigations

of polymers by electron microscopy. First, usual preparation techniques applied to inorganic samples cannot be applied to prepare ultrathin polymer samples since most of polymers are not self-supported and can be easily damaged during these thinning processes. Additionally, contrast in polymer sample is often very low because they typically consist of same light elements (C, H, O and others). Thus, special procedure to enhancing contrast such as staining with heavy elements may be required. The ideal polymer sample for TEM study should be thin enough for the electron transmission but also resembles structural and chemical properties in bulk samples.

Several preparation and investigation techniques have been developed to overcome these difficulties. The simplest but most efficient way to prepare a thin film of polymer is solution casting. For polymers that dissolve in volatile solvent, a drop of polymer solution is placed on a sample grid covered with support film (such as carbon or formvar). The excess solution on the grid surface can be removed by a filter paper. After drying in vacuum or dry air at certain temperature, a uniform thin film of polymer is made on the grid and is ready to be examined. However, a thin film sample prepared by this method may suffer from structural changes in the preparation and presents morphology that is completely different from the bulk materials.

The sizes of the macromolecule structures or morphological features of bulk polymers range from the smallest details that are just above the molecular level (several nm) to structures that are larger than 100 μm. One way to prepare a sample resembling such morphological properties in bulk polymers is to use ultramicrotomy. Ultramicrotomy has become a standard method used for the preparation of ultrathin sections of plastics, biological and biomedical objects. Typically, three steps are involved in sectioning with ultramicrotomy: specimen preparation, trimming and sectioning. For most of polymers either soft or hard at room temperature, the first step of specimen preparation is to embed a small piece of bulk sample into a low-viscous epoxy resin

medium[151]. After curing in the oven, the epoxy block that contains polymer sample is trimmed with a razor blade or trimming tool to cut extra epoxy around the sample and form a pyramid shape of surface. The trimmed block is mounted on a sample holder and sectioned by a glass knife or diamond knife with selected cutting speed and feed-in distance. The thin sections then can be picked up with a copper grid. Due to the different properties of polymers and epoxy, some polymers embedded may not be well penetrated and held tightly with epoxy, leading to the incomplete and defective sections. To avoid these defects, a bulk polymer can be directly trimmed and mounted on the holder to perform sectioning. For soft or thin samples that cannot support themselves at room temperature, cryo-section is required. Typically, a cryo-temperature is selected just below the glass transition temperature of the polymer and special cryo-diamond knife and sample colleting method are required to obtain ultrathin sections. Even though most of polymer can be prepared by ultramicrotomy either at room or cryo temperatures, it requires an experimentalist with extensive experience in preparing, cutting and collecting processes.

For powders and granules obtained directly from macromolecular synthesis, a grinding process (at room or cryo temperature) is often used to obtain very fine particles. The dispersion of these fine particles can be mounted on a carbon coated grid for direct TEM inspection. To investigate the internal particle structure in TEM, these particles can also be embedded and ultramicrotomed into thin slices as described in the last paragraph.

Although other methods such as spin coating and Focus Ion Beam are available for polymer sample preparations, they all need special devices and not suited for our samples. Thus, only three methods mentioned above were used in this dissertation. The details of preparation schemes using these methods will be discussed in the next Chapter.

3.6 Instrumentations

Most of polymeric samples for this study were prepared at Advanced Microscopy and Imaging Center (AMIC) at University of Tennessee. For dry samples, the embedded blocks were first trimmed by Leica EM Trim2 and sectioned with Leica Ultramicrotome EM-UC7 to produce ultrathin slices at room and cryo temperature. The solution casting and hydrated samples were prepared with Gatan cryoplunger CP3. The plunge freezer features an environmental chamber to control the relative humidity, which is useful to prepare hydrated samples.

Our studies of ionomers morphology were primarily performed on the VG HB501-UX dedicated STEM and Hitachi HF3300 TEM-STEM located at Oak Ridge National Laboratory. VG HB501- UX is a 100 kV dedicated STEM with Nion aberration corrector and Gatan Enfina parallel detection electron energy loss spectrometer. It provides 0.3 eV energy resolution for EELS and high resolution STEM giving a beam size close to 1 Å. Thus, it is capable of obtaining quality HAADF images with real atomic column resolution and comparable resolution EELS for elemental analysis. Hitachi HF3300 is a cold FEG TEM-STEM operated at 100 kV or 300 kV. It includes multiple detectors for many analytical studies: Bruker SDD-EDS, Gatan Quantum 953 EELS/GIF, SEM, BF-STEM, and HAADF-STEM Detectors. In addition, it features cryo and 360º rotational holder to perform cryo-TEM and electron tomography. Elemental mapping with EDS and EFTEM and cryo-TEM for hydrated specimens were conducted on this microscope. EELS of ionomers were obtained on Zeiss Libra 200 MC TEM-STEM located at UTK. Libra 200 MC is a 200 kV field-emission TEM/STEM microscopy with unique monochromator module and in-column omega energy filter, which together enable the highest resolution EELS and outstanding spectrum imaging. These features are crucial to obtain high resolution ELNES for electron sensitive polymers.

Chapter 4 Results and Discussion

4.1 Ab initio Study of Local Hydration and Proton Transfer of Polysulfone

We have undertaken *ab initio* electronic structure calculations in the present study to understand the local hydration and proton transfer characteristics of $sPSO_2$ polymers. Specifically, the structures of $sPSO_2$ dimers with various numbers of water molecules were examined. Two cases where sulfonic acid groups are either *ortho*- or *meta*- to the sulfone units are considered. The rotational energies were computed to investigate backbone rigidity as well as intermolecular hydrogen bonding among the sulfone units and sulfonated phenylene rings. Global minimum energy structures of dimers with multiple water molecules were obtained from various plausible starting configurations of the dimers with the water molecules. The energetics and associated structures were determined for the transfer of several distinct protons in close proximity to the acid groups of the $sPSO_2$ fragments.

This part is organized as follows: the first section contains a short description of the specific methodology used to determine the structure and energetics for all $sPSO_2$ ionomers. This is followed with a discussion about equilibrium structures and backbone rigidity of two different $sPSO_2$ fragments without the addition of any water molecules. The next section describes the microsolvation and associated proton dissociation in the two systems. Energetics for the transfer of different protons in various hydrogen bonding environments near protogenic groups is then presented.

4.1.1 Computational Details

The Gaussian 03 suite of programs[152] was used to perform all electronic structure calculations. Fully optimized geometries of $sPSO_2$ dimer molecules, using conjugate gradient methods without symmetry constraints, were initially obtained using Hartree–Fock theory with the 6–

31G** split valence basis set.[153-156] Subsequently, refined structures were determined by employing hybrid density functional theory (DFT) with Becke's 3 parameter functional (B3LYP) initially with the same basis set and then subsequently with the larger 6–311G** basis set.[157-160] Potential energies associated with rotating the sulfonated phenylene ring on the backbones were computed at the B3LYP/6–31G** level. The rotational energy barriers were then determined and compared for each polysulfone system. Minimum energy structures for each dimer with incrementally added water molecules (i.e., + $n$$H_2O$, where n = 1–6) were determined at the B3LYP/6–311G** level. The zero point energies (ZPEs) for each system were obtained from the vibrational frequencies, which were calculated at the same level of theory. Molecular binding energies for the water molecules and $sPSO_2$ dimers were determined from both the uncorrected and ZPE corrected total electronic energies. The counterpoise (CP) method of Boys and Bernardi was employed to compute the effect of basis set superposition error (BSSE) on all the computed binding energies.[160-163] For the systems at high levels of hydration (i.e., 5–6 water molecules in close proximity to the sulfonic acid groups), three proton transfers were examined with different neighboring conditions near the acidic group. The profiles of the energy corresponding to each of above proton transfers were obtained by performing potential energy surface (PES) scans at both the HF/6–31G** and the B3LYP/6–31G** level. These scans were based on optimized static structures and as such only reveal the relative tendencies in the proton transfer energetics, not absolute values. All calculations in this study were performed without consideration of solvent effects.

It is known that dispersion interactions are important for the systems containing aromatic groups and hydrogen bonding network.[164] We performed sample calculations using two types of density functionals including empirical corrections dispersion interactions (i.e., Grimme's

B97D[165] functional and long-range corrected (LC) hybrid density functionals wB97XD[166]). The structures of anhydrous and hydrated systems optimized at the B3LYP/6-31G** level were re-optimized using these two methods with the same basis set. The 'dry' $sPSO_2$ fragments exhibited nearly identical hydrogen bonding lengths between neighboring sulfonate groups when compared to the structures obtained with the B3LYP functional. The water binding energies obtained with B97D and wB97XD were slightly higher, but the same trend was observed as determined with B3LYP.

4.1.2 Global Minimum Energy Structures

In contrast to the PTFE backbone of PFSA polymers, $sPSO_2$ polymers possess aromatic phenylene backbones that are highly sulfonated and bridged with sulfone units. It is believed that these unique structures may potentially affect the local hydration and proton transfer properties. Fully optimized (B3LYP) conformations of the two different $sPSO_2$ dimer molecules: *meta-meta* $sPSO_2$ and *ortho-ortho* $sPSO_2$ (i.e., distinguished by the substituent positions of the sulfonic acid groups relative to the central sulfone unit) are shown in Figure 4.1. The global minimum energy structures for both fragments both exhibiting a *cis* conformation where two sulfonic acid groups reside on the same side of the backbone are displayed in Figure 4.1(a) and (b). Figure 4.1 (c) and (d) show minimum energy conformations for the same $sPSO_2$ fragments but with the sulfonic acid groups on opposite sides of the backbones (i.e., in a *trans* conformation). For all conformations shown in Figure 4.1, intermolecular hydrogen bonding is observed either between the $–SO_3H$ groups or between a $–SO_3H$ group and a central $–SO_2–$ unit. The corresponding O···O distances and O–H bond lengths are also shown in Figure 4.1. Structural parameters, including the dihedral angle for rotation of each aromatic ring about the C–S bonds ($D_{O\text{-}S\text{-}C\text{-}C}$), separation of the sulfonic acid groups (S···S), and the O–H bond length ($SO_2O\cdots H$), are reported

in Table 4.1. The total electronic energy and zero point energy are collected in the first and second rows of Table 4.2 and 4.3 for the *meta*- and *ortho*- $sPSO_2$ dimes, including those for corresponding *cis* and *trans* conformations.

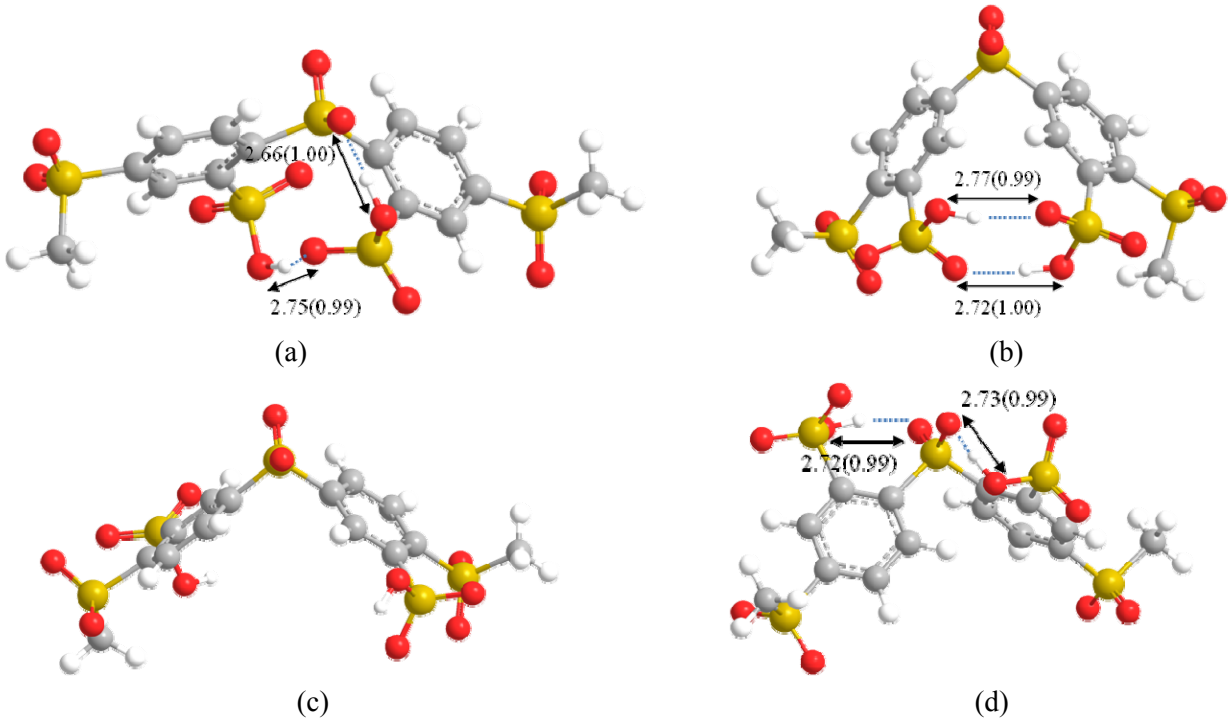

Figure 4.1. Fully optimized (B3LYP/6-311G**) global minimum energy structures of $sPSO_2$ dimer distinguished by the positions of sulfonic acid groups corresponding to the central sulfone are listed in: (a) *meta-meta* $sPSO_2$ and (b) *ortho-ortho* $sPSO_2$. The corresponding trans conformation of above $sPSO_2$ dimers are displayed in (c) and (d). The total electronic energies (with ZPE corrected) of *meta-meta* structure are 2.78 kcal/mol less than those of *ortho-ortho* dimer.

As observed in Figure 4.1(a), the relatively small separation of neighboring sulfonic acid groups (approximately 4.42 Å for the S···S distance) in the *meta-meta* structure brings about the formation of double hydrogen bonds between two $–SO_3H$ groups. Similar results were found in a prior investigation of the short side chain (SSC) PFSA fragments with kinked backbone structures and nearly the same separation of the sulfonic acid groups.[101] Comparison of the energies for the equilibrium structures reveals that the *cis* conformations are 5.41 and 2.91 kcal/mol lower in energy for the *meta-meta* and *ortho-ortho* fragments, respectively. These

results are in contrast to those observed for the SSC PFSA fragments, where the sulfonic acid groups are doubly hydrogen bonded in the *cis* conformation would lower total energies about 12.3 kcal/mol.[101] Clearly, the presence of such interactions between two neighboring protogenic groups greatly affects the conformation and stability of these fragments.

4.1.3 Backbone Conformation

In addition to an intermolecular interaction between the sulfonic acid groups, the interaction arising from neighboring rings is also considered to be an important factor affecting the conformation. As discussed previously, each sulfonic acid group in a $sPSO_2$ dimer is expected to interact with a neighboring sulfonic acid group or a sulfone unit. As a result, two neighboring phenylene rings tend to rotate about the C–S bond to minimize steric effects. Determination of global minimum energy structures (i.e., Figure 4.1(a) and (b)) of the dimers indicates that two rings tend to be arranged in an energetically favorable 'open book' configuration. Potential energy surface scans were performed (at the B3LYP/6–31G** level) for rotation of the phenylene rings about the C–S bond at 5º increments in order to assess the flexibility of the backbones. The torsional energy profiles associated with *meta-meta* and *ortho-ortho* $sPSO_2$ dimers are displayed in Figures 4.2 and 4.3, respectively. It is worth noting that the hydrogen bonding in both global minimum energy structures (the *cis* conformations shown in Figure 4.1 (a) and (b)) make it difficult to obtain continuous rotational energy profiles. This is in contrast to the corresponding *trans* conformations (Figure 4.1(c) and (d)), where the effects of intermolecular hydrogen bonding are minimized. Despite performing multiple scans starting from different structures to smooth out the surfaces, these surfaces are still relatively rough and appear to be discontinuous.

As displayed in Figure 4.2, doubly degenerate energy barriers occur when the plane of the phenylene ring rotates into the plane that is perpendicular to the second phenylene ring. Not surprisingly, two minimum energies structures were determined with 'open-book' orientation. Specifically, the average energy barrier in the *meta-meta* $sPSO_2$ dimer is about 3.3 kcal/mol. Considerably larger rotational energy barriers (i.e., 15.5 kcal/mol and 8.2 kcal/mol) are observed in the *trans* conformation of the *ortho-ortho* dimer (see Figure 4.1(d)) due to the hydrogen bonding between the $–SO_3H$ group and $–SO_2–$ unit. Again, rotational energy maximum are found when the two planes made by the rings are perpendicular to each other (see Figure 4.3). The largest energy barrier (i.e., 15.5 kcal/mol) is nearly 9 kcal/mol greater than that observed in PFSA fragments,[167] indicating that the phenylene backbone is substantially stiffer than a PTFE backbone.

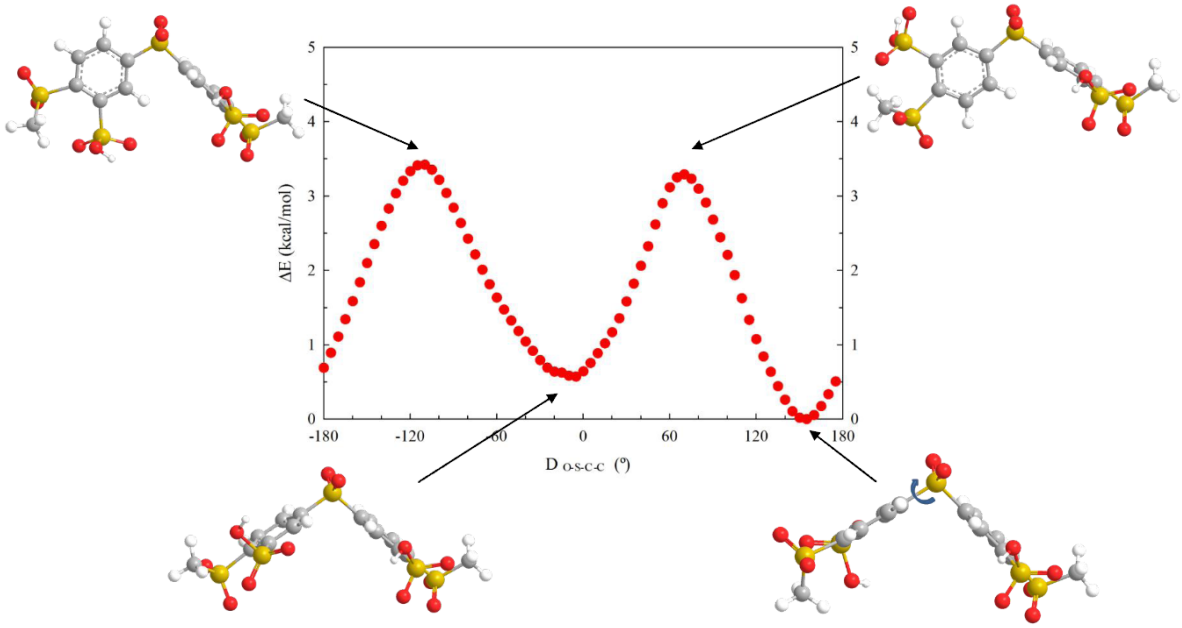

Figure 4.2. Relative rotational energies along central C-S bonds of *meta-meta* $sPSO_2$ dimer obtained at B3LYP/6-31G**. The starting structure possesses a trans conformation where $-SO_3H$ groups reside on opposite sides of $-SO_2-$ group. The total electronic energies of this structure are 3.41 kcal/mol more than the corresponding global minimum structures. Two peaks of relative rotational energies are 3.29 kcal/mol and 3.43 kcal/mol respectively.

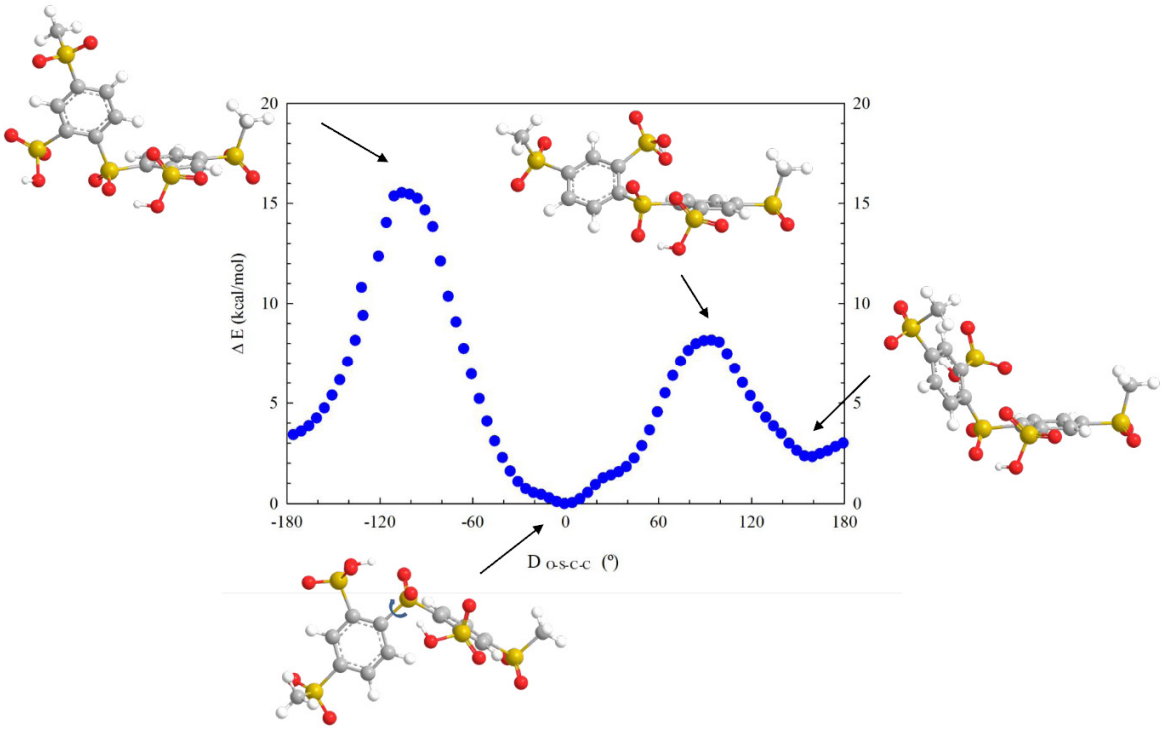

Figure 4.3. Relative rotational energies along central C-S bonds of *ortho-ortho* $sPSO_2$ dimer obtained at B3LYP/6-31G**. The starting structure possesses a *trans* conformation where $-SO_3H$ groups reside on opposite sides of $-SO_2-$ group. The total electronic energies of this structure are 2.91 kcal/mol more than the corresponding global minimum structures. Two peaks of relative rotational energies are 15.54 kcal/mol and 8.17 kcal/mol.

4.1.4 Microsolvation

It has been shown that the conformations of the equilibrium structures of the $sPSO_2$ dimers are significantly influenced by the configuration of the hydrogen bonding between the sulfonic acid groups and relative positions of the neighboring aromatic rings. In order to investigate proton transfer in close proximity to the sulfonic acid groups at low degrees of hydration, a small number of water molecules were incrementally added to each of the $sPSO_2$ fragments. The fully optimized structures (at B3LYP/6–31G** level) of multi-hydrated $sPSO_2$ dimers were obtained from a variety of starting structures as a function of the initial position of the water molecules. The resultant conformations of the *meta-meta* and *ortho-ortho* fragments are displayed in Figures 4.4 and 4.5, respectively. The binding energies of these fragments and water molecules were

calculated at B3LYP/6–31G** level and are reported in Tables 4.2 and 4.3. A selection of structural parameters (i.e., dihedral angles of rotating aromatic fragments, separation of sulfonic acid groups and the separation of the acidic proton from the conjugate base) of each of the molecules are listed in Table 4.1.

Table 4.1. Structural Data from optimized *meta-meta* and *ortho-ortho* $sPSO_2$[a]

+ *n* H_2O	D $_{O\text{-}S\text{-}C\text{-}C}$ [b]	D $_{O\text{-}S\text{-}C\text{-}C}$ [b]	S···S[c]	$SO_2O\cdots H$[d]
0	-7.7 (80.4[e])	9.3 (0.8)	4.42 (4.55)	0.99 1.00 (0.99 1.00)
1	12.7 (60.6)	21.7 (2.1)	4.93 (5.22)	0.99 1.08 (1.02 1.00)
2	7.8 (66.1)	29.6 (–4.9)	5.51 (5.03)	1.03 1.08 (1.04 1.00)
3	10.3 (68.3)	29.9 (–5.7)	5.27 (5.04)	1.48 1.41 (1.06 1.00)
4	5.1 (71.6)	33.4 (–6.6)	5.53 (5.01)	1.59 1.30 (1.58 1.00)
5	8.6 (76.6)	30.7 (–8.7)	5.49 (4.92)	1.76 1.36 (1.76 1.00)
6	9.8 (75.1)	32.0 (–8.0)	5.61 (4.88)	1.81 1.45 (1.83 1.00)

[a] For structures optimized at the B3LYP/6-31G** level; [b] Dihedral angles (º) for rotation of each aromatic ring about the C-S bonds; [c] Separation distance (Å) of two acidic groups; [d] Bond distances of O···H (Å) for each sulfonate group; [e] Values in parentheses are for *ortho-ortho* $sPSO_2$.

Table 4.2. Binding Energies for *meta-meta*-$sPSO_2$ + *n* H_2O [a]

+ *n* H_2O	E_{elec}[b]	E_{ZPE}[c]	ΔE[d] (kcal/mol)	ΔE_{ZPE}[e] (kcal/mol)	ΔE_{BSSE}[f] (kcal/mol)
0(*cis*)	-3435.22	0.30			
0(*trans*)	-3435.20	0.30			
1	-3511.67	0.32	20.1	18.1	12.6
2	-3588.12	0.35	40.3 (20.2[g])	36.4 (18.2)	25.6 (12.8)
3	-3664.57	0.37	60.0 (20.0)	53.0 (17.7)	42.1 (14.0)
4	-3741.02	0.40	80.0 (20.0)	71.0 (17.8)	55.7 (14.0)
5	-3817.47	0.42	95.3 (19.1)	84.0 (16.8)	68.6 (13.7)
6	-3893.92	0.45	112.3 (18.7)	97.4 (16.2)	74.9 (12.5)

[a] For structures optimized at the B3LYP/6-31G** level; [b] Total electronic energy in Hartrees; [c] Zero point energy (ZPE) in Hartrees; [d] Binding energy based on (uncorrected) E_{elec}; [e] Binding energy based on ZPE corrected E_{elec}; [f] Binding energy based on the CP correction to BSSE of optimized structure; [g] Values in parentheses are per water molecule.

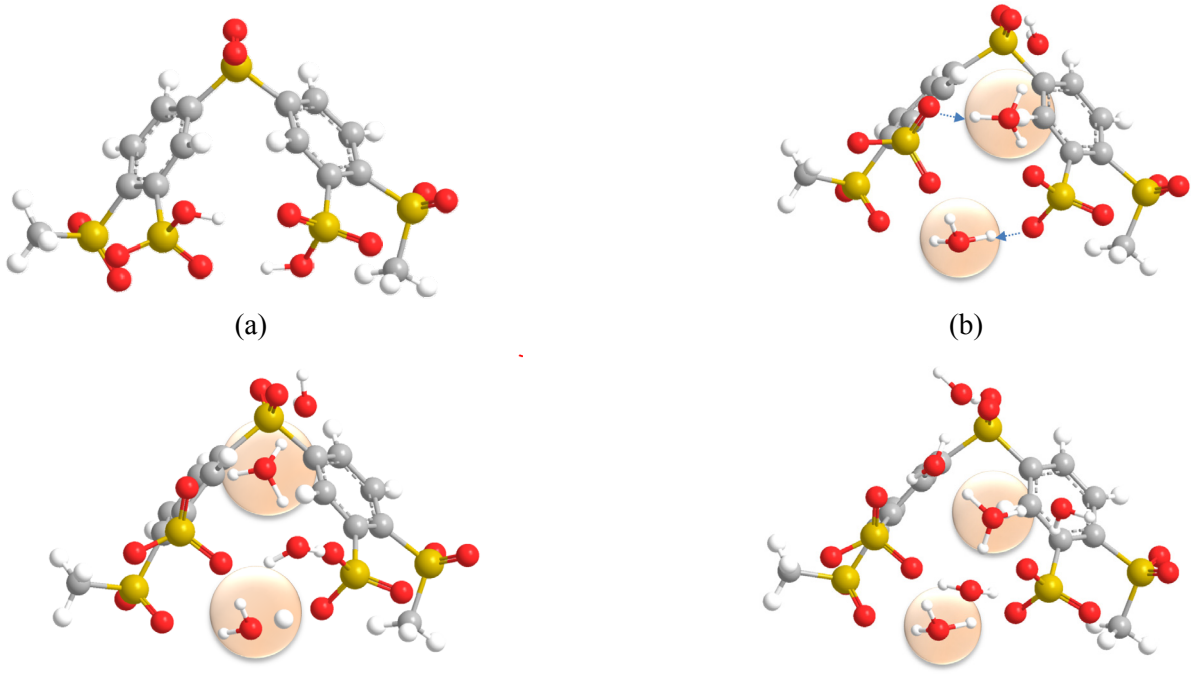

Figure 4.4. Fully optimized (B3LYP/6-31G**) global minimum energy structures of *meta-meta*-sPSO$_2$ dimer with *n* water molecules: (a) *n*=0; (b) *n*=3; (c) *n*=4; (d) *n*=6. The proton dissociation occurs when three water molecules were added.

Previous work[13, 102] involving the microsolvation of PFSA ionomers revealed that the onset of proton dissociation is mostly dependent upon the water content of the system (*i.e.,* H_2O/SO_3H), the backbone conformation, and the separation of the sulfonic acid groups. For isolated sulfonated systems such as triflic acid, the proton dissociation will not occur until three water molecules are added. In PFSA fragments with more than one sulfonic acid group, a continuous hydrogen bond network is usually formed between the terminal –SO_3H groups. It was shown that the number of water molecules required to form such hydrogen bonding is a function of the separation of the sulfonic acid groups.[101] Specifically, one, two, and three water molecules are required to bridge two sulfonic acid groups separated by five, seven, and nine difluoromethyl units (–CF_2–) on backbones.

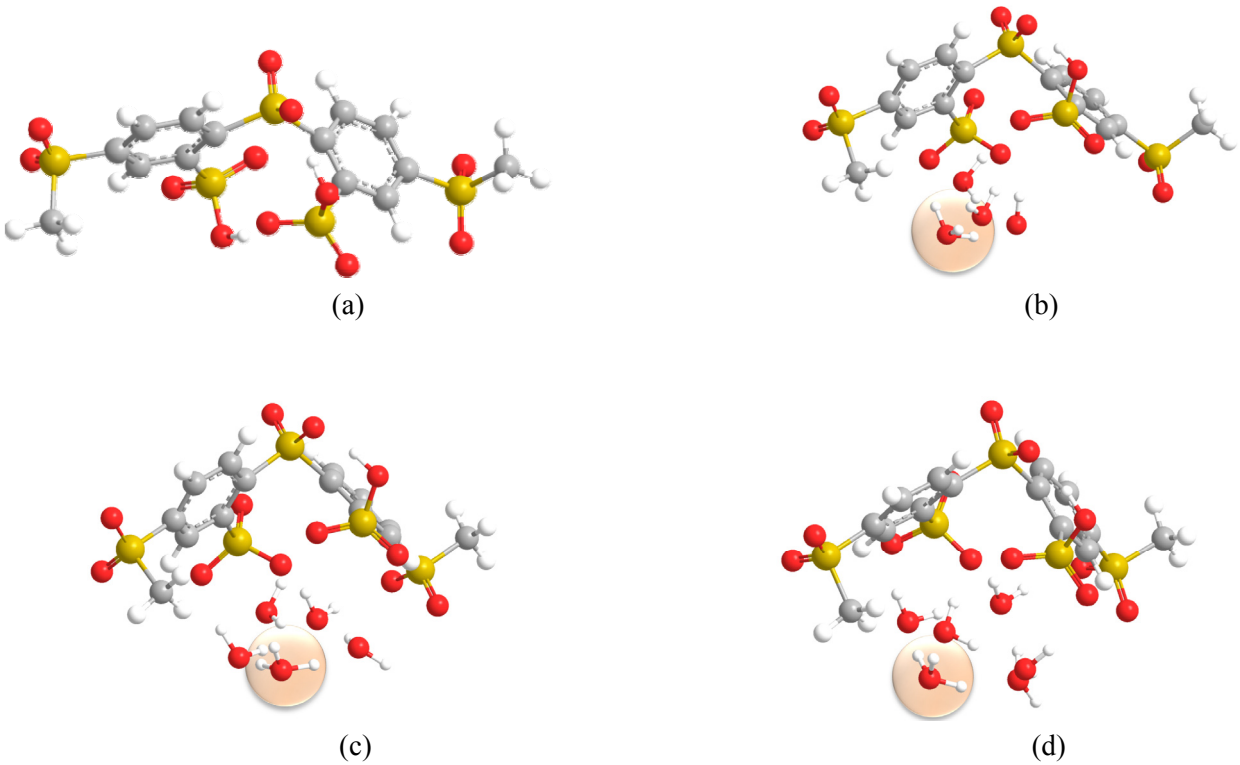

Figure 4.5. Fully optimized (B3LYP/6-31G**) global minimum energy structures of *ortho-ortho*-$sPSO_2$ dimer with *n* water molecules: (a) *n*=0; (b) *n*=3; (c) *n*=4; (d) *n*=6. The proton dissociation occurs when four water molecules were added.

Due to the aromatic backbone, the local hydration of the $sPSO_2$ fragments is quite different from what is found in PFSA fragments. In *meta-meta* $sPSO_2$ dimers, for instance, only three water molecules are necessary to witness dissociation of both protons from the acidic groups (as shown in Figure 4.4(b)). In contrast, it was found that for the fragments of the short-side-chain PFSA ionomers, at least five water molecules are needed to observe dissociation of both protons.[102] The protons dissociated from the sulfonic acid groups are stabilized by forming two hydronium ions highlighted in Figure 4.4(b). The first hydronium ion is hydrogen bonded with two sulfonic acid groups and a water molecule. The second one, however, closely interacts with two sulfonic acid groups and a sulfone unit. When the fourth water molecule is added, two water molecules form a hydrogen-bonded 'wire' connecting the two sulfonic acid groups (see Figure

4.4(c)). The protons, as expected, remain within the first hydration shell. Subsequently, an Eigen ion ($H_9O_4^+$) is observed when six water molecules are added to the system as displayed Figure 4.4(d). In the process of hydration, the hydronium ion, which is stabilized by two sulfonic acid groups and a sulfone unit, is nearly unaffected by the added water molecules. The other hydronium ion, however, is now fully hydrated by three water molecules and forms an Eigen ion indicating that the proton has shifted to the second hydration shell.

Table 4.3. Binding Energies for *ortho-ortho*-sPSO_2 + *n* H_2O[a]

+ *n* H_2O	E_{elec}[b]	E_{ZPE}[c]	ΔE[d] (kcal/mol)	ΔE_{ZPE}[e] (kcal/mol)	ΔE_{BSSE}[f] (kcal/mol)
0(*cis*)	-3435.22	0.30			
0(*trans*)	-3435.22	0.30			
1	-3511.67	0.32	16.3	14.0	9.8
2	-3588.12	0.35	34.2 (17.1[g])	28.9 (14.5)	19.0 (9.5)
3	-3664.56	0.37	50.0 (16.7)	42.5 (14.2)	29.4 (9.8)
4	-3741.01	0.40	67.5 (16.9)	57.1 (14.3)	40.8 (10.2)
5	-3817.46	0.42	89.8 (18.0)	76.2 (15.2)	52.1 (10.4)
6	-3893.92	0.45	110.3 (18.4)	93.1 (15.5)	64.6 (10.8)

[a] For structures optimized at the B3LYP/6-31G** level; [b] Total electronic energy in Hartrees; [c] Zero point energy (ZPE) in Hartrees; [d] Binding energy based on (uncorrected) total electronic energies; [e] Binding energy based on ZPE corrected E_{elec}; [f] Binding energy based on the CP correction to BSSE of optimized structure; [g] Values in parentheses are per water molecule.

The hydration of the *ortho-ortho* fragment displayed in Figure 4.5 is apparently different from the *meta-meta* fragment. In addition to the hydrogen bonding between the two sulfonic acid groups, hydrogen bonding was also observed between a sulfonic acid group and a sulfone unit as shown in Figure 4.5(a). This hydrogen bond is stable and is barely interrupted even after further water molecules are added. Thus, the hydration of the *ortho-ortho* fragment only occurs in the close proximity of one of the sulfonic acid groups, where at least four water molecules are

required to observe the transfer of a proton (see Figure 4.5(b)). These results suggest that the position of the sulfonic acid substituents will greatly change the local hydration and proton transfer of a $sPSO_2$ polymeric fragment.

Binding energies (per water molecule) were computed at the B3LYP/6-31G** level to obtain a measure of the interaction of the first hydration shell water molecules to the sulfonic acid groups. The computed BSSE corrected binding energies listed in the last columns of Tables 4.2 and 4.3 reveal that the water is consistently more strongly bound in the *meta-meta* fragments (approximately 3 kcal/mol higher binding energy per water molecule) than in the *ortho-ortho* fragments. This result is probably due to the fact that both sulfonic acid groups in the *meta-meta* $sPSO_2$ fragments are involved in forming hydrogen bonds to the dissociated protons. Furthermore, the relative trends in the (BSSE corrected) binding energies for *meta-* and *ortho-* fragments are virtually the same prior to proton dissociation: the magnitude of the binding energy increases with increasing hydration.

The dihedral angles are listed in the first two columns of Table 4.1 and indicate that the rotation of the phenylene rings occur in accordance with the hydration of the fragments. The degree of rotation is primarily determined by the separation of the sulfonic acid groups and degree of hydration. As discussed previously, the energy penalty for rotation of the rings in the *meta-* conformations are much lower than in the *ortho-* conformations. Therefore, a small variance in the dihedral angles associated with rotating the aromatic rings is expected for the *ortho-* fragments when the water molecules are added. For *meta-meta* $sPSO_2$, in contrast, rotation of the phenylene rings is more sensitive to the degree of hydration.

4.1.5 Proton Transfer

As mentioned earlier, the substituent position of the sulfonic acid groups on the aromatic rings have a significant influence on the formation of the hydrogen bond network and transfer of protons under limited hydration conditions. With an intermediate separation of the protogenic groups, the *meta-meta* fragment has a double hydrogen bond between a sulfonic acid pair when no water molecules are present. Once water molecules are incrementally added, both sulfonic acid groups participate in forming continuous hydrogen bonds and hence facilitate proton transfer from acidic sites to the adjacent water molecules. On the other hand, hydration of the *ortho-ortho* fragments (as seen in Figure 4.5(b)-(d)) only occurs in close proximity to a sulfonic acid group whereas the other one is strongly hydrogen bonded to a nearby sulfone unit. Hence, the hydration of the *ortho-ortho* acid dimer seems to resemble that of fragments with single sulfonic acid groups. As seen in Figure 4.5(b), four water molecules are needed to dissociate one proton. The acidic proton will not be transferred to the second hydration shell until the fifth water molecule is added (see Figure 4.5(c)).

It is known that the formation of a Zundel ion ($H_5O_2^+$) is important not only for the diffusion of protons in bulk water, but also the proton transfer in PEM ionomers at low degrees of hydration.[13, 101] As a result of the continuous hydrogen bond network formed between interacting terminal groups, shuttling of the dissociated proton between sulfonic acid groups and/or water molecules is now possible. Thus, three distinct proton transfers were considered differentiated on the basis of the environment in the proximity of one or two sulfonic acid groups. In each case, the hydrated proton is hydrogen bonded to either water molecules or sulfonic acid groups. The energetics associated with proton transfer in each system is then investigated by forcing a specific proton to move to the first hydration shell of a sulfonic acid. The proton transfer patterns

and corresponding energy profiles are illustrated in Figures 4.6-4.9. We have plotted the energy profiles as a function of the asymmetric stretching coordinate, q_{asym}, to facilitate comparison to proton transfer energetics obtained for other systems included the Zundel ion in bulk water.[73, 168, 169]

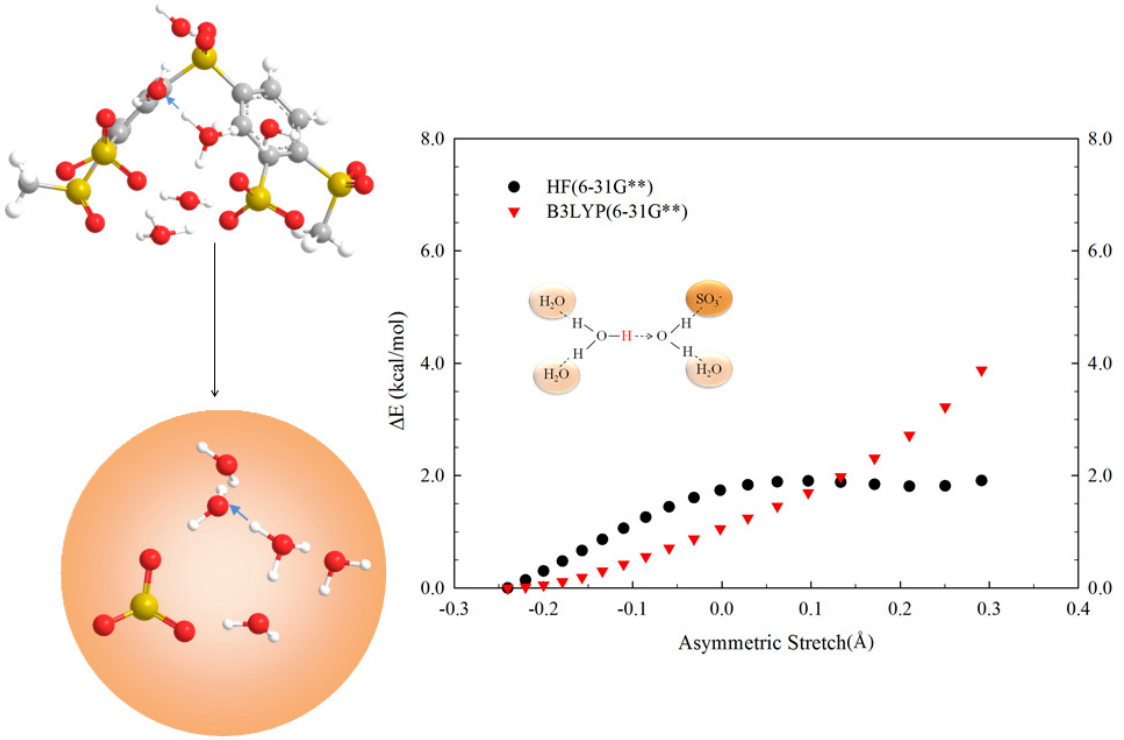

Figure 4.6. Relative energy profiles of proton transfer in the *meta*−*meta*-sPSO$_2$ dimer + 6H$_2$O at HF/6-31G** and B3LYP/6-31G** levels as a function of the asymmetric stretch coordinate. Only one −SO$_3$ group is involved in the transfer model. The energy barrier is 1.91 kcal/mol.

The initial structures of the first model (see Figures 4.6 and 4.7), are obtained from equilibrium structures of the *meta-meta*-sPSO$_2$ dimer with six water molecules and *ortho-ortho*-sPSO$_2$ dimer with five water molecules. In each of the cases, the selected proton (present as a hydronium ion hydrogen bonded to three water molecules) is transferred back to the oxygen atom of a water molecule bridging a sulfonic acid group and a water molecule. As a consequence of forming a contact ion pair in the final structures, the relative energy was observed to increase in both two

systems. However, distinctly different energy profiles were obtained dependent on the choice of the calculation method. The energy profiles computed withy the HF method show that the energy barriers are about 1.91 kcal/mol and 1.85 kcal/mol for the *meta-meta* and *ortho-ortho* systems, respectively. Hybrid DFT (B3LYP) calculations, however, failed to predict a distinct energy barrier with the formation of a Zundel ion in either system. Calculations based on B3LYP are usually more sensitive to the presence of intermolecular interactions than HF, and generally lead to a reorganization of the corresponding structures. This was confirmed by examining the structural changes throughout the potential energy surface scan conducted with the two methods: the hydrogen bonds (estimated by the O–H···O distances) obtained at the B3LYP/6-31G** level are always contracted by nearly 0.1 Å when compared to those obtained with HF.

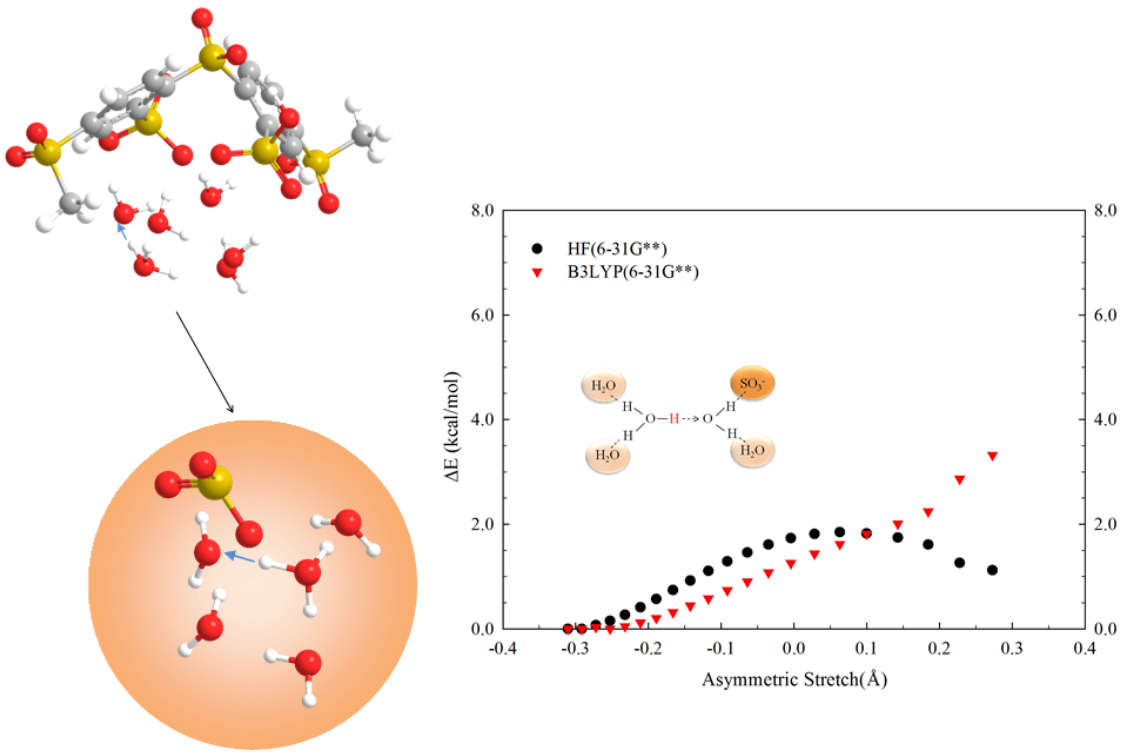

Figure 4.7. Relative energy profiles of proton transfer in the *ortho*−*ortho*-sPSO$_2$ dimer + 6H$_2$O at HF/6-31G** and B3LYP/6-31G** levels as a function of the asymmetric stretch coordinate. Only one −SO$_3$ group is involved in the transfer model. The energy barrier is 1.85 kcal/mol.

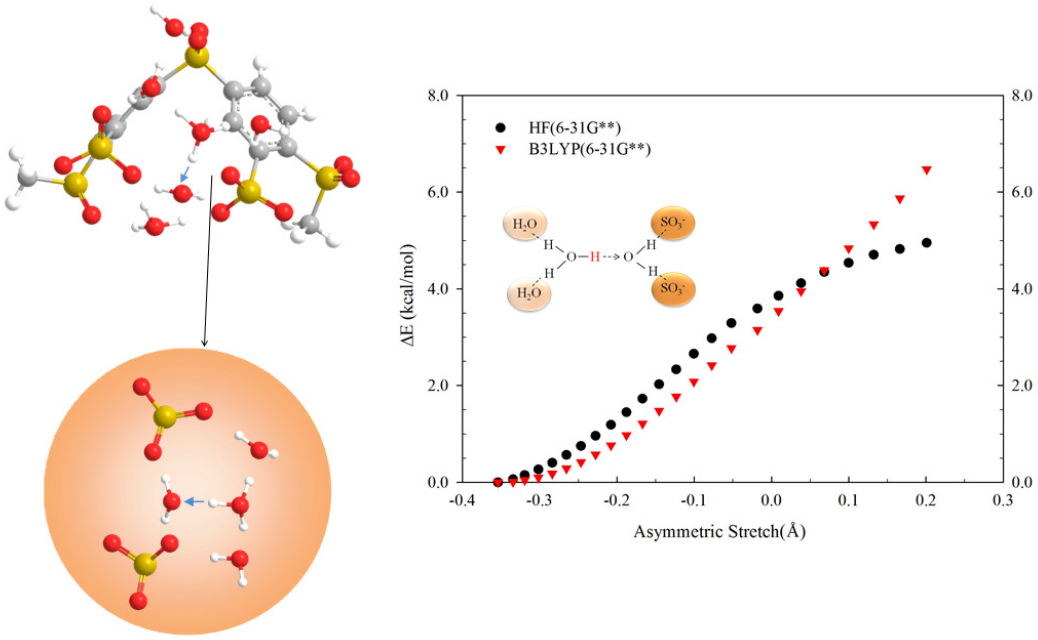

Figure 4.8. Relative energy profiles of proton transfer in the *meta*−*meta*-sPSO$_2$ dimer + 6H$_2$O at HF/6-31G** and B3LYP/6-31G** levels as a function of the asymmetric stretch coordinate. Two −SO$_3$ groups at the same side of the Zundel ion are involved in the transfer model. No apparent barrier was found.

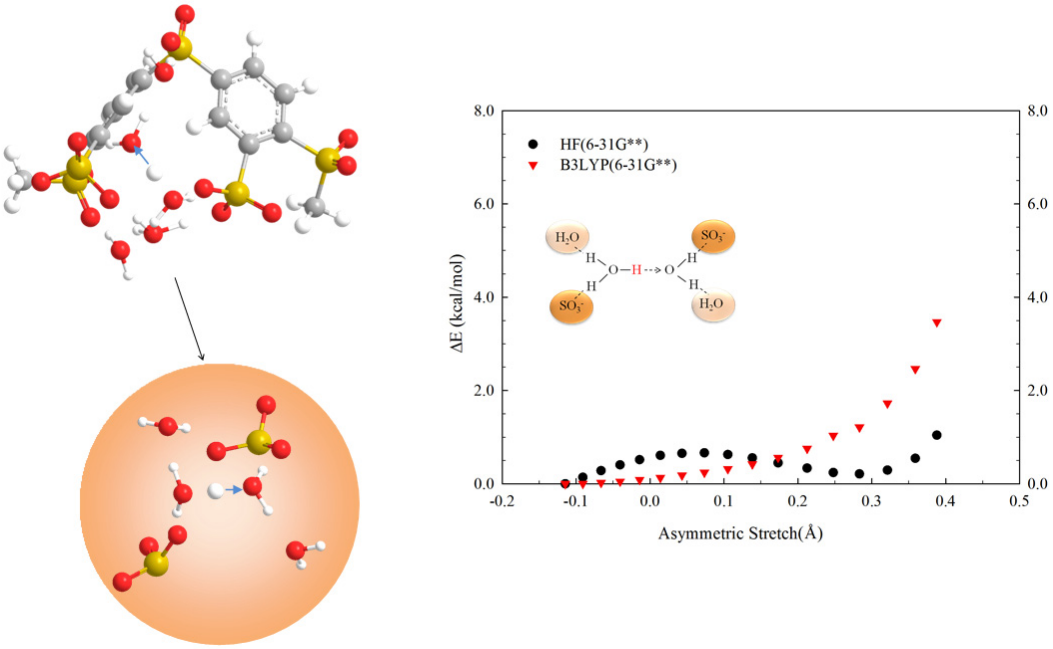

Figure 4.9. Relative energy profiles of proton transfer in the *meta*−*meta*-sPSO$_2$ dimer + H$_2$O at HF/6-31G** and B3LYP/6-31G** levels as a function of the asymmetric stretch coordinate. Two −SO$_3$ groups at opposite sides of Zundel ion are involved in the transfer model. The energy barrier is 0.66 kcal/mol.

The proton transfer path and corresponding energetic profiles for a second system are shown in Figure 4.8. Here the acidic proton is forced to transfer back to the water molecule that connects two terminal sulfonic acid groups. Transferring a proton in this manner leads to a particularly unfavorable structure and a constantly increasing energy. This indicates the role of neighboring sulfonic acid group is crucial to facilitate proton transfer. Both two calculation methods give nearly the same trend of energy profile prior to the formation of Zundel ion.

Once a pair of sulfonic acid groups is bridged by two water molecules, the excess proton tends to shuttle symmetrically between the two water molecules. This transfer pathway and the associated energetics are shown in Figure 4.9. Again, the two calculation methods exhibit different energy profiles: the presence of an energy barrier is only found in the HF calculations. It is also worth noting that the proton transfer in this manner corresponds to a very low energy barrier (only 0.66 kcal/mol) indicating that the proton transfer is almost barrierless resembling the 'rattling' that frequently occurs in bulk water. As this transfer only occurs within within the primary hydration shell of the sulfonic acid groups, it probably does not contribute to the overall proton conductivity.

4.1.6 Summary

Extensive searches for global minimum energy structures of two different $sPSO_2$ dimer fragments without water molecules revealed a preference for the *cis* conformation, where the two sulfonic acid groups are located on the same side of the backbone. The source of the stabilization is mainly due to the strong interaction of the sulfonic acid groups that is absent in a *trans* conformation and decreases as the separation of the groups is increased. Furthermore, rotational energy profiles determined from potential energy scans reveal that the aromatic backbones are much stiffer than the PTFE backbone found in PFSA ionomers. Specifically, the largest energy

penalty of rotating phenylene units (i.e., 15.5 kcal/mol for *ortho-ortho* $sPSO_2$) is found to be nearly twice that obtained by rotating CF_2 units in a PTFE backbone.

Prior investigation of the microsolvation of PFSA ionomers suggests that the minimum amount of water needed to witness dissociation of the protons is a function of the separation of the sulfonic acid groups. For $sPSO_2$ ionomers, however, the number of water molecules required to transfer a proton to the first hydration shell is closely related to the nature of hydrogen bonding in proximity of the sulfonic acid groups: three water molecules for the *meta*-conformation and four water molecules for the *ortho*- conformation. It is also worth noting that only three water molecules are needed to observe dissociation of both protons in the *meta-meta* $sPSO_2$ dimer, where both sulfonic acid groups facilitate the proton transfer. This suggests that the $sPSO_2$ ionomers may more effectively contribute mobile protons at low water contents.

Several distinct proton transfers in proximity to one or two sulfonic acid groups were examined by performing potential energy surface scans along individual hydrogen bonds. The energetics obtained at the HF/6-31G** level indicate that the energy barriers for transferring a proton when only one sulfonic acid group is present is approximately 1.9 kcal/mol, which is 2.1 kcal/mol lower than similar calculations for hydrated triflic acid molecules. On the other hand, the increasing energy associated with a second proton transfer indicates that the hydrated proton is highly unstable when it is hydrogen bonded to both two sulfonic acid groups. When two sulfonic acid groups are connected by two water molecules, the excess proton (existing as a Zundel ion) tends to shuttle through this continuous water wire back and forth with a relatively small energy barrier with 0.66 kcal/mol. This symmetric bidirectional transfer, however, in and of itself is not likely to contribute to long range proton transport.

In systems with hydrogen bonded water molecules, it is important to take into account the quantum nuclear effects due to the small mass of the protons. It has been shown that these effects play an important role in the proton transfer in water and hydrated systems.[170] However, the inclusion of them requires sophisticated *ab initio* path integral techniques which are not presently available with electronic structure calculations. Thus, the calculated proton transfer properties (*e.g.,* energetic barriers) may be influenced by these effects. In addition, the hydrogen bonding reorganization may account for the different energetic barriers calculated by HF and B3LYP. The results of this study should not be taken as absolute values, but rather as a relative comparison as to how neighboring sulfate groups and hydrogen bonding affect the energetics of proton transfer.

4.2 Modeling of Hydrated Morphologies of Polysulfone Ionomers

We have carried out mesoscale DPD simulations to investigate hydrated morphology of the polysulfone ionomers as a function of equivalent weight (EW), molecular weight (MW) and water content (λ). Hydrated $sPSO_2$ ionomers with EWs of 220, 360, 430, 781 and 1014 g/mol were modeled. MWs of these ionomers were varied in the range from 28800 to 68800 g/mol, which match the lower end of MWs determined from experiments.[21-23, 171] Water contents of 5, 7, 9, 11, 13 and15 H_2O/SO_3H were selected to study the evolution of nanoscale phase separations as a function of hydration levels. The short side chain (SSC) PFSA ionomer (EW=828) and Nafion (EW=1244) were also modeled and compared with $sPSO_2$ ionomers with EWs of 781 and 1014 in order to evaluated how the backbone and side chain chemistry effect on hydrated morphologies. Structural analysis of water clusters were performed based on the calculated radial distribution functions (RDFs) for water particles from simulations. Additionally, root mean

square (RMS) end-to-end distances of different types of ionomers were generated to characterize backbones aggregations as a function of water content and chain length.

This part is structured as follows: parameterization and modeling procedures for the systems investigated are outlined in the first section. Subsequently, comparable hydrated morphologies of PFSA and selected polysulfone ionomers are studied and presented in the next section. This is followed by two sections describing the effects of EWs and MWs on the morphologies of polysulfone membranes at various levels of hydration. Finally, influence of hydrated condition and chain length on aggregation and relaxation of hydrophobic backbones are discussed before summaries are presented.

4.2.1 Modeling Details

The general macromolecular structures of the $sPSO_2$ and PFSA ionomers in the simulations are shown in Figure 4.10. The macromolecule parameters (i.e., *m, n* and *p*) in the monomeric structure of each ionomer were selected to represent EWs and MWs that are close to the real ionomers. The selected EWs and MWs and corresponding macromolecule parameters for different ionomers are listed in Table 4.4. The various EWs of selected systems were determined by choosing different combinations of *m* and *n* in monomeric structures. Appropriate numbers of repeat units (i.e., *p*) are selected to obtain similar chain length and MWs to those of real systems.

Three different coarse-grained particles (*A, S* and *W*) were used to construct $sPSO_2$ ionomers (EW=220, 360, 430, 781 and 1014) with various water content (λ = 5, 7, 9, 11, 13 and 15). Each of repeat units consists of beads representing phenylene sulfone backbones (*A*: $-C_6H_3SO_2-$), hydrated sulfonic acid groups (*S*: $-SO_3H\cdot 3H_2O$) and water clusters formed by six water molecules (*W*: $6H_2O$). Similar approach were adopted to model PFSA membranes, which consist of four different types beads (*F, O* or *O′, S′* and *W*) representing PTFE backbones (*F*: $-(CF_2)_6-$),

ether side chains (*O*: $-OCF_2CF(CF_3)OCF_2-$ or *O′*: $-CF_2CF_2CF_2CF(OCF_3)-$), hydrated triflic acid groups (*S′*: $-CF_2SO_3H\cdot 3H_2O$) and water cluster (*W*: $6H_2O$), respectively.

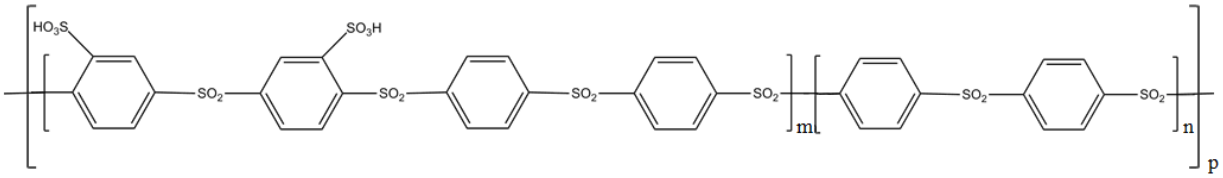

(a)

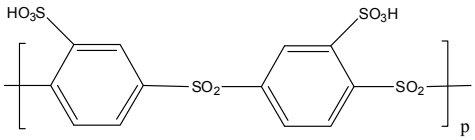

(b)

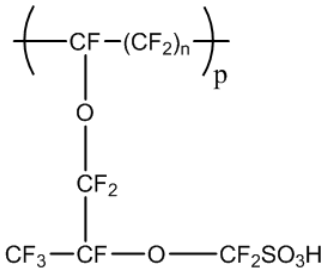

(c)

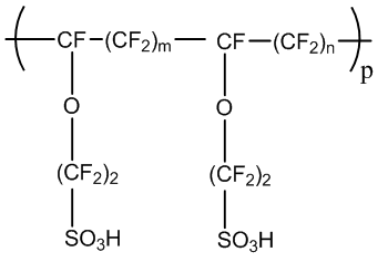

(d)

Figure 4.10 Macromolecular structures of various ionomers in the simulations: (a) $sPSO_2$ ionomers with EWs of 360, 430, 781 and 1014 g/mol; (b) Highly sulfonated $sPSO_2$ ionomer with EW=220 g/mol; (c) Nafion and (d) SSC PFSA ionomers. EWs and MWs of ionomers are determined by the choice of parameters: *m, n* and *p*.

As shown in Table 4.4, selected macromolecule parameters were used to ensure that the simulated $sPSO_2$ ionomers have different EWs, but are in the same range of MWs (i.e., 10^4 ~10^5 g/mol) as those obtained in GPC measurements. In addition, two different MWs for each ionomers were modeled to evaluate the effects of MWs on hydrated morphologies. The $sPSO_2$ and PFSA ionomers with similar EWs and MWs (i.e., $sPSO_2$-781 and SSC-828, $sPSO_2$-1014 and Nafion-1244) were prepared to obtain comparable morphologies for ionomers with aromatic and PTFE backbones.

Table 4.4. Macromolecule parameters for different ionomers with selected EWs and MWs

Ionomer	EW (g/mol)	MW (g/mol)	*m*	*n*	*p*
$sSPSO_2$	220	30800	-	-	70
		61600	-	-	140
	360	28800	1	0	40
		57600	1	0	80
	430	34400	4	2	10
		68800	4	2	20
	781	31200	2	6	10
		62400	2	6	20
	1014	30400	3	14	5
		60800	3	14	10
Nafion	1244	37320	-	17	30
		74640	-	17	60
SSC	828	66240	9	15	40

Table 4.5. Computed Flory-Huggins parameters χ and corresponding repulsion parameters a_{ij} describing pairwise conservative interactions of selected particles for different types of ionomers

	$sSPSO_2$			Nafion			SSC	
Pair	χ [a]	a_{ij} [b]	Pair	χ [a]	a_{ij} [b]	Pair	χ [a]	a_{ij} [b]
A-W	3.21	36.21	*F-W*	3.36	36.75	*F-W*	3.28	36.47
A-S	5.87	45.51	*F-S′*	7.44	51.01	*F- S′*	6.86	48.99
S-W	-0.55	23.08	*F-O*	1.23	29.30	*F-O′*	0.15	25.52
			S′-W	1.48	30.17	*S′-W*	1.24	29.34
			S′-O	2.70	34.44	*S′-O′*	6.24	46.82
			O-W	1.53	30.35	*O′-W*	3.15	36.01

[a] Calculated from optimized structures of particles obtained by use of MM and DFT methods; [b] For the default density of simulation box, ρ=3 particles per unit volume.

All DPD simulations were performed using the DPD modules in Material Studio suite of programs.[136] The structures of particles *A, F*, *O* and *O′* were optimized by molecular mechanics with COMPASS forcefiled parameters using Forcite module in Materials Studio. To incorporate the interactions due to hydrogen bonding in hydrated sulfonate groups and water clusters, structures of particle *S*, *S′* and *W* were optimized using density functional theory (DFT) at the B3LYP/6-31G** level with Gaussian 03. The simulated density was set as default value, ρ=3 (number of particles/unit volume). The interaction radius (r_c =4.5Å) was determined from the average size of beads. The Flory–Huggins parameters associated with bead-bead interactions were calculated using Blends and Synthia modules in Materials Studio, and were extracted to compute the DPD repulsion parameters by using equation: $a_{ij} = x/0.286 + 25$. These computed parameters are tabulated in Table 4.5. The spring constant was set to the default value of 4.0 k_BT/r_c^2, and temperature was fixed at 298 K in the DPD module. Initially, approximately 192000 DPD beads of the system were placed at independently randomized positions in a DPD simulation box (32 nm on each edge) and equilibrated for a period of up to 5.84 ns. Hydrated morphologies were investigated by the water density contour plots obtained from equilibrated meso-structures. The size distribution of the water clusters were studied by radial distribution functions (RDFs) of the water particles.

4.2.2 Comparable Morphologies of Polysulfone and PFSA ionomers

The morphologies as a function of water content were investigated for polysulfone and PFSA ionomers with similar EWs and MWs. The equilibrium morphologies at hydration level λ=7, 11 and 15 for $sPSO_2$-1014 (EW=1014 and MW=60800) and Nafion (EW=1244 and WM=74640) are illustrated in Figure 4.11. The corresponding water volume concentrations are 14.9, 21.2 and 26.6% for $sPSO_2$-1014 and 20.6, 28.9 and 35.7% for Nafion.

As shown in Figure 4.11, majority of the simulation box is occupied by the backbone beads depicted in red while water beads (in blue) are dispersed into the regions where hydrophilic beads (in green) aggregate. Water in $sPSO_2$-1014 ionomers shows greater connectivity than Nafion at the same level of hydration. When water content λ increases from 7 to 11, isolated water clusters in $sPSO_2$-1014 tend to develop fibrils-like shape of water-rich domains. This trend is more pounced at higher water content (λ=15) where water channels are formed with enlarged diameters. In the Nafion ionomer, however, strong phase separations emerge when hydration level increases: water starts to aggregate and form large clusters while remains isolated in the backbone matrix at high water content (λ=15).

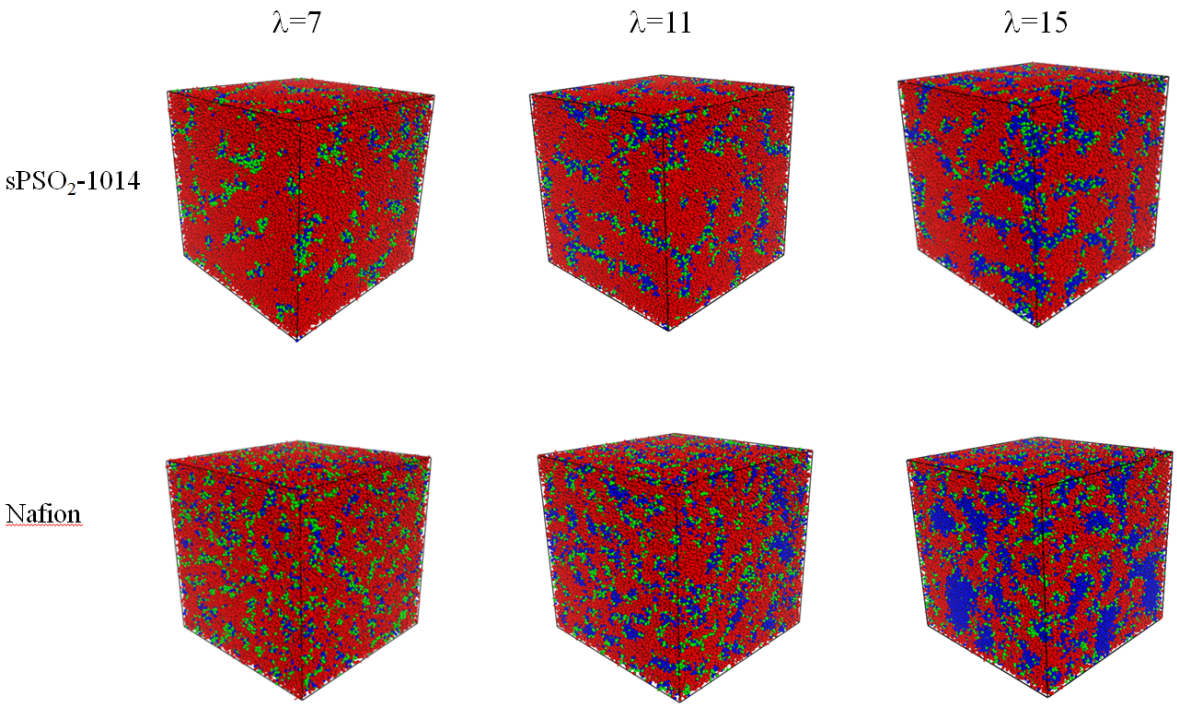

Figure 4.11. Comparison of equilibrium morphologies of the $sPSO_2$ (EW=1014) and Nafion (EW=1244) ionomers with water content λ=7, 11 and 15. Hydrophobic backbones of ionomers are represented by beads *A, F, O* and *O′* showing in red, while beads of sulfonated side chains and water clusters are in green and blue, respectively.

More details about water distributions in these ionomers can be seen in a series of 2D contour plots of water particle densities showing in Figure 4.12. The contour plots are obtained by mapping water particle densities on the cross sections of simulation boxes in the y-z planes for ionomers at different hydration levels. At the same level of hydration, more areas are occupied by the hydrophobic backbones in the $sPSO_2$ ionomers. This is evidenced by the larger blue areas appeared in the contour plots for $sPSO_2$-1014. By examining the water density maps at different water content, it can be seen that the growth of water clusters in Nafion is significantly affected by the hydration environment: the larger water-rich domains occur only at high water content. For $sPSO_2$-1014 ionomers, however, water is evenly distributed into well-connected hydrophilic channels and the size of water clusters progressively increases as the addition of water content.

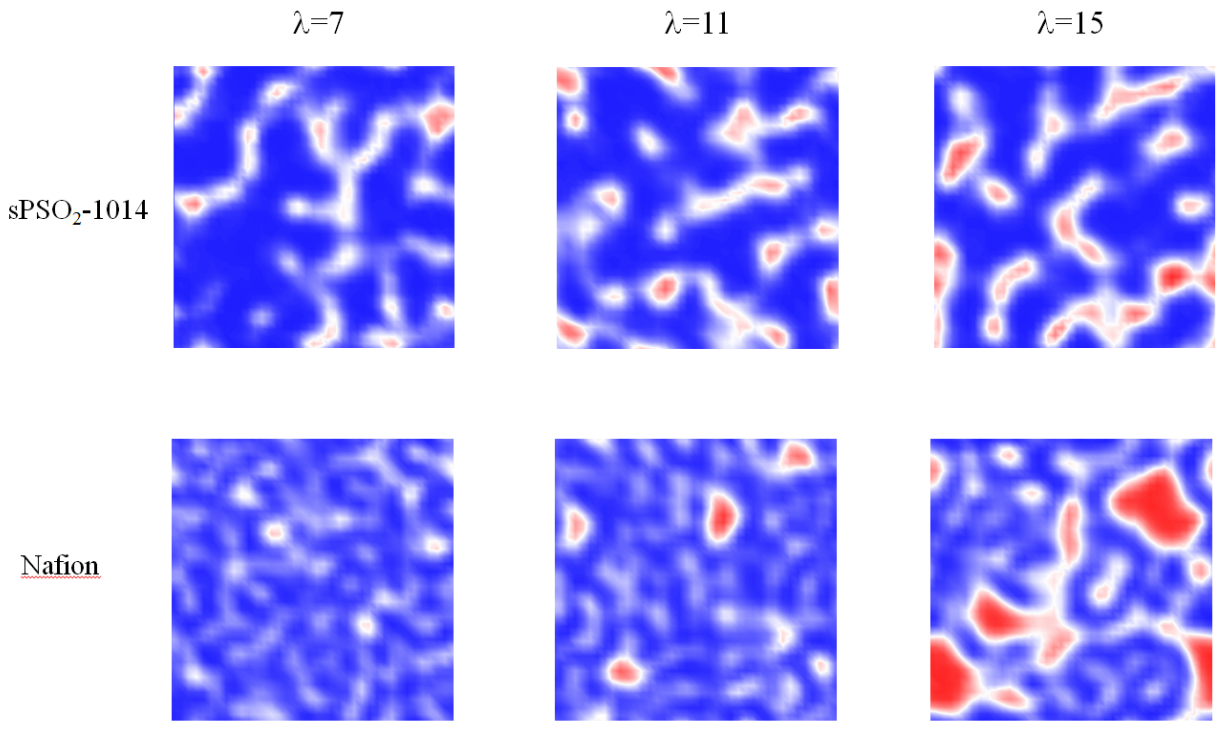

Figure 4.12. Contour plots of the densities of water particles mapped on the cross sections of simulation boxes for $sPSO_2$-1014 and Nafion at water content λ=7, 11 and 15. The water-rich regions are shown in red while backbone matrix is in blue. The densities of water and backbone beads are indicated by the intensities of colors.

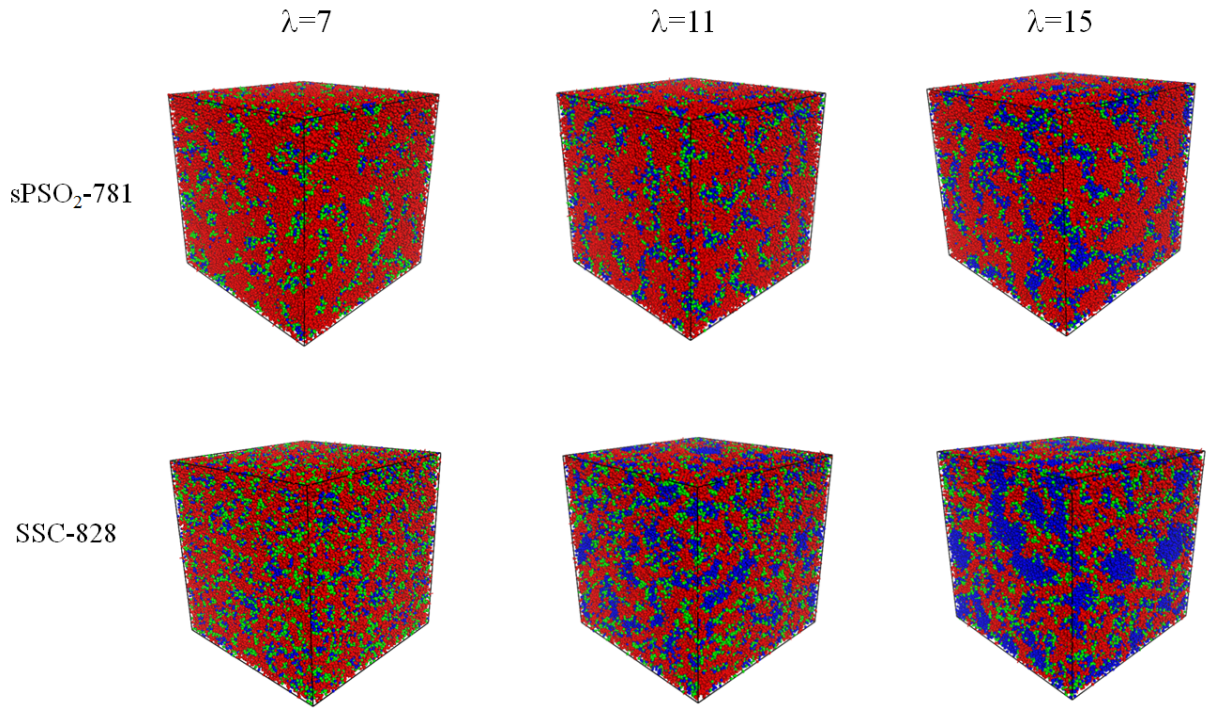

Figure 4.13. Comparison of equilibrium morphologies of the $sPSO_2$ (EW=781) and SSC (EW=828) ionomers with water content λ=7, 11 and 15. Hydrophobic backbones of ionomers are represented by beads *A, F, O* and *O'* showing in red, while beads of sulfonated side chains and water clusters are in green and blue, respectively.

The morphologies of $sPSO_2$ and PFSA ionomers with lower EWs (i.e., $sPSO_2$-781 and SSC-828) at different hydration levels (λ=7, 11 and 15) are compared in Figure 4.13. The corresponding water volume concentrations are 17.5, 25.0 and 31.3% for $sPSO_2$-781 and 28.0, 37.9 and 45.5% for SSC-828. With lower EWs, more hydrophilic beads are involved in the simulation boxes. Thus, both two ionomers possess more dispersed water distributions and larger fractions of hydrophilic areas than ionomers with higher EWs. A more detailed examination of water contour plots of the similar ionomers in Figures 4.14 and 4.12 clearly shows that a majority of hydrophilic domains are connected with water channels in the ionomers with lower EWs, which becomes more evident as water content increases. The same trend is found when comparison is made between $sPSO_2$-781 and $sPSO_2$-1014, and SSC-828 and Nafion. In comparison with Nafion, a slightly smaller and elongated water clusters are found in SSC-828. In

addition, lower densities of water are observed in the water clusters for SSC ionomers, which is visualized by the brighter colors of water-rich areas in contour plots. This indicates that the water molecules in hydrated $sPSO_2$ ionomers are more dispersed into the fine channels than PFSA membrane materials.

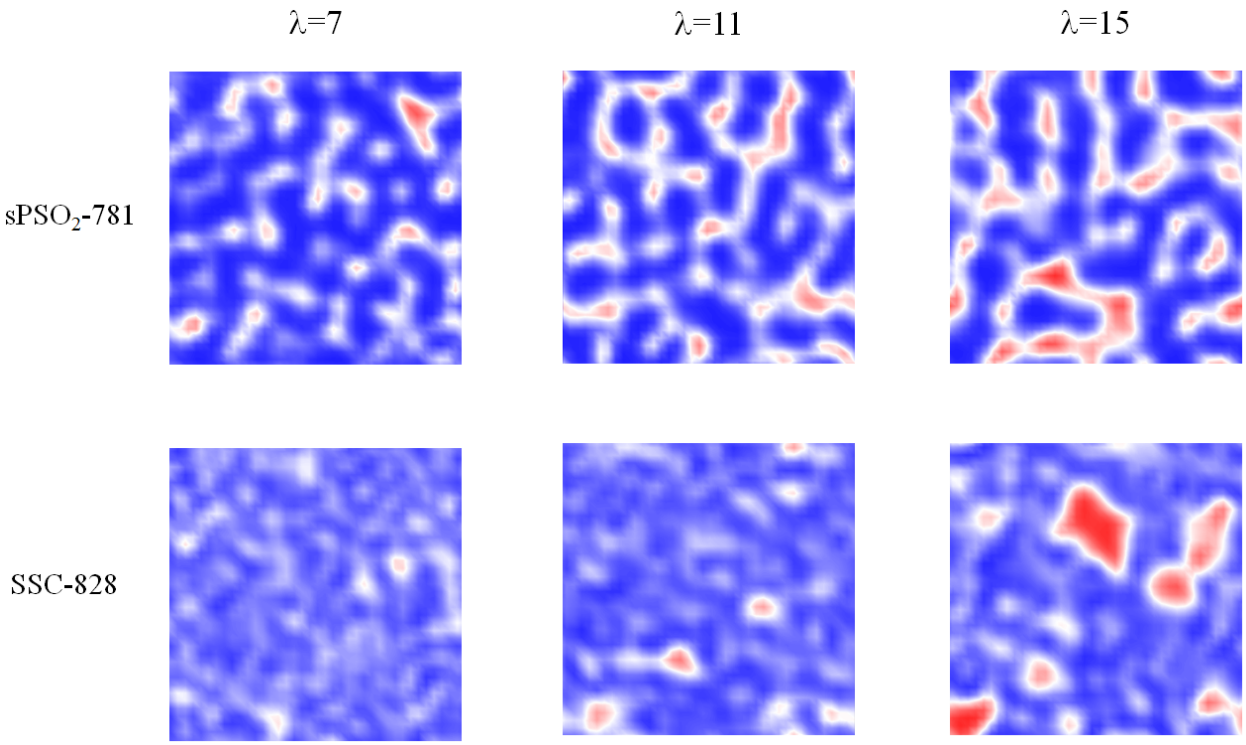

Figure 4.14 Contour plots of the densities of water beads mapped on the cross sections of simulation boxes for $sPSO_2$-781 and SSC-828 at water content λ=7, 11 and 15. The water-rich regions are shown in red while backbone matrix is in blue. The densities of water and backbone beads are indicated by the intensities of colors.

The morphological changes in these ionomers can be further studied by plotting the RDFs of water particles at different hydration levels. As observed in Figure 4.15 (a) and (c), polysulfone ionomers with different EWs possess similar shapes and positions of peaks in RDFs at the same hydration level. As water content increases, the first peaks in RDFs are attenuated and the following shoulders at larger radii become more pronounced. Consequently, the peaks are

gradually broadened, which leads to the extended RDFs that slowly approach the mean density (i.e., g(r)=1). The shapes of RDFs of PFSA systems seen in Figure 4.15 (b) and (d), in contrast, are more sensitive to the hydration level. The intensities and positions of the first peaks in PFSA ionomers are nearly unchanged. However, RDFs at large radii are further extended at high water content, leading to the appearance of large water clusters as seen in water density contour plots.

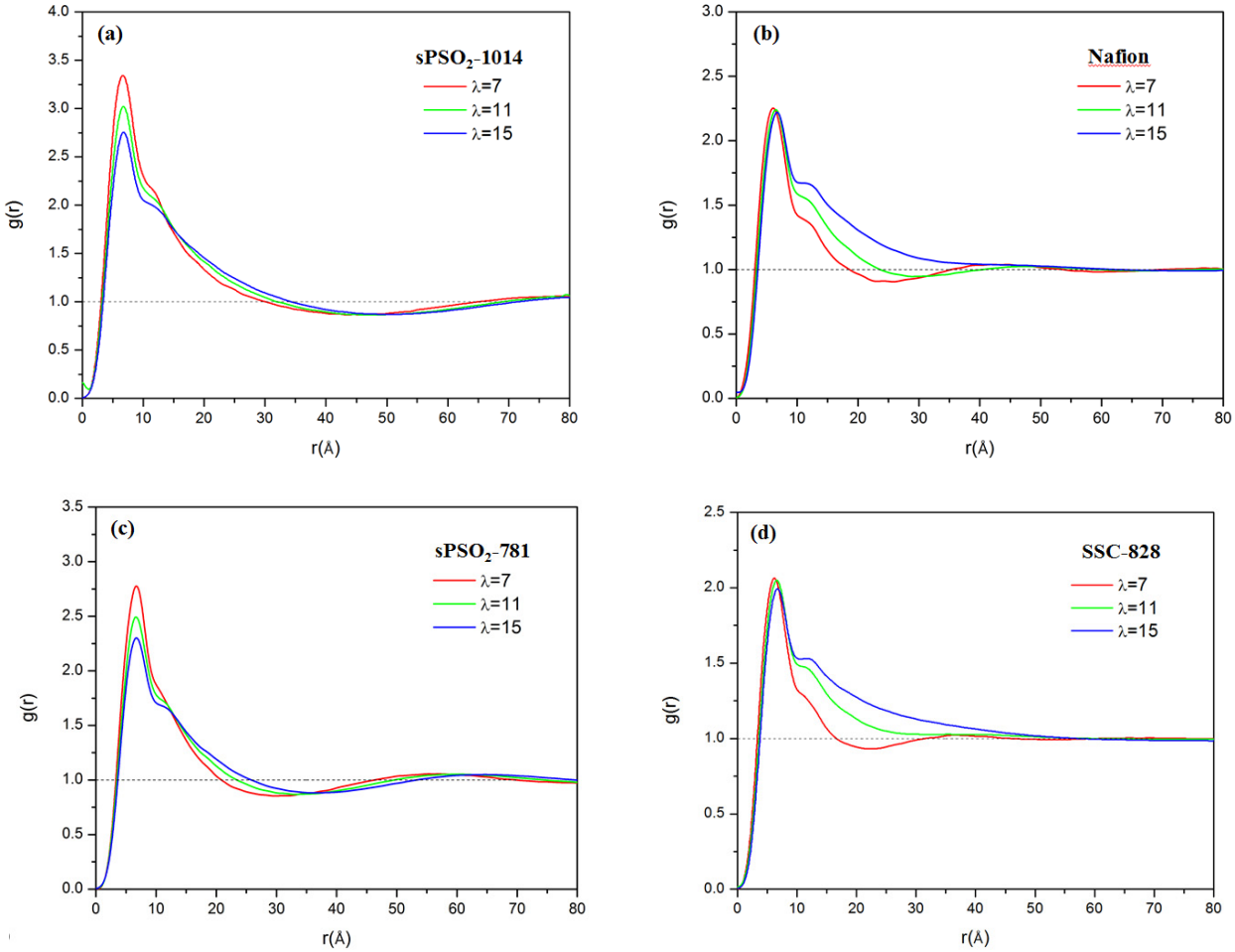

Figure 4.15. Radial distribution function of water particles for different ionomers with water content λ=7, 11 and 15: (a) $sPSO_2$-1014; (b) Nafion; (c) $sPSO_2$-781 and (d) SSC-828.

Both size and dispersion of water clusters change with the hydration levels for $sPSO_2$ and PFSA ionomers. In the highly hydrated condition, polysulfone ionomers are more likely to retain

an extended hydrophilic network connected with progressively swelling water clusters at various levels of hydration. In contrast, morphological structures in hydrated PFSA ionomers are characterized by the rapid growth of water clusters and strong phase separations particularly at high water content.

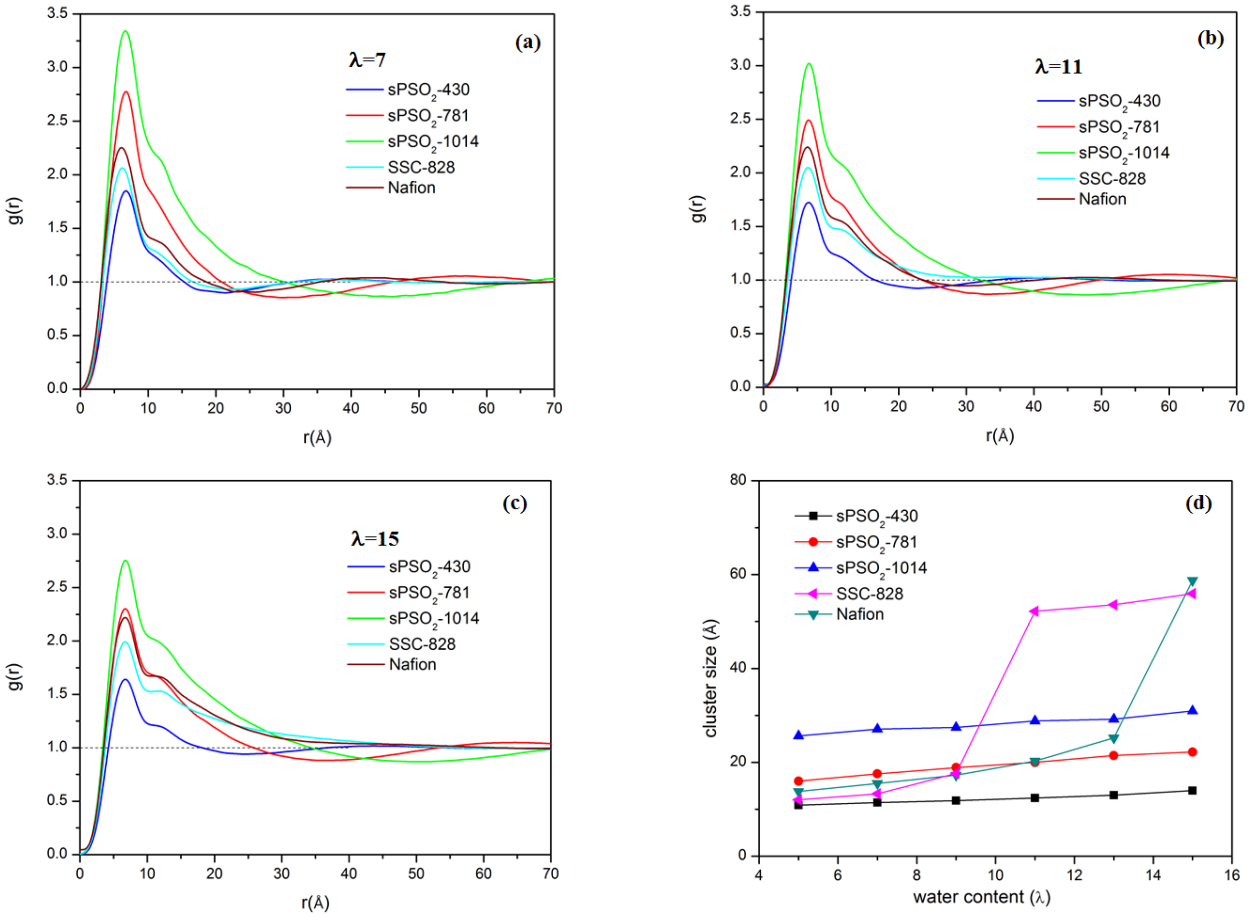

Figure 4.16. Comparison of radial distribution functions of water particles for different ionomers at the same water content (a) λ=7; (b) λ=11 and (c) λ=15, and (d) the average size of water clusters in these ionomers as a function of water content.

To quantify the morphological changes for different types of ionomers at various water content, RDFs of polysulfone ionomer with EWs of 430, 781 and 1014 were selected to compare with SSC-828 and Nafion at water content λ=7, 11 and 15 showing in Figure 4.16 (a)-(c).

Generally, intensities of the first peaks in RDFs are proportional to the EWs of ionomers. However, the peaks for PFSA ionomers always exhibit the lower intensities than polysulfone ionomers with the similar EWs, which indicates the more dispersed water distributions in PFSA ionomers. Another observation is the decay of extended RDFs to the mean density becomes considerably slower at higher water content for PFSA ionomers. The width of peaks (measured by the distance at which RDFs drop to the average density (i.e., g(r)=1)) increases as the water content increases, which indicates the swelling of water domains as increasing water content. The continuous water domains are formed as the increase of water at each site. In Figure 4.16 (d), the average sizes of water clusters in all polysulfone ionomers show a linear growth as a function of water content. In comparison, a rapid increase of water cluster is detected at water content λ=11 for SSC-828 and λ=15 Nafion.

4.2.3 Effect of Equivalent Weight

Hydrated morphology of $sPSO_2$ ionomers with different EWs at water content λ=7, 11, 15 are being studied to evaluate the effects of equivalent weight. The equilibrium morphologies of highly sulfonated polysulfone ionomers (i.e., $sPSO_2$-220 and $sPSO_2$-360 with 100% and 50% sulfonation, respectively) are shown in Figure 4.17. Nearly uniform distributions of water and backbone beads are observed for $sPSO_2$-220 ionomers, which is independent of hydration conditions. Although different morphologies are found between $sPSO_2$-220 and $sPSO_2$-360 ionomer at low water content, the similar sizes and distribution of water clusters are observed in these ionomers at high water content. More detailed mapping of water densities illustrated in Figure 4.18 confirms the existence of very fine water channels in highly sulfonated polysulfone ionomers. The morphologies of fully sulfonated $sPSO_2$-220 remain nearly unchanged as the hydration level changes, which indicate the potentially high proton conduction facilitated by the

well-connected hydrophilic pathways even at low water content. The evolution of micro phase separations in $sPSO_2$-360 is more evident than $sPSO_2$-220, which can be verified by the enhanced contrast of contour plots depicted in Figure 4.18.

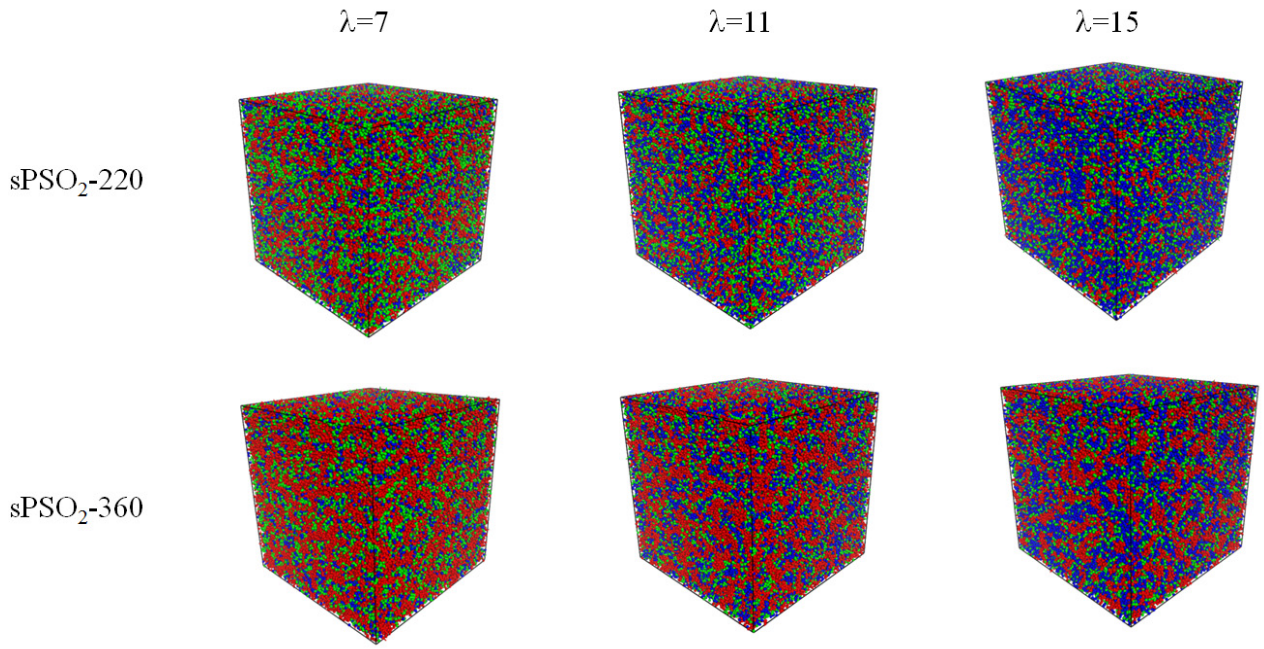

Figure 4.17. Equilibrium morphologies of the $sPSO_2$ with EWs of 220 and 360 g/mol at water content λ=7, 11 and 15. Hydrophobic fragment of ionomers are represented by beads *A* showing in red, while beads of sulfonated groups and water clusters are in green and blue, respectively.

RDFs of $sPSO_2$-220 and $sPSO_2$-360 ionomers with water content λ=7, 11 and 15 are plotted in Figure 4.19. Since water are more dispersed into hydrophilic domains for $sPSO_2$ ionomers with lower EWs, the intensities of the first peaks for $sPSO_2$-220 are somewhat reduced as compared to sPSO2-360. The shoulders next to the first peaks are slightly shifted to larger radii as the increase of water content in both of ionomers. This effect is substantiated for ionomers with larger EWs, where strong phase separations are present as the increase of equivalent weight.

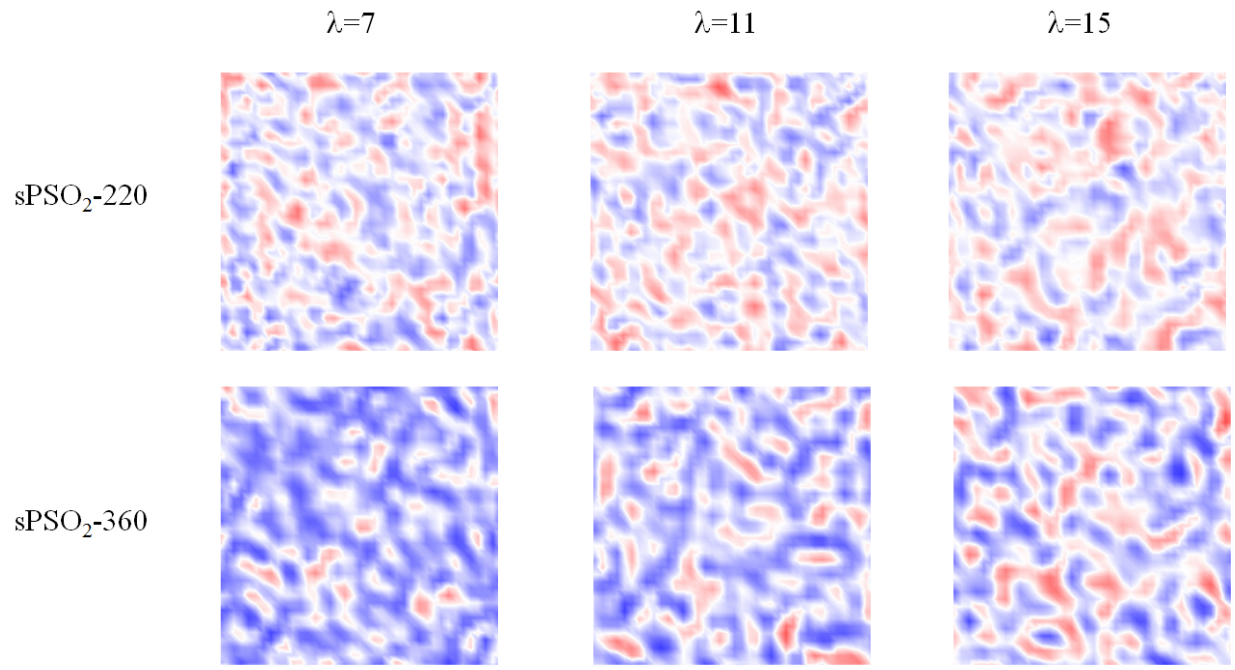

Figure 4.18. Contour plots showing the densities of water particles mapped on the cross sections of simulation boxes for $sPSO_2$ ionomers with EWs of 220 and 360 g/mol at water content λ=7, 11 and 15. The water-rich regions are shown in red while backbone matrix is in blue. The densities of water and backbone beads are indicated by their intensities.

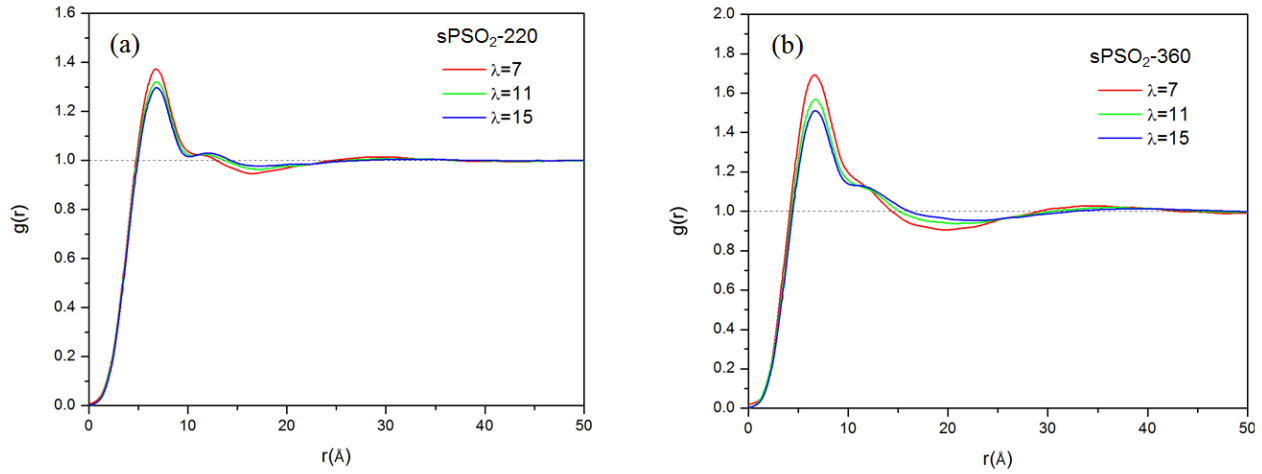

Figure 4.19. Radial distribution functions of water particles for $sPSO_2$ ionomers with different EWs at water content λ=7, 11 and 15: (a) $sPSO_2$-220 and (b) $sPSO_2$-360.

More detailed investigations of effects of EWs were undertaken for $sPSO_2$ ionomers with various EWs (or degree of sulfonation). The average size of water clusters as a function of EW at different levels of hydration is shown in Figure 4.20(a). Their dependences of water content are also plotted in Figure 4.20(b). As seen in Figure 4.20(a), the average size of water clusters increases as the EWs increase. The effects of EWs become greater when ionomers are in a highly hydrated condition (i.e., λ=15), which leads to a large extend of increase of cluster sizes. It is revealed that less water aggregation occurs with the increase of degree of sulfonation (from $sPSO_2$-1014 to $sPSO_2$-220). Figure 4.20(b) shows linear dependences of cluster sizes as a function of water content for all $sPSO_2$ ionomers. For the $sPSO_2$ ionomers with high concentration of sulfonate groups (i.e., EW=220, 360 and 430), cluster sizes increases much slower as a function of hydration level when compared to those with higher EWs. This can be seen in Figure 4.20 (b), where the slopes of lines increase with the EWs of ionomers.

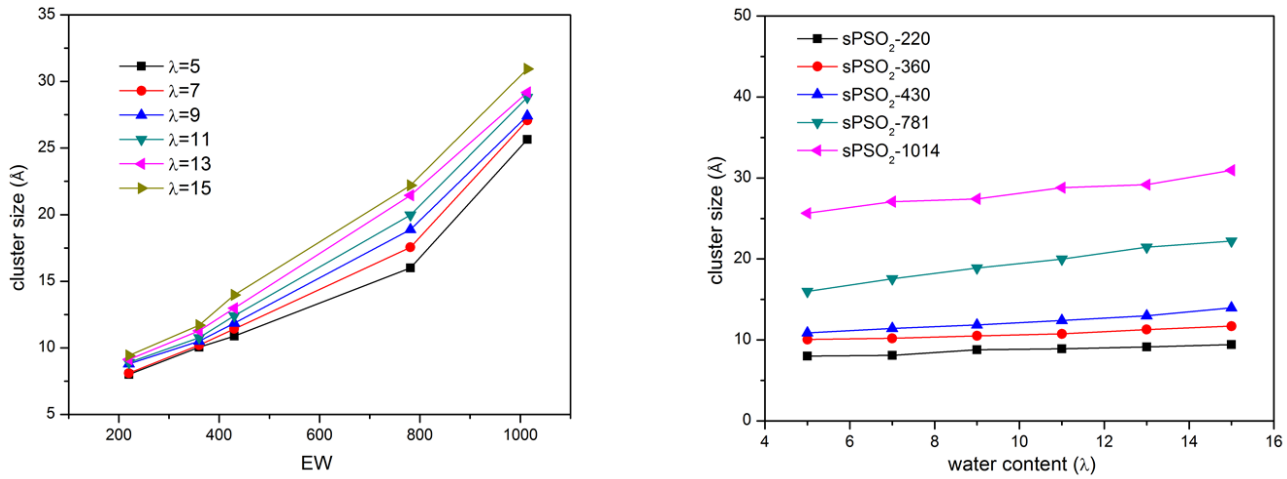

(a) (b)

Figure 4.20 Average size of water clusters of different $sPSO_2$ ionomers as a function of (a) EWs and (b) water content.

4.2.4 Effect of Molecular Weight

It has been shown that the MW has a strong influence on hydrated morphologies as a function of water content for SSC PFSA ionomers, particularly for those with high EWs at high hydration levels.[40] In order to investigate the effects of MW on the swelling behavior of $sPSO_2$ ionomer in different hydrated conditions, two set of macromolecule parameters were used to construct $sPSO_2$ ionomers at two distinct MWs as seen in Table 4.4. The Nafion membranes were also modeled at two MWs at the same hydration levels for the comparison. The MWs of $sPSO_2$ ionomers with different EWs were chosen in the same range as experimental data. The variation of average sizes of water clusters as a function of water content (λ =5~15) for $sPSO_2$ and Nafion ionomers at two MWs are plotted and shown in Figure 4.21 (a)-(f), respectively.

Nearly identical behavior of cluster growth are found for $sPSO_2$ ionomers with EWs of 430 and 781 as shown in Figure 4.21 (c) and (d). For the $sPSO_2$ ionomers consist of a large number of sulfonated groups (i.e., $sPSO_2$-220 and $sPSO_2$-360), the most noticeable differences of cluster sizes are observed at the lowest water content (λ =5). Figure 4.21 (a) and (b) show that both of the ionomers with high MWs would have slightly larger water clusters with the minimum hydration. As EWs increase, the effects of MWs become more important for $sPSO_2$ ionomers. As depicted in Figure 4.21(e), same trends of cluster growth are witnessed for $sPSO_2$-1014 ionomers at two distinct MWs. However, the hydrated ionomers with high MWs appear to form substantially smaller cluster sizes at all water contents. This effect is completely different from the behavior of Nafion shown in Figure 4.21(e), where MW shows strong effects on cluster sizes only at high water content.

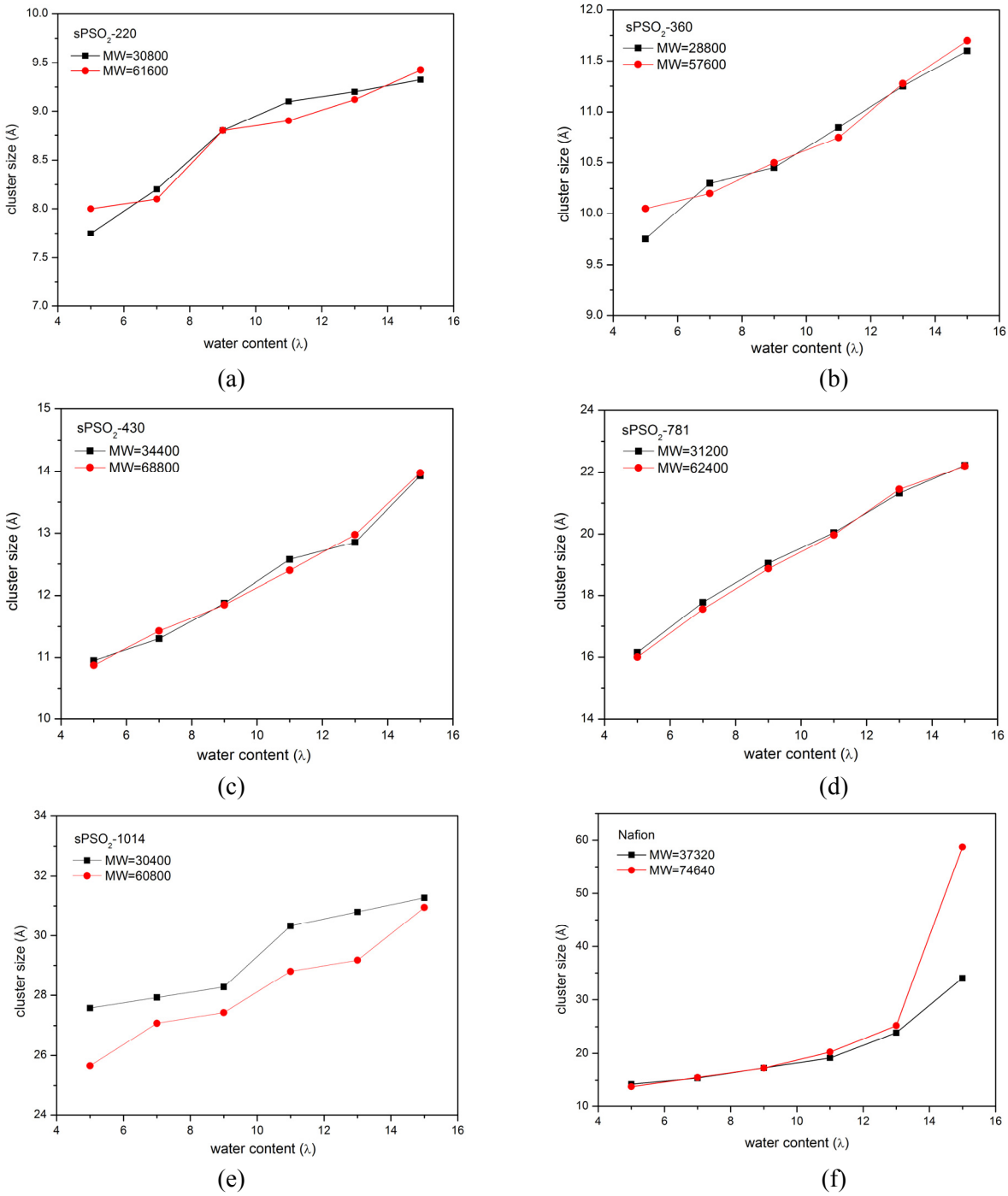

Figure 4.21. Average size of water clusters as a function of hydration levels for various ionomers with different MWs: (a) $sPSO_2$-220; (b) $sPSO_2$-360; (c) $sPSO_2$-430; (d) $sPSO_2$-781; (e) $sPSO_2$-1014 and (d) Nafion.

4.2.5 Backbone Aggregation and Flexibility

Along with the formation of ionic aggregates as the swelling of membranes, hydrophobic backbones are more likely to coil and reorganize into the ordered phase (i.e., crystalline regions). For linear polymers, the forming of crystalline domains is largely influenced by the backbone flexibility and effects solvent. These effects can be evaluated by studying the distributions of end-to-end distances (R) of polymer chains. They are also related to the radius of gyration, which provides the information about the size and dimension of polymer chains. The root mean square (RMS) endpoint distances ($<R^2>^{1/2}$) were calculated for various $sPSO_2$ ionomers at different water content while keeping the length of backbones (i.e., number of backbone particles in a modeled mesomolecule) a constant. The results for $sPSO_2$ ionomers with 200 and 400 backbone particles per chain are plotted in Figure 4.22 (a) and (b), respectively. It is compared with PFSA ionomers with 400 backbone particles per chain presented in Figure 4.22(c).

Although a certain degree of oscillations of RMS endpoint distances are detected for all $sPSO_2$ ionomers, most of them are in the same range and considered to be independent of water content. However, highly sulfonated $sPSO_2$-220 ionomer appear to show a discernible increase as water content for both of chain lengths. This is mainly due to the 100% sulfonation of backbones in $sPSO_2$-220, which makes the backbones more hydrophilic and easily expanded in the highly hydrated condition. For the $sPSO_2$ ionomers with high EWs, the calculated RMS endpoint distances are slightly decreased as water content increases. The similar behavior is seen in PFSA ionomers where backbones are easily coiled to form crystalline regions at high water content. This is consistent with the observations from water density maps for SSC-828 and Nafion ionomers, where strong phase separations occur only at high hydration level.

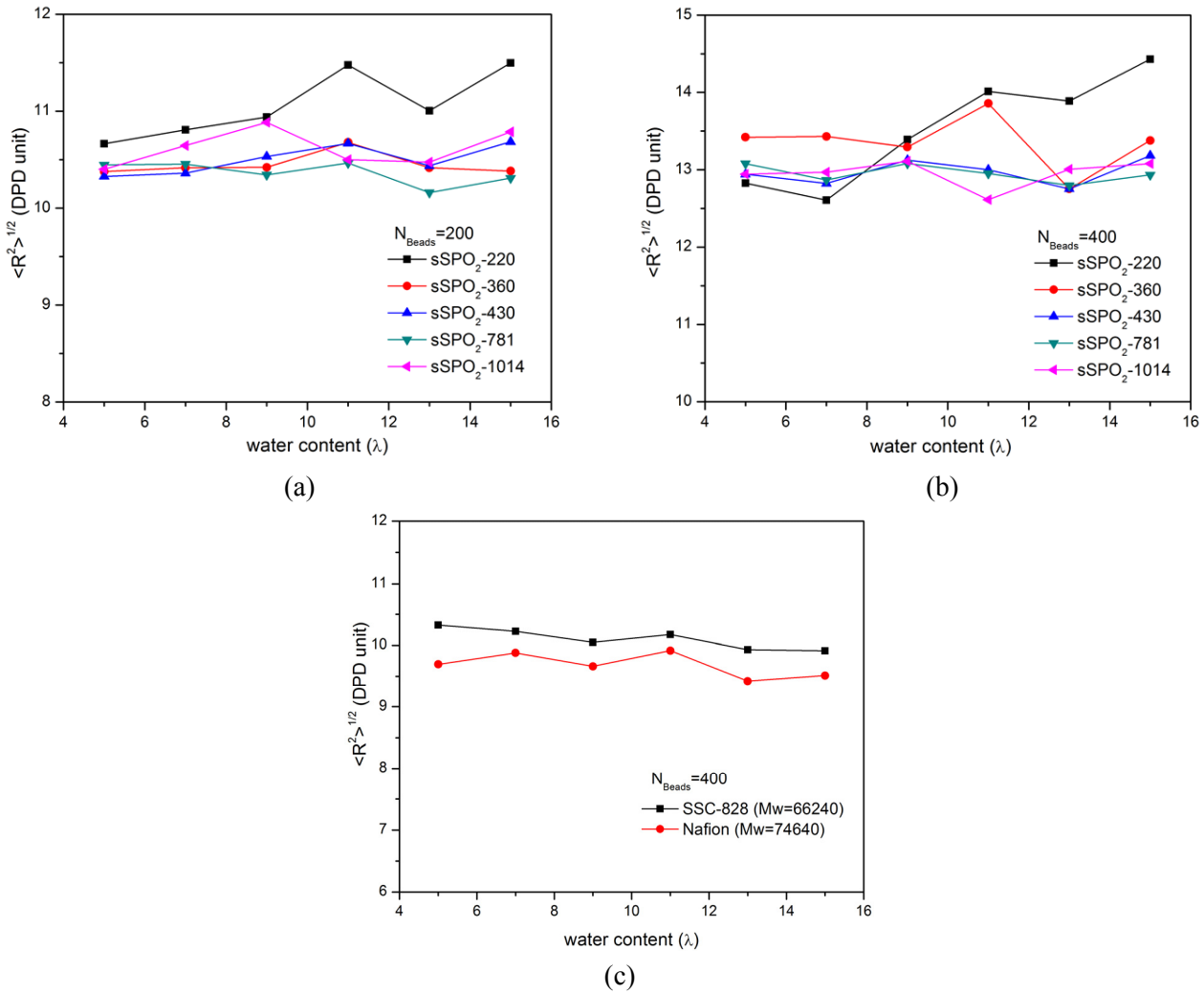

Figure 4.22. Root mean square endpoint distances (of simulated mesomolecules as a function of water content for (a) $sPSO_2$ ionomers with 200 beads per backbone chain; (b) $sPSO_2$ ionomers with 400 beads per backbone chain; (c) PFSA ionomers with 400 beads per backbone chain.

Considering the $sPSO_2$ and PFSA ionomers with the same length of backbones and water content, the RMS endpoint distances measure the stiffness of backbones. Generally, PTFE backbones in PFSA ionomers show more flexibility than aromatic backbones in $sPSO_2$ ionomers. Therefore, the average endpoint distances in PFSA ionomers are essentially smaller than $sPSO_2$ ionomers as compared in Figure 4.22 (b) and (c).

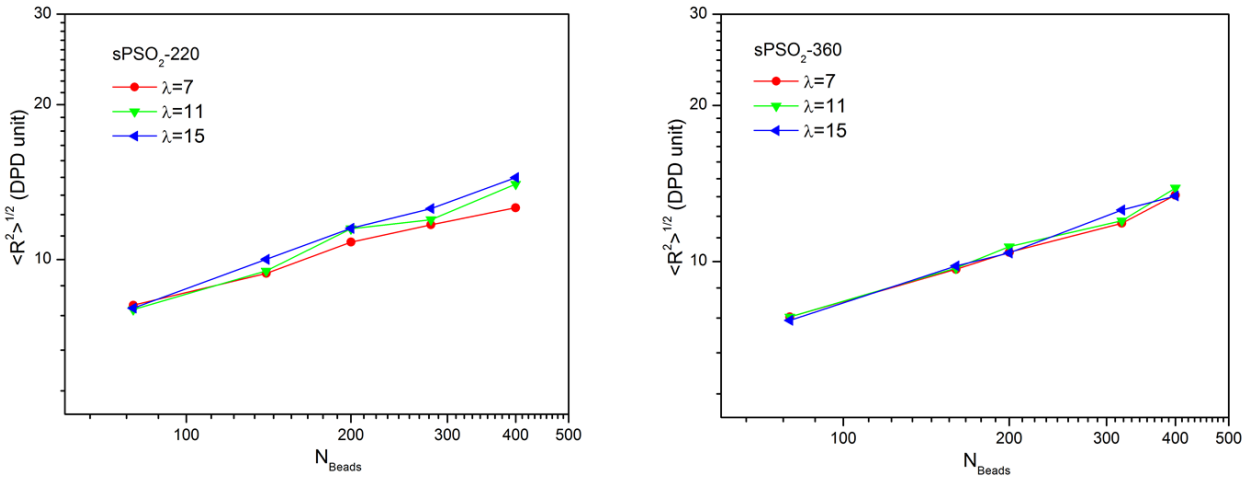

(a) (b)

Figure 4.23. Log-log plot of root mean square endpoint distances as a function of number of backbone beads per molecule for $sPSO_2$ ionomers at different water content (a) $sPSO_2$ -220 (b) $sPSO_2$-360.

For ideal chain polymer, the RMS endpoint distances is proportional to the length of chain by $<R^2>^{1/2} \propto N^{1/2}$, where N is the number of repeat units per chain. Two types of $sPSO_2$ ionomers with 100% and 50% sulfonation (i.e., $sPSO_2$-220 and $sPSO_2$-360) are modeled with various lengths of chains at three water contents. The corresponding log-log plots are shown in Figure 4.23(a) and (b). The endpoint distances of $sPSO_2$-220 ionomers at different hydration levels show almost linear dependences on the chain lengths with slope of 0.28, 0.35 and 0.37 for λ =7, 11 and 15, respectively. The corresponding slopes for $sPSO_2$-360 are 0.32, 0.34 and 0.35 for λ =7, 11 and 15, which are very close to $sPSO_2$-220 but are less affected by the water content. With the increasing number of hydrophilic groups, more restrictions may be applied to the polymer chains. This leads to more rigid backbones that behave differently as ideal chains.

4.2.6 Summary

We have studied hydrated morphologies of $sPSO_2$ ionomers with selected water content (λ=7, 11 and 15) using DPD simulations. At a low hydration level, the water beads are more likely to be equally distributed into hydrophilic domains for $sPSO_2$ ionomers. The well-connected water

channels are gradually developed among water clusters with the increasing water content. This is in contrast to PFSA ionomers where strong phase separations occur at high hydration level and generate large water clusters that are lack of adequate connectivity.

The effects of EWs and MWs on swelling properties of hydrated $sPSO_2$ ionomers are also investigated. We have modeled various $sPSO_2$ ionomers with EWs of 220, 360, 430, 781 and 1014 g/mol at two distinct MWs (from 28800 to 68800 g/mol). As the fraction of sulfonate groups increases (decrease of EWs), distribution of water is more dispersed and less dependent upon the hydration level. The highly sulfonated ionomers (i.e., $sPSO_2$-220 and $sPSO_2$-360) would establish a water connected pathway for proton conduction even at low water content. The growth of water clusters is also affected by the EWs. The sizes of water clusters change more rapidly for $sPSO_2$ with high EWs. Unlike PFSA ionomers, the MWs effects are nearly negligible for $sPSO_2$ ionomers with EWs below 781 g/mol. For $sPSO_2$ ionomers with high EWs, higher MWs tend to decrease the size of water cluster with the same extend at various water content. Smaller water channels are formed among hydrophilic regions in the $sPSO_2$-220 ionomer, the sizes of which are measured from 1.2 to 1.5 nm (compared to Nafion with ~3.5 nm) at water content λ=7. This property suggests the potentially high proton conduction in this type of ionomer, which may be facilitated by the well-connected hydrophilic pathways.

In order to study the properties of backbone aggregation and flexibility, RMS endpoint distances were calculated for the $sPSO_2$ and PFSA ionomers. Ionomer backbones with a high degree of sulfonation such as $sPSO_2$-220 are expected to be expanded more in a highly hydrated condition, which leads to a well dispersed water distribution in ionomers. In contrast, ionomers with less sulfonate groups (such as $sPSO_2$-1014 and PFSA ionomers) tend to form a strong phase separation partially due to the backbone aggregation at high hydration level.

4.3 Electron Microscopy of PFSA Ionomers

The purpose of the present study is to understand the microstructure of hydrated PFSA ionomers and identify relevant features that determine proton conductivity. Although SANS[33-35] and SAXS[29-32, 36] experiments have revealed that the microstructure of the PFSA ionomers varies with the level of hydration and molecular structure (i.e., equivalent weight (EW) and side chain length), these studies are not able to provide complete information of these ionomers due to the presence of a very fine phase separation between the hydrophobic polymer backbone and the aqueous domains containing the hydrated protons. In this study, we have used TEM/STEM equipped with an EELS detector to study the morphology and identify chemical composition and distributions of native dry and hydrated PFSA ionomers. We aim to validate structural models based on SAXS experiments and mesoscale simulations by combination of various electron microscopy techniques.

This part is organized as follows. The first section contains a detailed description of sample preparation and experimental methods. The results are then presented and discussed in the following section for formation of crystallites, morphologies of PFSA membranes in dry and hydrated conditions and corresponding elemental mapping in both of states.

4.3.1 Experimental Details

Three different PFSA membranes each of a distinct EW were examined in this study. The samples were originally received from DuPont, 3M, and Solvay Solexis in the form of a membrane (150-175 μm thickness) and/or dilute solution (5 wt. % dissolved in isopropanol). The chemical structures of these PFSA ionomers are shown in Figure 4.24 (a-c). Each ionomer consists of a highly hydrophobic PTFE backbone and hydrophilic side chains each terminated with a sulfonic acid group ($-SO_3H$). The hydrophobic PTFE backbone provides effective

mechanical stability, whereas the pendant sulfonic acid groups form interconnected domains with the absorbed water and are responsible for the conduits for proton transport. The difference between these ionomers is the length of their hydrophilic side chain and their EW (i.e., reciprocal of the ion exchange capacity). The side chain is the shortest for the Aquivion ionomer (made by Solvay Solexis) and longest for Nafion. In this study the morphology of dry and hydrated Nafion (EW = 1100 g/mol), 3M ionomer (EW = 825 and 636 g/mol) and Aquivion (EW = 830 g/mol) ionomers were analysed.

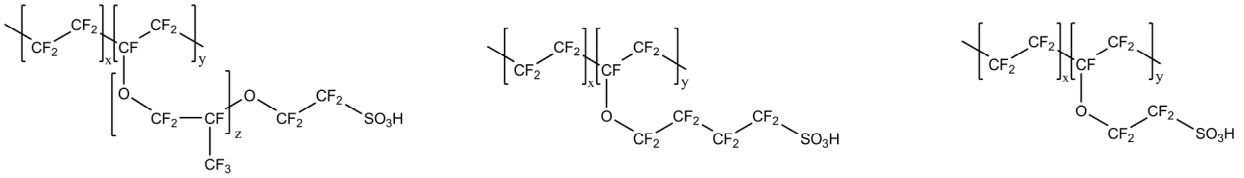

(a) (b) (c)

Figure 4.24. Chemical structures of PFSA ionomers: (a) Nafion; (b) 3M ionomer and (c) Solvay Solexis Aquivion ionomer. Each of them has a single sulfonic acid ($-SO_3H$) pendant group on the side chain. The equivalent weight (EW) is determined by the molecular weight of the side chain and on the choice of x, y and z.

Two different methods were employed to prepare dry samples. First, thin sections (~30 nm thickness) of dry PFSA membranes embedded in epoxy resin were prepared by ultra-microtome using a diamond knife and transferred to lacey carbon grids, as described in previous work.[116] This method has the ability to produce fairly large, uniformly thin areas without modifying morphological properties of the samples. However, the desirable thickness (~10 nm) for obtaining sufficient contrast in high resolution TEM images is difficult to achieve by this method due to the softness of the membrane samples. Thus, the thin sections of ion-exchanged samples prepared by neutralizing the membranes with $CaCl_2$ and KCl solution were used to obtain contrast-enhanced images for comparison purposes.

Another preparation method was utilized where the film was cast from solution using the cryo-plunger under cryo or room temperature. By this method, both dry and hydrated TEM samples were prepared. In the present work, the ionomer in an isopropanol solution was used to prepare solution cast samples, which showed similar properties as those prepared by sectioning.[172] To prepare the dry samples, approximately 2 – 5 μL of a 5 wt. % ionomer solution in isopropanol was dispensed onto a lacey carbon grid. The grid was double blotted to wick excess solution and dried in vacuum for 24 hours at room temperature. The hydrated samples were prepared under cryo-conditions: 1) Lacey carbon or Quantifoil grids were loaded into a relative humidity (RH) controlled chamber of the cryo-plunger; 2) A drop of ionomer solution (2 – 5 μL) was dispensed on the grid inside the chamber, double blotted for 4s and plunged into a temperature controlled liquid ethane bath at −172 °C; 3) The rapidly frozen hydrated sample was moved to a pre-cooled cryo grid box located on a screen mesh support within the cryo-workstation chamber, and safely transferred to a liquid nitrogen storage vessel to transport to the microscope. During the preparation of cryo samples, the inert liquid nitrogen helps in maintaining a blanket of cold and minimizing condensation of atmospheric oxygen onto the surface of ethane and providing a protective cryo interface for transferring the frozen hydrated grids within the workstation.

In this study, a dedicated STEM microscope VG-HB501UX and Hitachi HF-3300 TEM-STEM both equipped with EELS detector were used to study the morphology as well as the chemical information of the dry membrane samples. The HF-3300 TEM-STEM has cryo capabilities which enabled the study of frozen hydrated PFSA ionomers. STEM High Angle Annular Dark Field (HAADF or Z-contrast) imaging[141] and Bright Field (BF) imaging were used to determine the microstructure of hydrated and dry ionomers with and without ion-exchange. Moreover, spatially resolved Electron Energy Loss Spectroscopy (EELS),[145] spectrum imaging

and Energy-dispersive X-ray Spectroscopy (EDS)[138] were used to quantify the distribution of elements and chemical groups for regions of interest. The electron dose used during Z-contrast imaging and EELS acquisition was 3×10^4 – 3×10^5 electrons/nm^2 to minimize the polymer damage under electron beam.

4.3.2 Crystallites in PFSA Membrane

To study the nanoscale morphology of the ionomers, both bright field and Z-contrast images from STEM/TEM were acquired and analysed. In the bright field imaging mode, the direct electron beam passing through samples is detected. The contrast of image in this mode results from mass-thickness and diffraction of the samples: dark contrast is seen in thick areas and crystalline areas where heavy atoms are enriched (one example of 3M-636 is shown in Figure 4.25 (a)). In the Z-contrast imaging mode, however, only high angular elastic scattering electrons are detected. Hence, the contrast due to thickness variations is greatly reduced and areas with aggregated heavy elements are clearly visible as bright contrast proportional to their atomic number Z (see Figure 4.25 (b)).

The dry membrane samples were prepared by either sectioning or solution casting and were observed to possess nearly uniform thickness in the viewing region. Thus, the contrast in bright field images of non-ion exchanged samples is due to the crystalline ionomer backbones, whereas the contrast in Z-contrast images is primarily formed by the elemental composition and density variation. The bright regions in the Z-contrast images are considered to be aggregated hydrophilic side chains containing carbon, fluorine, oxygen and sulphur. It was also observed that degradation of the vinyl sulfonyl fluoride side chains often occurred when the samples were exposed to the electron beam, leading to the formation of KF or CaF_2 crystallites around the side

chains. Therefore, the lattice fringes present in images for ion exchanged samples are mostly attributed to the higher density of PTFE, KF, or CaF_2 crystallites.

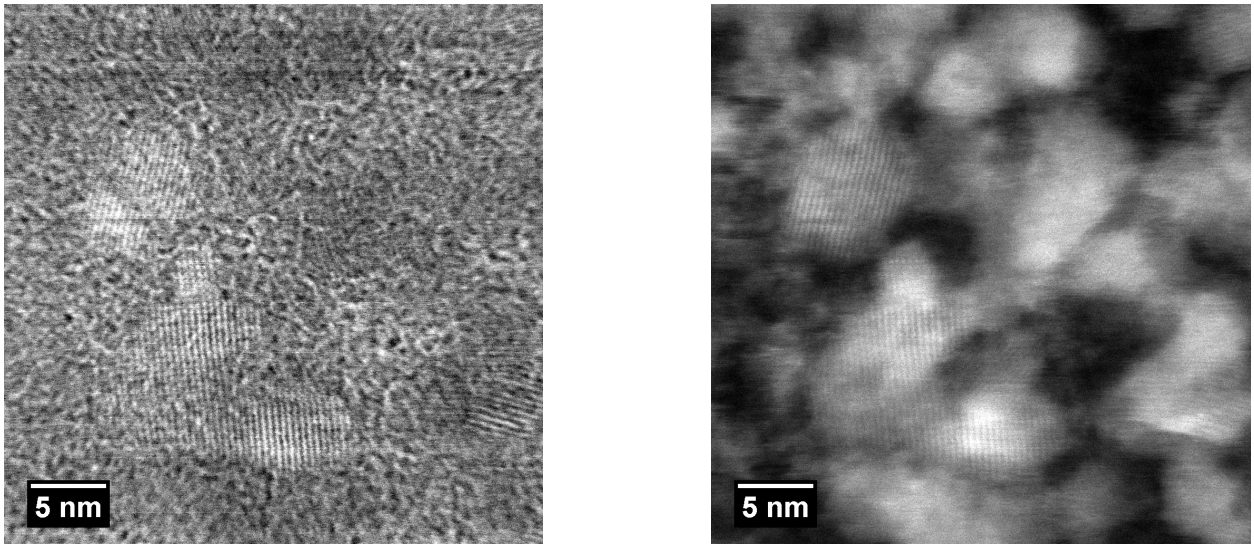

(a) (b)

Figure 4.25. (a) High Resolution (HR) TEM bright field image of the dry 3M-636 ionomer (non-ion exchanged) and (b) STEM Z-contrast image of the same area in dry 3M-636 ionomer.

For the non-ion exchanged ionomer samples, crystallites were observed with d-spacing of 0.442 ± 0.021nm corresponding to [100] planes of hexagonal poly-tetrafluoroethylene (PTFE) (P6mm space group) having lattice parameters: a = b = 0.565 nm and c = 1.950 nm. In addition to the PTFE crystallites, CaF_2 crystallites were observed for the Ca^{2+} ion exchanged ionomers. Crystallites of CaF_2 have cubic structures with lattice parameter 0.546 nm and space group Fm3m-225. The corresponding d-spacings of the CaF_2 crystallites were determined as: 0.321±0.011 nm [111], 0.190±0.005nm [220], 0.160±0.003 nm [311], and 0.139 ±0.001 nm [400] in contrast to 0.243 nm ± 0.002nm [200] for the PTFE crystallites. For the K^+ ion-exchanged ionomer, only KF crystallites were visible with d-spacing of: 0.311±0.022 nm [111],

0.265±0.013 nm [200], 0.186±0.001 nm [220], and 0.154±0.001 nm [311]. KF has cubic structure with lattice parameter of 0.535 nm and Fm3m-225 space group.

To quantify the morphology of crystallites in non-ion exchanged ionomers, the size of the PTFE crystallites in mutually perpendicular directions (i.e., x and y directions) and the nearest-neighbour (N-N) distances between adjacent crystallites were measured. The total area of the crystallites in the images and the corresponding areal coverage in images (i.e., areal density) were calculated. Fractal Dimensions (FD) were calculated by using the FRACEK[173] program to evaluate the similarity of the shape of the crystallites. The measurements were averaged over 25 or more HAADF/BF images and are summarized in Table 4.6.

Table 4.6. Morphology analysis of crystallites for dry and hydrated ionomers

Ionomer [a]	Crystallite size (x,y) (nm)		Areal density (%)	NN-distance (nm)
Nafion (Dry)	3.6±1.9	3.7±1.9	12.0±5.0	9.5±5.0
Aquivion-830 (Dry)	4.2±1.0	4.3±1.0	7.3±1.3	13.0±2.0
3M-825 (Dry)	6.5±1.5	6.5±1.9	16.0±7.0	10.0±4.0
3M-636 (Dry)	7.5±3.0	6.0±3.0	20.0±10.0	9.0±4.5
3M-636 (Hydrated)	4.5±1.0	6.2±1.2	6.6±1.0	12.0±4.0

[a] Dry samples were prepared using solution casting and ultra-microtome, hydrated samples are prepared using cryo-plunger from an ionomer solution.

As seen in Table 4.6, dry Nafion and Aquivion ionomers have comparable crystallite sizes (~ 4 nm) while 3M ionomers (both dry and hydrated) have larger crystallites (~6 nm). For the 3M membranes of lower EW (3M-636) a slight extension of crystallite in one direction is seen in the hydrated state. Moreover, hydrated 3M-636 has a smaller areal density and larger nearest neighbour distances in comparison with dry state, which imply that hydrophobic regions (i.e.,

PTFE crystallites) are increasingly dispersed upon hydration with an increase in the aggregation of water molecules into hydrophilic regions. Nearly identical Fractal Dimensions (~1.87) were calculated for all of the samples indicating the similarity in the backbone structure for three types of PFSA ionomers.

4.3.3 Morphology of PFSA Membrane

High resolution STEM Z-contrast imaging and DPD simulations were used to obtain comparable morphological representations for dry and partially hydrated ionomers. As shown in Figures 4.26-4.29, HAADF (Z-contrast) images of dry ionomer samples are compared with DPD simulations results obtained for the same ionomer with different water content (i.e., $\lambda = 9$ and $\lambda = 15$). The qualitative comparison in Figure 4.26 shows clearly that the length scale of the simulation results and the Z-contrast images of the unstained (i.e., non-ion exchanged) ionomers are in a good agreement. In a Z-contrast image, the bright regions represent hydrophilic sulfonate side-chains containing water molecules. Although the aggregated fluorocarbon crystallites cannot be observed in DPD simulations directly, water distribution maps from simulation indicate both water-rich regions (bright) and hydrophobic PTFE regions (dark). As seen in Figures 4.27-4.29, the images of dried 3M and Aquivion ionomers are qualitatively consistent with the simulation results for partially hydrated ionomers. However, clear differences are visible between dry and hydrated Nafion as shown in Figure 4.26: well-connected water channels are established even at low water content while only isolated hydrophilic domains are observed in the dry state.

A number of quantitative image analyses were carried out between simulation and experimental results. For 3M and Aquivion ionomers, the calculated areal coverage of hydrophilic regions (represented by the percentage of bright area in the image) in Z-contrast

images are ranged from 43% to 45%, which are in a good agreement with those calculated from simulations results (42–44% at low water content). This quantity for images of dried Nafion is below 40%, which is apparently lower than simulation results (45–47%). The qualitative and quantitative comparisons among three types of ionomers indicate that the distribution of ionic clusters within Nafion is largely affected by the present of water even in a minimal hydration condition, while ionomers with shorter side chains tend to preserve the microstructures of ionic clusters under the same conditions. This is consistent with comparable experimental measurement[174-176] of ionic conductivity between short-side-chain ionomer (i.e., 3M and Aquivion) and Nafion in the same non-fully hydrated condition.

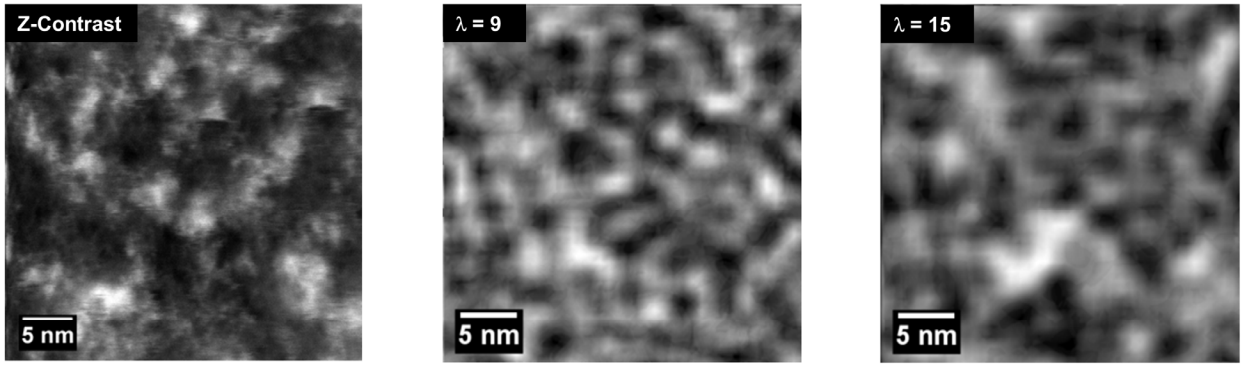

(a) (b) (c)

Figure 4.26. Comparison of the morphology of Nafion-1100: (a) HAADF (Z-contrast) images of dry ionomer samples prepared by solution casting at room temperature; (b, c) Contour plots of water density distribution obtained from DPD simulations for Nafion with EW=1244 at water content of $\lambda = 9$, and $\lambda = 15$, respectively. Bright regions in the Z-contrast image are areas containing high density of the sulfonic acid groups.

Compared to the Aquivion membranes, the longer vinyl fluoride linkages in the 3M membranes provide more flexibility for sulfonate terminated side chains forming hydrophilic aggregates in the fluorocarbon matrix. This leads to the larger and denser ionic aggregates observed in the 3M samples compared to Aquivion samples as seen in Figures 4.27 and 4.28.

The effect of EW on morphological properties can be seen from the different sizes and distributions of the ionic aggregates and water clusters in 3M-636 versus 3M-825 membranes. The high density of crystallites due to well-aligned longer backbones in high EW ionomers is responsible for the lower water uptake and fewer aggregates in the ionic clusters. Lower EW in the ionomer corresponds to a higher degree of sulfonation, which brings about the increase of swelling and consequent percolation of ionic clusters.

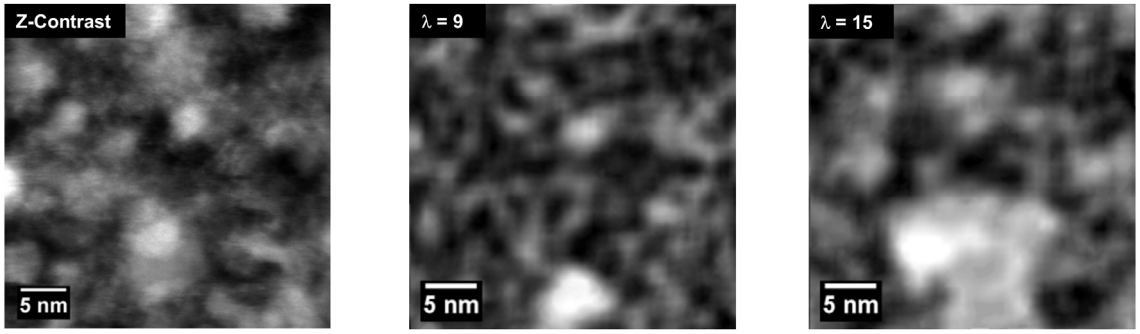

(a) (b) (c)

Figure 4.27. Comparison of the morphology of 3M-636: (a) HAADF (Z-contrast) images of dry ionomer samples prepared by solution casting at room temperature; (b, c) Contour plots of water density distribution obtained from DPD simulations for 3M PFSA ionomer with EW=635 at water content of $\lambda = 9$, and $\lambda = 15$, respectively.

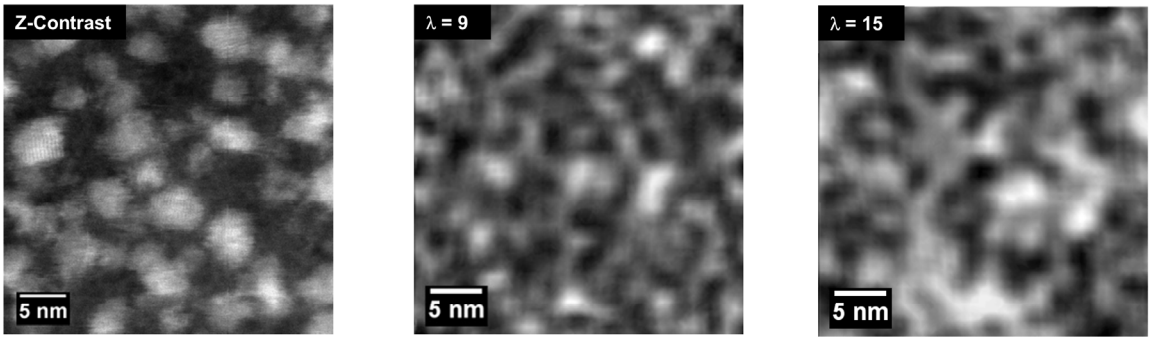

(a) (b) (c)

Figure 4.29. Comparison of the morphology of Aquivion-830: (a) HAADF (Z-contrast) images of dry ionomer samples prepared by solution casting at room temperature; (b, c) Contour plots of water density distribution obtained from DPD simulations for Aquivion with EW=849 at water content of $\lambda = 9$, and $\lambda = 15$, respectively.

4.3.4 Morphological Evolution in Hydrated Membranes

A variety of structural models (*e.g.,* cluster-network,[177, 178] polymeric bundle[179] and parallel cylinder[180]) of PFSA membrane have been developed based on SAXS/SANS experiments. However, they all lack a complete description of the microstructure evolution in response to changes of hydration. Despite the fact that a detailed description of the hydrated morphology is unclear, the occurrence of an ionomer peak and associated peak shift with increasing water content are generally considered as the result of the structural transition of swelling in the ionomers. We aim to obtain direct evidence of this behaviour in the hydrated PFSA ionomers using cryo-STEM/TEM imaging and compare the results with proposed morphological models.

As shown in Figure 4.30 (a-c), the bright area of the cryo-STEM images represent aggregated hydrophilic side chains while the dark background corresponds to the hydrophobic backbone matrix. In dry state, the isolated spherical ionic clusters are found to be evenly distributed in the perfluorinated matrix with the average diameter about 2 nm and inter-cluster distance about 3 nm, which is consistent with the morphology model proposed by Gebel[95]. At low water content, ionic conduction is still limited due to the localized ionic clusters and lack of connectivity. The water domains are gradually generated within ionic clusters distributed at polymer-water interfaces. As the water content increases, the diameter of the swelling ionic clusters increase while inter-cluster distances remain nearly unchanged, this leads to the percolation and coalescence between neighbouring ionic clusters. The percolation of ionic aggregates provides connected pathways for ionic carriers and thus promotes proton conduction. The network of water channels of hydrated ionomers can be visualized by the distributions of percolated ionic aggregates highlighted in Figure 4.30 (b) and (c).

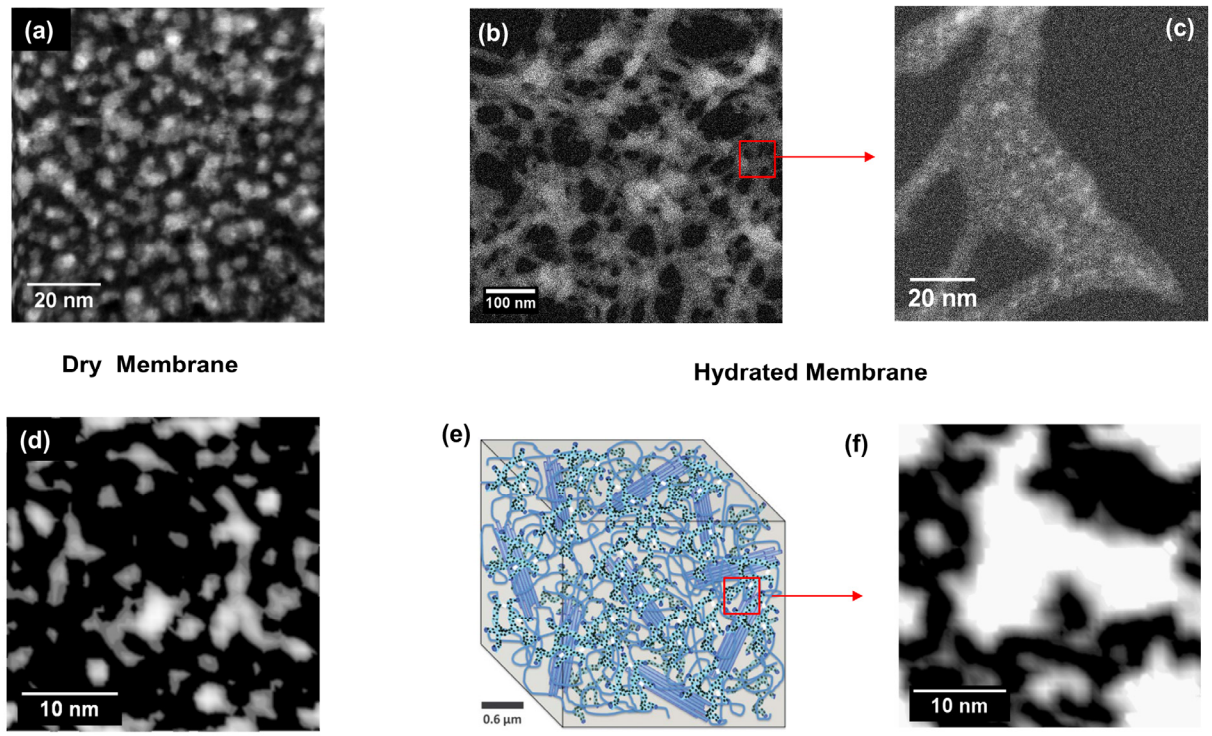

Figure 4.30. Comparison of Z-contrast images obtained from cryo-STEM and DPD simulation results for the same system: (a) Z-contrast image of dry 3M-636 ionomer; (b-c) Z-contrast images of hydrated 3M-636 ionomer prepared by cryo-plunger; (d) water distribution representation of the same ionomer at low water content ($\lambda = 6$) from our previous work[41]; (e) 'artist' depiction of the 3D continuous network (light blue regions) of ionic clusters (black dots) in a semi-crystalline fluorocarbon matrix (dark blue 'rods')[104]; (f) water distribution representation of the same ionomer under fully hydrated condition ($\lambda = 24$) from our prior simulations. [41]

As described in the SAXS models proposed by Gebel *et. al*,[95] the "structure inversion" occurs as water content increases due to the reorganization of swollen polymeric domains, leading to the entangled cylindrical polymer aggregates in dilute solution. However, this behaviour cannot be directly evidenced due to the difficulties in preparing fully hydrated ionomers (because of the build-up of frost on the surface of the grids during the cryo-plunge process). Although morphology of highly hydrated ionomers is unclear, the comparison of Z-contrast images for dry and partially hydrated ionomers clearly show the structural changes from isolated ionic clusters to continuous ionic channels in a semi-crystalline fluorocarbon matrix, which is consistent with DPD simulations[41] and simulated SAXS results[104] as shown in Figure 4.30 (d-f).

4.3.5 Elemental Mapping for Dry and Hydrated Membranes

Elemental mapping were performed in both TEM and STEM mode combined with EDS and EELS to identify the distribution of backbone and side chain elements in PFSA ionomers. The elemental mapping in polymers with EDS are challenging since characteristic X-rays signals generated from inelastic scattering are relatively weak for light elements that longer exposure is required, which introduces excessive radiation damages on samples. For this reason, the area of scanning for the EDS mapping is fairly large to prevent over exposure. In addition, 3M-636 samples seem more stable under electron beams, thus they were selected for the elemental mapping with EDS and EFTEM.

EDS maps of carbon, fluorine, oxygen and sulfur elements in hydrated 3M-636 ionomer are shown in Figure 4.31. The elemental maps indicate that PTFE backbones (with fluorine in green) occupy majority of sites forming a hydrophobic matrix while most of ionic clusters (with sulfur in yellow) are randomly distributed within the hydrophilic domains (with O in magenta).

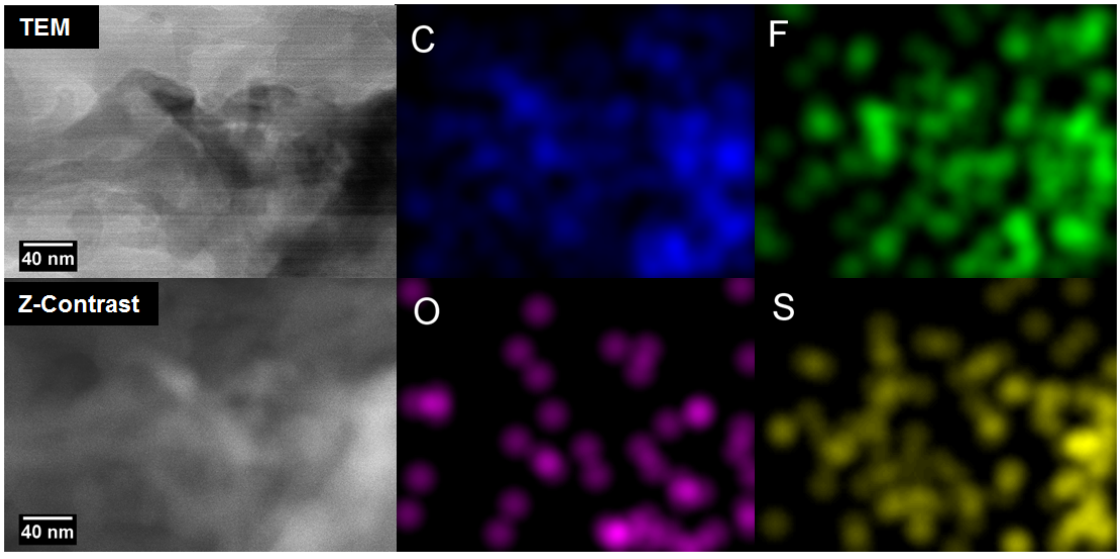

Figure 4.31. TEM and Z-Contrast images of cryo-plunged hydrated 3M-636 samples and corresponding EDS maps for carbon (blue), fluorine (green), oxygen (magenta) and sulfur (yellow).

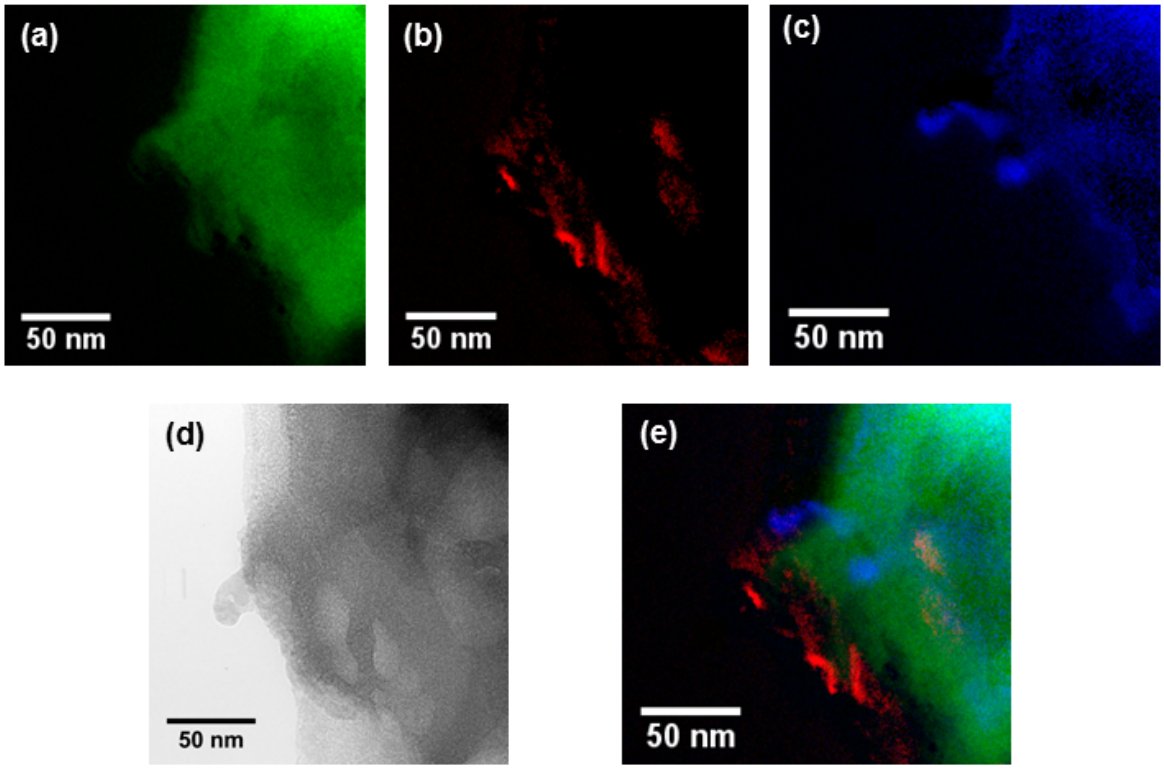

Figure 4.32. Cryo-EFTEM Map of cryo-plunged 3M-636 samples (a) C-K map; (b) S-L map; (c) O-L map; (d) Elastic filtered image and (e) composite RGB color map (green: carbon, red: sulfur, blue: oxygen).

As seen in Figure 4.32, elemental maps of carbon, sulfur and oxygen elements in hydrated 3M-636 are also collected by use of EFTEM in a cryo-TEM. The composite RGB color map shows how sulfonate groups (in blue) and water clusters (in red) are distributed in a PTFE matrix (in green). It reveals that the water clusters are more likely aggregate in the area where hydrophilic sulfonate groups accumulate. This is consistent with the EDS maps shown in Figure 4.31.

4.3.6 Summary

The HAADF and BF images of dry ionomer samples prepared by solution casting and thin sectioning confirm that crystallites in non-ion exchanged samples are solely due to the PTFE backbone in PFSA membranes. In addition, CaF_2 and KF crystallites are identified in Ca^{2+} and K^+ ion exchanged ionomers, which is caused by the electron damage of the sulfonate terminated

side chains. The images also show that the average crystallite size and areal density is higher for ionomers with short side chains and lower EW when compared to those of Nafion. There is an overall good agreement between the observed morphology from Z-contrast images for vacuum dried ionomer and the DPD simulation of hydrated equilibrium ionomers. The comparison between experiments and simulation shows that the microstructure of 3M and Aquivion membranes observed in dry state are mostly preserved in their partially hydrated states, while these microstructures are modified in dry Nafion as the addition of water content. An evidence of microstructural evolution in a hydrated ionomer is provided by cryo-STEM images of cryo-plunged 3M-636 samples. The qualitative comparison to the structural model derived from SAXS experiments confirms the presence of structural inversion of ionic clusters and web-like ionic channels in the hydrated condition.

4.4 EELS Investigations of Nafion and PTFE

In this part of study, the effects of side chains on the backbone conformations were investigated by electron energy loss spectroscopy in a TEM. Although many of studies have been focused on the structural and chemical properties of PFSA ionomers, most of efforts were made to understand the ionic aggregates while the information about backbone conformation and correlations to the effects of side chains are very limited. This is partially due to the difficulties to experimentally identify the changes associated with backbone structures under the influences of different length and chemistry of side chains. The present studies of optical properties and electronic structures of PTFE and Nafion using high resolution EELS provides a feasible way to determine the structural changes of backbones induced by side chains. In addition, *ab inito* DFT methods were employed to simulate the molecular conformation and polarization dependences of the low loss and core loss EELS and compare with experimental spectra. Several unknown

features were observed in the pre-plasmon region and the onset of carbon ionization edges. They are attributed to the presence of unique helical conformation and polarizability of PTFE chains in different thermally dependent crystalline phases.

This part is organized as follows. The first two sections contain detailed descriptions of experimental and simulation methods. The results are then presented and discussed in the following sections for comparable EELS results of Nafion and PTFE, EELS for different phases PTFE and effects of polarization on EELS of PTFE chains.

4.4.1 Experimental Details

Similar sample preparation protocols as described in the previous chapter were adopted to obtain thin sections of Nafion and PTFE by using ultramicrotome at temperatures below -80°C. The thickness of sections is typically in the range of 20~30 nm to ensure electron transparency and minimize multiple scattering effects in the resultant EELS spectra. The cryo-sectioned samples were collected on copper grids, warmed up to room temperature and then dried in vacuum for 24 hours. In this study, a 200 kV Zeiss Libra 200MC TEM-STEM equipped with monochromator was operated in the STEM mode to obtain EELS spectra with resolution of 0.15-0.3 eV (determined by the FWHM of the zero loss peaks). The electron dose used during EELS acquisition was less than 3×10^5 electrons/nm^2 to minimize the radiation damage of polymers.

4.4.2 Simulation Details

Ab inito DFT methods are now widely used to simulate and understand EELS spectra in both low loss and fine structures of core level excitations (i.e., ELNES).[146, 181, 182] In a DFT approach, ELNES is calculated under the assumption that the incoming and outgoing electrons are plane waves with wave vector $\mathbf{k}_i$ and $\mathbf{k}_f$. The differential cross section, which is the probability of scattering into a solid-angle element $d\Omega$ within an energy range of dE, is given by

$$\frac{d^2I}{d\Omega dE} = \frac{4\gamma^2}{a_0^2}\left|\frac{\langle f|\exp(i\mathbf{q}\cdot\mathbf{r})|i\rangle}{q^2}\right|^2, \tag{4.1}$$

where a_0 is the Bohr radius, γ is a relativistic correction factor, $\mathbf{q} = \mathbf{k}_f - \mathbf{k}_i$ is the momentum transfer vector of the incident electrons, $\mathbf{r}$ is the coordinate of the atomic electron excited, $|i\rangle$ and $|f\rangle$ represent the initial core level state and final unoccupied state in the conduction band. Thus, the fine structures of core level spectra can be calculated from the matrix elements determined by the relevant local angular-momentum-projected density of states.

In addition to the electronic structures and bonding information provided in ELNES, optical properties and inter-band transitions can be studied as well by EELS acquired in the low-loss region (<~50 eV). The low-loss part of the EELS spectrum can be described by the dielectric function ε as

$$\frac{d^2I}{d\Omega dE} \propto \mathrm{Im}\left(\frac{-1}{\varepsilon(\mathbf{q},E)}\right) = \frac{\varepsilon_2}{\varepsilon_1^2+\varepsilon_2^2}, \tag{4.2}$$

where the term $\mathrm{Im}(-1/\varepsilon)$ is called energy loss function (ELF) and ε_1 and ε_2 are the real and imaginary part of dielectric function. The dielectric function describes the response of the material to a time-dependent electromagnetic field. The polarizability of the system then can be treated as a sum over independent transitions with the random phase approximation. As shown in Figure 4.33, four crystalline phases representing different conformations of PTFE chains at various temperatures were used in simulations. Helical PTFE polymer chains were packed into hexagonal unit cells as illustrated in Figure 4.34. The structural parameters of thermally dependent phases of PTFE are listed in Table 4.7.

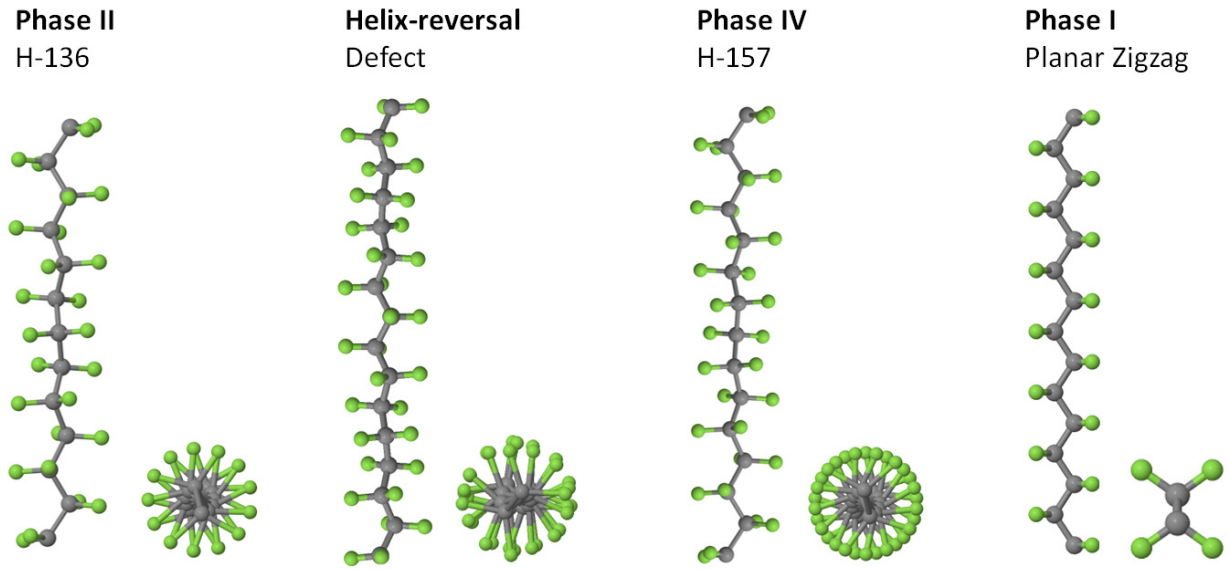

Figure 4.33. Molecular structures of PTFE chains in different polymorphic phases as temperature increases from 19 °C to 330 °C.

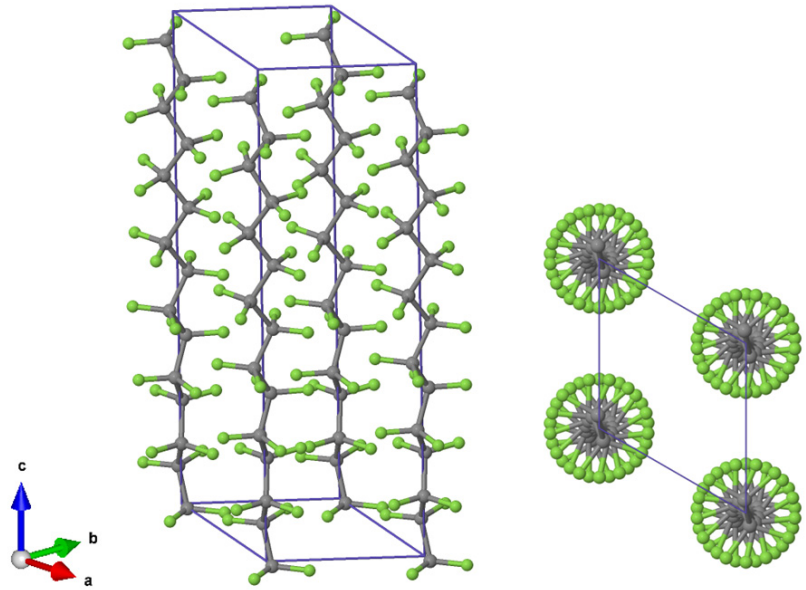

Figure 4.34. Unit cell structure of PTFE H-157, where helical PTFE chains are oriented in the direction of *c* axis.

The rigid-rod-like helical polymer chains are formed by the fluorine atoms rotating helically on the surface. The PTFE chains are aligned in the direction *c* axis leading to a highly oriented crystalline structure as shown in Figure 4.34.

Table 4.7. Structural parameters of temperature dependent phases of PTFE

Temp.	Phase	Molecular conformation	Unit cell parameters [a,b]
< 19°C	II	H136	$a=b$=5.54, c=17.06
			$\alpha=\beta$=90, γ=120
	Disordered	Helix-reversal Defect	$a=b$=5.70, c=20.60
			$\alpha=\beta$=90, γ=120
19-30°C	IV	H157	$a=b$=5.66, c=19.71
			$\alpha=\beta$=90, γ=120
30-330°C	I	Planar Zigzag	a=7.50, b=5.60, c=5.30
			$\alpha=\beta=\gamma$=90

[a] *a, b, c in* angstroms (Å); α, β, γ in degrees (°)
[b] Structural parameters taken from reference[183, 184]

The simulated EELS spectra presented here were performed using the pseudopotential DFT code CASTEP[185] which uses the random phase approximation (RPA) to calculate dielectric functions. The plane wave cut-off energy was chosen to be around 610 eV. Brillouin zone was sampled using Monkhorst-Pack scheme with maximum k-spacing of 0.07Å^{-1} for the ground state calculations and 0.04 Å^{-1} for the EELS calculations. The simulations were carried out with On-the-fly (OTF) pseudopotential using the GGA-PBEsol[186] exchange-correlation functional. The polarization of the electromagnetic field was taken into account by varying the directions of the electric field vector of the incident electrons. The momentum transfer vector **q** are chosen to be in the direction of [1 0 0], [0 1 0] and [0 0 1] for polarized systems. The three directional components were then averaged to simulate the optical response for polycrystalline systems. The instrumental smearing of 0.15eV and lifetime broadening of 0.17eV were both considered to

simulate core level spectra. The Gaussian broadening of 0.15eV was also applied to the simulated low loss spectra.

4.4.3 EELS of Nafion and PTFE

Figure 4.35 (a) shows EELS spectra of Nafion and PTFE in the low loss region (0-30 eV) acquired at the same experimental conditions followed by the removal of zero-loss and multiple scattering contributions. The bulk plasmon peaks (denoted as *e*) are found at 22.25 eV and 21.87 for Nafion and PTFE, respectively. Since the position and intensity of a plasmon peak are considered as a measure of the density of all valence electrons in materials, the 0.4 eV shift of plasmon peaks indicates the possible structural variations of Nafion backbones and pristine PTFE. Several pre-plasmon features in the range from 10 to 20 eV are also observed. Although these features have been seen in other polymers such as polystyrene and polyethylene, their contributions are often too weak to be analyzed correctly.[147, 187, 188] In both pristine PTFE and Nafion, we found well-defined peaks *c* and *d* with a separation of about 4 eV. These features can be attributed to the collective oscillations of valence electrons in σ and π bondings. In the range of 5-10 eV, the presence of two adjacent peaks is considered relating to the interband transitions (from occupied valence band to unoccupied conduction band). The peaks positioned in this range are often characterized as π^* excitations often seen in conjugated or aromatic polymers. These features are also observed for saturated linear polymers (such as PE) with high electron dose and are usually assigned as the degradation products containing unsaturated bonds in backbones.[187, 189] However, a series of tests with different electron dose show that these two peaks in Nafion and PTFE are not very sensitive to the electron radiation and are possibly related to the unique helical structures of PTFE chains. Moreover, different relative intensities of peaks *a* and *b* are

observed in Nafion and PTFE, which indicate potential changes of backbone structures in Nafion as compared to PTFE.

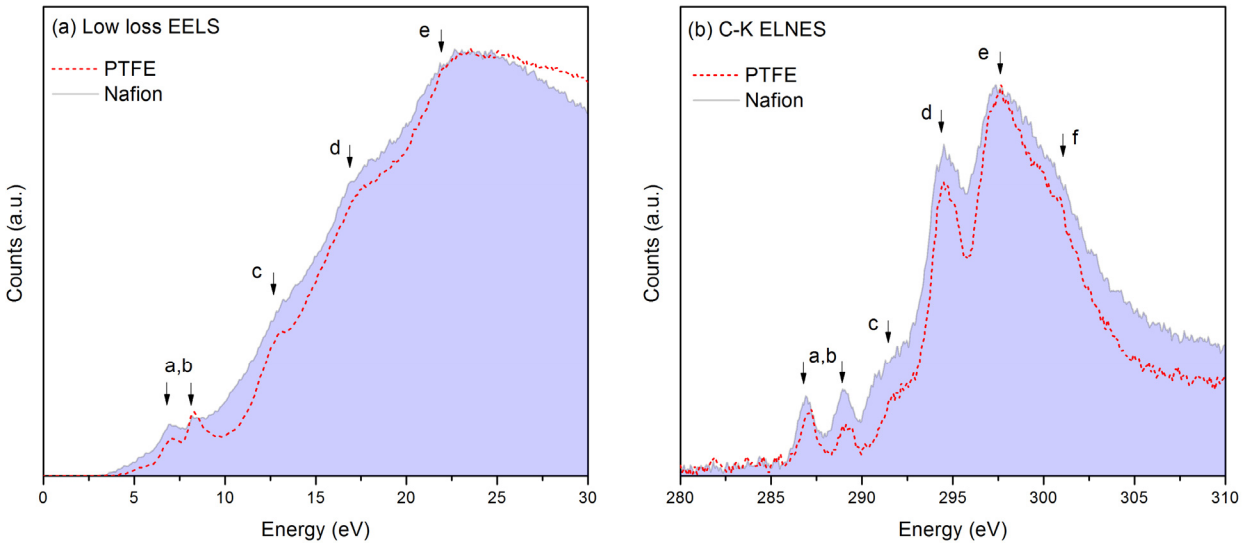

Figure 4.35. Comparison of EELS spectra of Nafion and PTFE acquired in the same experimental conditions: (a) low-loss (0-30eV); and (b) C-K ELNES (280-310 eV)

Fine structures of carbon K edges of Nafion and PTFE followed by background subtractions and multiple scattering removals are represented in Figure 4.35 (b). Six characteristic peaks and shoulders in the range of 280-310 eV are observed in Nafion and PTFE. The first two peaks (*a* and *b*) in the range of 285-290 eV are seen with a constant separation of about 2 eV. These features can be explained as the 1s→π* core electron excitations that are consistent with the first two valence excitation peaks observed in the low-loss region. The third peaks at 292 eV are mostly broadened indicating it is correlated to the overlap of conduction bands. The most pronounced peaks (*d* and *e*) can be assigned as the result of 1s→σ* excitations in C-F and C-C bondings. The attenuated peak *f* is considered as the part of EXELFS due to the nearest neighboring carbon atoms. Similar to the observations in low loss region, the relative intensities of peak *a* and *b* are sensitive to the structures of PTFE backbones.

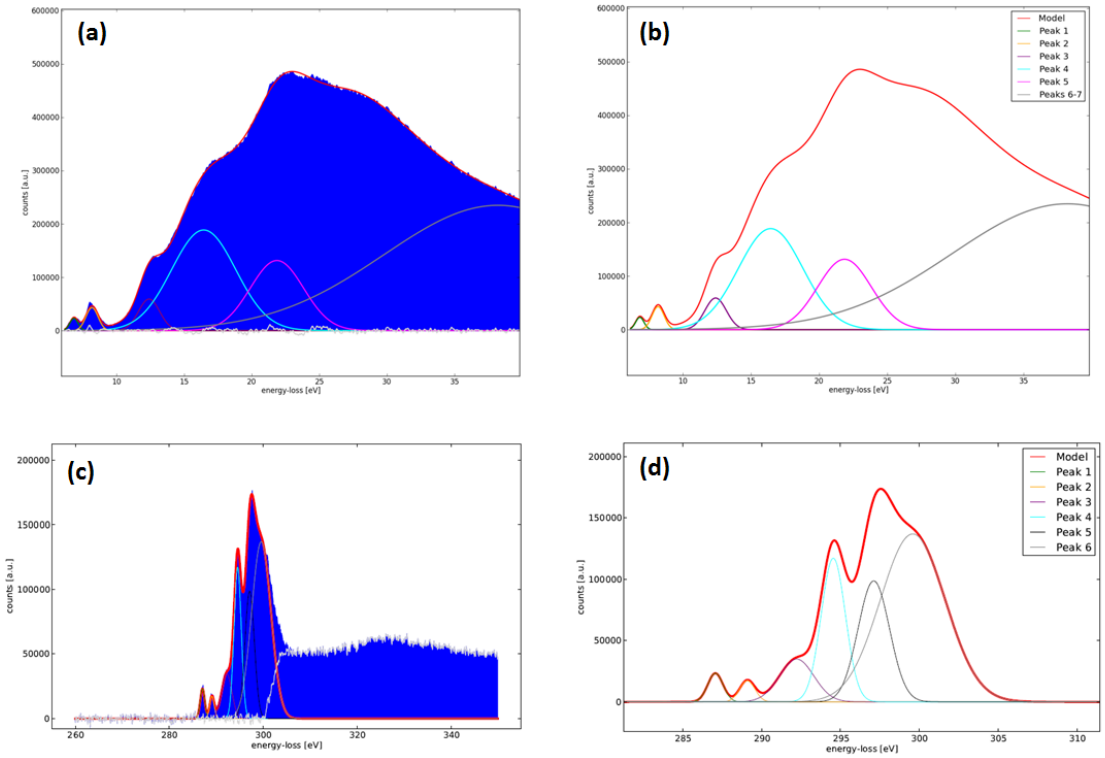

Figure 4.36. Quantitative analysis and fitting of EELS for PTFE: (a-b) Low loss; (c-d) Core loss C-K ELNES

Table 4.8. Peak analysis of fitted EELS spectra for PTFE

	Low Loss		C-K ELNES	
Peak #	Position (eV)	FWHM (eV)	Position (eV)	FWHM (eV)
1	6.85	0.72	287.06	1.13
2	8.19	1.05	289.08	1.14
3	12.41	1.85	292.22	2.57
4	16.45	5.59	294.54	1.82
5	21.87	4.65	297.11	2.35
6			299.58	4.85

The EELS spectra from experiments are then fitted with Gaussian functions as shown in Figure 4.36. A total of seven and six Gaussian functions were used to fit low-loss and core loss portions

of spectra for PTFE. As seen Figure 4.36 (a) and (c), the same level of noise (i.e., difference between experimental and modeled spectra) is observed in the background and fine structures regions. This indicates that experimental spectra can be well represented by the fitted curves with a minimized noise level. The peak positions and widths to fit the spectra are listed in Table 4.8.

4.4.4 Effect of Phase Transition

The structures and complex polymorphic behaviour of PTFE has been investigated by X-ray diffraction[190-192], electron microscopy[140, 193] and DFT calculations[184, 194, 195]. At atmospheric pressure, PTFE shows a unique crystalline phase transitions as temperature increases from 19 °C to melting point of 330 °C as shown in Figure 4.33. When temperature is below 19 °C, the structure is stabilized as Phase II (H136), where fluorine atoms rotate 6 turns as CF_2 groups repeat 13 times; Phase II transfers to Phase IV (H157) involving 15 CF_2 groups in 7 turns at 30 °C and converts to Phase I with planar zigzag as temperatures approaching melting point of 330 °C. Disordered phase with helix-reversal defects is also observed at room temperatures where the polymer chain incorporates a portion of helical structures in both H136 and H157 conformations with reversal rotations, which is called a helix-reversal defect.

Since the experimental EELS are sampled from a relatively large area of imperfect PTFE sample at room temperature, it is difficult to identify the specific features that correspond to the structures in a single phase. To investigate how the conformational changes in different phases is related to characteristic EELS spectra, both low loss and C-K ELNES are calculated for different phases and compared with experimental results as seen in Figure 4.37 (a) and (b).

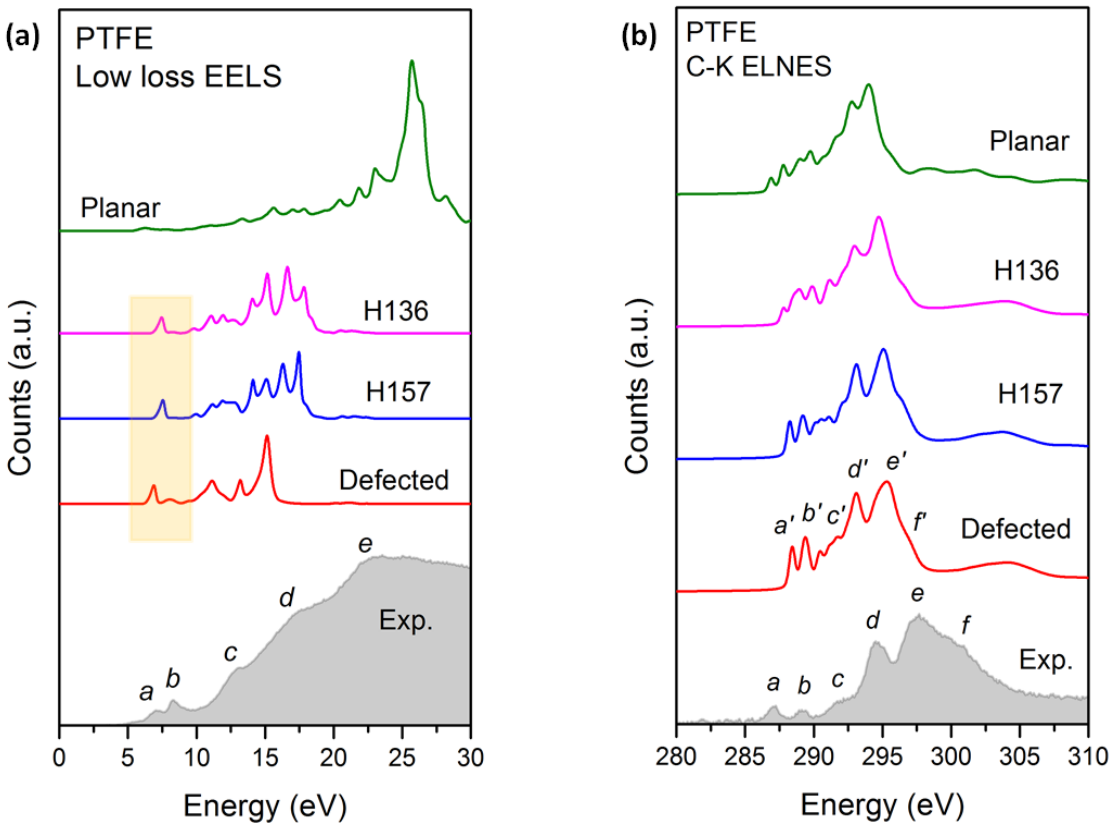

Figure 4.37. Simulated low loss and carbon K-shell excitation spectra for PTFE with different conformation (planar, H136, H157 and defected) are compared with experimental results.

As shown in Figure 4.37 (a), the slightly shifted bulk plasmon peak is only observed in simulated spectrum from planar conformation. Although the splitting of first two peaks are not well resolved, simulated spectra for H136, H157 and defected conformations have all reproduced several pre-plasmon features and the peak in the interband transitions region as highlighted in the figure. It indicates that the appearance of unknown features in the pre-plasmon region should be closely related to the unique helical conformation of PTFE chains. Calculated dielectric functions and energy loss functions of different conformations are also plotted in Figure 4.38 for further investigations.

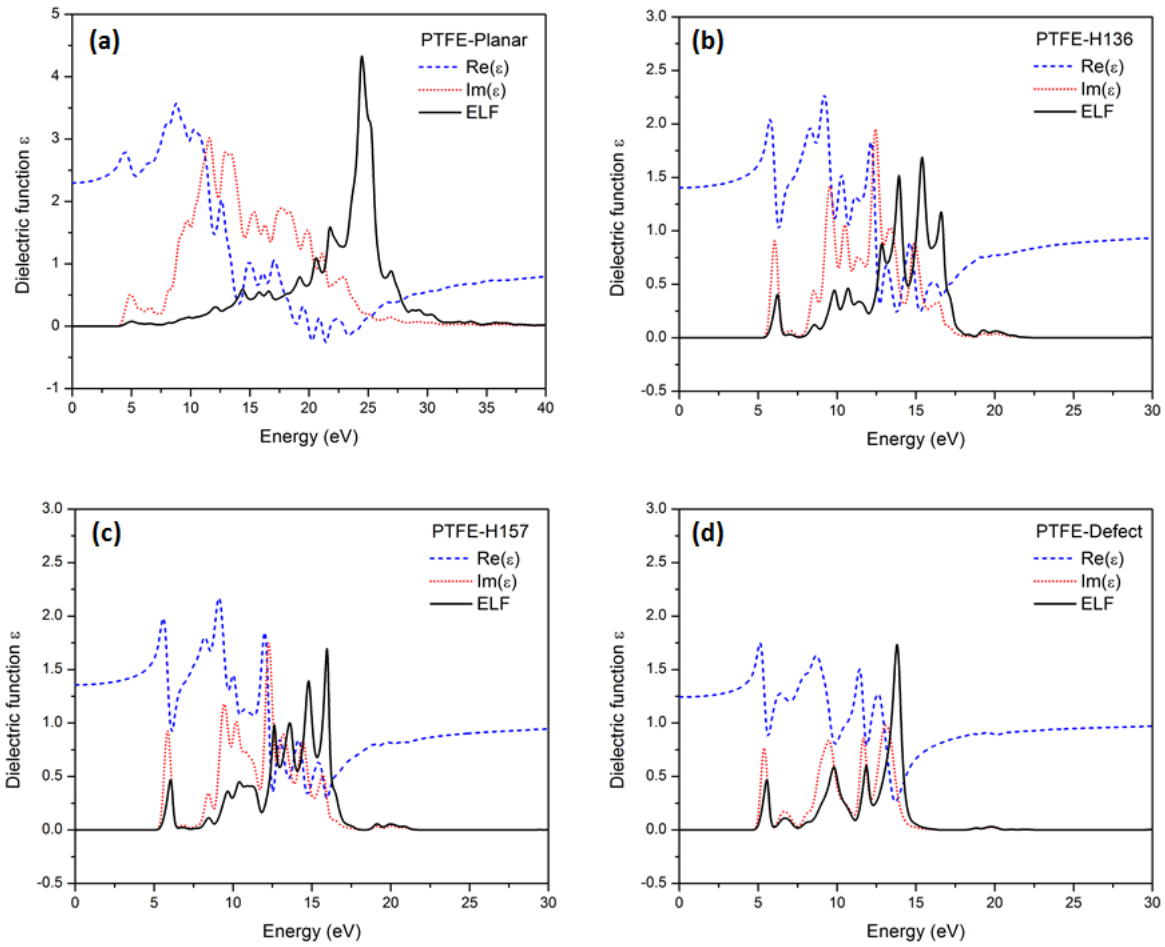

Figure 4.38. Real and imaginary part of dielectric functions ε and corresponding energy loss function for PTFE with different conformations.

In Figure 4.38 (a), the most intense peak in ELF is the bulk plasmon peak corresponding to Re(ε) crossing zero with a positive slope when Im(ε) is small. The presence of interband transitions around 6 eV are well simulated as seen in Figure 4.38 (b-d), where the Re(ε) are close to 1 and the energy is just below the energy of the peak in Im(ε).Several features in the range of 10-20 eV are also found, they are more likely to resemble the behavior of plamson oscillations rather than the interband transitions.

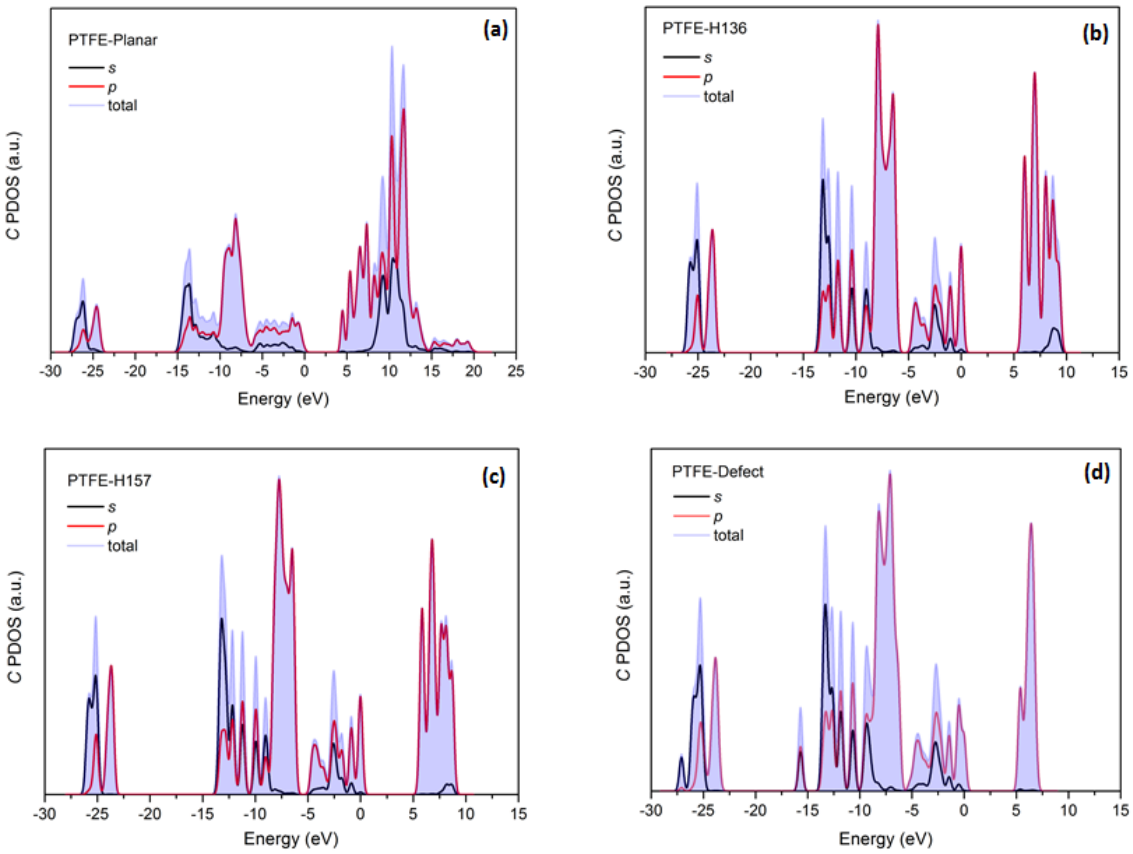

Figure 4.39. Projected Density of States (PDOS) of carbon calculated from band structure calculations for PTFE with different conformations

For core level C-K fine structures showing in Figure 4.37 (b), an overall good agreement is found between the simulated spectra for helical structures and experimental ELNES. The peaks observed for the defected structures resemble all features found in the experiment with a slightly narrowed energy range possibly due to the other broadening factors from the instruments. In ELNES, the unoccupied states and the bonding due to valence electrons can be measured by the projected density of states (PDOS) of the given atom. On the other hand, transitions by the valence electrons and collective oscillations of the valence electrons can be measured in low-loss EELS, which are related to the joint density of states (JDOS) of occupied and unoccupied electron states.

As illustrated in Figure 4.39, PTFE with helical conformations exhibit nearly identical DOS for the occupied states. The only noticeable difference between ordered (b and c) and disordered (d) helical structures is the increasingly suppressed *s* orbital and narrowed *p* orbital contributions in the conduction bands as the increasing length of chain. This is consistent with the sharpest peaks appeared in defected structures as seen in Figure 4.38 (b).

4.4.5 Polarization Dependence

For the anisotropic crystalline structures such as PTFE, the matrix element shown in Equation (4.1) will depend on the direction of momentum transfer **q** relative to the orientation of polymer chain axis (i.e., the crystal axis *c*). Considering a relatively large collection angle is used to acquire EELS in the electron microscope, the angular and momentum dependent EELS cannot be well resolved experimentally. Therefore, experimental spectra presented here contain information both from the longitude ($\mathbf{q} \parallel c$) and transverse ($\mathbf{q} \perp c$) components.

As discussed in the previous section, the comparison between experimental and simulated low loss EELS indicates that the characteristic peaks representing interband transitions are associated with the helical conformations of PTFE chains. The **q** dependence analysis of low loss EELS are now studied by decoupling the spectra into three polarized components in the directions of crystal axis as illustrated in Figure 4.34. Very weak polarization effects are detected in planar structure mainly due to the highly symmetric orientation of CF_2 groups. In contrary, a strong dependence of the directional **q** vector is found in the helical conformation, where the interband transition peak appeared at 6 eV is only seen in the excitation when incident electrons are parallel to the chain orientation. This behavior is also observed in other two conformations with helical backbones as seen in appendix.

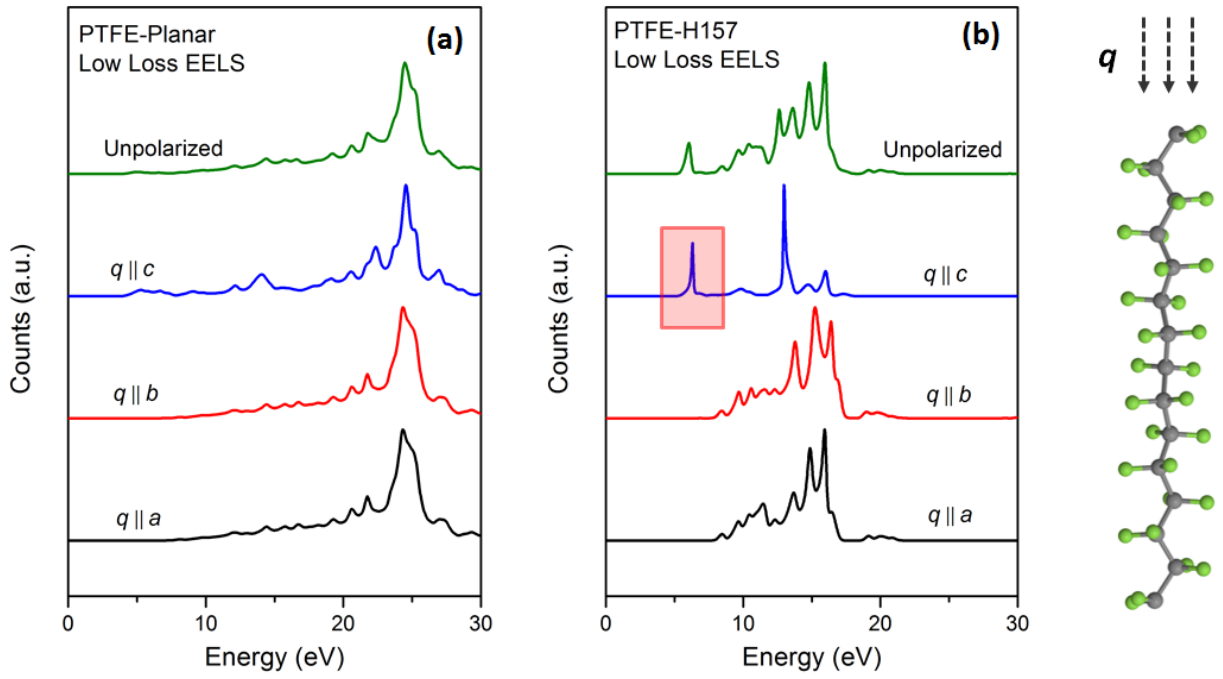

Figure 4.40. Calculated low loss EELS as a function of the direction of momentum vector q for (a) planar PTFE and (b) helical H157 PTFE. The highlighted area shows the characteristic peak at 6 eV corresponding to the longitude component of polarization ($\mathbf{q} \parallel c$) illustrated on the right.

Since the bondings in anisotropic PTFE Bonds are highly directional, the direction of corresponding orbital amplitude maximum on the excited atom determines the angular dependence of the K-shell spectra. The intensity of a resonance is largest when the electric field vector **E** lies along the direction of the final state bonding, and vanishes when **E** is perpendicular to it. Therefore, when incident beam is parallel to the chain axis ($\mathbf{q} \parallel c$), the σ* resonance is maximized for the bonding in the C-F direction while attenuated in the C-C direction. This effect is reversal the incident beam is applied in the direction perpendicular to the chain axis ($\mathbf{q} \perp c$).

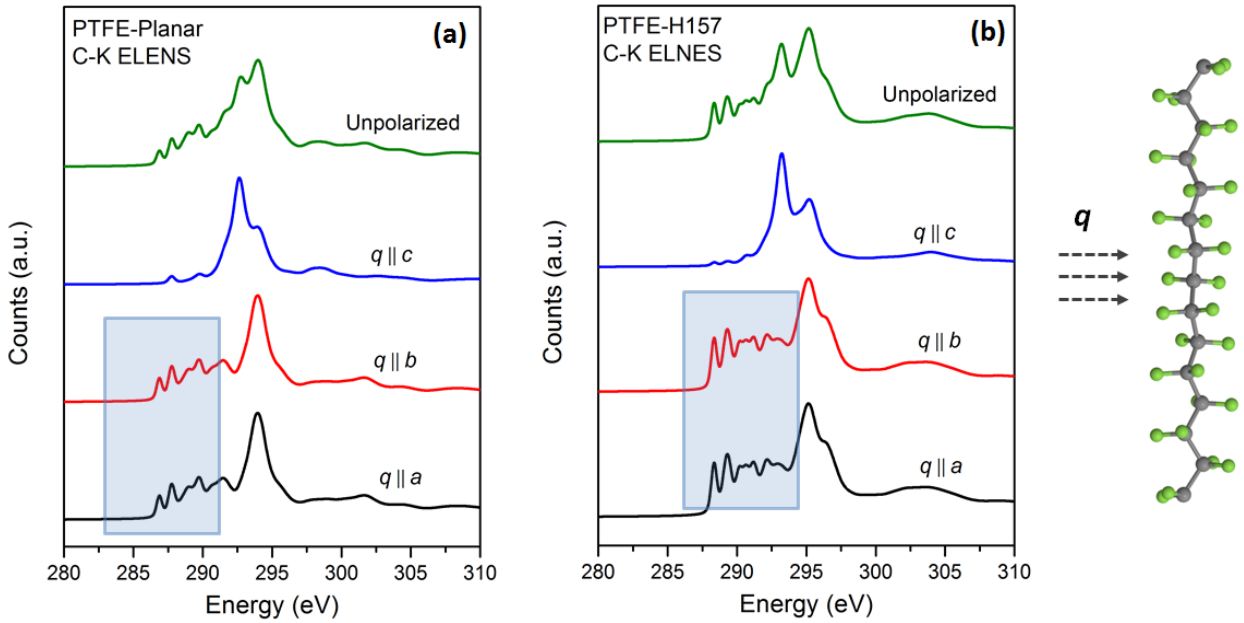

Figure 4.41. Calculated C-K ELNES as a function of the direction of momentum vector **q** for (a) planar PTFE and (b) helical H157 PTFE. The highlighted areas show the characteristic features in the range of 287-295 eV that are correlated with transverse component of polarization $\mathbf{q} \perp c$ illustrated on the right.

The effects of directional **q** vectors are represented in Figure 4.41 for both planar and helical conformations. Two strongest peaks at 293.2 and 295.3 eV are highly dependent upon the direction of **q** in both conformations. The peak at 293.2 eV is assigned to be the 1s→σ* transition due to the C-F bonding since it becomes dominant when $\mathbf{q} \parallel c$. In contrary, the peak at 295.3 eV is attributed to the 1s→σ* transition corresponding to C-C bonding which is maximized as $\mathbf{q} \perp c$. These assignments are in consistent with the previous NEXAFS studies of orientation of PTFE thin films.[196-198] Several features appeared in the fine structures of ionization edges (287-295eV) are seen in both conformations when **q** is perpendicular to the chain orientation. The first two peaks at around 287eV become more pronounced for the helical structures, which resemble the experimentally determined ELNES in the same range. Considering the highly polarized C-F bond and oriented C-C backbone, these features can be

interpreted as the results of the significant dipole contributions from the alternating C-F bonds in chains. The asymmetric helical structure may enhance this effect by introducing the helix dipole along the chain. The least symmetry in defected helical conformation shows the sharpest doublet peaks as seen in the appendix.

4.4.6 Summary

Nafion and pristine PTFE both consist of the same backbone structures are studied by electron energy loss spectroscopy (EELS) in the low loss and core loss regions. The experimentally determined EELS spectra show similar features in low loss and C-K ELNES spectra of these polymers. Different relative intensities of the first two characteristic peaks in the lower portion of spectra are observed in Nafion and PTFE, which indicates the possible structural changes of backbones in Nafion affected by the side chains.

In order to characterize several features that are first observed in EELS spectra of PTFE, *ab initio* DFT methods are employed to simulate EELS for several thermally dependent phases of PTFE crystals. The comparison of low loss EELS for different phases shows that the peaks corresponding to the interband transitions at 6 eV are highly dependent on the helical structures of backbone. The PTFE that contains helix-reversal defects is proven to resemble the experimental ELNES for C-K edge very well. The investigations of dielectric functions for different phases confirm the existence of quasi-plasmon features in the range of 20-30 eV for helical PTFE. In addition, projected density of states (PDOS) of carbon is calculated to evaluate the *s* orbital contribution to the total DOS. The generally sharper peaks appeared in the onset C-K edges for helical conformations can be ascribed to the suppressed *s* orbital DOS.

The polarization dependence of EELS is also investigated by varying the directions of the momentum vector **q** in incident electrons. Strong dependence of **q** directions in low loss region is

found in the helical structures, where the interband transition peaks only occur when electrons lie in the direction of chain orientation. Two major peaks residing at 293.2 and 295.3 eV are assigned as $1s \rightarrow \sigma^*$ transitions belonging to C-F bonding and C-C bonding, respectively. Presence of doublet peaks appeared at about 287 eV is interpreted as the results of the helix dipole induced by the highly polarized C-F bonds and the asymmetric helical conformation.

Chapter 5 Conclusions

As power generating devices that are both highly efficient and environmentally friendly, PEMFCs are considered to be promising candidates for automobiles and portable device applications. An electrolyte membrane exhibiting high proton conductivity is an important component that impacts the efficiency of a PEMFC, and consequently, numerous studies have been undertaken for the development of new membrane materials. PFSA ionomers, such as Nafion, are commonly used as the electrolyte materials that exhibit high proton conductivity in a fully hydrated environment. A novel class of sulfonated poly(phenylene) sulfone ($sPSO_2$) ionomers consisting of aromatic rings and sulfone units ($-SO_2-$) have recently been synthesized and characterized. These ionomers show not only considerable thermooxidative and hydrolytic stability but also much higher proton conductivity than observed in Nafion at elevated temperatures. In this dissertation, both computational and experimental methods were used to understand the proton transport, morphological and structural properties of sulfonated polysulfone ($sPSO_2$) and PFSA ionomers.

We have undertaken *ab initio* electronic structure calculations in the first part of dissertation to understand the local hydration and proton transfer characteristics of $sPSO_2$ ionomers. The primary hydration and energetics associated with the transfer of protons in oligomeric fragments of two $sPSO_2$ ionomers were evaluated. Our results indicate that the interaction between neighboring sulfonic acid groups affect both the conformation and stability of the fragments. The number of water molecules required to affect the transfer of a proton in the first hydration shell was observed to be a function of the hydrogen bonding in proximity of the sulfonic acid groups: 3 H_2O for the *meta*- and 4 H_2O for the *ortho*-conformations. Calculations of the rotational energy surfaces indicate that the aromatic backbones of $sPSO_2$ are much stiffer than the

polytetrafluoroethylene (PTFE) backbones in PFSA ionomers: the largest energy penalty for rotating phenylene rings (i.e., 15.5 kcal/mol for *ortho-ortho* sPSO2) is nearly twice that computed for the rotation of a CF_2 unit in a PTFE backbone. The energetics for the transfer of various protons in proximity to one or two sulfonate groups ($–SO_3–$) was also determined. The computed energy barrier for proton transfer when only one sulfonic acid group is present is approximately 1.9 kcal/mol, which is 2.1 kcal/mol lower than similar calculations for PFSA systems. When two sulfonic acid groups are bridged by water molecules, a symmetric bidirectional transfer occurs, which gives a substantially small energy barrier of only 0.7 kcal/mol.

In addition to proton transport and structural properties studied in the first part, we have also carried out mesoscale DPD simulations to investigate hydrated morphology of the polysulfone ionomers as a function of EW, MW and water content. The simulations show that the water clusters are more likely to be equally distributed into hydrophilic domains for $sPSO_2$ ionomers at low hydration levels. The well-connected water channels are gradually developed among water clusters with the increasing water content. This is in contrast to PFSA ionomers where strong phase separation occurs at high hydration levels and results in large water clusters that lack adequate connectivity. The effects of EWs and MWs on swelling properties of hydrated $sPSO_2$ ionomers are also investigated. As the fraction of sulfonate groups increases (i.e., decrease in EW), the water is more dispersed and less dependent upon the hydration level. The highly sulfonated ionomers (i.e., $sPSO_2$-220 and $sPSO_2$-360) establish water connected pathways for proton conduction even at relatively low water contents. Smaller water channels are formed among hydrophilic regions in the $sPSO_2$-220 ionomer, the sizes of which are estimated to be from 1.2 to 1.5 nm (compared to Nafion with ~3.5 nm) at a water content where λ=7. This

property suggests the potentially high proton conductivity of this ionomer may be due to the well-connected hydrophilic pathways. The growth of water clusters is also affected by the MW. For $sPSO_2$ ionomers with high EW, higher MW tends to decrease the size of the water clusters when at similar water content. Endpoint distance distributions of the backbones were also calculated for the $sPSO_2$ and PFSA ionomers to study the chain aggregation and flexibility. Ionomer backbones with a high degree of sulfonation such as $sPSO_2$-220 are expected to expand to a greater extent under highly hydrated conditions, which leads to a well dispersed water distribution in the ionomer. In contrast, ionomers with a lower number of sulfonate groups (such as $sPSO_2$-1014 and PFSA ionomers) tend to form a strong phase separation partially due to the backbone aggregation at high hydration level.

In order to understand the microstructure of hydrated PFSA ionomers and relevant features that determine proton conductivity, we have used various electron microscopy techniques to visualize and characterize morphological changes of the ionomers as a function of water content. The HAADF and BF images of dry ionomer samples prepared by solution casting and thin sectioning confirm that crystallites in non-ion exchanged samples are solely due to the PTFE backbone in PFSA membranes. In addition, CaF_2 and KF crystallites are identified in Ca^{2+} and K^+ ion exchanged ionomers, which is caused by the electron damage of the sulfonate terminated side chains. The images also show that the average crystallite size and areal density is higher for ionomers with short side chains and lower EW when compared to those of Nafion. There is an overall good agreement between the observed morphology from Z-contrast images for vacuum dried ionomer and the DPD simulation of hydrated equilibrium ionomers. The comparison between experiments and simulation shows that the microstructure of 3M and Aquivion membranes observed in dry state are mostly preserved in their partially hydrated states, while

these microstructures are modified in dry Nafion as the addition of water content. An evidence of microstructural evolution in a hydrated ionomer is provided by cryo-STEM images of cryo-plunged 3M-636 samples. The qualitative comparison to the structural model derived from SAXS experiments confirms the presence of structural inversion of ionic clusters and web-like ionic channels in the hydrated condition.

High resolution electron energy loss spectroscopy in a TEM was employed to determine the effects of the side chains on the backbone conformations of PFSA ionomers. Nafion and pristine PTFE both consist of the same backbone structure and were examined by EELS in the low loss and core loss regions. The experimentally determined EELS spectra show similar features in low loss and C-K ELNES spectra of these polymers. Different relative intensities of the first two characteristic peaks in the lower portion of the spectra are observed in Nafion and PTFE, which indicates the possible structural variations of the backbones in Nafion are due to the presence of the side chains. Several features that are first observed in the EELS spectra of PTFE were further studied and simulated with *ab initio* DFT methods. The low loss EELS spectra for different phases of PTFE show that the peaks corresponding to the interband transitions at 6 eV are highly dependent on the helical structure of the backbone. The simulated spectrum of PTFE contains helix-reversal defects and is proven to resemble the experimental ELNES for C-K edge very well. Investigation of the dielectric functions for the different phases confirms the existence of quasi-plasmon features in the range of 20-30 eV for helical PTFE. The polarization dependence of EELS is also investigated by varying the direction of the momentum vector **q** in incident electrons. Strong dependence of the **q** direction in the low loss region is found in the helical structures, where the interband transition peaks only occur when electrons lie in the direction of chain orientation. Two major peaks residing at 293.2 and 295.3 eV are assigned as $1s \rightarrow \sigma^*$

transitions belonging to C−F bonding and C−C bonding, respectively. The presence of doublet peaks appeared at about 287 eV is interpreted as the result of the helix dipole induced by the highly polarized C−F bonds and the asymmetric helical conformations.

In summary, the results obtained in this study suggest that information concerning structure-property relationships in the materials systems considered (i.e., polysulfone and PFSA ionomers) is the key for successful application of these materials as the PEM in a fuel cell. The multiscale simulations and analytical electron microscopy techniques together provide not only the knowledge of their essential properties but also the directions for further improvements.

References

1. Y. Shao, G. Yin, Z. Wang and Y. Gao, *Journal of Power Sources*, 2007, **167**, 235-242.

2. B. Smitha, S. Sridhar and A. A. Khan, *Journal of Membrane Science*, 2005, **259**, 10-26.

3. K. D. Kreuer, S. J. Paddison, E. Spohr and M. Schuster, *Chemical Reviews*, 2004, **104**, 4637-4678.

4. P. Costamagna and S. Srinivasan, *Journal of Power Sources*, 2001, **102**, 242-252.

5. M. A. Hickner and B. S. Pivovar, *Fuel Cells*, 2005, **5**, 213-229.

6. B. C. H. Steele and A. Heinzel, *Nature*, 2001, **414**, 345-352.

7. N. P. Brandon, S. Skinner and B. C. H. Steele, *Annual Review of Materials Research*, 2003, **33**, 183-213.

8. M. Doyle and G. Rajendran, *Handbook of Fuel Cells-Fundamentals Technology and Applications*, John Wiley & Sons, Chichester, UK, 2003.

9. K. D. Kreuer, *Handbook of Fuel Cells-Fundamentals Technology and Applications*, John Wiley & Sons, Chichester, UK, 2003.

10. G. Alberti, M. Casciola, U. Costantino, R. Narducci, M. Pica and M. Sganappa, *Desalination*, 2006, **199**, 4-5.

11. M. E. Schuster and W. H. Meyer, *Annual Review of Materials Research*, 2003, **33**, 233-261.

12. J. Roziere and D. J. Jones, *Annual Review of Materials Research*, 2003, **33**, 503-555.

13. S. J. Paddison, *Device and Materials Modeling in PEM Fuel Cells*, Springer, New York, NY, 2009.

14. J. Jagur-Grodzinski, *Polymers for Advanced Technologies*, 2007, **18**, 868-868.

15. M. A. Hickner, H. Ghassemi, Y. S. Kim, B. R. Einsla and J. E. McGrath, *Chemical Reviews*, 2004, **104**, 4587-4611.

16. H. R. Allcock and R. M. Wood, *Journal of Polymer Science Part B: Polymer Physics*, 2006, **44**, 2358-2368.

17. N. G. Boyle, V. J. McBrierty and D. C. Douglass, *Macromolecules*, 1983, **16**, 75-80.

18. C. Yang, P. Costamagna, S. Srinivasan, J. Benziger and A. B. Bocarsly, *Journal of Power Sources*, 2001, **103**, 1-9.

19. S. J. Paddison and R. Paul, *Physical Chemistry Chemical Physics*, 2002, **4**, 1158-1163.

20. R. B. Moore III and C. R. Martin, *Macromolecules*, 1989, **22**, 3594-3599.

21. M. Schuster, K.-D. Kreuer, H. T. Andersen and J. Maier, *Macromolecules*, 2007, **40**, 598-607.

22. C. C. de Araujo, K. D. Kreuer, M. Schuster, G. Portale, H. Mendil-Jakani, G. Gebel and J. Maier, *Physical Chemistry Chemical Physics*, 2009, **11**, 3305-3312.

23. M. Schuster, C. C. de Araujo, V. Atanasov, H. T. Andersen, K.-D. Kreuer and J. Maier, *Macromolecules*, 2009, **42**, 3129-3137.

24. T. J. F. Day, U. W. Schmitt and G. A. Voth, *Journal of the American Chemical Society*, 2000, **122**, 12027-12028.

25. M. Tuckerman, K. Laasonen, M. Sprik and M. Parrinello, *J. Phys. Chem.*, 1995, **99**, 5749-5752.

26. W. Münch, K. D. Kreuer, W. Silvestri, J. Maier and G. Seifert, *Solid State Ionics*, 2001, **145**, 437-443.

27. M. Eikerling, A. A. Kornyshev, A. M. Kuznetsov, J. Ulstrup and S. Walbran, *J. Phys. Chem. B*, 2001, **105**, 3646-3662.

28. K. A. Mauritz and R. B. Moore, *Chemical Reviews*, 2004, **104**, 4535-4585.

29. T. D. Gierke, G. E. Munn and F. C. Wilson, *Journal of Polymer Science Part B: Polymer Physics*, 1981, **19**, 1687-1704.

30. E. J. Roche, M. Pineri and R. Duplessix, *J. Polym. Sci. : Polym. Phys. Ed.*, 1982, **20**, 107-116.

31. G. Gebel and R. B. Moore, *Macromolecules*, 2000, **33**, 4850-4855.

32. H. G. Haubold, T. Vad, H. Jungbluth and P. Hiller, *Electrochimica Acta*, 2001, **46**, 1559-1563.

33. P. Aldebert, B. Dreyfus and M. Pineri, *Macromolecules*, 1986, **19**, 2651-2653.

34. A. L. Rollet, G. Gebel, J. P. Simonin and P. Turq, *J. Polym. Sci. Pt. B-Polym. Phys.*, 2001, **39**, 548-558.

35. M. H. Kim, C. J. Glinka, S. A. Grot and W. G. Grot, *Macromolecules*, 2006, **39**, 4775-4787.

36. M. Bass, A. Berman, A. Singh, O. Konovalov and V. Freger, *J. Phys. Chem. B*, 2010, **114**, 3784-3790.

37. D. Y. Galperin and A. R. Khokhlov, *Macromolecular Theory and Simulations*, 2006, **15**, 137-146.

38. J. T. Wescott, Y. Qi, L. Subramanian and T. W. Capehart, *Journal of Chemical Physics*, 2006, **124**, 134702.

39. D. S. Wu, S. J. Paddison and J. A. Elliott, *Energy & Environmental Science*, 2008, **1**, 284-293.

40. D. S. Wu, S. J. Paddison and J. A. Elliott, *Macromolecules*, 2009, **42**, 3358-3367.

41. D. S. Wu, S. J. Paddison, J. A. Elliott and S. J. Hamrock, *Langmuir*, 2010, **26**, 14308-14315.

42. G. Dorenbos and K. Morohoshi, *Journal of Materials Chemistry*, 2011, **21**, 13503-13515.

43. A. J. Appleby and F. R. Foulkes, *Fuel Cell Handbook*, Van Nostrand Reinhold, New York, NY, 1989.

44. P. Costamagna and S. Srinivasan, *Journal of Power Sources*, 2001, **102**, 253-269.

45. S. Banerjee and D. E. Curtin, *Journal of Fluorine Chemistry*, 2004, **125**, 1211-1216.

46. P. L. Antonucci, A. S. Arico, P. Creti, E. Ramunni and V. Antonucci, *Solid State Ionics*, 1999, **125**, 431–437.

47. S. Wasmus, A. Valeriu, G. D. Mateescu, D. A. Tryk and R. F. Savinell, *Journal of Membrane Science*, 2000, **185**, 78-85.

48. S. M. Haile, D. A. Boysen, C. R. I. Chisolm and R. B. Merle, *Nature*, 2001, **410**, 910-912.

49. R. Hooper, L. J. Lyons, M. K. Mapes, D. Schumacher, D. A. Moline and R. West, *Macromolecules*, 2001, **34**, 931-936.

50. R. Hooper, L. J. Lyons, D. Moline and R. West, *Organometallics*, 1999, **18**, 3249.

51. M. Popall, R. Buestrich, G. Semrau, G. Eichinger, M. Andrei, W. O. Parker, S. Skaarup and K. West, *Electrochimica Acta*, 2001, **46**, 1499-1508.

52. H. Schmidt, *Journal of Non-Crystalline Solids*, 1985, **73**, 681.

53. Q. Li, R. He, J. O. Jensen and N. J. Bjerrum, *Chemistry of Materials*, 2003, **15**, 4896-4915.

54. G. Alberti and M. Casciola, *Solid State Ionics*, 2001, **145**, 3-16.

55. J. T. Wang, R. F. Savinell, J. Wainright, M. Litt and H. Yu, *Electrochimica Acta*, 1996, **41**, 193-197.

56. Q. Li, R. He, J. O. Jensen and N. J. Bjerrum, *Fuel Cells*, 2004, **4**, 147-159.

57. J. M. Larson, S. J. Hamrock, G. M. Haugen, P. Pham, W. M. Lamanna and A. B. Moss, *Journal of Power Sources*, 2007, **172**, 108-114.

58. O. Savadogo and B. Xing, *Journal of New Materials for Electrochemical Systems*, 2000, **3**, 345-349.

59. K. D. Kreuer, A. Fuchs, M. Ise, M. Spaeth and J. Maier, *Electrochimica Acta*, 1998, **43**, 1281-1288.

60. M. F. H. Schuster, W. H. Meyer, M. Schuster and K. D. Kreuer, *Chemistry of Materials*, 2004, **16**, 329-337.

61. K. D. Kreuer, *Journal of Membrane Science*, 2001, **185**, 29-39.

62. H. R. Allcock, M. A. Hofmann, C. M. Ambler, S. N. Lvov, X. Y. Zhou, E. Chalkova and J. Weston, *Journal of Membrane Science*, 2002, **201**, 47-54.

63. W. Cui, J. Kerres and G. Eigenberger, *Separation and Purification Technology*, 1998, **14**, 145-154.

64. J. Kerres, A. Ullrich, F. Meier and T. Haring, *Solid State Ionics*, 1999, **125**, 243-249.

65. J. Kerres and A. Ullrich, *Separation and Purification Technology*, 2001, **22-23**, 1-15.

66. K. D. Kreuer, *Chemistry of Materials*, 1996, **8**, 610-641.

67. D. Marx, *ChemPhysChem*, 2006, **7**, 1848-1870.

68. C. J. D. Von Grotthuss, *Ann. Chim.*, 1806, **LVIII**, 54.

69. N. Agmon, *Chemical Physics Letters*, 1995, **244**, 456-462.

70. M. Eigen, *Angewandte Chemie International Edition*, 1964, **3**, 1-19.

71. M. Eigen and L. D. Maeyer, *Proceedings of the Royal Society A*, 1954, **247**, 505.

72. G. Zundel, *Advances in Chemical Physics*, 2000, **111**, 1.

73. D. E. Sagnella and M. E. Tuckerman, *Journal of Chemical Physics*, 1998, **108**, 2073-2083.

74. M. E. Tuckerman, D. Marx and M. Parrinello, *Nature*, 2002, **417**, 925-929.

75. O. Markovitch, H. Chen, S. Izvekov, F. Paesani, G. A. Voth and N. Agmon, *The Journal of Physical Chemistry B*, 2008, **112**, 9456-9466.

76. Y. J. Lee, T. Murakhtina, D. Sebastiani and H. W. Spiess, *Journal of the American Chemical Society*, 2007, **129**, 12406-12407.

77. S. Scheiner, *Annual Review of Physical Chemistry*, 1994, **45**, 23-56.

78. T. Komatsuzaki and I. Ohmine, *Molecular Simulation*, 1996, **16** 321-344.

79. S. J. Paddison, *Journal of New Materials for Electrochemical Systems*, 2001, **4**, 197-207.

80. S. J. Paddison, L. R. Pratt and T. A. Zawodzinski, *J. Phys. Chem. A*, 2001, **105**, 6266-6268.

81. R. Basnayake, G. R. Peterson, D. J. Casadonte and C. Korzeniewski, *J. Phys. Chem. B*, 2006, **110**, 23938-23943.

82. A. Venkatnathan, R. Devanathan and M. Dupuis, *J. Phys. Chem. B*, 2007, **111**, 7234-7244.

83. R. Devanathan, A. Venkatnathan and M. Dupuis, *J. Phys. Chem. B*, 2007, **111**, 8069-8079.

84. R. Devanathan, A. Venkatnathan and M. Dupuis, *J. Phys. Chem. B*, 2007, **111**, 13006-13013.

85. S. J. Paddison, L. R. Pratt, T. Zawodzinski and D. W. Reagor, *Fluid Phase Equilibria*, 1998, **150**, 235-243.

86. S. J. Paddison and E. Tschuikow-Roux, *J. Phys. Chem. A*, 1998, **102**, 6191-6199.

87. M. Eikerling, S. J. Paddison and T. A. Zawodzinski, *Journal of New Materials for Electrochemical Systems*, 2002, **5**, 15-23.

88. S. Urata, J. Irisawa, A. Takada, S. Tsuzuki, W. Shinoda and M. Mikami, *Physical Chemistry Chemical Physics*, 2004, **6**, 3325-3332.

89. S. J. Paddison, K. D. Kreuer and J. Maier, *Physical Chemistry Chemical Physics*, 2006, **8**, 4530-4542.

90. L. Vilciauskas, S. J. Paddison and K.-D. Kreuer, *J. Phys. Chem. A*, 2009, **113**, 9193-9201.

91. C. Wang and S. J. Paddison, *Physical Chemistry Chemical Physics*, 2009, **12**, 970-981.

92. T. J. Peckham and S. Holdcroft, *Adv. Mater.*, 2010, **22**, 4667-4690.

93. W. Y. Hsu and T. D. Gierke, *Journal of Membrane Science*, 1983, **13**, 307-326.

94. A. Eisenberg and H. L. Yeager, *Perfluorinated ionomer membranes*, American Chemical Society, Washington, DC, 1982.

95. G. Gebel, *Polymer*, 2000, **41**, 5829-5838.

96. T. Xue, J. S. Trent and K. Osseo-Asare, *Journal of Membrane Science*, 1989, **45**, 261-271.

97. Z. Porat, J. R. Fryer, M. Huxham and I. Rubinstein, *J. Phys. Chem.*, 1995, **99**, 4667-4671.

98. J. A. Elliott, S. Hanna, A. M. S. Elliott and G. E. Cooley, *Physical Chemistry Chemical Physics*, 1999, **1**, 4855-4864.

99. A. Vishnyakov and A. V. Neimark, *J. Phys. Chem. B*, 2001, **105**, 7830-7834.

100. S. Urata, J. Irisawa, A. Takada, W. Shinoda, S. Tsuzuki and M. Mikami, *J. Phys. Chem. B*, 2005, **109**, 4269-4278.

101. S. J. Paddison, *Annual Review of Materials Research*, 2003, **33**, 289-319.

102. S. J. Paddison and J. A. Elliott, *J. Phys. Chem. A*, 2005, **109**, 7583-7593.

103. S. J. Paddison and J. A. Elliott, *Physical Chemistry Chemical Physics*, 2006, **8**, 2193 - 2203.

104. J. A. Elliott, D. Wu, S. J. Paddison and R. B. Moore, *Soft Matter*, 2011, **7**, 6820-6827.

105. S. Yamamoto and S. A. Hyodo, *Polym. J.*, 2003, **35**, 519-527.

106. K. D. Kreuer, *Solid State Ionics*, 1997, **97**, 1-15.

107. J. Ceynowa, *Polymer*, 1978, **19**, 73-76.

108. S. Rieberer and K. H. Norian, *Ultramicroscopy*, 1992, **41**, 225-233.

109. B. P. Kirkmeyer, R. C. Puetter, A. Yahil and K. I. Winey, *Journal of Polymer Science Part B: Polymer Physics*, 2003, **41**, 319-326.

110. J. H. Laurer and K. I. Winey, *Macromolecules*, 1998, **31**, 9106-9108.

111. B. P. Kirkmeyer, A. Taubert, J.-S. Kim and K. I. Winey, *Macromolecules*, 2002, **35**, 2648-2653.

112. S. Yakovlev and M. Libera, *Microscopy and Microanalysis*, 2006, **12**, 996-997.

113. M. Libera and S. Yakovlev, *Microscopy and Microanalysis*, 2007, **13**, 1256-1257.

114. A. Sousa, A. Aitouchen and M. Libera, *Ultramicroscopy*, 2006, **106**, 130-145.

115. H. W. Rollins, T. Whiteside, G. J. Shafer, J.-J. Ma, M.-H. Tu, J.-T. Liu, D. D. DesMarteau and Y.-P. Sun, *Journal of Materials Chemistry*, 2000, **10**, 2081-2084.

116. D. A. Blom, J. R. Dunlap, T. A. Nolan and L. F. Allard, *Journal of the Electrochemical Society*, 2003, **150**, A414.

117. W. Kubo, K. Yamauchi, K. Kumagai, M. Kumagai, K. Ojima and K. Yamada, *J. Phys. Chem. C*, 2010, **114**, 2370-2374.

118. J. Drennan, R. Webb, K. Nogita, R. Knibbe, G. Auchterlonie, K. Tatenuma and J. Hunter, *Solid State Ionics*, 2006, **177**, 1649-1654.

119. F. Scheiba, N. Benker, U. Kunz, C. Roth and H. Fuess, *Journal of Power Sources*, 2008, **177**, 273-280.

120. S. Yakovlev and K. H. Downing, *Physical Chemistry Chemical Physics*, 2013, **15**, 1052-1064.

121. M. Praprotnik, L. D. Site and K. Kremer, *Annual Review of Physical Chemistry*, 2008, **59**, 545-571.

122. D. Young, *Computational Chemistry: A Practical Guide for Applying Techniques to Real World Problems*, John Wiley & Sons, New York, NY, 2001.

123. F. Jensen, *Introduction to Computational Chemistry*, John Wiley & Sons, New York, NY, 1999.

124. A. Hinchliffe, *Modelling Molecular Structures*, John Wiley & Sons, Chichester, UK, 2000.

125. D. D. Fitts, *Principles of Quantum Mechanics As Applied to Chemistry and Chemical Physics*, Cambridge University, Cambridge, UK, 1999.

126. W. Kohn, A. D. Becke and R. G. Parr, *J. Phys. Chem.*, 1996, **100**, 12974-12980.

127. E. G. Lewars, *Computational Chemistry Introduction to the Theory and Applications of Molecular and Quantum Mechanics*, Kluwer Academic, New York, NY, 2004

128. C. J. Cramer, *Essentials of Computational Chemistry: Theories and Models*, John Wiley & Sons, New York, NY, 2004.

129. P. Hohenberg and W. Kohn, *Physical Review*, 1964, **136**, B864.

130. W. Kohn and L. J. Sham, *Physical Review*, 1965, **140**, A1133.

131. A. D. Becke, *Physical Review A*, 1988, **38**, 3098.

132. S. F. Sousa, P. A. Fernandes and M. J. Ramos, *The Journal of Physical Chemistry A*, 2007, **111**, 10439-10452.

133. S. J. Paddison and T. A. Zawodzinski Jr, *Solid State Ionics*, 1998, **113-115**, 333-340.

134. R. Martin, *Electronic Structure: Basic Theory and Practical Methods*, Cambridge University Press, Cambridge, UK, 2004.

135. R. D. Groot and P. B. Warren, *Journal of Chemical Physics*, 1997, **107**, 4423-4435.

136. in *Materials Studio*, Accelrys Inc., San Diego, CA, USA, 2005.

137. P. J. Hoogerbrugge and J. M. V. A. Koelman, *EPL (Europhysics Letters)*, 1992, **19**, 155.

138. D. B. Williams and B. C. Carter, *Transmission Electron Microscopy : A Textbook for Materials Science*, Springer, Boston, MA, 2009.

139. G. H. Michler, *Electron Microscopy of Polymers*, Springer, Berlin, Germany, 2008.

140. C. J. G. Plummer and H. H. Kausch, *Polymer Bulletin*, 1996, **37**, 393-397.

141. S. J. Pennycook, *Ultramicroscopy*, 1989, **30**, 58-69.

142. S. Yakovlev, X. Wang, P. Ercius, N. P. Balsara and K. H. Downing, *Journal of the American Chemical Society*, 2011, **133**, 20700-20703.

143. O. L. Krivanek, M. F. Chisholm, V. Nicolosi, T. J. Pennycook, G. J. Corbin, N. Dellby, M. F. Murfitt, C. S. Own, Z. S. Szilagyi, M. P. Oxley, S. T. Pantelides and S. J. Pennycook, *Nature*, 2010, **464**, 571-574.

144. S. Yakovlev and M. Libera, *Micron*, 2008, **39**, 734-740.

145. R. F. Egerton, *Rep. Prog. Phys.*, 2009, **72**, 016502.

146. V. J. Keast, A. J. Scott, R. Brydson, D. B. Williams and J. Bruley, *Journal of Microscopy*, 2001, **203**, 135-175.

147. K. Varlot, J. M. Martin, C. Quet and Y. Kihn, *Ultramicroscopy*, 1997, **68**, 123-133.

148. L. F. Drummy, R. J. Davis, D. L. Moore, M. Durstock, R. A. Vaia and J. W. P. Hsu, *Chemistry of Materials*, 2010, **23**, 907-912.

149. S. Yakovlev, M. Misra, S. Shi, E. Firlar and M. Libera, *Ultramicroscopy*, 2010, **110**, 866-876.

150. M. L. Baker, J. Zhang, S. J. Ludtke and W. Chiu, *Nat. Protocols*, 2010, **5**, 1697-1708.

151. A. R. Spurr, *Journal of ultrastructure research*, 1969, **26**, 31-43.

152. M. J. Frisch, G. W. Trucks, H. B. Schlegel, G. E. Scuseria, M. A. Robb, J. R. Cheeseman, V. G. Zakrzewski, J. J. A. Montgomery, R. E. Stratmann, J. C. Burant, S. Dapprich, J. M. Millam, A. D. Daniels, K. N. Kudin, M. C. Strain, O. Farkas, J. Tomasi, V. Barone, M. Cossi, R. Cammi, B. Mennucci, C. Pomelli, C. Adamo, S. Clifford, J. Ochterski, G. A. Petersson, P. Y. Ayala, Q. Cui, K. Morokuma, N. Rega, P. Salvador, J. J. Dannenberg, D. K. Malick, A. D. Rabuck, K. Raghavachari, J. B. Foresman, J. Cioslowski, J. V. Ortiz, A. G. Baboul, B. B. Stefanov, G. Liu, A. Liashenko, P. Piskorz, I. Komaromi, R. Gomperts, R. L. Martin, D. J. Fox, T. Keith, M. A. Al-Laham, C. Y. Peng, A. Nanayakkara, M. Challacombe, P. M. W. Gill, B. Johnson, W.Chen, M. W. Wong, J. L. Andres, C. Gonzalez, M. Head-Gordon, E. S. Replogle and J. A. Pople, in *Gaussian 03*, Gaussian, Inc., Wallingford CT, Revision C.02 edn., 2004.

153. C. C. J. Roothaan, *Reviews of Modern Physics*, 1951, **23**, 69.

154. J. A. Pople and R. K. Nesbet, *Journal of Chemical Physics*, 1954, **22**, 571-572.

155. R. McWeeny and G. Diercksen, *Journal of Chemical Physics*, 1968, **49**, 4852-4856.

156. H. B. Schlegel, *J. Comput. Chem.*, 1982, **3**, 214-218.

157. A. D. Becke, *Journal of Chemical Physics*, 1993, **98**, 5648-5652.

158. C. Lee, W. Yang and R. G. Parr, *Physical Review B*, 1988, **37**, 785.

159. A. D. McLean and G. S. Chandler, *Journal of Chemical Physics*, 1980, **72**, 5639-5648.

160. N. Kobko and J. J. Dannenberg, *J. Phys. Chem. A*, 2001, **105**, 1944-1950.

161. S. F. Boys and F. Bernardi, *Molecular Physics*, 1970, **19**, 553 - 566

162. S. Simon, M. Duran and J. J. Dannenberg, *J. Phys. Chem. A*, 1999, **103**, 1640-1643.

163. J. Garza, J. Z. Ramirez and R. Vargas, *J. Phys. Chem. A*, 2005, **109**, 643-651.

164. S. Grimme, *Wiley Interdisciplinary Reviews: Computational Molecular Science*, 2011, **1**, 211-228.

165. S. Grimme, *J. Comput. Chem.*, 2006, **27**, 1787-1799.

166. J.-D. Chai and M. Head-Gordon, *Physical Chemistry Chemical Physics*, 2008, **10**, 6615-6620.

167. S. J. Paddison and J. A. Elliott, *Solid State Ionics*, 2006, **177**, 2385-2390.

168. D. Wei and D. R. Salahub, *Journal of Chemical Physics*, 1994, **101**, 7633-7642.

169. J. Lobaugh and G. A. Voth, *Journal of Chemical Physics*, 1996, **104**, 2056-2069.

170. J. A. Morrone and R. Car, *Physical Review Letters*, 2008, **101**, 017801.

171. V. Atanasov, M. Buerger, A. Wohlfarth, M. Schuster, K.-D. Kreuer and J. Maier, *Polymer Bulletin*, 2011, 1-10.

172. C.-H. Ma, T. L. Yu, H.-L. Lin, Y.-T. Huang, Y.-L. Chen, U. S. Jeng, Y.-H. Lai and Y.-S. Sun, *Polymer*, 2009, **50**, 1764-1777.

173. E. Sezer, *Comput. Geosci.*, 2010, **36**, 391-396.

174. V. Arcella, C. Troglia and A. Ghielmi, *Industrial & Engineering Chemistry Research*, 2005, **44**, 7646-7651.

175. A. S. Arico, V. Baglio, A. Di Blasi, V. Antonucci, L. Cirillo, A. Ghielmi and V. Arcella, *Desalination*, 2006, **199**, 271-273.

176. S. J. Hamrock and M. A. Yandrasits, *Polym. Rev.*, 2006, **46**, 219-244.

177. W. Y. Hsu and T. D. Gierke, *Journal of the Electrochemical Society*, 1982, **129**, C121-C121.

178. W. Y. Hsu and T. D. Gierke, *Journal of Membrane Science*, 1983, **13**, 307-326.

179. L. Rubatat, G. Gebel and O. Diat, *Macromolecules*, 2004, **37**, 7772-7783.

180. K. Schmidt-Rohr and Q. Chen, *Nature Materials*, 2008, **7**, 75-83.

181. P. Rez and D. A. Muller, *Annual Review of Materials Research*, 2008, **38**, 535-558.

182. V. J. Keast, *Journal of Electron Spectroscopy and Related Phenomena*, 2005, **143**, 97-104.

183. E. Clark, in *Physical Properties of Polymers Handbook*, ed. J. Mark, Springer New York, 2007, ch. 38, pp. 619-624.

184. M. D'Amore, G. Talarico and V. Barone, *Journal of the American Chemical Society*, 2006, **128**, 1099-1108.

185. S. J. Clark, M. D. Segall, C. J. Pickard, P. J. Hasnip, M. I. J. Probert, K. Refson and M. C. Payne, *Zeitschrift fur Kristallographie*, 2005, **220**, 567-570.

186. J. P. Perdew, A. Ruzsinszky, G. I. Csonka, O. A. Vydrov, G. E. Scuseria, L. A. Constantin, X. Zhou and K. Burke, *Physical Review Letters*, 2008, **100**, 136406.

187. J. J. Ritsko, *The Journal of Chemical Physics*, 1979, **70**, 5343-5349.

188. J. J. Ritsko and R. W. Bigelow, *The Journal of Chemical Physics*, 1978, **69**, 4162-4170.

189. M. K. Barbarez, D. K. D. Gupta and D. Hayward, *Journal of Physics D: Applied Physics*, 1977, **10**, 1789.

190. C. W. Bunn and E. R. Howells, *Nature*, 1954, **174**, 549-551.

191. J. J. Weeks, E. S. Clark and R. K. Eby, *Polymer*, 1981, **22**, 1480-1486.

192. A. Klug and R. E. Franklin, *Discussions of the Faraday Society*, 1958, **25**, 104-110.

193. H. D. Chanzy, P. Smith and J.-F. Revol, *Journal of Polymer Science Part C: Polymer Letters*, 1986, **24**, 557-563.

194. B. L. Farmer and R. K. Eby, *Polymer*, 1985, **26**, 1944-1952.

195. M. Springborg and M. Lev, *Physical Review B*, 1989, **40**, 3333-3339.

196. D. G. Castner, K. B. Lewis, D. A. Fischer, B. D. Ratner and J. L. Gland, *Langmuir*, 1993, **9**, 537-542.

197. L. J. Gamble, B. Ravel, D. A. Fischer and D. G. Castner, *Langmuir*, 2002, **18**, 2183-2189.

198. C. Ziegler, T. Schedel-Niedrig, G. Beamson, D. T. Clark, W. R. Salaneck, H. Sotobayashi and A. M. Bradshaw, *Langmuir*, 1994, **10**, 4399-4402.

Appendices

Appendix A. Simulations of EELS

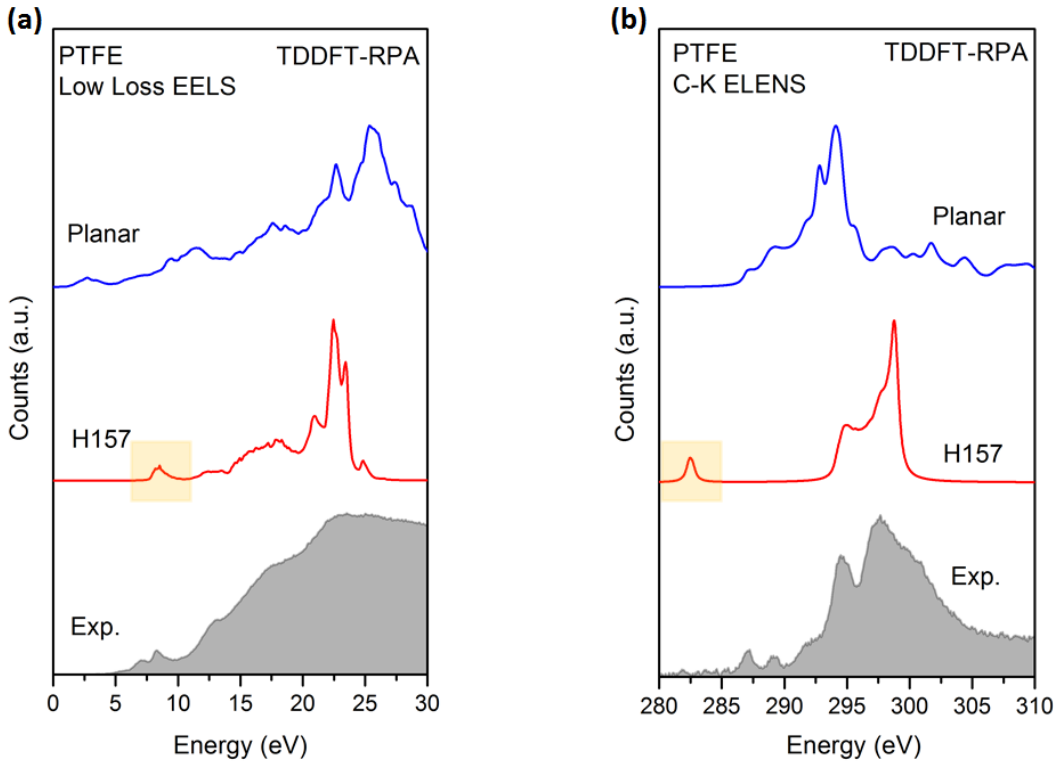

Figure A.1. Calculated low loss EELS and C-K ELNES for PTFE using TDDFT-RPA method. The highlighted areas show the features dependent upon the presence of helical conformations.

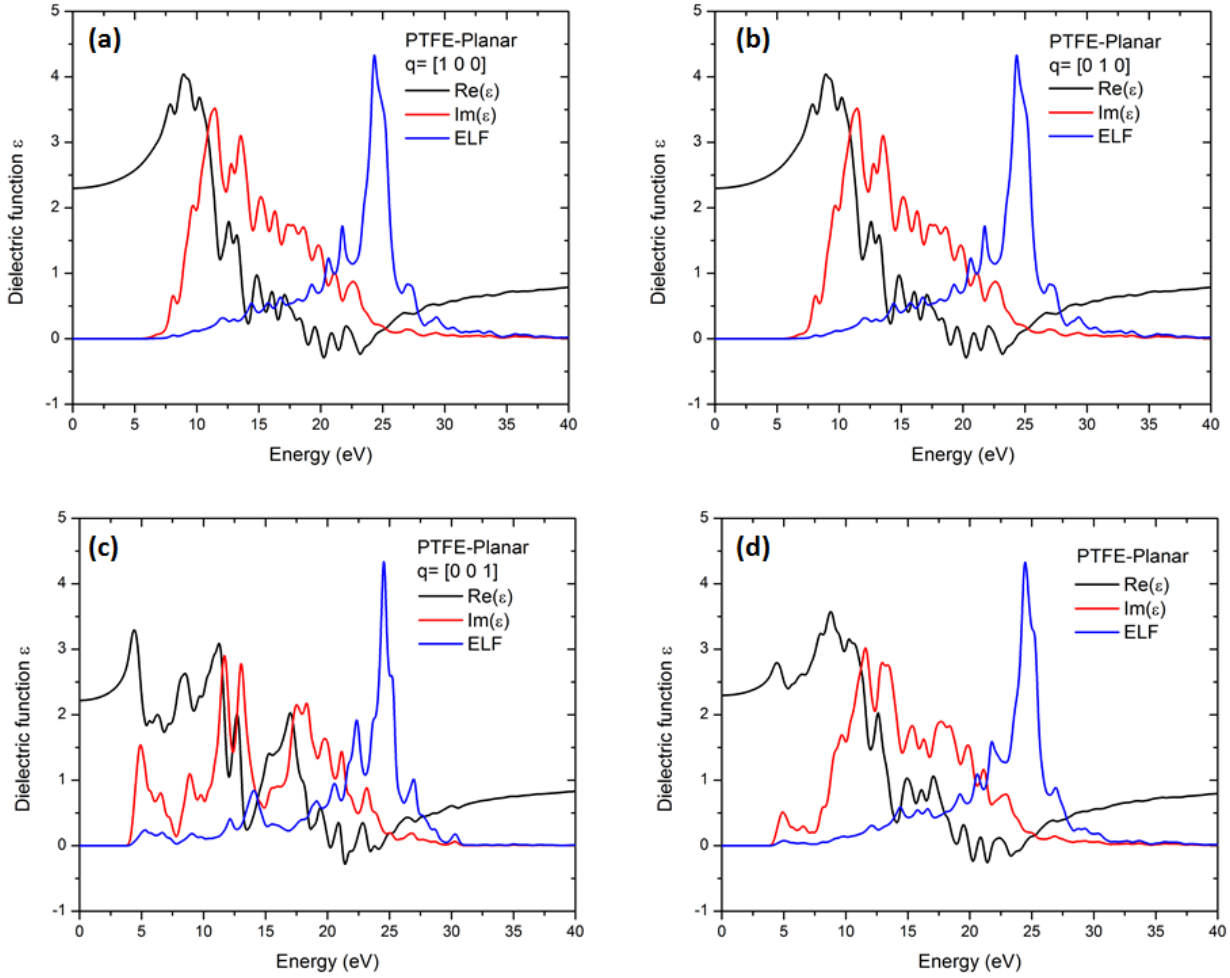

Figure A.2. Calculated real and imaginary parts of the dielectric function and corresponding energy loss function of planar PTFE as a function of momentum transfer **q**.

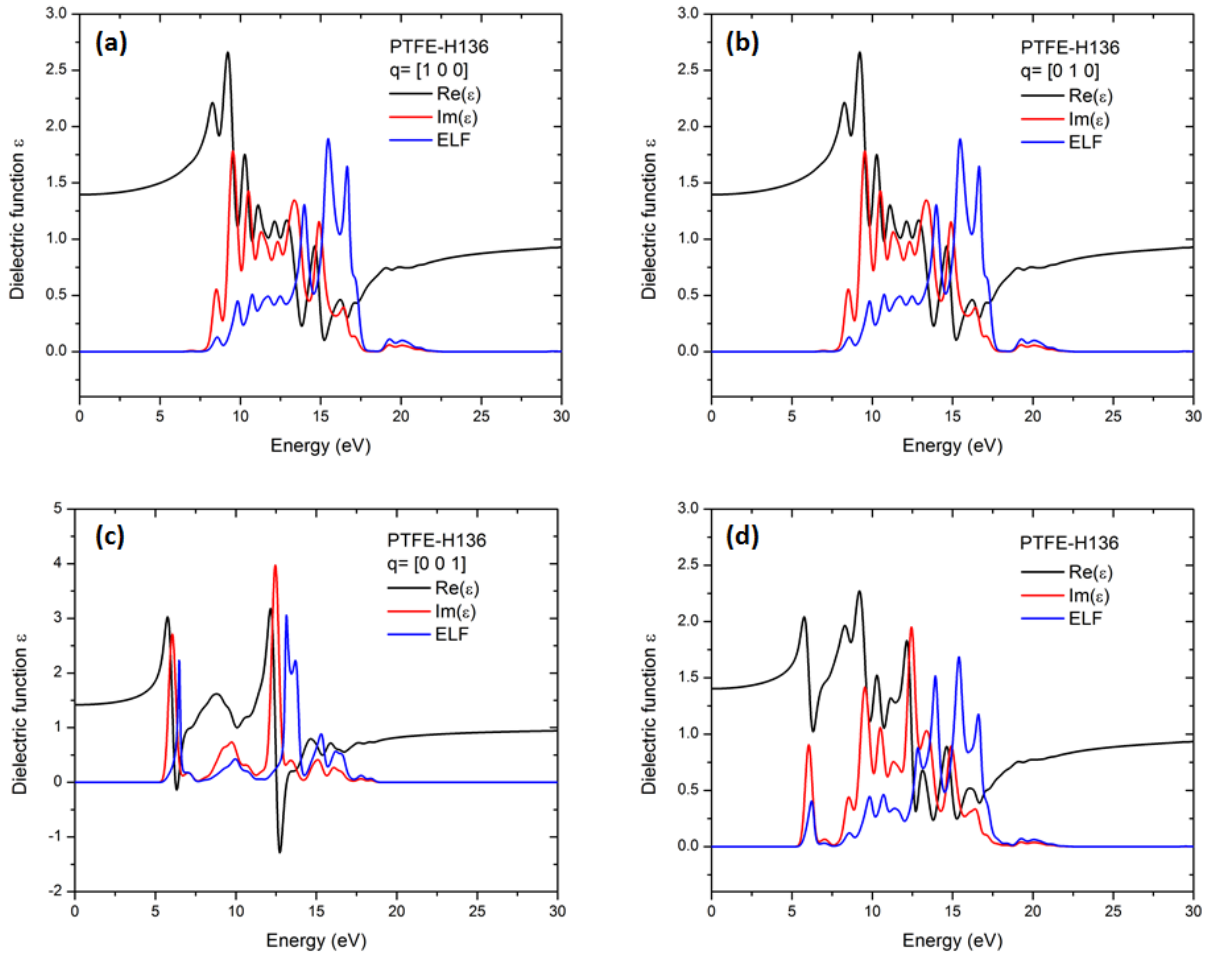

Figure A.3. Calculated real and imaginary parts of the dielectric function and corresponding energy loss function of helical H136 PTFE as a function of momentum transfer **q**.

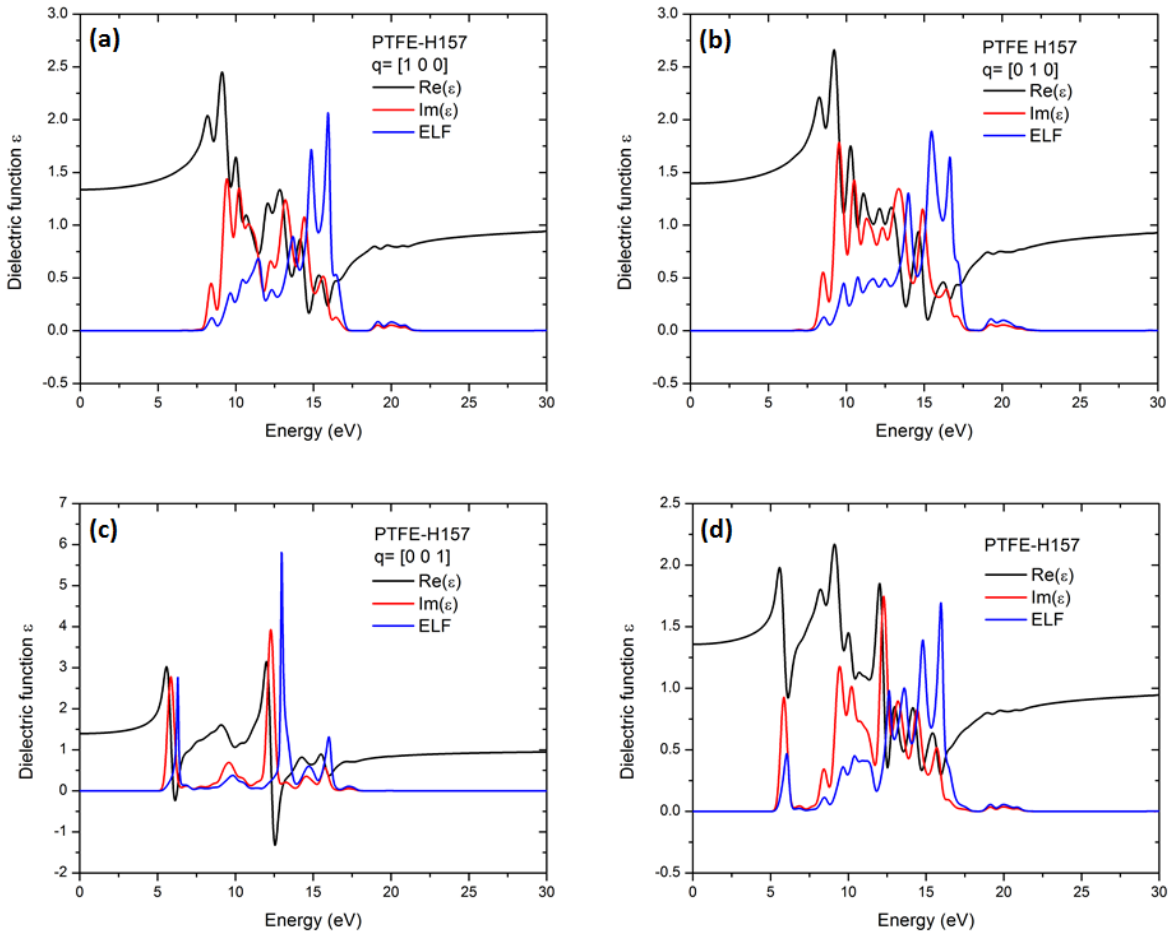

Figure A.4. Calculated real and imaginary parts of the dielectric function and corresponding energy loss function of helical H157 PTFE as a function of momentum transfer **q**.

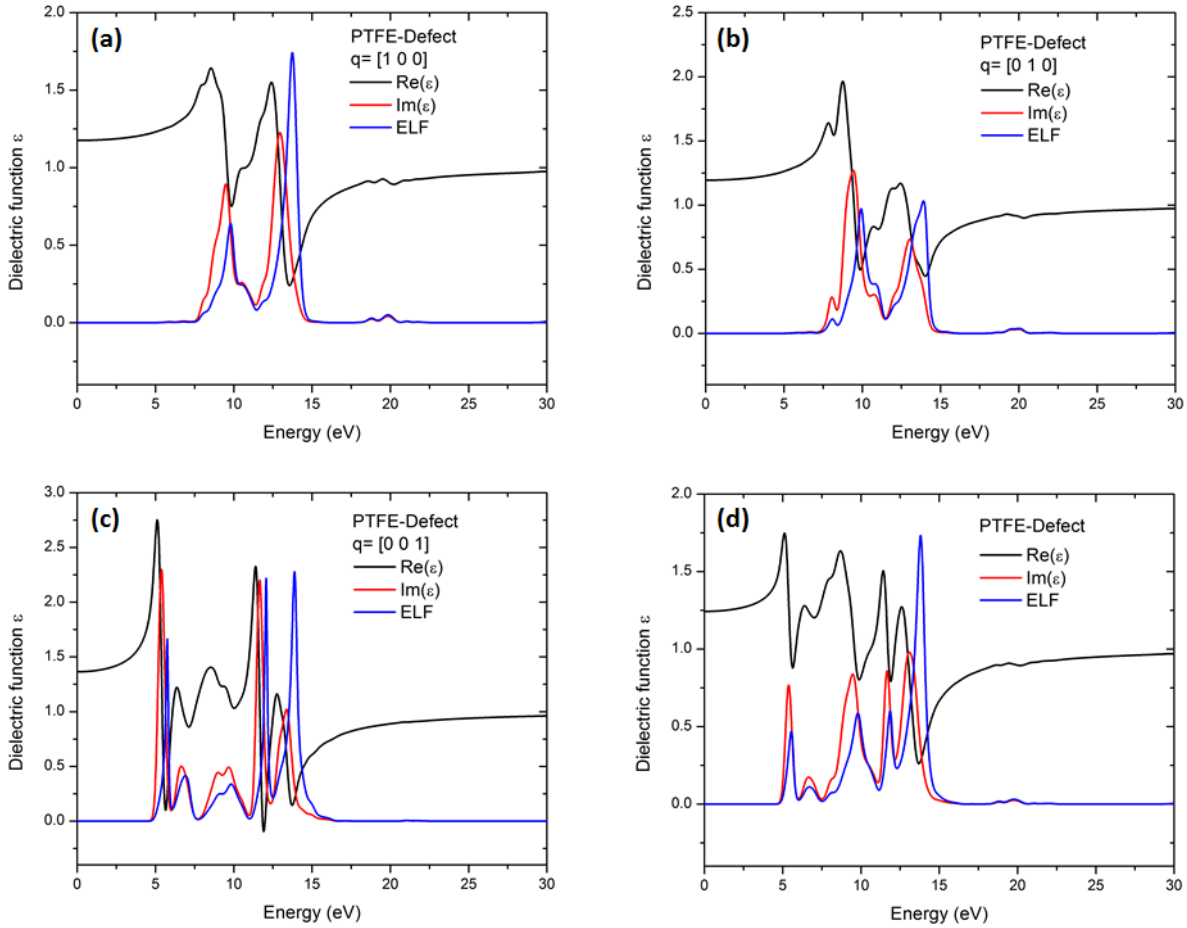

Figure A.5. Calculated real and imaginary parts of the dielectric function and corresponding energy loss function of helical defected PTFE as a function of momentum transfer **q**.

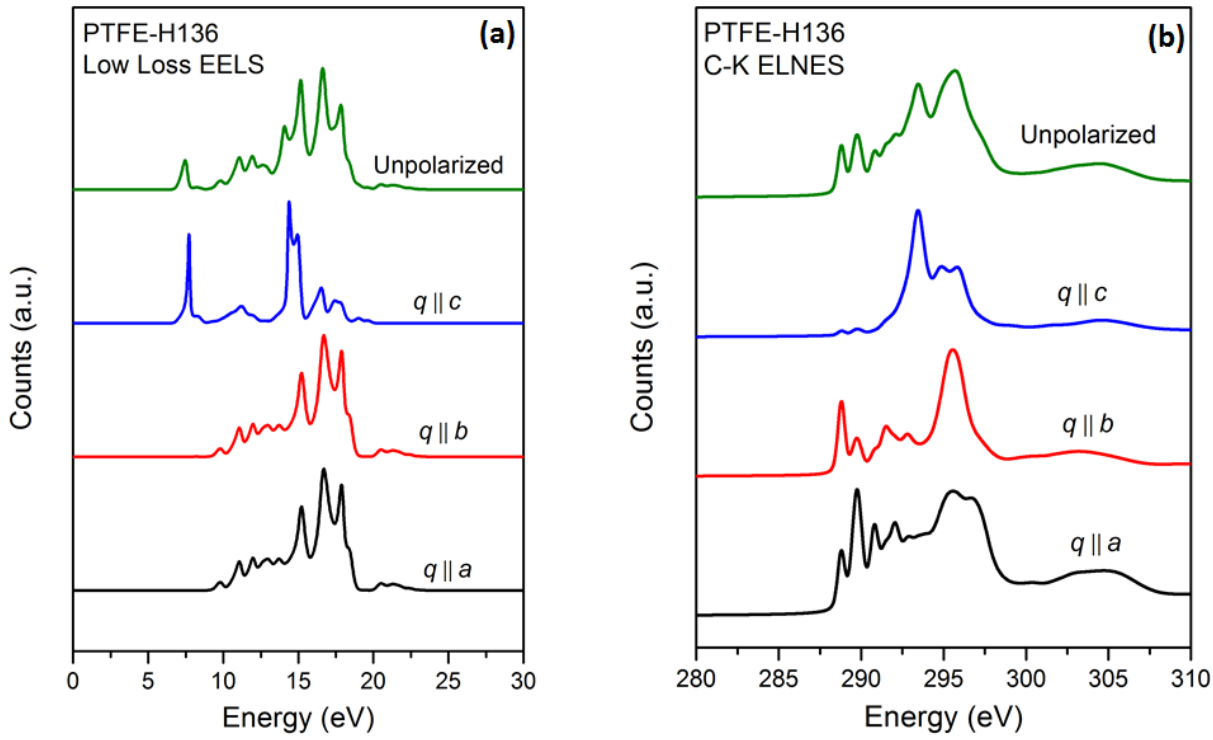

Figure A.6. Calculated low loss EELS and C-K ELNES for PTFE-H136 as a function of momentum transfer **q**.

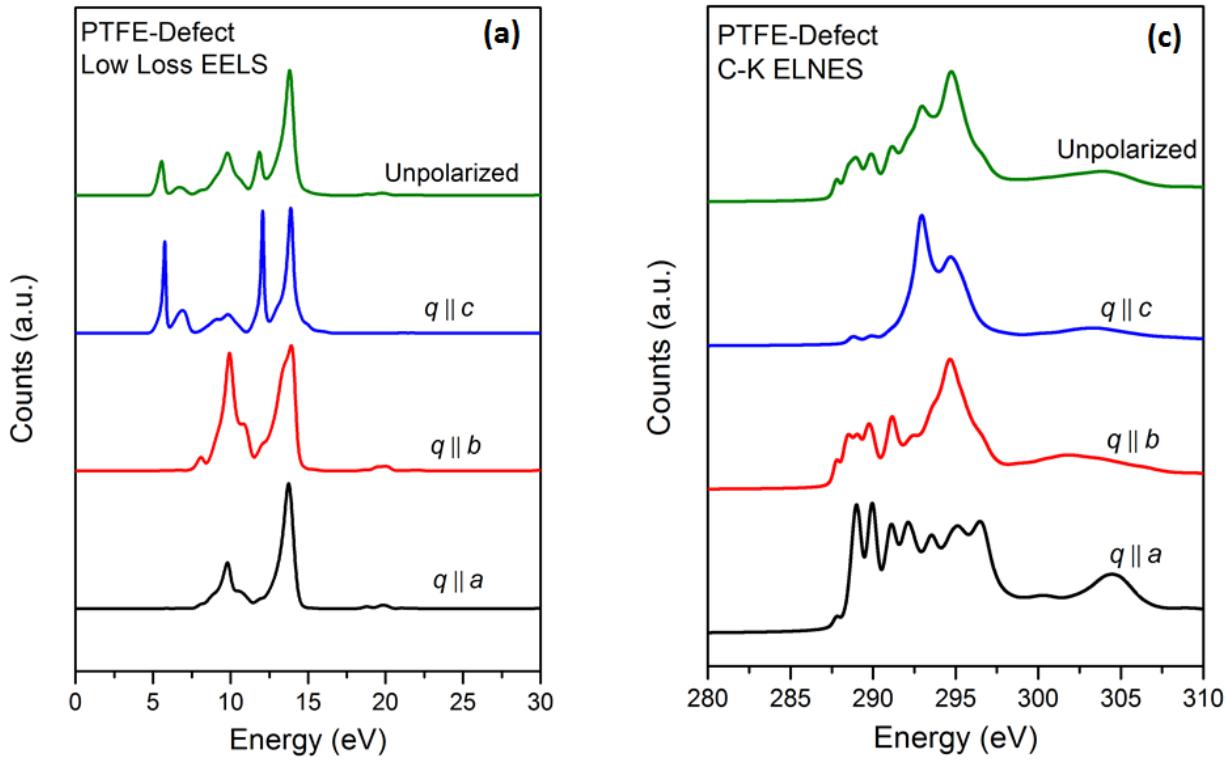

Figure A.7. Calculated low loss EELS and C-K ELNES for defected PTFE as a function of momentum transfer **q**.

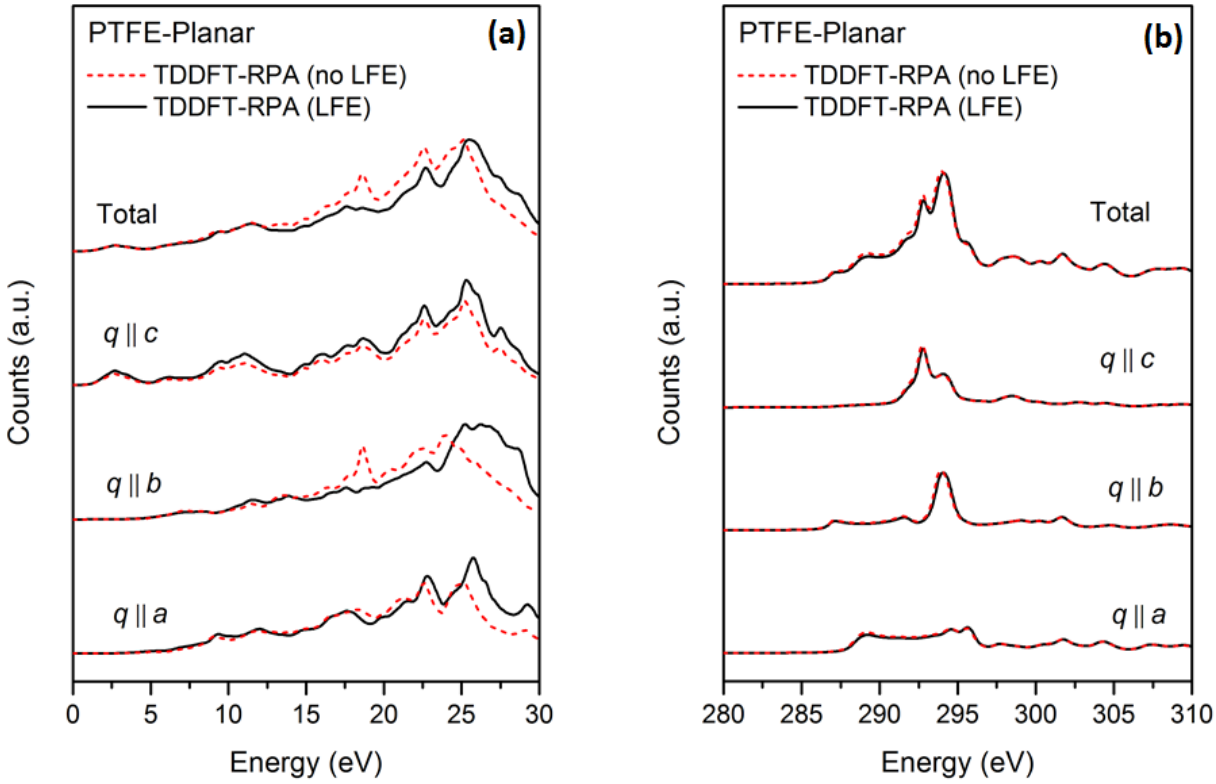

Figure A.8. Calculated low loss EELS and C-K ELNES for planar PTFE using TDDFT-RPA method with and without consideration of the local field effect.

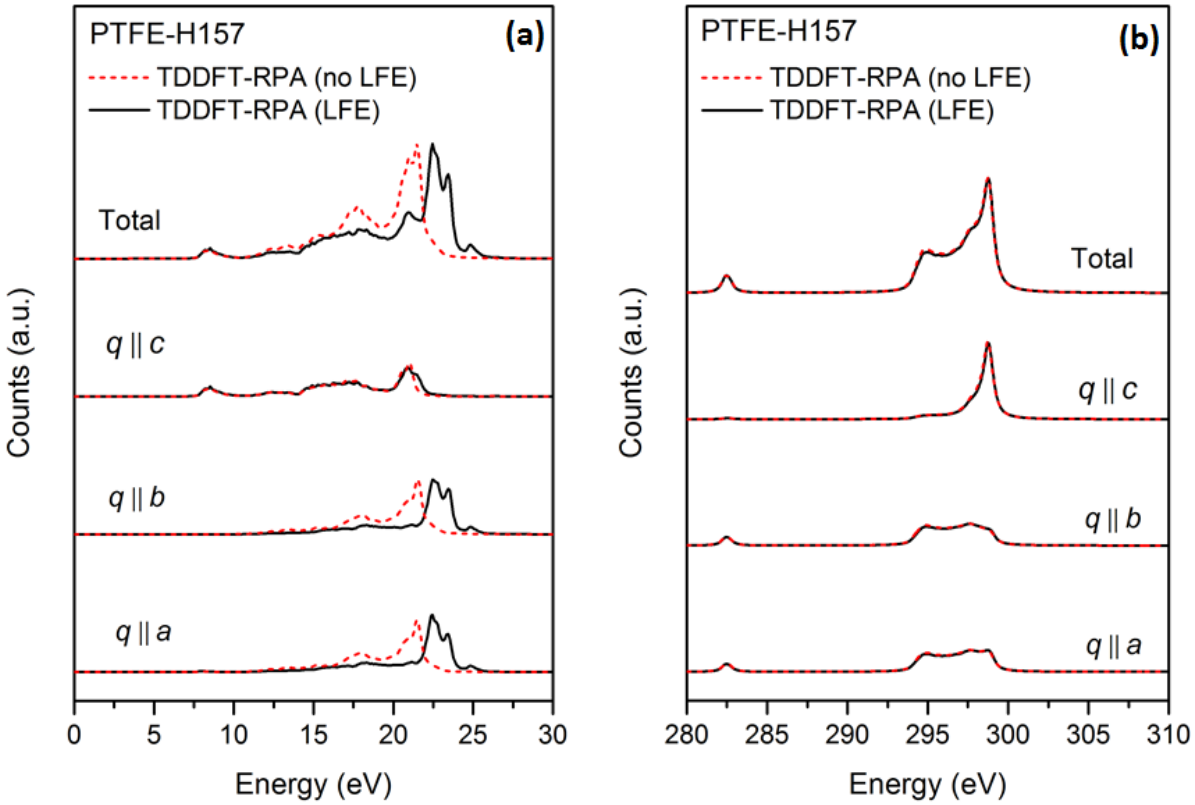

Figure A.9. Calculated low loss EELS and C-K ELNES for PTFE H157 using TDDFT-RPA method with and without consideration of the local field effect.

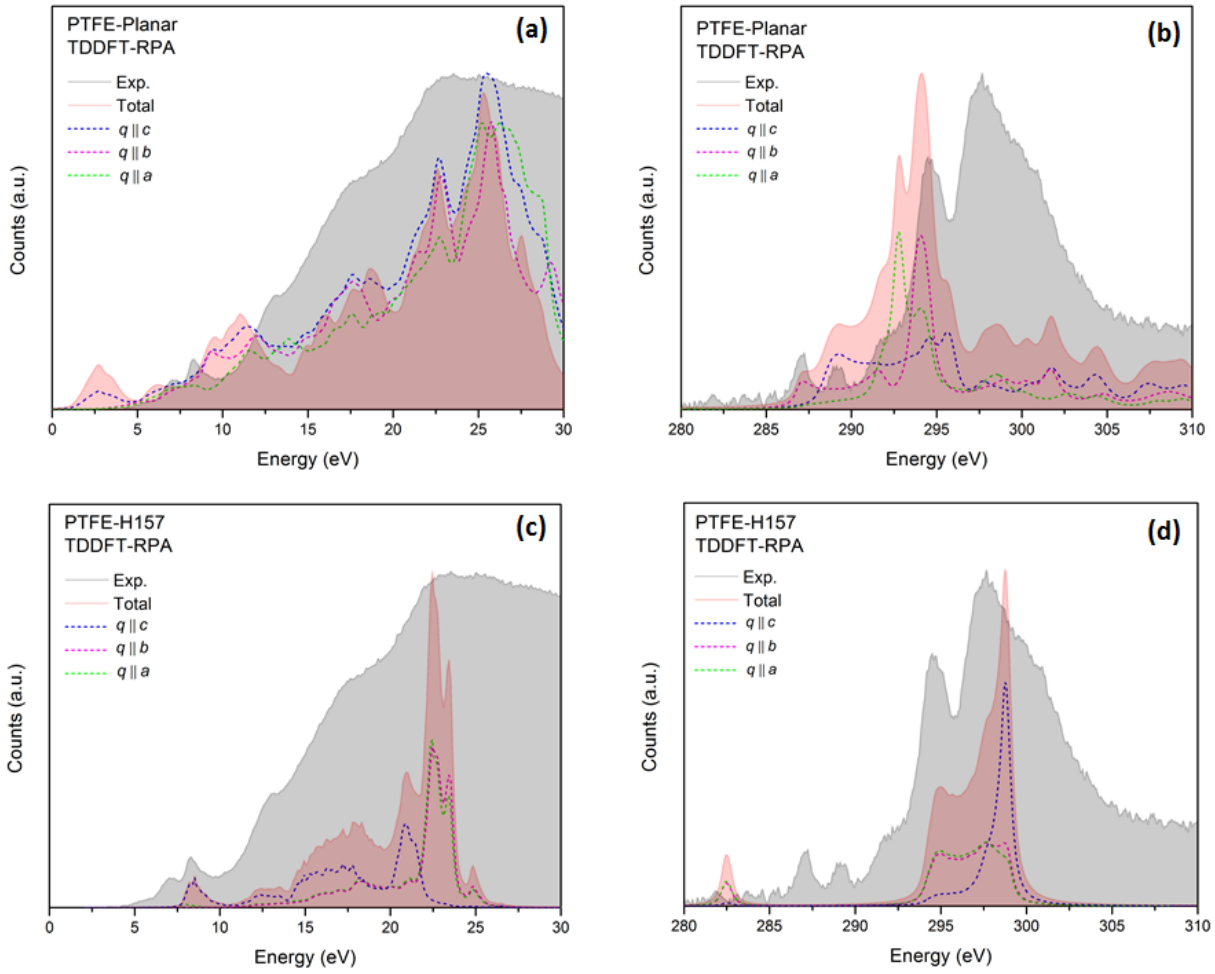

Figure A.10. Calculated low loss EELS and C-K ELNES for planar and helical H157 PTFE using TDDFT-RPA method compared with experimental results.

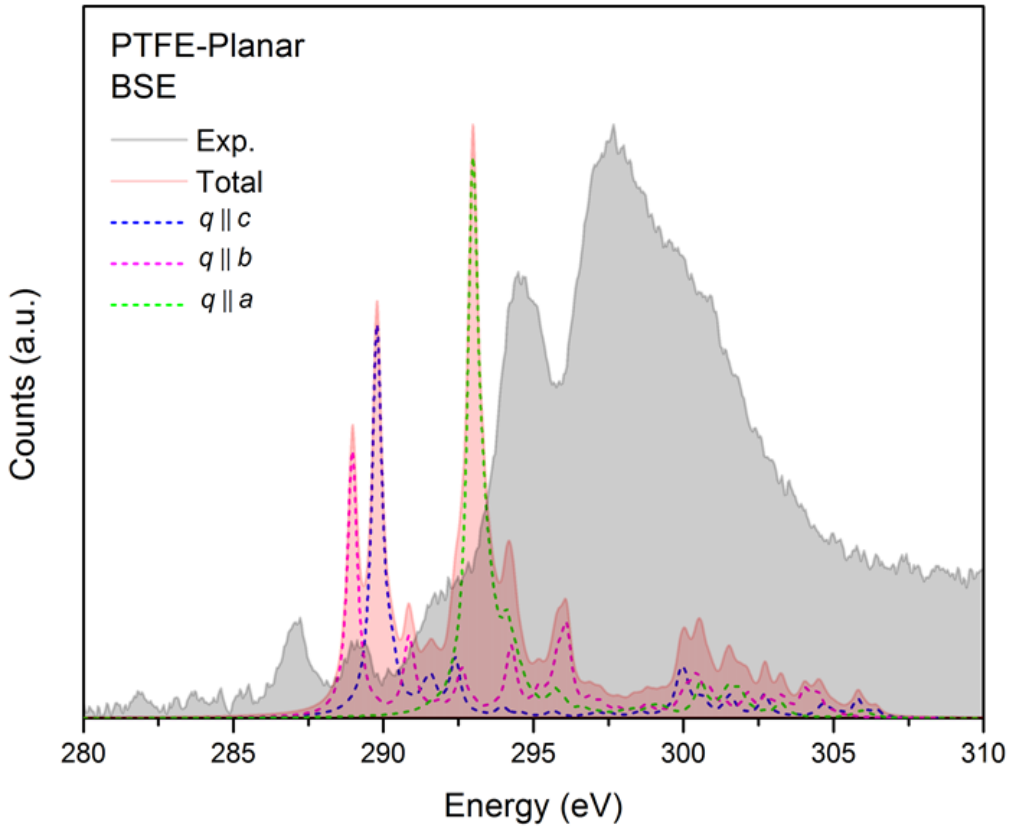

Figure A.11. Calculated C-K ELNES for planar H157 PTFE using BSE method compared with experimental results.

Appendix B. Selected Publications and Presentations

Publications:

1. **Wang, C**.; Krishnan, V.; Wu, D.; Bledsoe, R.; Paddison, S.J.; Duscher, G., Evaluation of the Microstructure of Dry and Hydrated Perfluorosulfonic Acid Ionomers: Microscopy and Simulations, *Journal of Materials Chemistry A*, 2013, 1, 938-944.
2. **Wang, C.**; Paddison, S. J., Hydration and Proton Transfer in Highly Sulfonated Poly(phenylene sulfone) Ionomer: An Ab Initio Study, *Journal of Physical Chemistry A*, 2013, 117(3), 650-660.
3. **Wang, C.**; Clark, J. K.; Kumar, M.; Paddison, S. J., An Ab Initio Study of the Primary Hydration and Proton Transfer of CF_3SO_3H and $CF_3O(CF_2)_2SO_3H$: Effects of the Hybrid Functional and Inclusion of Diffuse functions, *Solid State Ionics*, 2011, 199-200, 6-13.

Presentations:

1. **Wang, C**; Paddison, S.J and Duscher, G, "Mesoscale Modeling of Hydrated Morphology in Sulfonated Poly(phenylene sulfone) Ionomers", *221st ECS Meeting,* Seattle, WA, May 2012. (*Oral*)
2. **Wang, C** and Paddison, S.J, "Microsolvation and Proton Transfer in Highly Sulfonated Poly(phenylene sulfone) Ionomers", *219th ECS Meeting*, Montreal, QC, Canada, May 2011. (*Oral*)
3. **Wang, C**; Krishnan, V; Duscher, G and Paddison, S.J, "Evaluation of the Microstructure of Dry and Hydrated Perfluorosulfonic Acid Ionomers", *37th Annual Fall Meeting of the Appalachian Regional Microscopy Society*, Knoxville, TN, Oct. 2012.
4. **Wang, C** and Paddison, S.J, "Multiscale Modeling of Highly Sulfonated Poly(phenylene sulfone) Ionomers", *Fall Creek Falls 2011 Conference - Virtualizing Energy*, Gatlinburg, TN, Sept. 2011.
5. **Wang, C**; Krishnan, V; Duscher, G and Paddison, S.J, "Investigating the Microstructure of Perfluorosulfonic Acid (PFSA) Ionomers Used as Polymer Electrolyte Membranes", *Microscopy & Microanalysis 2011 Meeting*, Nashville, TN, Aug. 2011.
6. **Wang, C** and Paddison, S.J, "Proton transfer in highly sulfonated poly(phenylene sulfone) polymers: An ab initio study", *PacifiChem 2010*, Honolulu, HI, Dec. 2010.

Vita

Chen Wang was born on Jan. 28th, 1982 in Suzhou, China. After he received his B.S. in materials science at the Nanjing University of Technology in 2004, he worked as a product engineer in an FRP composite materials manufacturer for two years. In 2006, Chen received a graduate student assistantship from the University of Alabama, Huntsville, and joined Dr. Stephen J. Paddison's research group with a primary focus on computational studies of PEM materials. He graduated in Aug. 2008 with a Master's degree in materials science under the supervision of Dr. Paddison, and began his Ph.D. studies in chemical engineering at the University of Tennessee, Knoxville in Jan. 2009. His research involves using ab initio electronic structure calculations to investigate various ionomers for application as fuel cell membranes. He also used electron microscopic imaging and analysis to validate membrane morphologies obtained from DPD and/or CGMD simulations. His work resulted in three publications by the time he received his Ph.D. in the summer of 2013 with two others in preparation.